ACTIVITY REPORT 2020

CORSO DI DOTTORATO DI RICERCA IN FISICA
UNIVERSITÀ DEGLI STUDI DI MESSINA

Dipartimento di Scienze Matematiche e Informatiche, Scienze Fisiche e Scienze della Terra (MIFT)

COORDINATORE: VINCENZA CRUPI

Coordinatore del Dottorato di Ricerca in Fisica

Prof.ssa Vincenza Crupi

Comitato Organizzatore

Prof.ssa Vincenza Crupi
Dott. Giuseppe Paladini

Collegio Docente

Docenti e Ricercatori UNIME

Prof.ssa Branca Caterina
Dott. Corsaro Carmelo
Dott. Costa Dino
Prof.ssa Crupi Vincenza
Dott. Di Stefano Omar
Prof.ssa Fazio Enza
Prof. Magazù Salvatore
Prof. Majolino Domenico
Prof. Mandaglio Giuseppe

Prof. Neri Fortunato
Prof.ssa Orecchio Barbara
Prof. Patanè Salvatore
Prof.ssa Presti Debora
Prof. Prestipino Giarritta Santi
Prof.ssa Saija Rosalba
Prof. Savasta Salvatore
Prof. Sergi Alessandro
Prof.ssa Silipigni Letteria

Dott. Stassi Roberto
Prof. Torrisi Lorenzo
Prof. Trifirò Antonio
Prof.ssa Trimarchi Marina
Prof.ssa Venuti Valentina
Prof. Wanderlingh Ulderico

Personale non accademico dipendente di altri Enti e Personale docente di Università Straniere

Dott.ssa Curatolo Maria Cristina
Dott.ssa Cutroneo Mariapompea
Dott. Gucciardi Pietro Giuseppe
Dott. Maragò Onofrio
Dott. Micali Norberto
Dott.ssa Puglisi Rosaria Anna
Dott. Saija Franz
Dott. Trusso Sebastiano

I membri del collegio evidenziati in **grassetto** fanno parte del Consiglio ristretto di Dottorato.

Dottorato di Ricerca in Fisica
Università Degli Studi di Messina

ACTIVITY REPORT
2020

Dipartimento di Scienze Matematiche e Informatiche, Scienze Fisiche e Scienze della Terra

Università degli Studi di Messina
Viale F. Stagno d'Alcontres 31, 98166, Messina

Vincenza Crupi Coordinatore

https://www.unime.it/it/dottorato/fisica

Indice

Reports Studenti di Dottorato Ciclo XXXIV

Reports Studenti di Dottorato Ciclo XXXV

Reports Studenti di Dottorato Ciclo XXXVI

Seminari del Dottorato di Ricerca in Fisica

Organizzazione del Dottorato di Ricerca in Fisica

Collegio dei Docenti del Dottorato di Ricerca in Fisica

Tesi e Argomenti di Ricerca Studenti del Dottorato di Ricerca in Fisica

Pubblicazioni degli Studenti del Dottorato di Ricerca in Fisica

Alta Formazione, Ricerca Scientifica e Relazioni Internazionali

Messina, 1 Novembre 2020

Carissimi Colleghi e carissimi Studenti del Corso di Dottorato,

Abbiamo appena concluso un Anno Accademico quanto mai inaspettatamente difficile a causa della pandemia da COVID-19 che ha colpito tutti noi indistintamente in modo improvviso, privandoci della nostra libertà quotidiana, del calore di un abbraccio, portandoci, talvolta a diffidare del nostro vicino di stanza. Purtroppo, stiamo iniziando un nuovo Anno Accademico che, almeno al momento, non si preannuncia migliore del precedente.

L'Ateneo di Messina ha saputo però reagire prontamente a questa emergenza, fornendo a tutte le professionalità presenti al suo interno, a noi docenti, agli studenti e al personale tecnico-amministrativo i più appropriati strumenti telematici che hanno sostituito a volte completamente, vedi il lungo periodo di lockdown dei mesi scorsi, e successivamente parzialmente, tutte le attività normalmente svolte in presenza.

Gli studenti del XXXV ciclo non hanno sicuramente iniziato serenamente il loro percorso formativo per come avrebbero invece meritato, così come i dottorandi del XXXIV ciclo non stanno certamente completando il loro percorso per come lo avevano immaginato inizialmente e, ancora i dottorandi del XXXVI ciclo appena immatricolati non si stanno di certo approcciando al corso di dottorato con troppe rassicurazioni! E che dire degli studenti del XXXIII ciclo che affronteranno il passo conclusivo per l'acquisizione del titolo di Dottore di Ricerca in Fisica tra qualche settimana, nella modalità in remoto, del tutto nuova e permettetemi di dire, asettica per la mancanza del sostegno dei colleghi e/o dei parenti e amici.

Ma nonostante le innumerevoli difficoltà, anche quest'anno ho voluto fortemente che si realizzasse il volume dell'Activity Report 2020 che, come da tradizione, raccoglie tutte le attività formative ed in particolare quelle legate alla ricerca espletate dai dottorandi dei vari cicli, a partire dall'appena istituto XXXVI ciclo fino all'uscente XXXIV. E a proposito del XXXVI ciclo, ho il piacere di sottolineare che sono pervenute quest'anno 33 domande di partecipazione all'esame di ammissione al corso di dottorato, delle quali 4 da parte di laureati stranieri extra-comunitari. Le posizioni utili per l'ammissione al XXXVI ciclo sono state ben 8: 5 con borsa su fondi di Ateneo UNIME, di cui 1 su progetto industriale STMicroelectronics, azienda leader nel settore di componenti elettronici, una sesta su progetto industriale SIFI, azienda di prodotti oftalmologici, con borsa finanziata dall'azienda stessa e 2 posizioni senza borsa. Inoltre, è stata attribuita al Corso di Dottorato una borsa aggiuntiva sul Programma Operativo della Regione Siciliana, Fondo Sociale Europeo 2014/2020 (Avviso pubblico n. 37/2020) assegnata, per scorrimento di graduatoria, ad una delle due posizioni inizialmente senza borsa. A queste 9 posizioni, se ne aggiunge una ulteriore finanziata con un assegno di ricerca (tipologia D – Grant) nell'ambito del progetto Horizon 2020 – Grant Agreement for Marie Sklodowska-Curie Innovative Training Networks (MSC-ITN), vinta da uno studente spagnolo.

Mai come quest'anno, il corso di Dottorato di Ricerca in Fisica si è manifestato in tutto il suo carattere interdisciplinare e "industriale" grazie alla presenza di dottorandi in possesso di laurea magistrale di area scientifico-tecnologica diversa dalla laurea in Fisica e altresì grazie alle partnerships (vere e proprie convenzioni) con aziende private di alta qualificazione scientifica che incentivano il settore R&D, quali le sopracitate STMicroelectronics e SIFI, che hanno creduto nel Corso di Dottorato e pertanto investito in esso, anche in termini finanziari, tramite progetti di ricerca finalizzati.

Non posso che concludere questa breve introduzione augurando a tutti i ragazzi di iniziare questo Anno Accademico 2020/2021 con l'onestà intellettuale che dovrebbe contraddistinguere sempre un vero ricercatore, e con il giusto entusiasmo nonostante il delicato periodo storico che stanno/stiamo vivendo. Infine, esorto tutti noi ad essere ottimisti e fiduciosi nel futuro e in quel progresso scientifico che sono certa ci farà recuperare al meglio, il meglio di questo percorso formativo fondamentale nel panorama della ricerca universitaria.

Reports

Studenti di Dottorato di Ricerca

Ciclo XXXIV

Advanced Synthesis and Characterization of Quantum Silicon Nanowires

G. Borghè[1−2,*], C. Bongiorno[2], S. Patanè[1], A. La Magna[2], G. Mannino[2], R. A. Puglisi[2]

[1]*Department of mathematics and Computer Science, Physics and Earth Science (MIFT), University of Messina, Viale F. Stagno d'Alcontres, 31, 98166 Messina, Italy*

[2]*2Consiglio Nazionale delle Ricerche (CNR) Istituto per la Microelettronica e Microsistemi (IMM), Strada Ottava 5, Zona Industriale, 95121 Catania, Italy*

[3]*Department of theoretical physics, New University of Physics, Physics City, Physicland*

*Corresponding Author email: gborgh@unime.it

Abstract

Silicon nanowires (Si-NWs) are versatile structures with excellent electro-optical properties for applications in several technological fields such as photovoltaics, photonics or plasmonics. This manuscript deals with the synthesis by Chemical Vapor Deposition (CVD) of Si-NWs with diameters of a few tens of nanometers. The first goal of this activity report, of the second year of PhD, is to replace the classic metal catalyst, gold (Au), with tin (Sn), which improves the electro-optical performance of the Si-NWs and it is cost-effective. It also aims to deepen the understanding of the plasmonic properties of Si-NWs, still not entirely clear, at low energy (UV-Vis), an energy range of increasing scientific and technological interest. The characterizations of the morphological, structural and plasmonic properties are pursued through different advanced techniques, including SEM, TEM, STEM, EELS.

Keywords: nanowires, VLS, CVD, plasmon resonance, EELS.

Introduction

Si-NWs are promising structures showing interesting electrical and optical properties for applications in many technological fields. For example, they represent versatile building blocks for nanoelectronics devices such as field effect transistors [1]. In photovoltaics they are used to increase the efficiency of solar cells [2]; in photocatalysis are useful to degrade organic molecules [3]; in photodetectors nanowires of a certain radius absorb only certain wavelengths acting as spectrometer [4]. They find applications also as biosensors [5] or in photonics as resonant cavities to obtain lasers [6]. Si-NWs additionally show to support plasmonic resonances, the in-phase and collective oscillation of free electrons that occurs in a material at a certain frequency, precisely that of plasma. Plasmon resonances make Si-NWs promising for applications in various technological fields. However, low-energy plasma resonances (180 - 600 nm in wavelength) in Si-NWs are not yet fully rationalized due both to the difficulty of structures synthesis with diameters of a few tens of nanometers, and to the limitations due to the characterization technique. In this work Si-NWs are obtained through the vapor-liquid-solid (VLS) mechanism [7] by the Induced Plasma Chemical Vapor Deposition (IP-CVD) technique using gold (Au) or tin (Sn) as nano-catalysts. Gold is the most common catalyst [8] but it is expensive and

creates traps states in the Si electronic structure, so it is necessary to remove it at the end of growth to preserve the electrical performance [9]. We propose Sn as an alternative catalyst: it does not generate trap states in Si, it is abundant in nature, it is low cost and shows a lower eutectic temperature which Si than Au of over 120 $^\circ C$. Moreover, Sn does not represent a dopant for Si. However, the wires morphology obtained using Sn is still unoptimized. This work deals with the synthesis and advanced characterization of Si-NWs, grown with Sn as a metal catalyst, by observing the systems produced through electron microscopy techniques; the second goal of this paper is to show preliminary studies of the electronic phenomena exhibited at low-energy (4-7 eV) by the nanowires, commonly attributed to plasmonic resonances in litterature [10] with diameters below 50 nm obtained with Au. The main techniques used are STEM and EELS.

Materials and Methods

Si-NWs growth

Si-NWs growth is carried out by CVD through the VLS mechanism using Au or Sn as catalysts. The substrates (CZ <100> 6" inches p-type Si 1x1cm^2) are cleaned by sonication bath in organic solvents for about 5 min each. Then a dip in HF (1%) is performed to etch the native

oxide. The substrate is loaded into the sputter chamber for the metal deposition. Finally, the system is transferred into the CVD chamber, heated at 380 $^\circ C$ for 1 h under vacuum before the starting depositions to allow the coalescence of the Au/Sn dots. Whereupon growth takes place at 380 $^\circ C$ for 30 min with a pressure equal to 20 mTorr and a plasma power between 20 and 40 W. Silane (SiH_4) is the Si gas source.

TEM analysis

The Si-NWs are collected onto a metallic meshed grid by mechanical stripping. STEM/EELS analyses were performed at 200kV using a JEOL JEM-ARM200F cold FEG microscope. A 2D scan of the primary beam across a single nanowire is carried out, using pixel size of 1.3 nm and 0.025 eV per pixel on the 2K Gatan camera. The energy range of the EELS spectra acquisition is from 0 to 45 eV with an energy resolution of 0.45 eV. The zero-loss peak was removed from all raw spectra using a power law fitting procedure with a background energy window 0.5 eV wide and located between 0.8 and 1 eV.

Results and discussion

Figure 1(a) and (b) show SEM micrographs in planar view for two Si-NWs arrays synthetized using Au (a) and Sn (b) as catalyst respectively, showing the typical appearance of the growth products.
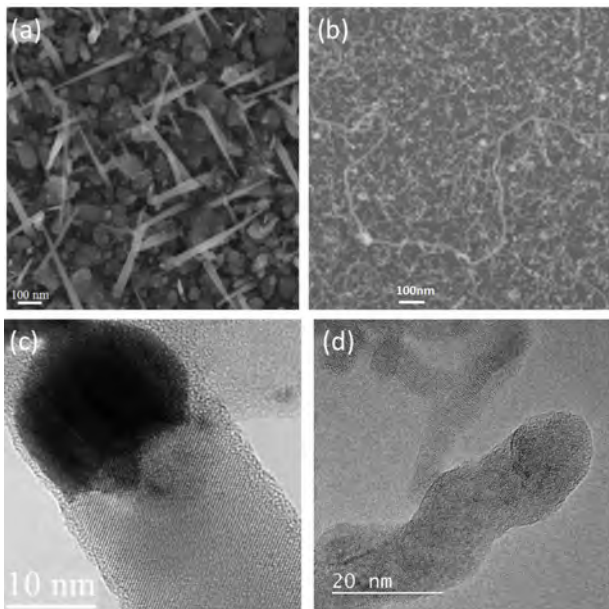

Figure 1: *SEM micrographs in planar view showing the typical aspect of a Si-NWs array obtained respectively using (a) Au and (b) Sn as metal catalysts. High resolution TEM micrographs acquired for two previously isolated Si-NWs obtained using respectively Au (c) and Sn (d) as metal nanocatalyst for the growth*

Both samples show good homogeneity over um^2 areas and high density of the produced nanostructures. It can be observed that the wires obtained using Sn as catalyst have irregular morphology and lengths with greater variability than the Si-NWs obtained with Au. Figure 1(c) and (d) show HR-TEMs images for two Si-NWs previously isolated from the two arrays showed in (a) and (b) respectively. In figure 1(c) it is possible to distinguish the reticular planes indicating that the nanostructure is crystalline. This wire shows a homogeneous crystalline structure, and it is straight all along its length, sign that there is only one crystallographic direction prevailing during the growth and that this has a role on the NW morphology. The dark particle at the top of the wire tip is the residual gold catalyst dot remaining at the end of the growth. The wire in figure 1(d) is polycrystalline as can be observed from the several reticular planes orientation detected by TEM. The worm-like morphology indicates that the crystallographic orientation again plays a role during the growth [11]. The wires morphology obtained with Sn as catalyst have to be further optimized to reach the same morphological results obtained with gold and work is underway to this direction. For this reason, we performed the plasmonic investigations on Si-NWs obtained with Au.
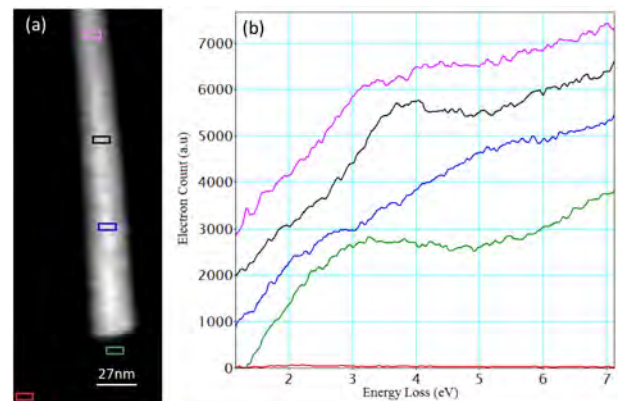

Figure 2: *(a) Energy Filtered TEM micrograph acquired at 17 eV for an isolated Si-NW grown with Au as catalyst. (b) Electron Energy Loss Spectroscopy graphs extracted from different areas of the wire, along the axis, as indicated by the coloured boxes in a. All the curves are vertically shifted for a clearl view*

Figures 2 (a) and (b) show respectively a part of a Si-NW with a diameter of 35 nm and a length of 420 nm and its relative EELS spectra axially extracted at several heights inside and near it, all the curves are vertically shifted for a clear view, in correspondence of the coloured boxes as detailed in (a). All the coloured boxes have the same area, equivalent to 6x12 nm^2, in order to obtain a normalized EELS signal intensity in all cases. The scans start from a region outside the NW, as shown by the red curve extracted from the box of the same colour in the EF-TEM micrograph reported in figure 2(a) and acquired at 17 eV,

the Si bulk plasmon resonance, to estimate the SI-NW dimensions. The red curve is useful to estimate the background noise in vacuum away from the wire. The curves show a spatial dependence of the low energy signals: the shape of the EELS spectra in the energy region between 2 and 7 eV changes locally indicating different spectral features point by point. A broad signal, maybe the convolution of several contributions, centered at about 4 is clearly visible moving axially from the tip. The characteristics of the EELS curve in this energy range vary locally; the intensity of the 4 eV plasmonic signal changes losing its intensity along the wire axis. The peak gradually disappears and finally falls down only into a certain area of the wire, while a hump appear at slightly higher energy, as can be verified looking at the blue curve. Then it starts growing again moving axially in the wire until it regains its intensity (black curve) and no longer undergoes significant variations in intensity (pink curve). This phenomenon seems to show a certain symmetry and therefore some geometric dependence.

We then decided to scan radially at two heights with respect to the wire bottom tip: at 112 nm away from it, where the 4 eV signal is intense and at 56 nm where it falls, similarly to the previous figure, as indicated by the coloured boxes depicted in the EF-TEM in figure 3(a). Also in this case, the scans start outside the wire for an estimation of the background noise.
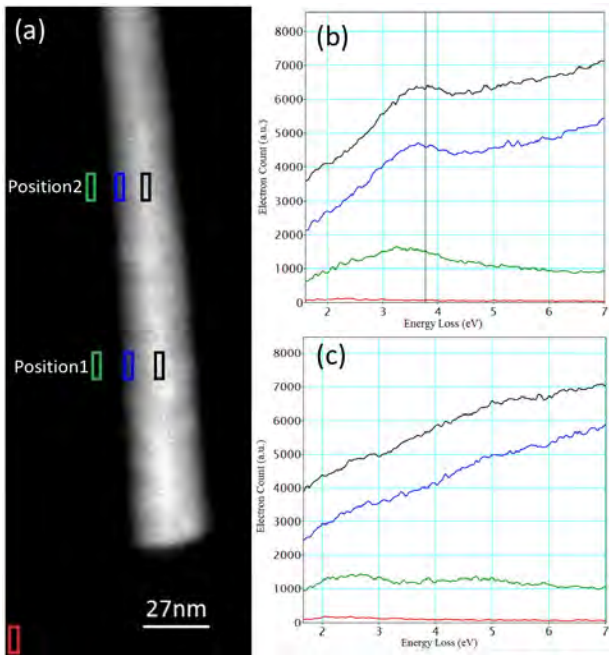

Figure 3: *(a) EF-TEM micrograph acquired at 17 eV for an isolated Si-NW. (b) EELS graphs extracted from different areas of the wire, as indicated by the coloured boxes in a, by moving radially along the wire, respectively at two different heights: 56 nm and 112 nm away from the wire bottom tip. All the curves are vertically shifted for a clearl view. Vertical lines highlight the main low energy signals at about 4.*

The results shown in figure 3(b) and 3(c), showing the EELS spectra vertically shifted for a clear view, respectively display that by moving radially from outside of the structure towards the inside, we clearly always distinguish the 4 eV broaded signal at position 1 in all extracted curves as highlighted by the black vertical line; instead at about 4 eV in position 2 the peak is always absent along the wire radius. We can conclude that the spectral characteristics in this energy range are radially isotropic. This trend of the EELS signals, and the phenomenon for which there is an area of the Si-NW where the 4eV signal breaks down can be explained by admitting a harmonic behaviour of the siganls typical of a resonant cavity. Also in the literature indeed this model is proposed even for nanorods of different materials and larger diameters (of the order of hundreds of nanometers) [12], referring to them to as Fabry-Perot resonators. In our Si-NWs the low-energy surface plasmons are likely to propagate axially in a single Si-NW being reflected at the ends. The reflected portion interferes with the plasmon wave traveling in the opposite direction leading to the appearance of interference fringes. In this way the regions in which the signal falls, such as at 56 nm, correspond to the minima of the fringes, that is the antinodes of the distribution of the electric field. The areas in the nanostructure in which the signal is intense correspond to the maximums of the interference fringes, or the nodes of the electric field distribution. This well rationalizes the experimentally observed behavior in our Si-NWs.

Conclusions

In this report we summarize the main points of the research activity carried out during the second year of the PhD. We have grown Si-NWs with diameters below 50 nm via CVD. The wires are obtained with two different metal catalysts, namely Au, still the most common and Sn, a promising alternative. Sn aims to overcome the disadvantages of gold and at the same time to reduce synthesis costs for large-scale applications. The structures obtained with it, although they show a worm-like morphology to be further optimized, are polycrystalline, a promising result for many electronic applications. Plasmonic investigations carried out in the range of low energies (3.5-6 eV) reveal the presence of surface low-energy plasmons, with longitudinal resonances.

Acknowledgement

References

[1] Cui, Y., Zhong, Z., Wang, D., Wang, W. U., Lieber, C. M.: *High performance silicon nanowire field effect transistors.* In: Nano letters, 3(2), 149-152(2003)

[2] Puglisi, R. A., Garozzo, C., Bongiorno, C., Di Franco, S., Italia, M., Mannino, G., ... La Magna, A.: *Molecular doping applied to Si nanowires array based solar cells.* In: Solar Energy Materials and Solar Cells, 132, 118-122(2015)

[3] Shao, M., Cheng, L., Zhang, X., Ma, D. D. D., Lee, S. T.: *Excellent photocatalysis of HF-treated silicon nanowires.* In: Journal of the American Chemical Society, 131(49), 17738-17739(2009)

[4] Meng, Jiajun, Jasper J. Cadusch, and Kenneth B. Crozier: *Detector-only spectrometer based on structurally colored silicon nanowires and a reconstruction algorithm.* In: Nano letters 20.1, 320-328(2019)

[5] Huang, S., Zhang, B., Shao, Z., He, L., Zhang, Q., Jie, J., Zhang, X. : *Ultraminiaturized stretchable strain sensors based on single silicon nanowires for imperceptible electronic skins.* In: Nano letters, 20(4), 2478-2485(2020)

[6] Li, C., Liu, Z., Chen, J., Gao, Y., Li, M., Zhang, Q.: *Semiconductor nanowire plasmonic lasers.* In: Nanophotonics, 8(12), 2091-2110(2019)

[7] Wagner, A. R., Ellis, S. W.: *Vapor liquid solid mechanism of single crystal growth* In: Applied physics letters, 4(5), 89-90(1964)

[8] Puglisi, R. A., Bongiorno, C., Caccamo, S., Fazio, E., Mannino, G., Neri, F., ... La Magna, A.: *Chemical Vapor Deposition Growth of Silicon Nanowires with Diameter Smaller Than 5 nm.* In: ACS omega, 4(19), 17967-17971(2019)

[9] Puglisi, R. A., Bongiorno, C., Borgh, G., Fazio, E., Garozzo, C., Mannino, G., ... La Magna, A.: *Study on the physico-chemical properties of the Si nanowires surface.* In: Nanomaterials, 9(6), 818(2019)

[10] Wang, J., Wang, X. J., Jiao, Y., Li, Q., Chu, M. W. and Malac, M.: *From nanoparticle to nanocable: Impact of size and geometrical constraints on the optical modes of SI/SIO2 core/shell nanostructures.* In: Appl. Phys. Lett. 95, 133102(2009)

[11] Yu, D. P., Xing, Y. J., Hang, Q. L., Yan, H. F., Xu, J., Xi, Z. H., Feng, S. Q.: *Controlled growth of oriented amorphous silicon nanowires via a solid–liquid–solid (SLS) mechanism.* In: Physica E: Low-dimensional Systems and Nanostructures, 9(2), 305-309(2001)

[12] Rossouw, D., Couillard, M., Vickery, J., Kumacheva, E., Botton, G. A.: *Multipolar plasmonic resonances in silver nanowire antennas imaged with a subnanometer electron probe.* In: Nano letters, 11(4), 1499-1504(2011)

EMG null space control during force task and fNIRS monitoring of motor cortex after MRgFUS treatment

S. Gurgone[1,*], D. Borzelli[2], P. de Pasquale[2], D. J. Berger[3], A. d'Avella[2], G. Acri[2], V. Venuti[1]

[1] *Department of Mathematical and Computer Sciences, Physical Sciences, and Earth Sciences, University of Messina, Messina, Italy*

[2] *Department of Biomedical and Dental Sciences and Morphofunctional Imaging, University of Messina, Messina, Italy*

[3] *Centre of Space Bio-Medicine and the Department of Systems Medicine, University of Rome Tor Vergata, Rome, Italy*

*Corresponding Author email: sgurgone@unime.it

Abstract

In this work, a new method to control an extra degree of freedom using EMG null space control, during an isometric force reaching task performed by human subjects, is studied. Due to the redundancy of musculoskeletal system, many muscle activation patterns do not generate movement, and could be used to control external devices while performing natural movements. Here we show that null space control is feasible, but task difficulty must be optimized according to the individual control ability. Furthermore, a new approach using fNIRS is studied for monitoring of patients affected by essential tremor or Parkinson's disease, through measurement of changes in cerebral hemodynamics during simple hand motor tasks, before and after a MRgFUS treatment.

Keywords: electromyography, myoelectric control, EMG null space, augmentation, fNIRS, MRg-FUS, essential tremor, Parkinson's disease.

Introduction

In the first part of this study, the possibility of controlling an extra degree of freedom (DoF) through the electromyographic (EMG) null space, while simultaneously performing a force task, is explored. Myoelectric control, i.e. the control of a device using EMG signals, is commonly used for devices such as prostheses and exoskeletons, and for studying human motor control. Myoelectric control of a prosthesis is possible by detecting the movement an individual intends to perform using EMG signals recorded from different muscles [1]. Myoelectric exoskeletons can be employed as well for rehabilitation of injured or disabled people, or for assistance [2].

Myoelectric control has also been applied to investigate basic principles of human motor control. Using EMG signal to control an end-effector in a virtual environment, it is possible to apply a perturbation to the mapping between motor commands and the motion of the end-effector, such that new muscle synergies are required to span the entire workspace [3].

Up to date, myoelectric control has been used in devices that either replace or assist a limb, or for tasks in virtual spaces, related to physiological aspects but not to real tasks. However, it could be used to control devices concurrently with the natural limbs, augmenting human abilities. Different approaches for augmentation have been recently investigated, but none used EMG signals from a limb performing other movements. EMG null space control, which has been applied to compensate perturbations during force tasks [4] and control the impedance of robots [5], could be a feasible approach. Due to the redundancy of the musculoskeletal system, in which many more muscles are present than the natural DoFs, many combinations of EMG signals do not generate movement, and can be applied to control external devices to augment human capabilities.

Here, we wanted to assess the performance of participants in a task involving generating isometric forces in different spatial directions while simultaneously controlling an extra DoF.

Moreover, a novel approach combining magnetic resonance guided focused ultrasound (MRgFUS) and functional near-infrared spectroscopy (fNIRS) is studied for treatment and monitoring of patients affected by essential tremor or Parkinson's disease.

In recent years, new techniques for treatment of movement disorders have been developed to avoid using ablative functional neurosurgery techniques as deep brain stimulation, which could bring to complications due the positioning of electrodes inside the brain. Among these, MRgFUS is one of the most promising techniques which has already many clinical applications [6], including the treatment of essential tremor (ET) and Parkinson's disease (PD). MRgFUS allows a non-invasive thalamotomy by combining FUS for cerebral tissue ablation and MR for targeting the ablation site.

While the effects of MRgFUS treatment on cerebral ac-

tivity during rest using functional magnetic resonance imaging (fMRI) have been largely investigated, the effects of MRgFUS treatment during the performance of motor tasks are still largely unknown. For this purpose, fNIRS could be better suited because measurements can be performed even when patients are sitting on a chair, walking or running, while fMRI is quite sensible to movement artefacts and its magnetic field could interfere with other instrumentation. fNIRS is a spectroscopic technique that allows to detect changes in oxygenated and deoxygenated haemoglobin (HbO and HbR, respectively), induced by neural activity, through the measurement of near-infrared light absorption (in the range 700-900 nm of the electromagnetic spectrum) [7]. Together with the possibility of performing measurements during motor tasks, fNIRS presents some advantages as lower costs, higher portability and higher temporal resolution with respect to other techniques. However, it also presents some limitations, such as lower spatial resolution and difficulty in detecting signals from deep brain structures. Nonetheless, this technique is still a promising tool in neurorehabilitation for monitoring patient status after brain damage [8].

Here, we wanted to assess how well fNIRS could be used for monitoring the status of patients affected by bilateral essential tremor or Parkinson's disease, measuring changes in HbO and HbR during left and right finger-tapping tasks before, one week after, and one month after an MRgFUS treatment.

Material and Methods

EMG Null Space Control

Subjects

Eight naïve right-handed volunteers (mean ± SD age 27.5 ± 7.8 years, age range 20–45, 2 females), with normal or corrected to normal vision, no reported neurological disorders or upper right limb injuries, participated in the experiments after giving written informed consent.

Setup and protocol

Participants sat on a gaming chair in front of a desktop, with the right hand inserted in an orthosis rigidly connected to a force transducer. Car belts immobilized their torso and shoulders (Fig. 1). They wore 3D shutter glasses and saw stereoscopically a scene visualized on a monitor, consisting of a virtual desktop and a cursor displaced in real-time by the force exerted on the orthosis. The motion of this cursor was simulated as a mass-spring-damper system with critical damping, accelerated by the force applied by the participant.

Surface EMG activity was recorded from 15 muscles acting on the shoulder and elbow, and acquired at 1000 Hz with active bipolar surface electrodes (Delsys Trigno Wireless System), bandpass filtered (20 – 450 Hz), 1000 gain. Participants' skin was cleansed with alcohol and electrodes were placed on the muscle belly, orienting them along the main direction of the fibres.
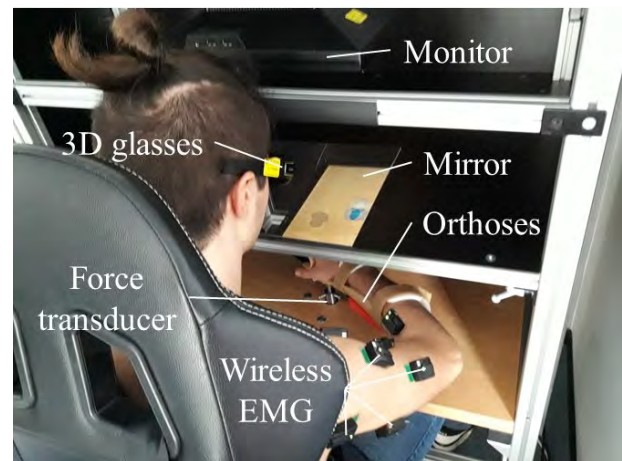

Figure 1: *Photo of the setup used for the experiment.*

The experiment was divided into 17 blocks in the following sequence (in parentheses the number of blocks):

- Maximum voluntary force (MVF) block (1): was used to normalize the distance of the targets used in the other blocks. Participants were asked to exert their MVF along the antero-posterior direction on the horizontal plane;

- Force control (FC) block (1): participants were asked to move a virtual spherical cursor into a spherical target in one of 20 spatial directions (distance 15% or 25% of MVF), and to keep it inside (holding phase) for 0.5 s (time limit: 4 s). EMG and force data from this block were used to normalize EMG signal and to estimate by regression the EMG-to-force matrix H, such that $F = Hm$, where F and m are the force and EMG activation vectors. The null space of H, i.e. the set of vectors n that satisfy the relation $Hn = 0$, was calculated as an orthonormal matrix N (using the MATLAB function "null");

- Null space estimation (NSE) block (1): participants had to hold the cursor inside a target placed in the origin for 1 s, while an oscillation perturbed the motion of the cursor. The oscillation could be reduced by increasing the null space activation, therefore subjects were instructed to stiffen their right arm and shoulder. The directions of largest variability in the collected EMG data (estimated by principal component analysis) were used for the control of the extra DoF;

- Ellipsoidal force control (EFC) block (1): FC block with 8 planar targets (3 repetitions) at 20% of MVF with an ellipsoidal cursor and targets;

- Null space control (NSC) block (12): in addition to reaching the target by force control, participants had also to rotate an ellipsoidal cursor, around an axis parallel to the forearm, by null space activation and stay inside an ellipsoidal target for 1 s. All the targets had the same orientation of 60 degrees (20% of the maximum null space activation in the NSE block);

- EFC block (1).

Data analyses were made with custom-made software written with MATLAB®(MathWorks Inc., Natick, MA) and Java®.

Control of the Extra DoF

The EMG data collected in the NSE block allowed the estimation of the null space dimensions used by each participant through principal component analysis (PCA). A number of components explaining 80% of the total variation of the EMG data was selected to control the extra DoF in the NSC blocks.

Data Analysis and Statistics

Data collected during all trials performed by participants were visually inspected and those trials presenting EMG artefacts were discarded (mean ± STD over participants: 13.1 ± 7.6 over 536). R^2 for the reconstruction of 3D forces was calculated for the force control blocks to check the validity of the H matrix. Task performance was quantified by the fraction of trials in which the cursor reached the target (reaching success rate, RSR) and in which it was kept in the target for 1 s (holding success rate, HSR), by the angular deviation of the cursor rotation angle with respect to target rotation angle, and by the maximum "holding" time of the cursor in the target.

Statistical analysis were performed using MATLAB. For the NSC blocks, a generalized linear mixed model (GLMM, function "fitglme") was fitted separately to the reaching and holding success rates, while a linear mixed model (LMM, function "fitlme") was fitted separately to the angular deviation and the holding time of all subjects together to assess their dependence on block and target (fixed effects) taking into account the variability across participants (random effect).

fNIRS monitoring after MRgFUS treatment

Subjects

17 patients from IRCCS Centro Neurolesi Bonino-Pulejo of Messina (Italy), 11 affected by essential tremor and 6 by Parkinson's disease, age range 57-82, 6 females, participated in the experiment after giving written informed consent. Four subjects with no neurological diseases participated in the experiment as control subjects.

Setup and protocol

The experiment consisted in three sessions: one day before the FUS treatment (S0), one week after (S1) and one month after the FUS treatment (S2). In all of them, subjects performed both a right and a left finger tapping task (RFT and LFT, respectively). At the beginning of each trial, the initial 10 s were spent to allow for signal stabilization. After that, 25 s of activation were alternated with 15 s of rest, and the sequence was repeated for six

times (total duration of each trial: 250 s). Control subjects performed a single session, and the collected data were used as references.

Data were acquired using an Hitachi ETG-4100 NIRS system, which uses NIR light of two wavelengths (695 nm and 830 nm) to measure concentration changes of HbO and HbR levels in the brain, with a sampling rate of 10 Hz. A configuration matrix of 3 x 5 optodes, 8 sources and 7 detectors, for a total of 22 channels, was positioned above the forehead to acquire signal mostly from the frontal and parietal cortices. Subjects' hair were cut before each session to reduce noise generated by hair presence, although other sources of noise still remained, such as the scalp depth and the conformation of the head, which can affect radiation absorption and scattering.

Data analysis was performed by the NIRS-SPM (Statistical Parametric Mapping) software (version 4, revision 1) [9], integrated in MATLAB®R2009a.

Data Analysis and Statistics

As a first step, fNIRS HbO and HbR data were low-pass filtered using the canonical haemodynamic response function (HRF) filter to remove high-frequency noise and temporal correlations (when the residual signal at the specific time is correlated with its temporal neighbours), following the so-called "precoloring" method [9]. Baseline correction was performed, subtracting the value of concentration change at initial time.

For statistics, a generalized linear model (GLM) was fitted to the pre-processed data using the NIRS-SPM software. The data were described as a linear combination of explanatory variables plus an error term and a drift term taking into account the global drift of fNIRS signal, calculated using a wavelet minimum description length algorithm [9]. In a matrix form, the model can be written as:

$$\mathbf{S} = \mathbf{X}\boldsymbol{\beta} + \boldsymbol{\epsilon} + \boldsymbol{\theta}, \qquad (1)$$

in which $\mathbf{S}$ is the matrix of the haemodynamic signal, the measurement model of which is derived from modified Beer-Lambert law [9], $\mathbf{X}$ is the model design matrix, $\boldsymbol{\beta}$ is the vector of unknown strength responses, $\boldsymbol{\epsilon}$ is the noise vector, and $\boldsymbol{\theta}$ is the global drift vector. The GLM was applied to HbO and HbR, as well as to the total haemoglobin (HbT), data using the NIRS-SPM software, to calculate interpolated statistical activation change maps and see which regions of the cerebral cortex were significant active, during FT tasks, with respect to the rest phases. Euler's correction has been used for the calculation of t-statistics coefficient [9].

Results and Discussion

EMG Null Space Control

In the FC and in the first EFC block participants were able to control the cursor with a mean RSRs of 92 ± 6 % and 88 ± 25 %, and a mean HSRs of 63 ± 19 % and 67 ± 31 %, while the mean force reconstruction R^2 was 0.76 ± 0.11 and 0.78 ± 0.13. During the 12 NSC blocks

the maximum mean RSR was of 92 ± 9 %, but the maximum mean HSR was of only 43 ± 30 %. Nonetheless, the GLMM analysis showed a significant increase in the mean RSR as a function of block ($p < 0.001$, slope 0.05), as well as in the mean HSR ($p < 0.001$, slope 0.04), which means that on average participants improved their performances, although high variability was present among them as indicated by the high standard deviation (see Fig. 2). Similar results were obtained for mean holding time and angular deviation, with respectively positive and negative slopes in the LMM (0.009 and -0.12 respectively, $p < 0.001$ for both, see Fig. 2).
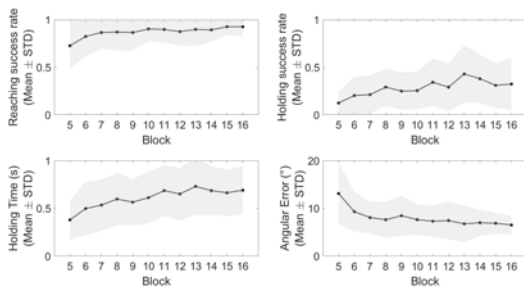

Figure 2: *Mean reaching and holding success rates, holding time and angular error.*

fNIRS monitoring after MRgFUS treatment

Preliminary results of the analysis on HbO, HbR and HbT data showed that ET patients presented no significant changes, for S0, in HbO and HbR concentrations during LFT in right hemisphere (which instead should normally present activation) and during RFT in left hemisphere (specularly to LFT), while significant changes were visible for S1 and S2. PD patients showed similar behaviour, except that in S2 there were no significant changes as in S0 (see Fig. 3 for examples). A deeper data analysis is, at present, in progress.

Conclusion

First, we demonstrated that EMG null space activation can be used to control an extra DoF while performing simultaneously an isometric force-control task. Participants were able to control the position and orientation of an ellipsoidal cursor to match different target position and orientations using both force and null space control. However, inter-individual variability in holding performance was observed. Future work is needed to investigate individual abilities and to understand how to optimize a null space control interface according to those.

Then, we showed that fNIRS can be used for the monitoring of patients, affected by essential tremor or Parkinson's disease, that underwent a MRgFUS treatment. Preliminary results showed that MRgFUS was more effective for ET patients than for PD patients. Further work, as group analysis, is needed to better understand the validity of this approach.
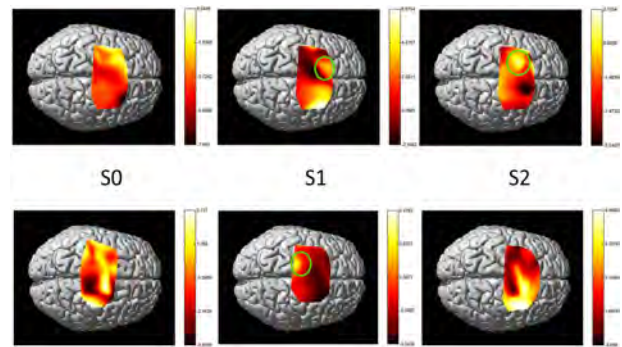

Figure 3: *HbR data from RFT of an ET patient (upper row) and a PD patient (lower row).*

Acknowledgement

References

[1] Vujaklija, I.: *New developments in prosthetic arm systems.* ORR Volume 8, 31–39 (2016).

[2] Ambrosini, E.: *A myocontrolled neuroprosthesis integrated with a passive exoskeleton to support upper limb activities.* J. Electromyogr. Kinesiol. **24**(2), 307–317 (2014).

[3] Berger, D. J.: *Differences in Adaptation Rates after Virtual Surgeries Provide Direct Evidence for Modularity.* Journal of Neuroscience, **33**(30) (2013).

[4] Borzelli, D.: *Muscle patterns underlying voluntary modulation of co-contraction.* PLOS ONE 13, e0205911 (2018).

[5] Ajoudani, A.: *Tele-impedance: Towards transferring human impedance regulation skills to robots.* IEEE Int. Conf. on Robotics and Automation, Saint Paul, MN, pp. 382-388 (2012).

[6] Weintraub, D., & Elias, W.J.: *The emerging role of transcranial magnetic resonance imaging-guided focused ultrasound in functional neurosurgery.* Mov. Disord., 32, 20-27 (2017).

[7] Arenth, P.M.: *Applications of functional near-infrared spectroscopy (fNIRS) to Neurorehabilitation of cognitive disabilities.* Clin. Neuropsychol., 21, 38-57 (2007).

[8] Acri, G., d'Avella, A., Gurgone, S., Venuti, V., Majolino, D., et al.: *A functional NIRS study of changes induced in the motor cortex by MRgFUS therapy.* Brain Sciences (to be submitted).

[9] Ye, J.C.: *NIRS-SPM: Statistical parametric mapping for near infrared spectroscopy.* NeuroImage, 44, 428-447 (2009).

Effect of interface and bulk charges on the breakdown of nitrided gate oxide on 4H-SiC

B. Mazza[1−2,∗], S. Patane'[1], F. Cordiano[2], M. Giliberto[2], G. Martorana[2], G. Renna[2], G. Franco[2]

[1] *Dipartimento di Scienze Matematiche ed Informatiche, Scienze Fisiche e Scienze della Terra, Universita' degli Studi di Messina, Messina*

[2] *STMicroelectronics, Stradale Primosole, 50, 95125 Catania*

[∗]Corresponding Author email: bruna.mazza@unime.it

Abstract

The disadvantage of 4H-SiC/SiO$_2$ interface with respect the Si/SiO$_2$ is the high trap density which limits the channel mobility and gate oxide stability and often leads to early PowerMOSFET failure. One important process improvement is the nitridation of the oxide. In this work we provide several techniques to characterize the nitridation effect validating the better performances of NO nitridation either on near interface oxide traps (NIOTs) and bulk charges passivation or on gate oxide reliability.

Keywords: 4H-SiC, MOSFET, nitrided oxide, breakdown.

Introduction

Silicon carbide (4H-SiC) is a promising material for high-power devices thanks to its high breakdown electric field, wide band gap and high thermal conductivity[1]. The material has gained considerable attention for future power electronics in the context of hybrids and electrical vehicles and conversion systems also for renewable energies. Then the purpose of process improvements is mainly dedicated to increase efficiency in order to reduce the power loss in the PowerMOSFET. Specifically, major initiatives are under way to improve the inversion channel mobility and gate oxide stability in order to further reduce the on-resistance and enhance the gate oxide reliability. Both aspects are related to the defects near the SiO$_2$/SiC interface. A common way to is to improve the field effect μ_{FE} mobility, extracted from Id-Vg transfer characteristics, which is often limited by the high density of interface defects (Dit)[2], carbon clusters and traps [3] which reduce the free carriers in the inversion channel or scatter carriers located at SiO$_2$/SiC. Experiments[4][7] have demonstrated that nitridation provides important improvements in the quality of SiO$_2$/SiC interface.

Experimental

The PowerMOSFET transistors that we characterized in this work are built on 6" wafers on n-type (0001) 4H-SiC 350 μm thick substrate doped 4-5E18 cm^{-3} and resistivity of 0.012-0.025 Ω*cm. The n-epitaxy layer is 6 μm thick and doped 1.5E16 cm^{-3}. Over the Epi Layer a 50-nm-thick oxide has been deposited, through a Low Pressure Chemical Vapor Deposition (LPCVD DCS) in High Temperature Oxidation (HTO) furnace under dichlorosilane (SiH$_2$Cl$_2$) ambient. This process is followed by a Post Oxidation Annealing (POA) performed on horizontal furnaces to properly nitridated the SiC/SiO$_2$ interface.

Two different versions of POA have been settled in this work using identical temperature ramps using different gaseous precursors in N$_2$O or NO environment with annealing temperature in range of 1150-1300C. In both POA processes, NO molecules are responsible for the interface nitridation. When NO is generated from N$_2$O molecules pyrolysis, a certain amount of N$_2$ and O$_2$ is also produced generating a not desirable interface oxidation. The total mutual amount of N$_2$, O$_2$ and NO produced by N$_2$O pyrolysis is also affected by many process parameters which often are very difficult to keep under control. On the other hand, NO molecules are very stable when temperature is less than 1300C. For all the above reasons NO POA process is strongly recommended in a production line [8].
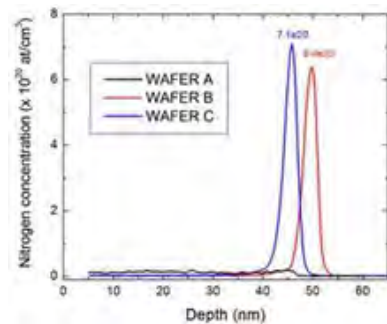

Figure 1: *Dinamic TOF-SIMS profiles comparison between NO and N$_2$O post oxidation annealing.*

Before the definition of a frozen oxidation flow, several deposition and post oxidation annealing process trials have been processed on blanket wafers. Then, the Dynamic TOF-SIMS analysis profiles and, in particular, the quantification of the Nitrogen concentration peak at SiC/SiO_2 supported the choice of the best reaction time, which has been set in order to obtain the N concentration peak of about 7e20 at/cm^2 as reported in Figure 1.

Discussion

All the test reported on this paper have been performed on a MPI TS2000-DP semiautomatic probe station equipped with a Keysight B1505A device analyzer with an external LCR Keysight E4980 meter dedicated for C-V/G-V measurement and HPSMU (high power source measure unit) for I-V test. This paper provides analysis aimed at the investigation and the understanding of the mechanisms and effects associated with annealing of gate oxides in NO and N_2O environments, by several electrical techniques targeted either to charge trapping analysis or dielectric breakdown. The former provides an evidence of the better NO SiO_2/SiC interface traps annealing, forcing a Constant Current Stress (CCS) from both the PowerMOSFET interfaces (Poly-SiO_2 and SiC-SiO_2). The commonly used methods[9] to determine interface traps effects and to evaluate and calculate the density of states are related to the analysis of the Conductance-Voltage (G-V) peaks, detected by Capacitance-Voltage (C-V) test at different frequencies (from 20Hz to 1MHz). In particular, C-V have been carried out starting by a very slow ramp rate of around 60mV/s assuming to stimulate the charge de-trapping from the levels inside the SiC bandgap. The most significant results come from the C-V and , in particular, from the G-V measurement performed at the low frequency of 20Hz, with an oscillation amplitude of 1V where the conductance peaks are detected between -5Vg and -10Vg showed in Figure 2.
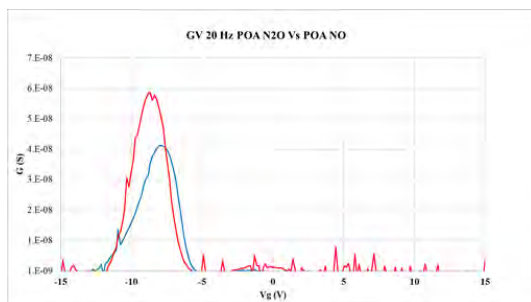

Figure 2: *G-V Characteristics comparison between N_2O vs NO samples.*

The reason is that such test provides a qualitative reference for the method we propose where we apply a DC I-V (Current-Voltage) test, in a Voltage regime not critical for gate charge injection in the gate oxide. Then we correlate the nitridation efficiency in terms of traps reduction in the SiC band-gap and the peak displacement
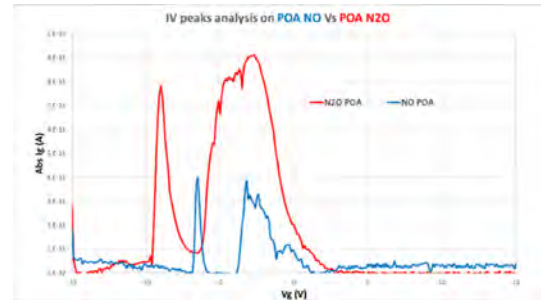
gate current[10] as shown in Figure 3.

Figure 3: *I-V Characteristics comparison between N_2O vs NO samples. Peaks from N_2O sample are higher and wider than NO one*

The shape of the I-V peaks are better detected than G-V at 20Hz and, in particular, the NO trials ones look sharper and their height is significant lower than N_2O trials, as NO process better saturates dangling bond at SiC/SiO_2 interface reducing charge trapping/detrapping due to interface defects, so that we can state that we have a qualitative nitridation efficiency evidence by the I-V current peak. This result suggested us to investigate on more lots and wafers the nitridation efficiency by I-V test as POA process monitor. So we took 5 wafers coming from 5 different lots either for NO POA process or N_2O one. It was possible to perform the I-V test as it doesn't damage the all device and it is possible to put the wafer again in the production after test. As it is clear looking at Figure 4, it is confirmed not only the peak shape and the intensity of the two processes (lower peak heights on NO POA), but moreover we can demostrate by an easy test as I-V ramp, how much difficult is N_2O process reproducibility. Looking at I-V curves carried out by N_2O process samples, they are located at different voltages with different peak intensity. It is related to the difficulty to provide a constant, stable and reproducible amount of N_2, O_2 and NO during N_2O pyrolysis at different process times. Differently, the I-V characteristic coming from several wafers coming from lots diffused at different process time are superimposed with a low variation. This trial confirms also the relation between the peaks eight and the nitridation dangling bonds treatment.
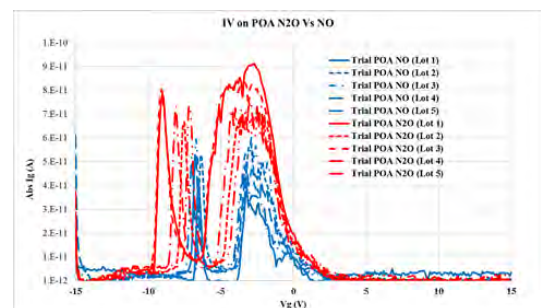

Figure 4: *I-V Characteristics comparison between N_2O vs NO samples. It is an evidence also of NO process stability*

Moreover, the purpose of the investigation was the characterization of the charging trapping properties at SiC/SiO$_2$ interface and in the gate oxide bulk. In this work we demostrate that the charge sensing techniques, which are commonly used to track and spatially locate the trapped charges (both positive and negative) in the gate oxide bulk is also efficient to track also the trapped charge as a function of the injected electron fluence at SiC/SiO$_2$ interface. This test is represented by the drift of reading parameters such as CV, Transistor Threshold and the voltage where the Fowler-Nordheim (F-N) conduction starts (at $+$/-10nAmps) induced by stress current in order to model the transistor aging. The stress between two readouts increases according to a power law starting from 360ms to 3600s per single stress pulse. Then we represent the estimated trapped charge and the position of the charge centroids, as function of the cumulated current stress time following the method shown by DiMaria and Stasiak [11]. In particular, Figure 5 shows how the charge sensing method probe the charge centroid for N$_2$O process near the interface and confirms the lower efficiency in the treatment of near interface oxide traps (NIOTs) than NO process. The chart represent an ideal gate oxide cross section between SiC and Poly.

The dashed lines represent the gate oxide thickness which is higher on N$_2$O process as it provide a thin oxidation layer at SiC/SiO$_2$ interface.
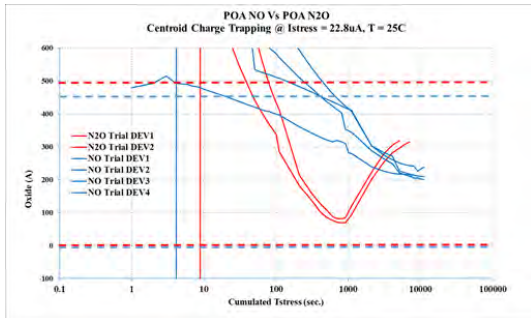

Figure 5: *Charge trapped under Constant Current Stress Injection on both samples. During stress N2O trial traps until the SiC/SiO$_2$ interface unlike NO sample which traps only in the bulk of the oxide*
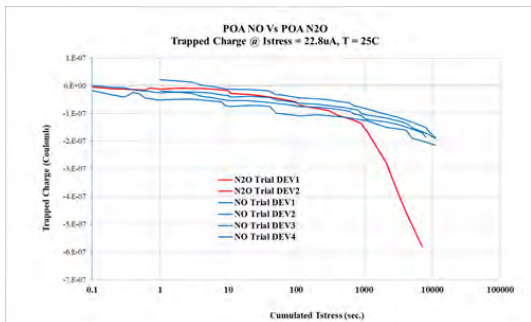

Figure 6: *Charge trapped under Constant Current Stress Injection on both samples. After 10ks stress an higher negative charge is trapped in the N$_2$O Sample*

A simulation of the impact of the nitridation is also under evaluation to quantify the energy level of the interface state related to gate voltage where the peak current has been detected. To complete the characterization, and to confirm the advantages in terms of reliability, a Time Dependent Dielectric Breakdown (TDDB) test under Constant Voltage stress (CVS) at 200C and 9MV/cm and 9.5MV/cm has been performed. In Figure 7, we represent the weibull plot coming from the cumulative failure distribution collected under 9MV/cm constant gate field stress at 200C for both the samples.
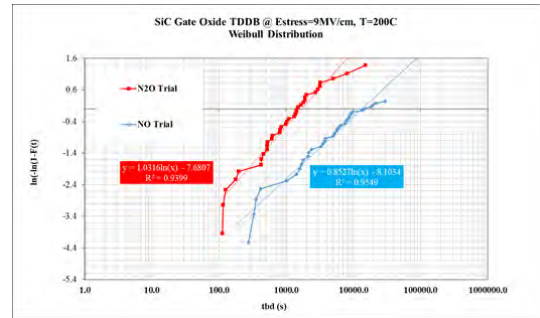

Figure 7: *Cumulative failure distribution of time to breakdown under constant field stress at 200C.*

The study allows us then to take under control the gate oxide resistance and leakage evolution under accelerated conditions as high voltages and temperatures and a first evaluation of oxide reliability improvement induced by NO POA process.

Conclusion

The hypothesis of a better effect of the nitrogen induced by NO process near the SiO$_2$/SiC interface has been validated by the C-V test and by the analysis of the peaks detected by Ig-Vg and the data are summarized in Table I.

TABLE I.		SUMMARY OF THE DATA RELATED TO THE TWO SAMPLES				
	Thickness	DUTs	Tbd (s) under 9MV/cm 200C	Channel Mobility (cm/Vs)	I-V peak (A)	Charge Trapped position
N2O	500Å	36	1719	41	~85pA	~30 Å
NO	470Å	48	14609	52	~40pA	~200 Å

Figure 8: *Significant results of the trials under analysis.*

This provide a useful and easy method to be implemented in production to have an efficient monitoring of interface states reduction. Furthermore, FN as function of the stress time is correlated to the charge centroid in the investigated POA schemes. The different impact of the POA on the gate oxide lifetime is estimated. Finally, the reduced amount of charges obtained by POA NO allowed to achieve the best performance under high voltage stress improving the time to breakdown. Hence, charge

distribution obtained with different POA is correlated to the resulting oxide lifetime. Surprisingly we demostrate that a simple I-V test in a gate voltage range lower than Fowler-Nordheim conduction could represent a nitridation monitor efficiency. For all the above reasons NO POA process is strongly recommended in a production line.

References

[1] T.Kimoto, J.A.Cooper: *Fundamentals of Silicon Carbide Technology: Growth, Characterization, Devices and Applications.* John Wiley Sons Singapore Pre. Ltd, 2014

[2] H.Yoshioka,J.Senzaki,A.Shimozato,Y.Tanaka and H.Okumura: *N-channel field-effect mobility inversely proportional to the interfacestate density at the conduction band edges of SiO2/4H-SiC interfaces.* AIP ADVANCES 5, 017109(2015).

[3] T.L.Biggerstaff, C.L.Reynolds, T.Zheleva,A.Lelis, D.Habersat, S.Haney, S.H.Ryu, A.Agarwal and G.Duscher: *Relationship between 4H-SiC SiO2 transition layer thickness and mobility.* Appl. Phys. Lett. 95, 032108 (2009)

[4] P. Fiorenza, F. Iucolano, G.Nicotra, C. Bongiorno, I. Deretzis, A. La Magna, F. Giannazzo , M. Saggio, C. Spinella, F. Roccaforte: *Electron trapping at SiO2/4H-SiC interface probed by transient capacitance measurements and atomic resolution chemical analysis.* Nanotechnology 29, 395702 (2018).

[5] R.Arora,J.Rozen,D.Fleetwood,K.F.Galloway, C.Xuan Zhang,J.Han,S.Dimitrijev,F.Kong, L.CFeldman,S.T.Pantelides, and R.D.Schrimpf: *Charge Trap-ping Properties of 3C- and 4H-SiC MOS Capacitors With Nitrided Gate Oxides.* Ieee transactions on nuclear science, vol. 56, no. 6, December 2009.

[6] P.Jamet and S.Dimitrijev: *Physical properties of N2O and NO-nitrited gate oxides grown on 4H-SiC.* App.Phys.Lett.79 (2001) 323-325

[7] P.Jamet, S.Dimitrijev and P.Tanner: *Effect of Nitridation in gate oxides grown on 4H-SiC.* J.Appl.Phys.90 (2001) 5058-5063.

[8] A. Severino, N.Piluso, M.A. Di Stefano, F.Cordiano, M. Camalleri, G. Arena: *Study of the Post-Oxidation-Annealing (POA) process on deposited high-temperature oxide (HTO) layers as gate dielectric in SiC MOSFET.* Materials Science Forum (Volume 963)

[9] R.Engel-Herbert, Y.Hwang and S.Stemmer: *Comparison of methods to quantify interface trapdensities at dielectric/III-V semiconductor inter-faces.* JOURNAL OF APPLIED PHYSICS 108,124101 2010

[10] P. Fiorenza, A. Frazzetto, A. Guarnera, M. Saggio, F. Roccaforte: *Fowler-Nordheim tunneling at SiO2/4H-SiC interfaces in metal-oxide-semiconductor field effect transistors.* Appl. Phys. Lett. 105, 142108 (2014)

[11] D.J.DiMaria and J.W.Stasiak: *Trap creation in silicon dioxide produced by hot electrons.* J. Appl.Phys. 65, 2342 (1989)

Patient-specific dose rate assessment in ^{18}F-Choline PET via Monte Carlo simulation of radiation-matter interaction

D. Pistone[1,2,*], G. Mandaglio[1,2], L. Auditore[3], A. Italiano[1,2], E. Amato[2,3]

[1]*MIFT Department, University of Messina, Messina, Italy*
[2]*INFN Sezione di Catania, Catania, Italy*
[3]*BIOMORF Department, University of Messina, Messina, Italy*

[*]Corresponding Author email: dpistone@unime.it

Abstract

Monte Carlo (MC) simulation of radiation emitted by radiopharmaceuticals and its interaction with living matter is the gold standard technique for internal dosimetry in nuclear medicine. In this work the results of the voxel-level patient-specific MC dose rate evaluation for a case of ^{18}F-Choline PET/CT diagnostic exam are reported. The simulations have been developed by means of the GEANT4-based toolkits GATE and GAMOS, using CT scan as input data to build 3D digital phantoms and PET scan to model 3D radionuclide distributions. Focus was put on background and artifacts treatment, employing a threshold-based PET scan filtering procedure. The comparison between filtered and native PET simulations showed a non-negligible influence of PET noise on dose rate estimation in the regions outside the patient body and in air-rich low density organs and tissues, in particular lungs. Moreover the results obtained with GATE and GAMOS showed a better agreement in these regions in the case of filtered PET simulations.

Keywords: nuclear medicine, internal dosimetry, PET, ^{18}F-Choline, GATE, GAMOS, GEANT4.

Introduction

Nuclear medicine (NM) is a medical speciality employing radionuclides, administered to patients as radiopharmaceuticals, for diagnostic and therapeutic purposes. Diagnostic procedures in NM include Positron Emission Tomography (PET) and Single Photon Emission Computed Tomography (SPECT) [1]; therapeutic procedures belong to the field of Molecular RadioTherapy (MRT) [2]. In all such studies a fundamental aspect is Internal Dosimetry (ID), i.e. the quantification of absorbed dose to different organs and tissues of the patient [3]. In fact the damage inflicted to patologic tissues - consequently the efficacy of MRTs - and in general the radiation exposure benefit-risk analysis depend on dose [2, 4]. Therefore the diagnositcs protocols decision, the MRT planning and monitoring and the related radiation protection rely on ID [5].
Different modelizations of human anatomy can be adopted in ID, the main ones being mathematical geometries and voxel geometries (population average models or patient-specific), and as well different dosimetric calculation approaches can be followed: dose-point kernels convolution [6], S values approach [7, 8], direct MC simulation [9]. Direct MC using functional and morphological imaging as input data is the gold standard for ID [10, 11], providing higher accuracy at the expense of longer computational time. In this work it is reported how this latter approach was used to perform the voxel-level patient-specific dose rate assessment for a case of ^{18}F-Choline PET/CT diagnostic exam. Focus was put on the investigation of the influence of PET scan background noise on the dosimetric outcomes, applying a threshold-based filtering technique and comparing the filtered PET simulations with the native PET ones. The simulations employed have been developed with the toolkits GATE [12] and GAMOS [13], both based on GEANT4 [14], one of the most validated and widely used softwares for the simulation of the radiation-matter interaction.

Materials and methods

Input data for the dose rate study were the co-registered PET and Computed Tomography (CT) scans (a coronal slice in Fig. 1a) acquired in a diagnostic ^{18}F-Choline PET/CT exam performed with the Philips Gemini TF 16 scanner at the Nuclear Medicine Unit of the University Hospital "G. Martino" in Messina (Italy); details on the used scans are described in [15]. ^{18}F-Choline is a PET radiopharmaceutical commonly used in the diagnosis and monitoring of prostate cancer, taking advantage of the enhanced choline uptake in such neoplastic tissues [16].
MC simulations were implemented independently with GATE v8.1 and GAMOS v6.0.0, using in both cases the

CT images to model a voxelized phantom reproducing the patient's body morphology, and PET images to model a voxelized radionuclide spatial distribution. The phantom definition procedure differs in the two toolkits. GATE assigns to each CT voxel a material (i.e. a chemical composition) on the basis of user defined Hounsfield Units (HU) intervals, defines submaterials (with same chemical composition) from HU subintervals and assigns a density to each submaterial on the basis of a HU-to-density calibration relation, in our case the one reported in [15]. GAMOS assigns to each CT voxel a density directly converting through the HU-to-density relation and assigns a material on the basis of user defined density intervals. The five intervals of density (and correspondingly HU) reported in Tab. 1 identify the materials used:

Material	HU intervals	ρ (g/cm^3)
air	HU $\leq$ -855.7	$\rho \leq 0.10$
lung tissue	-855.7 < HU $\leq$ -126.5	$0.10 < \rho \leq 0.85$
adipose tissue	-126.5 < HU $\leq$ -39.0	$0.85 < \rho \leq 0.94$
soft tissue	-39.0 < HU $\leq$ 343.6	$0.94 < \rho \leq 1.2$
bone	HU > 343.6	$\rho > 1.2$

Table 1: *HU intervals and corresponding density (ρ) intervals for the materials [15] used in the simulations.*

All the other aspects of the simulation are instead equivalent for GATE and GAMOS. The radionuclide distribution constituting the emitting source was implemented associating to each PET voxel an event generation probability through linear conversion of its activity concentration value. The decay of the radionuclides, ^{18}F, was simulated through the GEANT4 module *G4RadioactiveDecay*, and the interactions of their daughters with the phantom matter was simulated through the *G4EmStandardPhysics_option3* physics list [17], applying a secondary particles production cut of 50 μm.
Absorbed doses D_{ijk} and their statistical uncertainties δ_{ijk} were scored at voxel level, with the same resolution of the phantom matrix. Output dose maps were divided for the total number of generated events in the simulation, N_{evts}, and multiplied by the whole body total activity at the PET acquisition time $t = t_s$, $A(t_s) = \sum_{ijk} A_{ijk}(t_s)$, obtaining the dose rate maps. Therefore for each voxel:

$$\dot{D}_{ijk}(t_s) = (D_{ijk}/N_{evts}) \cdot A(t_s) \qquad (1)$$

From the dose rate maps we furthermore evaluated dose rate average values in selected Volumes of Interest (VOIs) and built Dose Rate Volume Histograms (DRVHs) referred to the VOIs. The VOIs were defined using the software 3DSlicer [18], segmenting on the CT images the following organs (shown in Fig. 1a): liver (L.), right lung (R.L.), left lung (L.L.).

To investigate and quantify the influence on the dose rate outcomes of reconstruction background noise present into the PET images, we developed a threshold-based filtering procedure of the PET scan and performed further simulations using as input data for the radionuclide distribution the filtered PET. Firstly we set to zero all the

PET voxels corresponding to CT voxels to whom air is assigned as material, thus with HU < -855. Then we set to zero all the PET voxels with activity concentration below 100 Bq/mL. Aim of the filtering procedure was to minimize the probability of generating decays in areas where radiopharmaceutical presence is unrealistic, actually corresponding to air, inside and outside the patient body, and to materials not belonging to the patient body, like the PET/CT bed. The same outputs as for the native PET simulations were deduced: dose rate maps, dose rate average values into VOIs and DRVHs. Referring to Eq. 1, also in the case of filtered PET, $A(t_s)$ was anyways retrieved from the native PET, in order for the overall procedure to ensure the conservation of the total rate of decays.

Results and discussion

The average dose rates $\langle \dot{D} \rangle = \langle \dot{D}_{ijk}(t_s) \rangle$ in each VOI for native PET and filtered PET simulations are presented in Tab. 2, together with their corresponding average statistical uncertainties $\langle \delta \rangle = \langle \delta_{ijk} \rangle$, the relative per cent difference ε between the mean values obtained with GATE and GAMOS, the mean value $\langle \varepsilon_{ijk} \rangle$ of the voxel-level relative per cent differences ε_{ijk} between GATE and GAMOS, and the relative per cent differences κ between the mean values obtained with filtered and native PET simulations (all these quantities are described more in detail in [15]).

VOI	L.	R.L.	L.L.
Volume (cc)	1074	2091	1797
$\langle \dot{D} \rangle$ GATE (μGy/min)	83.34	71.42	59.79
$\langle \delta \rangle$ GATE (%)	±5.55	±14.55	±15.60
$\langle \dot{D} \rangle$ GAMOS (μGy/min)	84.28	62.74	50.67
$\langle \delta \rangle$ GAMOS (%)	±5.55	±13.20	±14.28
ε (%)	-1.11	+13.83	+18.01
$\langle \varepsilon_{ijk} \rangle$ (%)	-0.44	+12.83	+17.26
$\langle \dot{D} \rangle$ GATE $_{fil}$ (μGy/min)	86.27	38.36	28.55
$\langle \delta \rangle$ GATE $_{fil}$ (%)	±5.63	±19.80	±22.21
$\langle \dot{D} \rangle$ GAMOS $_{fil}$ (μGy/min)	86.82	37.38	26.96
$\langle \delta \rangle$ GAMOS $_{fil}$ (%)	±5.62	±17.72	±20.21
ε $_{fil}$ (%)	-0.64	+2.60	+5.91
$\langle \varepsilon_{ijk} \rangle$ $_{fil}$ (%)	-0.40	+9.40	+14.66
κ GATE (%)	+3.51	-46.29	-52.25
κ GAMOS (%)	+3.02	-40.42	-46.80

Table 2: $\langle \dot{D} \rangle$, $\langle \delta \rangle$, ε, $\langle \varepsilon_{ijk} \rangle$ and κ in the defined VOIs .

Considering the results of the simulations employing native PET, a very good agreement between GATE and GAMOS was found for the liver VOI, within about 1% considering both ε and $\langle \varepsilon_{ijk} \rangle$. Instead for lungs VOIs wider differences were observed, with GATE overestimating their dose rates with respect to GAMOS, as it can be seen also comparing the dose rate map slices in Fig. 1b and 1c. These larger differences are attributable to the different density assignment procedure followed by the two toolkits, which appears to have more impact for low density voxels, as in lungs, causing wider differences

in their dose outcomes than in more dense voxels, as in liver.

Considering the results of the filtered PET simulations with respect to the native PET ones, a slight increase of the average dose rate in liver, of about 3% in terms of κ, is observed with both GATE and GAMOS when using filtered PET. Instead a 40% up to 50% decrease of average dose rate is observed for lungs, still with both toolkits. This significant lowering of dose rate in lungs with respect to the native PET simulations can be appreciated also in Fig. 2 (in the case of GATE), moreover showing the reduction of dose rate background in the air outside the body and in air-rich spots of abdomen and oro-nasal cavity.

Comparing GATE and GAMOS filtered PET simulations results, an excellent agreement in liver is obtained, with $\varepsilon_{\mathrm{fil}}$ and $\langle \varepsilon_{ijk} \rangle_{\mathrm{fil}}$ below 1%, and the agreement for lungs improves significantly with respect to native PET simulations, with $\varepsilon_{\mathrm{fil}}$ going down below 3% in R.L. and below 6% in L.L.. This evidence can be observed also in terms

of DRVHs, shown in Fig. 3, noticing that while for the native PET simulations there is a certain difference between GATE and GAMOS lungs dose rates in less than the 60% of the volume, for the filtered PET simulations there is an excellent agreement. This fact supports the hypothesis that the difference in density assignment procedure of GATE and GAMOS has more influence for low density and lowly perfused voxels, like the ones of lungs, since the PET filtering reduces their contribution to the dose rate outcomes, bringing GATE and GAMOS results to find closer agreement. From DRVHs in Fig. 3 it can be also noticed the already mentioned decrease of lung dose rates in filtered PET simulations with respect to native PET ones. The obtained results lead to the conclusion that unfiltered PET MC simulations generate a significant amount of decays in the air inside lungs and other anatomical districts due to PET background noise, causing a non negligible overestimation of dose rates with respect to filtered PET simulations.
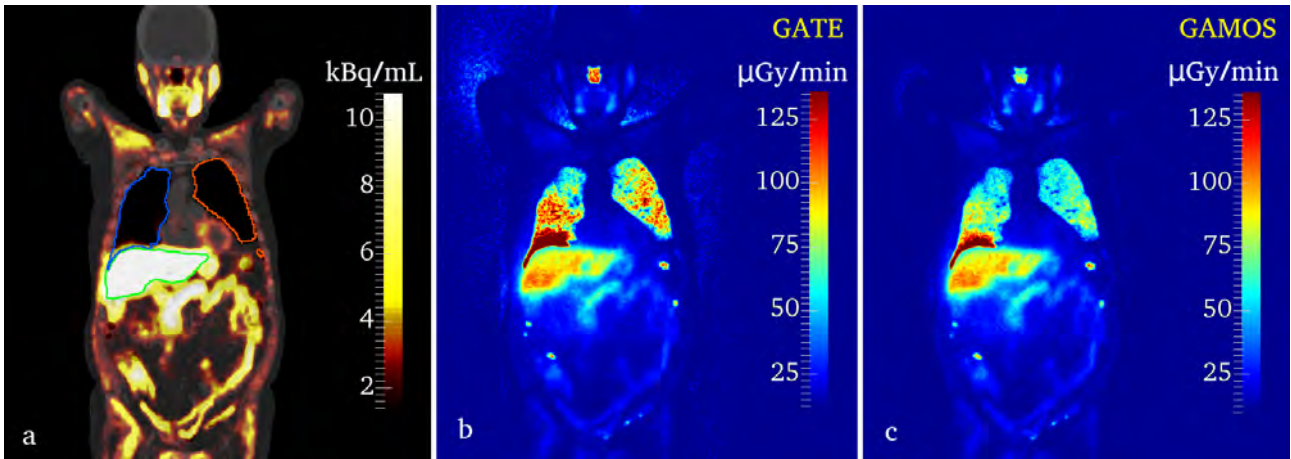

Figure 1: *CT and* ^{18}*F-Choline PET fusion of coronal slices (a) with VOIs contours (green: L., blue: R.L., orange: L.L.) and corresponding dose rate slices estimated with GATE (b) and GAMOS (c) using native PET.*
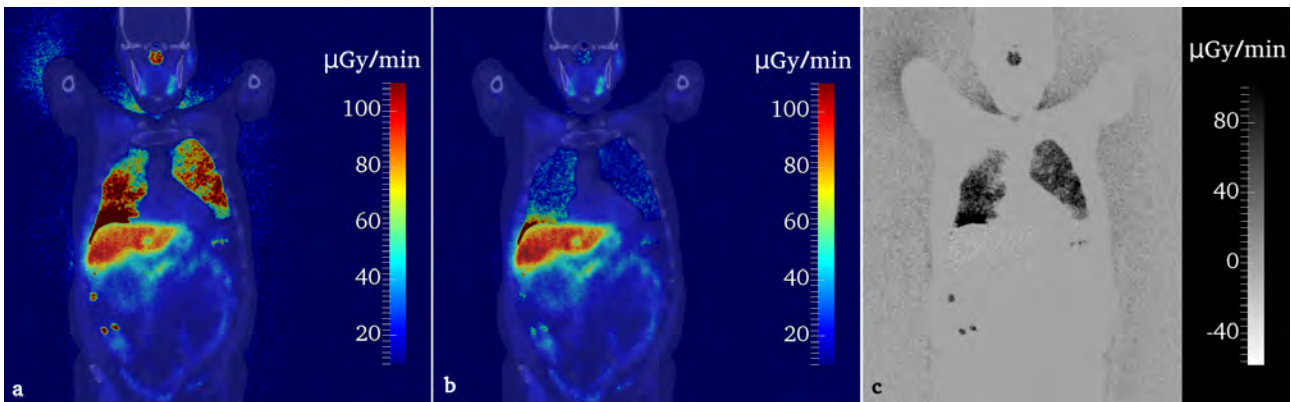

Figure 2: *Coronal slices of dose rate (fused with CT to visualize body morphology) estimated with GATE using native PET (a) and filtered PET (b), and the corresponding slice obtained by logical subtraction of filtered dose rate map from native one (c), highlighting the differences between the two simulations outcomes.*
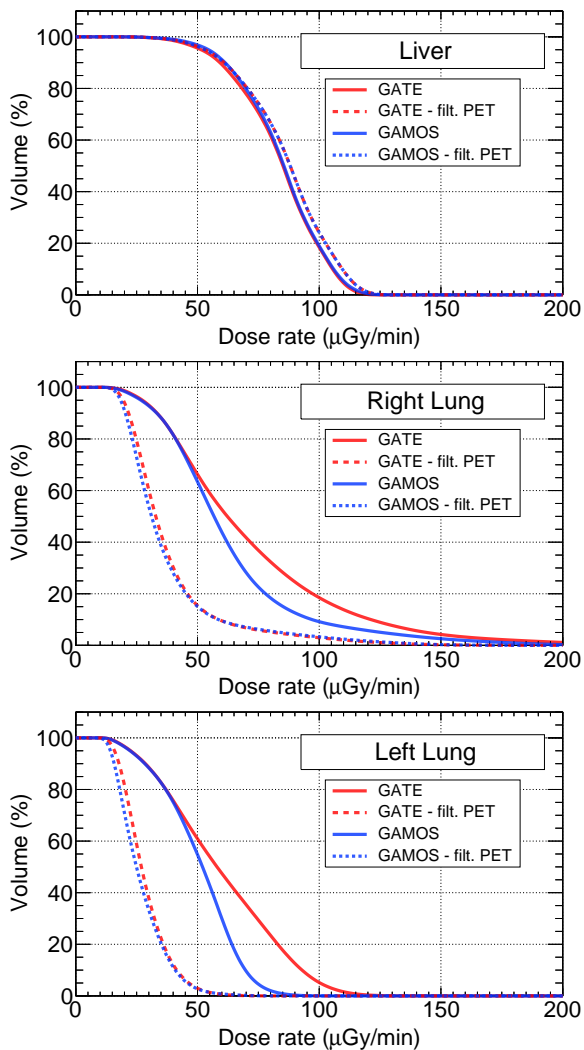
Figure 3: *DRVHs in the defined VOIs.*

Conclusions

The dose rate assessment performed by means of MC simulations with GATE and GAMOS for a ^{18}F-choline PET exam has been reported. Dose rate 3D maps, dose rate average values into liver and lungs VOIs and DRVHs were evaluated. A threshold-based PET filtering technique was adopted to minimize the decay generation in unrealistic locations, mainly air inside and outside the patient body, in order to evaluate dose rate artifacts and overestimations due to PET background noise. A dose rate decrease between about 40% and 50% was observed in lungs VOIs for filtered PET simulations, and a general lowering of background and high-dose-rate spots corresponding to air-rich regions was also obtained. Filtered PET simulations also showed an increased agreement between GATE and GAMOS results in lungs VOIs, supporting the hypothesis that the differences between GATE and GAMOS density assignment procedures have more influence on low density and lowly perfused voxels.

Well designed filtering procedures of functional scans used as input for MC simulations could enable to reproduce more realistically the systems to be simulated for internal dosimetry and improve the dosimetric assessment for organs like lungs, with a substantial presence of air inside them, by reducing the contribution of decays simulated in unrealistic, actually non-perfused, regions.

References

[1] Boccato Payolla, F. et al., *Radiopharmaceuticals for diagnosis in nuclear medicine: a short review*, Ecletica Quim J. **44**(3) 11-19 (2019), DOI: https://doi.org/10.26850/1678-4618eqj.v44.3.2019.p11-19

[2] Strigari, L. et al., *The evidence base for the use of internal dosimetry in the clinical practice of molecular radiotherapy*, Eur. J. Nucl. Med. Mol. Imaging **41** 1976–1988 (2014), DOI: https://doi.org/10.1007/s00259-014-2824-5

[3] Stabin, M.G. et al., *Radiation dosimetry in nuclear medicine*, Appl. Radiat. Isot. **50**(1) 73-87 (1999), DOI: https://doi.org/10.1016/S0969-8043(98)00023-2

[4] Fahey, F. et al., *Dose optimization in nuclear medicine*, Seminars in Nuclear Medicine **44**(3) 193-201 (2014), DOI: https://doi.org/10.1053/j.semnuclmed.2014.03.006

[5] Stokke, C. et al., *Dosimetry-based treatment planning for molecular radiotherapy: a summary of the 2017 report from the Internal Dosimetry Task Force*, Eur. J. Nucl. Med. Mol. Imaging **4** 27 (2017), DOI: https://doi.org/10.1186/s40658-017-0194-3

[6] Giap, H.B. et al., *Validation of a dose-point kernel convolution technique for internal dosimetry*, Phys. Med. Biol. **40** 365-381 (1995), DOI: https://doi.org/10.1088/0031-9155/40/3/003

[7] Bolch, W.E. et al., *MIRD pamphlet No. 17: the dosimetry of nonuniform activity distributions–radionuclide S values at the voxel level*, J. Nucl. Med. **40**(1) 11S–36S (1999), PMID: https://pubmed.ncbi.nlm.nih.gov/9935083/

[8] Amato, E. et al., *Monte Carlo study of voxel S factor dependence on tissue density and atomic composition*, Nucl. Instrum. Methods Phys. Res. A **729** 870-876 (2013), DOI: https://doi.org/10.1016/j.nima.2013.08.059

[9] Amato, E. et al., *A Monte Carlo model for the internal dosimetry of choroid plexuses in nuclear medicine procedures*, Phys. Med.: EJMP **49** 52-57 (2018), DOI: https://doi.org/10.1016/j.ejmp.2018.05.005

[10] Dewaraja, Y.K. et al., *MIRD Pamphlet No. 23: Quantitative SPECT for Patient-Specific 3-Dimensional Dosimetry in Internal Radionuclide Therapy*, J. Nucl. Med. **53** 1310-1325 (2012), DOI: https://doi.org/10.2967/jnumed.111.100123

[11] Auditore, L. et al., *Internal dosimetry for TARE therapies by means of GAMOS Monte Carlo simulations*, Phys. Med.: EJMP **64** 245-251 (2019), DOI: https://doi.org/10.1016/j.ejmp.2019.07.024

[12] Jan, S. et al., *GATE: a simulation toolkit for PET and SPECT*, Phys. Med. Biol. **49** 4543-4561 (2004), DOI: https://doi.org/10.1088/0031-9155/49/19/007

[13] Arce, P. et al., *GAMOS: A Geant4-based easy and flexible framework for nuclear medicine applications*, 3162–3168 (2008), DOI: https://doi.org/10.1109/NSSMIC.2008.4775023

[14] Agostinelli, S. et al., *Geant4 — a simulation toolkit*, Nucl. Instrum. Methods Phys. Res. A **506**(3) 250–303 (2003), DOI: https://doi.org/10.1016/S0168-9002(03)01368-8

[15] Pistone, D. et al., *Monte Carlo based dose-rate assessment in ^{18}F-Choline PET Examination: A comparison between GATE and GAMOS codes*, Atti Accad. Pelorit. Pericol. Cl. Sci. Fis. Mat. Nat. **98**(1) A5 (2020), DOI: https://doi.org/10.1478/AAPP.981A5

[16] Jadvar, H., *Molecular Imaging of Prostate Cancer: PET Radiotracers*, Am. J. Roentgenol. **199**(2) 278-291 (2012), DOI: https://doi.org/10.2214/ajr.12.8816

[17] Geant4 Collaboration, *Physics Reference Manual Release 10.6*, Geant4 website, http://geant4-userdoc.web.cern.ch/geant4-userdoc/UsersGuides/PhysicsReferenceManual/BackupVersions/V10.6/html/index.html last accessed on 2020-12-18

[18] Slicer Wiki contributors, *3DSlicer User Manual Documentation/4.10*, Slicer Wiki, https://www.slicer.org/wiki/Documentation/4.10 last accessed on 2020-12-18

Calculations of optical forces and optical trapping of dust particles by T-matrix methods

P. Polimeno[1,2,*], M. A. Iatì[2], O. M. Maragò[2], R. Saija[1]

[1] *Dipartimento di Scienze Matematiche e Informatiche, Scienze Fisiche e Scienze della Terra, Università degli Studi di Messina, I-98166, Messina, Italy*
[2] *CNR-IPCF, Istituto per i Processi Chimico-Fisici, I-98158, Messina, Italy*

[*]Corresponding Author email: polimenop@unime.it

Abstract

We show optical tweezers can be used to trap and characterize extraplanetary nano- and micro-particles. In particular, through the T-matrix formalism, we calculate radiation pressure and optical trapping properties of a variety of complex particles of astrophysical interest.

Keywords: optical trapping, optical scattering, optical manipulation.

Introduction

Focused light can be properly exploited to manipulate single or complex nanostructures [1–3]. A wide variety of dielectric, metal, and/or biological particles from the nano- to the microscale can be trapped, pushed, or binded thanks to Optical Tweezers (OT) directly in liquid, air or vacuum environment [4–6]. In their standard configuration, OT consist of a single laser beam generally focused by a high numerical aperture (NA) objective to a diffraction-limited spot [1, 2]. Thus, a nanoparticle can be trapped near the focal point by optical forces associated with the high intensity gradients surrounding the focal region [1, 2]. Thanks to their high application flexibility, the OT can be exploited in fields not yet fully developed such as the spatial explorations. This idea, originally born from the main space agencies, *e.g.*, NASA, wants to satisfy the need in researching new methodologies in the collection and analysis field of extraplanetary particles in situ or return to Earth [7]. In other words, the OT could provide new information on space materials that is currently unreachable, *e.g.*, the dust volatile component not detectable in situ by the Rosetta/ESA dust instruments (GIADA, MIDAS, COSIMA) and not retrievable by samples return missions, or have biases due to collection media contamination, *e.g.* cometary dust samples trapped in aerogel and returned by the Stardust/NASA space probe [8, 9]. Our work fits into this context calculating theoretically the light pressure and optical trapping properties on a variety of realistic dust particle models. Therefore, we show the solar radiation calculations that to a major understanding of micro-particle dynamics in space. Finally, we consider and compare optical trapping features of dust particles in standard OT in water (typical laboratory conditions) with those calculated for OT in air or in space.
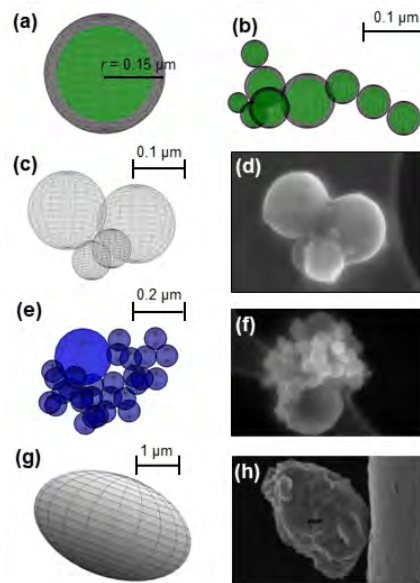

Figure 1: *Scattering models with shapes inspired by interplanetary particles collected in the DUSTER mission [10]. In (a) and (b), the models emulate hypothetical interstellar dust grains where the olivine is considered covered by a carbon layer. In (c), the model of a silica particle arranged in quenched melt spheres shown in the TEM image (d). In (e), the model of condensed Ca[O] nanograins that are accreted onto a larger melted aggregate of tiny carbonate grains shown in the TEM image (f). In (g), a model of an ellipsoidal fassaite shown in the TEM image (h). Here, we consider an effective refractive index constructed mixing silica (53%), CaO (27%), FeO (10%), Al_2O_3 (10%), according to the Bruggeman criterion [12].*

Model and methods

We consider several models of extra-planetary dusts, some of which collected in the Duster mission [10]. In Fig. 1, their sketches are shown. On the top of the Fig. 1, stratified single/aggregated spheres emulate hypothetical interstellar dust grains whose constituents are olivine (core) and aliphatic carbon (shell) [11]. The sphere radius of Fig. 1a is $r = 0.15$ μm. On the other hand, the cluster of Fig. 1b is composed by 9 spheres of different sizes with the major semi-axis $r = 0.16$ μm. In Fig. 1c, we present a model according to a Field Emission Scanning Electron Microscope (FESEM) image of a silica particle clustering arranged in quenched melt spheres, shown in Fig. 1d, and collected in the DUSTER mission [10]. The model is composed by 4 spheres of different radius with the major semi-axis $r = 0.23$ μm. Fig. 1g represents the model of condensed Ca[O] nanograins that are accreted onto a larger melted aggregate of tiny carbonate grains, shown in the TEM image of Fig. 1e, and collected in the DUSTER mission [10]. The larger sphere is calcite and the other spheres are CaO. The cluster model is composed by 30 spheres, and its major semi-axis has $r = 0.25$ μm. The Fig. 1g shows the model of a fassaite ellipsoidal, collected during DUSTER mission, and shown in a TEM image of Fig. 1h [10]. We consider an effective refractive index constructed mixing silica (53%), CaO (27%), FeO (10%), Al_2O_3 (10%), according to the Bruggeman criterion [12]. The major semi-axis is 2 μm.

All non-spherical models are oriented in such a way that their major axis is aligned with the incident light propagation direction. The optical force that we calculate for each particle stems from the electromagnetic momentum conservation during the light scattering process [2, 13]. This means that Maxwell's equations and the integration of the averaged Maxwell stress tensor have to be performed [13, 14]. However, such calculations can be computationally complex, e.g. when we deal with non-spherical or non-homogeneous particles, and the use of approximations and suitable calculation techniques can be often advantageous [2, 3]. Therefore, the calculation of the solar radiation pressure and optical trapping forces on model particles of Figs. 1a - 1f is carried out with the T-matrix formalism because the particle size is comparable with the light wavelength. Such method appears to be computationally advantageous because any particle can be modeled through a sphere, clusters or aggregates of spheres, spheres with spherical (eccentric) inclusions, and multilayered spheres [13, 15, 16]. On the other hand, when particle size is largest than the light wavelength such as in the model particle case of Fig. 1g, the calculation is carried out in the ray optics approximation. Despite the ellipsoidal shape of the dust grain, we exploited the optimized computational MATLAB codes for dielectric particles provided by Callegari et al. [17] (http://opticaltweezers.org/software/otgo-optical-tweezers-geometrical-optics/).
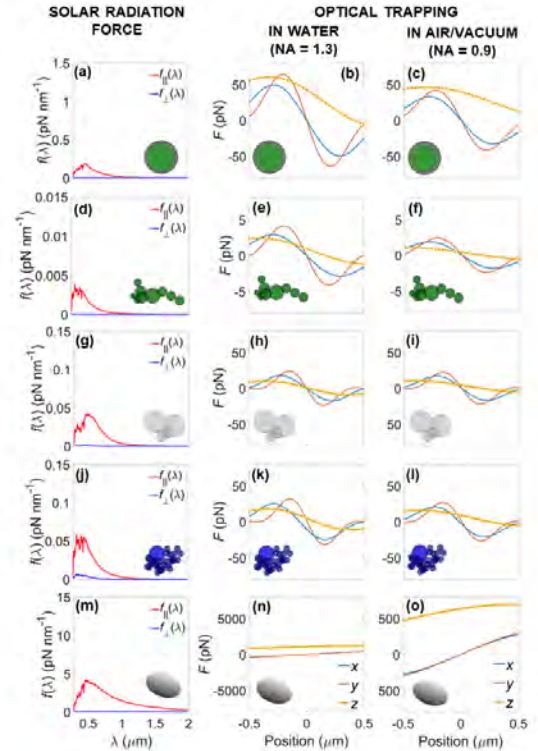
Results and discussion

Figure 2: *In the left column, optical forces distributions exerted by the Sun on dust particles modeled as shown in Fig. 1. The optical force parallel, $f_\parallel(\lambda)$ (blue line), and perpendicular, $f_\perp(\lambda)$ (red line), are intended respect to the light propagation direction $\hat{\mathbf{k}}$. Instead, in the other two columns, the optical trapping forces, F, along x- (blue line), y- (red line), and z-directions (yellow dots) are pictured in two distinct cases when the particle is in water (center) and in air (right). (a), (b), (c), concern the calculations on olivine-aliphatic carbon core-shell sphere. (d), (e), and (f) show are related to the quenched melt silica. (j), (k), and (l) show results for the bunch-of-grape carbon Ca-rich. (m), (n) and (o) concern the fassaite ellipsoid. For the optical trapping calculations the laser power is fixed at 50 mW and the wavelength at 0.83 μm.*

With these premises, the radiation forces $\bar{\mathbf{F}}$ that the Sun exerts upon the considered particles are calculated as:

$$\bar{F}_s = \int_\lambda \mathrm{d}\lambda \, f_s(\lambda) \,, \qquad (1)$$

$$f_s(\lambda) \equiv \frac{i_\odot(\lambda)}{I_\odot} \, F_{\mathrm{rad},s}(\lambda) \,, \qquad (2)$$

where the index $s = (\parallel, \perp)$ specifies respectively the parallel and the orthogonal component of $F_{\mathrm{rad},s}(\lambda)$ respect to the radiation incident direction $\hat{\mathbf{k}}$. The expressions of

$F_{\mathrm{rad},s}$ are the ones provided by Jones et al. [2] in the ray optics approximation, and by Borghese et al. when T-Matrix approach is used [13]. The term $f_s(\lambda)$ specifies the spectral force distribution obtained scaling the computation outputs $F_{\mathrm{rad},s}(\lambda)$ upon the solar radiation intensity distribution $i_\odot(\lambda)$ normalized at the solar irradiance $I_\odot$, i.e., $I_\odot = \int_\lambda \mathrm{d}\lambda\, i_\odot(\lambda) = 1.34$ kW/m^2 [18]. Therefore, the considered spectrum is chosen in the range $\lambda = [0.28 - 2]$ μm that is when the light emission by the Sun has the maximum intensity. In the left column of the Fig. 2, we plot the solar radiation forces distributions $f_s(\lambda)$ (Eq. 2) upon all models presented in the Fig. 1. The parallel component $f_\parallel$ is predominant over the perpendicular one $f_\perp$. In fact, the parallel component to the incident field depends on the extinction of the electromagnetic field while the transverse one is related to the asymmetry parameters g_i which takes in account the eventual non-sphericity of the scatterer [13, 19]. Consequently, for the spherical and cylindrical particles the component $f_\perp$ is identically zero due to the axial symmetry in which the models are located with respect to the incident ray direction (Figs. 2a, and 2m). Instead, concerning Figs. 2d, and 2g which regard clusters of spheres displaced in a rather elongated way, the perpendicular component appears to be much smaller than the parallel one. The reason has to be found in the fact that the major inertial axis of such models, much larger than the other two, is aligned with the incident field. In fact, the rather elongated structures at the nanoscale tend to align with the incident electric field lines in accordance with Borghese et al. [20]. Therefore, their symmetries appear to be almost cylindrical, and $f_\perp$ is relatively low but not properly zero. In fact, the related $\bar{F}_\perp \neq 0$, as shown in Tab. 1. On the other hand, in Fig. 2j we report the non-symmetrical model of the bunch-of-grape carbon Ca-rich. Here, $f_\perp$ is manifestly non zero such as $\bar{F}_\perp \simeq 1.46$ pN, almost the same magnitude order of $\bar{F}_\parallel \simeq 18.2$ pN (Tab. 1). Summing up, $f_\parallel$ shape is quite similar to the solar irradiance spectrum in the VIS/near IR range due to the Eq. 2. It takes into account how solar radiation optically interacts with the considered extra-planetary dusts, exerting forces $\sim 10^{-12}$ N. Therefore, $f_\parallel$ is proportional to the geometrical cross-section, and a correlation is possible to verify comparing, for each model, σ_{geom} with the integrated force component $\bar{F}_\parallel$ (Tab. 1). Instead, the possible occurrence of the perpendicular component has a particular importance for the dynamics of the non-symmetric structures, as, for instance, it has been recognized in the interstellar dusts [21]. A further systematic characterization of optical forces on these particles is achieved by calculating optical trapping forces in OT, i.e a single Gaussian beam focused by a high-NA objective. In our calculations the laser wavelength is fixed at 0.83 μm, that is a typical wavelength for OT experiments in the near-infrared, and the power $P = 50$ mW. In the right two columns of Fig. 2, we show the three Cartesian components of the trapping forces in the neighborhood of the OT paraxial nominal focus placed at the origin of the coordinate system ($x = y = z = 0$). The trapping arises when the focused incoming field generates a restoring force proportional to the particle's displacement from an equilibrium point, and that, for small displacements, behaves harmonically [2, 3]. Therefore, trap stiffnesses are defined as:

$$\kappa_i \equiv \left.\frac{\mathrm{d}F_i}{\mathrm{d}x_i}\right|_{x_{\mathrm{eq},i}}. \qquad (3)$$

We calculate optical trapping in water ($n_{\mathrm{m}} = 1.33$) with an objective NA $= 1.3$ (middle column of Fig. 2) and in air or vacuum ($n_{\mathrm{m}} = 1$) with NA $= 0.9$ (right column of Fig. 2). The higher NA in water causes the equilibrium point C_{eq} to be closer to the nominal focus than in air. This is confirmed by comparing the graphs in Fig. 2, central column (in water), with those of the right column (in air). The dielectric particles, such as the quenched melt silica (Figs. 2h, 2i), and carbonate cluster (Figs. 2k, 2l) exhibit fairly stable trapping. Even the interstellar dust model of a sphere aggregate can be trapped thanks to the relatively low extinction (Figs. 2e, 2f). Indeed, for these model particles we are able to extrapolate the trapping constants along the axial direction, κ_z, and along the perpendicular direction, $\tilde{\kappa} \equiv (\kappa_x + \kappa_y)/2$ (Tab. 1). On the other hand, model particles, like the interstellar dust sphere (Figs. 2b, 2c), or the ellipsoidal fassaite (Figs. 2n, 2o), can not be trapped neither in water nor in air. The reason is to be found in their large size (fassaite) and on their strong absorption (interstellar dust, and fassaite).

MODELS	r (μm)	σ_{geom} (μm^2)	$\bar{F}_\parallel$ (pN)	$\bar{F}_\perp$ (pN)	σ_{ext} $\lambda=0.83$ μm (μm^2)	κ_z WATER (pN·μm⁻¹)	$\tilde{\kappa}$ WATER	κ_z AIR/VACUUM	$\tilde{\kappa}$ AIR/VACUUM
	0.15	$7.06 \cdot 10^{-2}$	60.74	0	$4.11 \cdot 10^{-2}$	No trapping			
	0.16	$1.99 \cdot 10^{-2}$	0.95	$3.09 \cdot 10^{-3}$	$2.42 \cdot 10^{-4}$	5.50	24.50	2.00	14.50
	0.23	$7.85 \cdot 10^{-2}$	15.78	0.20	$7.96 \cdot 10^{-3}$	42.50	195.50	25.50	158.50
	0.25	$1.77 \cdot 10^{-1}$	18.20	1.46	$1.15 \cdot 10^{-2}$	63.00	248.5	31.00	171.00
	2.00	12.57	$2.56 \cdot 10^{3}$	0	-	No trapping			

Table 1: *Summary table of radiation pressure and optical trapping properties. For each model particle we show: the radius, r, or the radius of the smallest sphere enclosing the cluster; the geometric cross-section, σ_{geom}; the integrated optical force on the solar intensity spectrum along the parallel, $\bar{F}_\parallel$, and perpendicular direction, $\bar{F}_\perp$; the extinction cross-section σ_{ext} at the trapping wavelength $\lambda = 0.83$ μm; and the optical trap stiffnesses along the optical axis, κ_z, and perpendicular to it, $\tilde{\kappa}$, in water and in air.*

Conclusions

We studied computationally the solar radiation force and optical trapping properties for different extra-planetary

and interstellar dust particles. We showed that the radiation force exerted by the Sun is not trivially negligible and it can actively influence the dynamics of such nano- and micro-structures. Furthermore, we calculated single-beam optical trapping properties for these model particles both in water and in air with parameters close to typical optical tweezers experiments in the near-infrared. We found that weakly absorbing and nanoscale particles can be captured, while particles with stronger absorption show a scattering component of the optical force that prevents optical trapping in a standard single-beam optical tweezers.

References

[1] Ashkin, A.: *Acceleration and Trapping of Particles by Radiation Pressure.* Phys. Rev. Lett., **24**(4), 156 (1970).

[2] Jones, P. H., Maragò, O. M., Volpe, G.: *Optical Tweezers: Principles and Applications.* Cambridge, UK: Cambridge University Press (2015).

[3] Polimeno, P., Magazzù, A., Iatì, M. A., Patti, F., Saija, R., Degli Esposti Boschi, C., Donato, M. G., Gucciardi, P. G., Jones, P. H., Volpe, G., Maragò, O. M.: *Optical Tweezers and their Applications.* J. Quant. Spectrosc. Radiat. Transf., **218**, 131–150 (2018).

[4] Maragò, O. M., Jones, P. H., Gucciardi, P. G., Volpe, G., Ferrari, A. C.: *Optical Trapping and Manipulation of Nanostructures.* Nat. Nanotechnol., **8**, 807–819 (2013).

[5] Ashkin, A., Dziedzic, J.M., Bjorkholm, J.E., Chu, S.: *Observation of a Single-Beam Gradient Optical Trap for Dielectric Particles.* Opt. Lett., **11**, 288-290 (1986).

[6] Ashkin, A., Dziedzic, J. M.: *Optical Trapping and Manipulation of Viruses and Bacteria.* Science, **235**, 1517–1520 (1987).

[7] Stysley, P.: *Laser-Based Optical Trap for Remote Sampling of Interplanetary and Atmospheric Particulate Matter.* NASA-GSFC (2014).

[8] Rotundi, A., Baratta, G. A., Borg, J., Brucato, J. R., Busemann, H., Colangeli, L., D'Hendecourt, L., Djouadi, Z., Ferrini, G., Franchi, I. A., et others: *Combined micro-Raman, micro-Infrared, and Field Emission Scanning Electron Microscope Analyses of Comet 81P/Wild 2 Particles Collected by Stardust.* Meteorit. Planet. Sci., **43**, 367–397 (2008).

[9] Rotundi, A., Rietmeijer, F. J. M., Ferrari, M., Della Corte, V., Baratta, G. A.,

Brunetto, R., Dartois, E., Djouadi, Z., Merouane, S., Borg, J., et others: *Two Refractory Wild 2 Terminal Particles from a Carrot-Shaped Track Characterized Combining MIR/FIR/Raman Microspectroscopy and FE-SEM/EDS Analyses.* Meteorit. Planet. Sci., **49**, 550–575 (2014)

[10] Rietmeijer, F. J. M., Della Corte, V., Ferrari, M., Rotundi, A., Brunetto, R.: *Laboratory Analyses of Meteoric Debris in the Upper Stratosphere from Settling Bolide Dust Clouds.* Icarus, **266**, 217–234 (2016)

[11] Iatì, M. A., Saija, R., Borghese, F., Denti, P., Cecchi-Pestellini, C., Williams, D. A.: *Stratified Dust Grains in the Interstellar Medium–I. An Accurate Computational Method for Calculating their Optical Properties.* Mon. Not. R. Astron. Soc., **384**, 591–598 (2008)

[12] Bohren, C. F., Huffman, D. R.: *Absorption and Scattering of Light by Small Particles.* John Wiley & Sons (2008)

[13] Borghese, F, Denti, P., Saija, R.: *Scattering from Model Nonspherical Particles: Theory and Applications to Environmental Physics.* Springer Science & Business Media (2007)

[14] Mishchenko M. I., Travis, L. D., Lacis, A. A.: *Scattering, absorption, and Emission of Light by Small Particles.* Cambridge University Press (2002)

[15] Waterman, P. C.: *Symmetry, Unitarity, and Geometry in Electromagnetic Scattering.* Phys. Rev. D, **3**, 825 (1971)

[16] Borghese, F., Denti, P., Toscano, G., Sindoni, O. I.: *An Addition Theorem for Vector Helmholtz Harmonics.* J. Math. Phys., **21**, 2754–2755 (1980)

[17] Callegari A., Mijalkov M., Gököz, A. B., Volpe, G.: *Computational Toolbox for Optical Tweezers in Geometrical Optics.* JOSA B, **32**, B11–B19 (2015)

[18] Standard, ASTM: *G173-03-Standard Tables for Reference Solar Spectral Irradiances: Direct Normal and Hemispherical on 37 Tilted Surface.* Ann. Book of ASTM Standards 2003, **14**, (2012)

[19] Saija, R., Iatí, M. A., Giusto, A., Denti, P., Borghese, F.: *Transverse Components of the Radiation Force on Nonspherical Particles in the T-matrix Formalism.* JQSRT, **94**, 163–179 (2005)

[20] Borghese, F., Denti, P., Saija, R., Iatì, M. A., Maragò, O. M.: *Radiation Torque and Force on Optically Trapped Linear Nanostructures.* PRL, **100**, 163903 (2008)

[21] Klačka, J., Kocifaj, M.: *Motion of Nonspherical Dust Particle under the Action of Electromagnetic Radiation.* JQSRT, **70**, 595–610 (2001)

Radon exhalation from the beach sand of Pizzo Calabro (Central Calabria)

D. Romano[1,*], S. Magazù[1], F. Italiano[2], G. Sabatino[1], F. Caridi[1], A. Tripodo[1], M. T. Caccamo[1]

[1] *Dipartimento di Scienze Matematiche e Informatiche, Scienze Fisiche e Scienze della Terra (MIFT), Università di Messina, Messina 98166, Italy*
[2] *Istituto Nazionale di Geofisica e Vulcanologia, Palermo 90146, Italy*

*Corresponding Author email: dromano@unime.it

Abstract

Radon exposure can be a cause of lung cancer. When radon atoms decay, radioactive particles are released, generating health hazards if humans are in proximity of the radioactive source. With the main aim to contribute in the field of health hazard, in this paper we report the radiological results of analyses performed on the heavy-mineral sand coming from the Tyrrhenian coast of Pizzo Calabro (Central Calabria). The sand is made up by different mineral phases such as quartz, feldspar, garnet, monazite and zircon. These minerals originated from dismantling of granitic and metamorphic rocks outcropping in the Serre Massif. Heavy-mineral materials are extracted from quarries and used in construction. In this study, we investigated the amount of radon released from the heavy-minerals sand. Moreover, we defined the potential indoor radiological hazard. The release of radon from the sand was evaluated in terms of ^{222}Rn exhalation rate by using a customized close-looped chamber attached to a RAD 7 detector. The measured values of ^{222}Rn surface and mass exhalation rates are $0.29 \div 0.05 Bq\ m^{-2}h^{-1}$ and $2.95 \div 0.4 mBq\ kg^{-1}h^{-1}$, respectively.
The indoor radon concentration generated from heavy-mineral materials, if used as building material, varies from $0.24 to 2.36 Bq m^{-3}$: these values are lower than the reference limit adopted by the Italian legislation. The results obtained from this study define those heavy-mineral sediments as low Rn-emitting materials

Keywords: Radon; Radiological measurements; Radiation monitoring; Radiation damage evaluation methods..

Introduction

Radon is a colorless and odorless inert noble gas produced from the natural decay series of uranium and thorium. The main isotopes is the ^{222}Rn (half-life of 3.8 days), occurring as an intermediate product in the ^{238}U decay series and which is generated by the ^{226}Ra α decay. Radon, as well as other radionuclides, may be harmful for human health. In order to contribute in the main field of radiological hazard, here we investigate the radon release from the heavy-mineral sands of Pizzo Calabro (Tyrrhenian coast of Central Calabria). These beach sands mainly derive from the dismantling process affected the crystalline rocks outcropping in the Serre Massif (Central Calabria). Old and recent studies (e.g. [1–3]) demonstrated that the beach sediments located along Calabrian coasts contain heavy minerals such as zircons and monazites. Moreover, in the last 40 years, the release of radon from these mineral phases was widely evaluated (e.g. [4–9]). After the study performed by Sabatino et al. [3], who firstly reported the radiological, mineralogical and geochemical features of the heavy-mineral sands collected along the Pizzo Calabro coast, further radiological analyses have been performed on these beach sands, and the results are presented in this work. The ^{222}Rn surface and mass exhalation rate were calculated by using a customized close-looped container attached to a RAD 7 radon detector. Although the beach sands of Pizzo Calabro are not used as building materials, granular sediments containing variable amounts of monazite and zircon are extracted from quarries located in Calabria, and they are used in construction. In light of this evidence, evaluating the release of radon from the monazite and zircon-bearing sands collected at Pizzo Calabro, can be useful to assess the health hazard connected to the building use of heavy-mineral sediments. For this reason, the contribution to the indoor radon activity concentration potentially derived from the building use of the Pizzo Calabro sands was estimated.

Materials and methods

Samples

Samples of heavy-mineral sand were collected in 2017 on the beach of Pizzo Calabro. The radiological, mineralogical and geochemical characterization of these samples was published in Sabatino et al. [3]. SEM-EDX, XRPD and MRS analyses carried out on the sediments showed that sands are composed of quartz, feldspar, garnet, ilmenite, REE-phosphates (Ce-monazite) and zircon mineral phases. Moreover, the sands exhibit ^{222}Ra, ^{232}Th and ^{40}K mean activity concentrations of $230 Bqkg^{-1}$, $2241 Bqkg^{-1}$ and $243 Bqkg^{-1}$, respectively.
One of the ten samples collected in 2017 was further analysed in 2019 in order to define the radon exhalation properties, and the results are reported in this paper. The sample was dried at 105°C in an oven for 24 h and then cooled in a desiccator to constant weight, in agreement with the procedure adopted in Sabatino et al. [3]. After that, samples were sieved to obtain a particle size less than 2 mm and then analysed for the radon exhalation.

Radon exhalation

The ^{222}Rn emanation coefficient was evaluated by enclosing 0.8 L of the sand sample in a handmade container (volume of 8 L), which is connected to a dryer unit (filled with a desiccant) and to an electronic radon detector (RAD 7) through a piping system forming a closed loop in which air circulates (Fig.1).
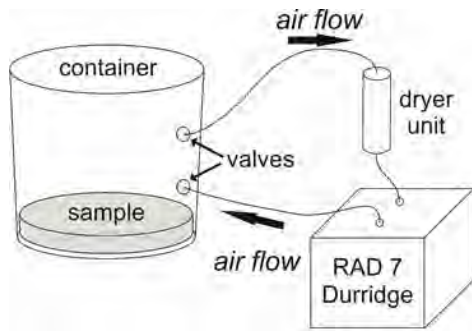

Figure 1: *The radon concentration in the chamber tends to an equilibrium value. Saturation time is controlled by back diffusion effects and leakage from container.*

In order to minimize air leakage and avoid back diffusion effects, silicon was placed along the piping system, and the effective volume of the system was >10 times larger than the pore volume of the samples [10]. The RAD 7 [11] relies on a solid-state ion-implanted planar silicon alpha detector placed inside a 0.7 L internal cell, which allows the measurement of the radon activity concentration by using the activity of relative daughters (i.e. ^{218}Po and ^{214}Po.). The sand sample was sealed in the container and the radon activity concentration in the air volume increases exponentially and tends to an equilibrium value. The sample remained sealed for four weeks,

in order to ensure the establishment of the secular equilibrium between ^{222}Ra and ^{222}Rn [12]. After that, the activity concentration of ^{222}Rn released into the air volume was measured (C_{Rn}). Then, the ^{222}Rn exhalation rate (E) was determined by the following formula [12]:

$$E = \frac{C_{Rn}(\lambda + \lambda l)V}{X} \qquad (1)$$

where $\lambda(h^{-1})$ is the ^{222}Rn decay constant, V (m^3) is the effective volume of the system and X is the total surface of the sample exposes in the container (in m^2) or the mass of the sample (in kg), depending on which the exhalation rate will be expresses per unit of surface area (surface exhalation rate, E_S, $Bq\ m^{-2}h^{-1}$) or per unit of mass (mass exhalation rate, E_M, $Bqkg^{-1}h^{-1}$). The leakage from the system (λl) is equal to $6.96 \times 10^{-3}h^{-1}$ [13].

Indoor radon concentration

The contribute to the total indoor radon concentration derived only from radon exhalation from building materials ($Ci_{Rn(bm)}\ Bq\ m^{-3}$) can be estimated by knowing the surface exhalation rate of the material by the following equation [14]:

$$Ci_{Rn(bm)} = \left[\sum_{i=1}^{n} w_{si} \cdot E_{Si} \right] \frac{S}{V\lambda_v} \qquad (2)$$

where $E_{Si}(Bqm^{-2}h^{-1})$ is the surface exhalation rate, w_{si} is the surface fractional usage of the building material, $S/V(m^{-1})$ is the surface to volume ratio of the room and $\lambda_v(h^{-1})$) is the annual average room ventilation rate. Calculations were made considering a ventilation rate (λ_v) of 0.2 and 2 h^{-1} [15] and a room model with dimensions of (4 x 5 x 2.8) m^3 and a surface volume ratio $S/V = 1.6m^{-1}$.

Results and Discussion

The activity concentration of ^{222}Rn (C_Rn) released from the heavy-mineral sand sample into the air volume of the container, measured after four weeks, is $44.8 \pm 7 Bq\ m^{-3}$. The ^{222}Rn mass exhalation rate, calculated after the experiment with the equation 1, is $2.95 \pm 0.4 mBqkg^{-1}h^{-1}$. This values is rather similar to those measured by Pinto et al. [9] for the medium to coarse fraction of the monazite-rich beach sands from southern India coasts (range $0.8 - 3.9\ mBq\ kg^{-1}\ h^{-1}$). Regarding the ^{222}Rn surface exhalation rate of the studies sands, it was derived to be $0.29 \pm 0.05\ Bq\ m^{-2}h^{-1}$. This value was compared with literature data of the more common building materials used in Italy. The comparison indicates that the surface exhalation rate estimated for the Pizzo Calabro sand is much lower than those of volcanic rocks (e.g. Black pozzolana from Colli Albani 37 $Bqm^{-2}h^{-1}$, "Peperino" from Marino 3.4 $Bq\ m^{-2}h^{-1}$, and "Tufo giallo napoletano" from Campania Region $2.7 Bq\ m^{-2}h^{-1}$; [16]), whereas it is slighly higher than values of carbonate rocks (e.g. "Travertino" from Tivoli $0.065 Bq\ m^{-2}h^{-1}$; [16]), which are not regarded as hazardous materials concerning the radon release.

Monazite, zircon and other heavy minerals occur in the crystalline rocks that crop out in the Serre Massif (e.g. [17]). During the Quaternary, this portion of Calabria, as well as the Sila and the Aspromonte Massifs, have been affected by an intense erosion phases which caused the removal of large volume of materials from the reliefs generating alluvial and marine deposits containing heavy minerals. As a matter of fact, previous studies [1, 2, 18] reported the presence of monazite and zircon in the Quaternary sediments of Calabria. The Pizzo Calabro sands are not used as building materials; on the other hand, a number of quarries in central Calabria produce Quaternary sands for building purposes. Consequently, the presence of heavy minerals, such as monazite and zircon, in the building materials coming from central Calabria is highly probable.

With the aim of understanding if the occurrence of these minerals is harmful for humans in terms of radon exposure, the contribution to the indoor radon concentration derived from the potential use in construction of the Pizzo Calabro sand was evaluated. For residential dwellings, the reference level of indoor radon concentration adopted by the Italian legislation [19] is $300 \ Bq \ m^{-3}$. For dwellings located in a temperate climate, the contribution of radon coming from building materials is around 20% of total indoor radon [20]. Hence, considering the indoor radon reference level of $300 \ Bq \ m^{-3}$, the maximum contribution from a building material should be equal to $60 \ Bq \ m^{-3}$.

In a room model of $4x5x2.8m^3$, with by a ventilation rate ranging from $0.2 to 2h^{-1}$, the ^{222}Rn concentration calculated with the equation 2 resulted to be in the range of $0.24 - 2.36 \ Bq \ m^{-3}$, which is considerably lower than the $60 Bq \ m^{-3}$ threshold. Therefore, our estimations testify that the potential presence of heavy minerals in the calabrian building materials does not represent a health hazard due to the indoor radon.

Conclusion

The radon release from a sample of heavy-mineral sand from Pizzo Calabro was addressed in the present paper. The ^{222}Rn exhalation properties reflects the presence of the heavy minerals in the analysed sands. The ^{222}Rn surface exhalation rate is rather similar to that of carbonate rocks often used in construction in Italy. Our results seem to confirm that the U and Th- rich mineral phases (i.e. monazite and zircon) do not enhance the hazard connected to the radon exhalation. This is due to the fact that the indoor radon concentration, originated from the building use of the monazite and zircon-bearing sands, are well below the Italian legislation threshold.

Acknowledgments

References

[1] Brondi, A. et al: *Valutazioni delle concentrazioni di minerali pesanti nelle spiagge calabresi.* Industria Mineraria **23**, 233 (1971).

[2] Clerici, C.: *Les placers de la plateforme calabrienne.* Boll. Assoc. Min. Subalp. **20**, 25 (1983).

[3] Sabatino, G. et al.: *Radiological assessment, mineralogy and geochemistry of the heavy-mineral placers from the Calabrian coast (South Italy).* J. Instrum. **14**, (2019).

[4] Barretto, P.M.: *Emanation Characteristics of Terrestrial and Lunar Materials and the 222Rn Loss Effect on the U–Pb System Discordance.* Ph. D thesis, Rice University, (1973).

[5] Garver, E. and Baskaran, M.: *Effects of heating on the emanation rates of radon- 222 from a suite of natural minerals.* Appl. Radiat. Isot. **61**, 1477 (2004).

[6] El Afifi, E.M. et al.: *Evaluation of U, Th, K and emanated radon in some NORM and TENORM samples.* Radiat. Meas. **41**, 627 (2006).

[7] Verità, E. et al.: *Radon exhalation rates from zircon sands and ceramic tiles in Italy.* Radioprot. **41**, 445 (2009).

[8] Pinto, P.V, et al.: *Mass exhalation rates, emanation coefficients and enrichment pattern of radon, thoron in various grain size fractions of monazite rich beach placers.* Radiat. Meas. **130**, 106220 (1999).

[9] Krupp, K., et al.: *Radon emanation coefficients of several minerals: How they vary with physical and mineralogical properties.* Am. Mineral. **102**, 1375 (2017).

[10] Petropolous, M.P. et al: *Building materials radon exhalation rate: ERRICA intercomparison exercise results.* In: "Radon in the Living Environment" April 19–23, Athens, Greece (2006).

[11] Durridge Company: *RAD 7, electronic radon detector user manual* . (http:// www.durridge.com), (2018).

[12] Ishimori, Y. et al: *Measurement and calculation of radon releases from NORM residue.* Techical Report Series 474 Vienna, IAEA (2013).

[13] Dentoni, V. et al: *atural radioactivity and radon exhalation rate of Sardinian dimension stones.* Constr. Build. Mater. **247**, 1 (2020).

[14] Romano, D. et al: *Natural radioactivity of the crystalline basement rocks of the Peloritani Mountains (north-eastern Sicily, Italy): measurements and radiological hazard.* Radiat. Prot. Dosim. **191**, **452**, (2020).

[15] UNSCEAR: *Report to general assembly of the United Nations Scientific Committee on the effects of atomic radiation.* United Nations, New York (2000) [ISSN 0255-1373].

[16] TUCCIMEI, P. ET AL: *Simultaneous determination of ^{222}Rn and ^{220}Rn exhalation rates from building materials used in Central Italy with accumulation chambers and a continuous solid state alpha detector: Influence of particle size, humidity and precursors concentration.* Appl. Radiat. Isotopes **64**, 254–263 (2006).

[17] FORNELLI, A. ET AL: *Multi-stage melting in the lower crust of the Serre (southern Italy).* J. Petrol. **43**, 2191 (2002).

[18] BRONDI, A. ET AL: *Sulla provenienza dei diversi tipi di zircone e monazite contenuti nei sedimenti fluviali della Calabria.* Rend. SIMP **28**, 31 (1972).

[19] ITALIAN LEGISLATION: *D. Lgs. 101/2020.*

[20] UNSCEAR: *Sources and effects of ionizing radiation, Report to the general assembly of the United Nations with scientific annexes.* United Nations, New York (1993) [ISBN 92-1-142200-0].

Reports

Studenti di Dottorato di Ricerca

Ciclo XXXV

SiC Power MOSFET - AFM & Raman analyses

L. Anoldo[1−2,*], S. Patanè[1], S. Bevilacqua[2], A. Russo[2]

[1]*Dipartimento di scienze Matematiche ed Informatiche, scienze Fisiche e scienze della Terra; Università degli studi di Messina*

[2]*ADG R&D Power Discrete & Technologies DEVICE ENG group SMART Lab; ST Microeletronics, Stradale Primosole, 50,95125 Catania*

*Corresponding Author email: laura.anoldo@gmail.com

Abstract

Today, it is essential to produce energy-efficient electronic devices. Wide bandgap materials are the best candidates as they can operate at high temperatures and exhibit very high conductivity. Silicon Carbide, Sic, (SiC) plays an important role in this field thanks to its properties of electric transport, its high breakdown voltage and its efficiency at high frequencies. However, the industrial level SiC wafers are affected by high number of defects. In this regard, we studied and characterized these defects using spectroscopic and microscopy techniques. In particular we focused on the study of a Threading Dislocation affecting a power MOSFET.

Keywords: Threading Dislocation, AFM microscopy, Raman spectroscopy, SiC Power MOSFET.

New Band Gap Materials

Power electronics is a constantly evolving field, and nowadays the cutting-edge technologies point out SiC (Silicon Carbide) and GaN (Gallium Nitride) as the key players in the production of electronic devices. Indeed, Wide Band Semiconductors (WBG) semiconductors overcome the theoretical limits of silicon and therefore offer significant performance improvements allowing operation under severe conditions. Nowadays they represent the two columns of the modern technological progress allowing the design of a new generation of power devices that guarantee innovative performances in terms of maximum efficiency with minimum losses [1].

Within a SiC crystal the Si and C atoms form very strong tetrahedral covalent bonds (bond energy = 4.6 eV) via sharing of electron pairs in sp3 hybrid orbitals. SiC occurs in many crystalline structures, named polytipes.
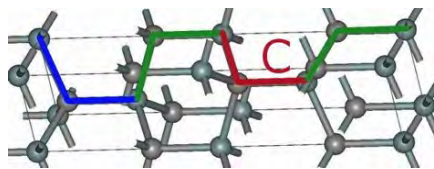

Figure 1: *4H-SiC stacking sequence.*

Polytypes consist of the same percentage of carbon and silicon atoms arranged in different crystalline structures that are identical in two dimensions and differ in the third. Thus, they can be viewed as layers stacked in a certain sequence. Clearly, each polytype has a different band structure and distinct electrical and optical properties. The most common hexagonal polytypes are 2H-SiC,

4H-SiC and 6H-SiC. As can be seen from the Figure 1 below, the 4H-SiC stacking sequence is characterized by a unit that is repeated every 4 bilayers and, in each layer, the Si (or C) atoms have a hexagonal arrangement.

Advantages

- Less on-resistance
- High breakdown voltage
- High thermal conductivity
- High-level performances at high frequencies
- Very good electrical transport properties

Disadvantages

SiC-based devices today are leader in the field of power electronics. However, the industrial use of this material is a challenge due to the large number of defects that populate its crystalline structure.

Defects can be divided into two categories:

- Intrinsic
  that are observed in as-grown n-type and p-type SiC epitaxial layers and are due to the thermodynamics of the solid state and populate all crystals

- Extrinsic
  that are induced by stoichiometry and impurities.

  - Point Defects
  - Line Defects
  - Surface Defects

Threding Dislocation

A dislocation is a defect in a crystalline structure that extends along a line. Unlike point defects, it is in fact an extended defect. As mentioned, a dislocation is more precisely a linear defect of a crystalline structure. Most dislocations in 4H-SiC homoepitaxial layers originate from dislocations in 4H-SiC substrates. Therefore, the dislocation density of a SiC homoepitaxial layer depends greatly on the quality of the substrate, assuming that the epitaxial growth process is sufficiently optimized.

Major dislocations in SiC substrates include the Threading Screw Dislocation (TSDs), the Threading Edge Dislocation (TEDs), and Basal Plane Dislocations (BPDs) [2].
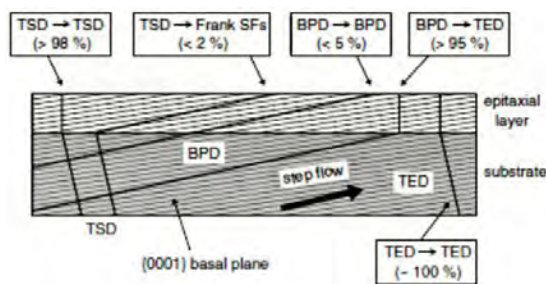

Figure 2: *Replication and conversion of dislocation observed in 4H-SiC epitaxial layers by CVD [2].*

Figure 4 illustrates the dislocation replication and conversion typically observed in 4H-SiC epitaxial layers grown on off-axis 0001 by CVD. Almost all the TSDs in a substrate are replicated in an epilayer, but a small portion (typically <2%) of TSDs are converted to Frank-type partial dislocations (removal of part of a close-packed layer of atoms) [2].

Threding Screw Dislocations

The Threding Screw Dislocations (TSD) are line defects (i.e. missing atom files). TSDs are extremely deleterious for electrical applications, because they can have free bonds that give rise to electrically active centers in the conduction zones of the device. If they do not intercept other defects to join, they go through the layer, reaching the surface, ruining the homogeneity of the sample. Extensive studies conducted by our working group have shown that this type of defect is due to a dislocation of the crystallographic planes of epitaxy. Being the epitaxy a layer grown on a substrate, the study is going on to see if these TSDs extend from the substrate to inside the epitaxy. The analyzed sample seems to confirm this theory, the work is in progress in order to have more statistics to support this hypothesis.

Experimental

During this work, there were essentially 2 jobs:
the first involves the study of a TSD in a Silicon Carbide Power MOSFET device, through the use of an Atomic Force Microscope; the second involves an analysis of Thermo-Mechanical stress on a Silicon Carbide MOSFET device, through the use of Raman Spectroscopy.

Atomic Force Microscopy

The AFM has three major abilities: force measurement, topographic imaging, and manipulation. In force measurement, AFMs can be used to measure the forces between the probe and the sample as a function of their mutual position. This can be applied to perform force spectroscopy, to measure the mechanical properties of the sample, such as the sample's Young's modulus, a measure of stiffness. For imaging, the reaction of the probe to the forces that the sample imposes on it can be used to form an image of the three-dimensional shape (topography) of a sample surface at a high resolution. This is achieved by raster scanning the position of the sample with respect to the tip and recording the height of the probe that corresponds to a constant probe-sample interaction (see section topographic imaging in AFM for more details). The surface topography is commonly displayed as a pseudocolor plot [3]. In manipulation, the forces between tip and sample can also be used to change the properties of the sample in a controlled way. Examples of this include atomic manipulation, scanning probe lithography and local stimulation of cells. Simultaneous with the acquisition of topographical images, other properties of the sample can be measured locally and displayed as an image, often with similarly high resolution. Examples of such properties are mechanical properties like stiffness or adhesion strength and electrical properties such as conductivity or surface potential. In fact, the majority of SPM techniques are extensions of AFM where the probe is specialized to detect one or other interaction with the sample surface [4].

Instrumentation

The AFM probe consists of a cantilever with a sharp tip (the probe) at its end that is used to scan the specimen surface. The cantilever is typically made of silicon or silicon nitride with a tip radius of curvature on the order of nanometers. When the tip is brought into proximity of the sample surface, forces between the tip and the sample lead to a deflection of the cantilever according to Hooke's law [5]. Depending on the situation, forces that are measured in AFM include mechanical contact force, van der Waals forces, capillary forces, chemical bonding, electrostatic forces, magnetic forces etc. As depicted above, along with force, additional quantities may simultaneously be measured through the use of specialized types of probes. The AFM can be operated in a number of modes, depending on the application. In general, possible imaging modes are divided into static (also called contact) modes and a variety of dynamic (non-contact or "tapping") modes where the cantilever is vibrated or oscillated at a given frequency [6].

Sample Preparation an Measurement

The TDS defect rarely can be highlighted in poly. The physical search for this defect is carried out using the Scanning Electron Microscope, SEM. The sample is subjected to a delayering process that uses some selective acids to remove the oxides and the metallization. When the final layer of epitaxy is exposed, inspection under an electron microscope is able to highlights the defect.
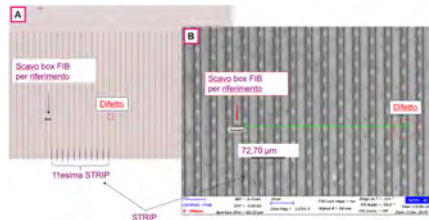

Figure 3: *TDS individuation.*

Once the defect has been located, in order to be able to trace it easily, a hole was made by using the FIB, in correspondence to the TSD and at a distance of 11 strips; as you can see from the image 5 A&B.
At this point, finding the TDS is simple and we can see its shape in the following image.
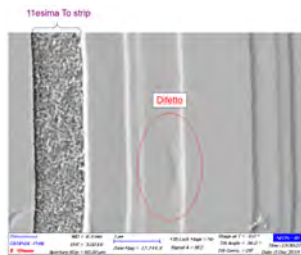

Figure 4: *Threading Dislocation.*

The same TDS was imaged by AFM driving the cantilever in tapping mode. To this purpose we used a Si cantilever oscillating at 348KHz; the dynamic working mode chosen allows us to detect the height and the phase signals at the same time. As expected the phase signal is much sensitive and allows us to clearly highlight the TDS comparing to the height topography.
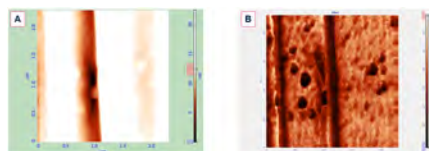

Figure 5: *AFM Thopography (A) and Phase (B).*

The next step of the study consists of characterize the sample by the Raman spectroscopy. The inspection are shows in Figure 8.
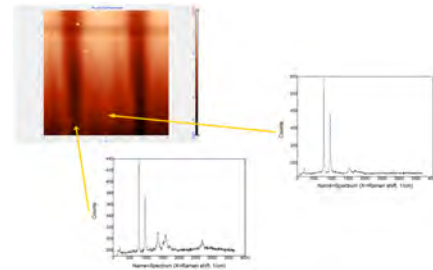The identification and characterization of peaks is a work still in progress.

Figure 6: *Raman inspection.*

However, after the Raman study we performed again the AFM measurement obtaining very intriguing results.
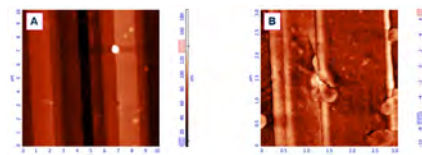

Figure 7: *AFM Thopography (A) and Phase (B).*

As you shown in Figure 9 (and even better in Figure 9B) the Threading Dislocation has changed its shape during the Raman measurements, may be due to the interaction with the LASER that locally can heat the sample surface. New measurements on several samples are currently under development; The purpose of these investigations is to understand the relationship between the TDS slipping and the temperature; since the devices, during their operating cycle, undergoes repetitive thermal stress.
From the Raman inspections it has been seen that the layers of the device have different Raman peaks, in terms of position and shape. This gives indications on how the layers are thermally stressed during their use. In this regard, more accurate spectroscopic analysis were performed to find a link between the thermo-mechanical deformations and the Raman peaks.

Raman Spectroscopy

Raman spectroscopy (named after Indian physicist C. V. Raman) is a spectroscopic technique typically used to determine vibrational modes of molecules and crystals, although rotational and other low-frequency modes of systems may also be observed [7]. Raman spectroscopy is commonly used to provide a structural fingerprint by which molecules can be identified.
Raman spectroscopy relies upon inelastic scattering of photons, known as Raman scattering. A source of monochromatic light, usually from a laser in the visible, near infrared, or near ultraviolet range is used, although X-rays can also be used. The photons laser light interact with molecular vibrations, namely the phonons or other excitations in the system, resulting in the energy of the laser photons being shifted up or down. The shift in energy gives information about the vibrational modes in the system. Infrared spectroscopy typically yields similar, complementary, information. Elastic scattered radi-

ation at the wavelength corresponding to the laser line (Rayleigh scattering) is filtered out by either a notch filter, edge pass filter, or a band pass filter, while the rest of the collected light reaches the detector.

Spontaneous Raman scattering is typically very weak; as a result, for many years the main difficulty in collecting Raman spectra was separating the weak inelastically scattered light from the intense Rayleigh scattered laser light (referred as "laser rejection"). Modern instrumentation almost universally employs notch or edge filters for laser rejection. Dispersive single-stage spectrographs (axial transmissive (AT) or Czerny–Turner (CT) monochromators) paired with CCD detectors are most common.

Instrumentation

Technological advances have made Raman spectroscopy much more sensitive, particularly since the 1980s. The most common modern detectors are now charge-coupled devices (CCDs). Photodiode arrays and photomultiplier tubes were common prior to the adoption of CCDs. The advent of reliable, stable, inexpensive lasers with narrow bandwidths has also had an impact [8].

- Lasers
  The ultimate resolution of the spectrum relies on the bandwidth of the laser source used [9]. Generally shorter wavelength lasers give stronger Raman scattering due to the $\nu 4$ increase in Raman scattering cross-sections, but issues with sample degradation or fluorescence may result [8]. Continuous wave lasers are most common for normal Raman spectroscopy, but pulsed lasers may also be used [9][10].

- Detectors for dispersive Raman
  In most cases, modern Raman spectrometers use array detectors such as CCDs. Various types of CCDs exist which are optimized for different wavelength ranges. Intensified CCDs can be used for very weak signals and/or pulsed lasers [8][11]. The spectral range depends on the size of the CCD and the focal length of spectrograph used. It was once common to use monochromators coupled to photomultiplier tubes [8].

- Filters
  As stated above, in order to collect high quality and low intensity Raman spectra, it need to filter out the Rayleigh signal using a laser rejection filter installed in the optical path. Notch or long-pass optical filters are typically used for this purpose [8]. However, Volume hologram filters are becoming more common which allow shifts as low as 5 cm^{-1} to be observed.

Our Goal

During the normal working the devices undergoes to very high current pulses that lead to quick termo-mechanical stress, these devices are created in such a way as to support a certain thermo-mechanical stress but, if the stress exceeds their limit, as defined by Young's module, the

device will break.

Our goal is to identify this limit, creating a link between deformation and Raman spectrum, indeed the position and shape of the Raman peak allows us to understand if the material is stressed.

Data results

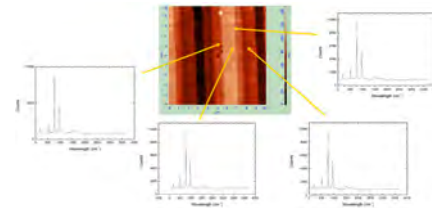Initial measurements have been made and show in Figure 10. The data are being processed.

Figure 8: *Raman spectra.*

Conclusion

The AFM analysis highlight that the TDS quickly evolves also with a relatively low thermal jump, as above underlined if a TDS reach the active part of the device, it will break, hence this point is crucial to improve the quality and the reliability of SiC power devices.

Moreover, the Raman spectroscopy allows us to highlight the presence of stress phenomena in the semiconductor layers and structures and a deeper understanding of the thermo-mechanical processes. In perspective to improve the performance of the devices and their lifetime, it is thought to realize stripes with tensile stress able to counterbalance the thermo-mechanical effect of epitaxial growth.

References

[1] Taku Hamaguchi: *I: ROHM Semiconductor, Santa Clara, CA.*

[2] T. Kymoto, J.A. Cooper: *Fundamentals of silicon carbide technology, Growth,Characterization*

[3] Frank Ohnesorge: *True atomic resolution by atomic force microscopy through repulsive and attractive forces, Science, 1 January 1993*

[4] AFMworkshop: *Atomic Force Microscopy Research involving the study of Neglected Tropical Diseases.*

[5] B. Cappella, G. Dietler: *Force-distance curves by atomic force microscopy, Surface Science Reports, 2012-12-03*

[6] G. Binnig, C. F. Quate, Ch. Gerber: *Atomic Force Microscope, Physical Review Letters, 1986*

[7] D.J. Gardiner: *Practical Raman spectroscopy, Springer-Verlag, 1989*

[8] McCreery, L. Richard: *Raman spectroscopy for chemical analysis, New York: John Wiley & Sons, 2000*

[9] Philipp Kukura, David W. McCamant, Richard A. Mathies: *Femtosecond Stimulated Raman Spectroscopy, Annual Review of Physical Chemistry, 2007*

[10] Anastasia B. S. Elliott, Raphael Horvath, Keith C. Gordon: *Vibrational spectroscopy as a probe of molecule-based devices, Chem. Soc. Rev. 41 (5): 1929–1946, 2012*

[11] Evtim V. Efremov, Joost B. Buijs, Cees Gooijer, Freek Ariese: *Fluorescence Rejection in Resonance Raman Spectroscopy Using a Picosecond-Gated Intensified Charge-Coupled Device Camera, Applied Spectroscopy, 2007*

Forward Tagger Trigger Efficiency Study for MesonEx Experiment

L. Biondo[1,2,3,*], G. Mandaglio[1,2]

[1] *Dipartimento MIFT, University of Messina, Messina, Italy*
[2] *INFN sezione di Catania, Catania, Italy*
[3] *Thomas Jefferson National Accelerator Facility, 628 Hofstadter Road, Suite 6, Newport News, VA 23606*

*Corresponding Author email: lbiondo@unime.it

Abstract

The CEBAF Large Acceptance Spectrometer for operation at 12 GeV beam energy (CLAS12) in Hall B at Jefferson Laboratory is used to study electro-induced nuclear and hadronic reactions. This spectrometer provides efficient detection of charged and neutral particles over a large fraction of the full solid angle. All the CLAS12 capabilities are being used in a broad program to study the structure and interactions of nucleons, nuclei, and mesons, using polarized and unpolarized electron beams and targets for beam energies up to 11 GeV. The MesonEx experiment use CLAS12 to investigate how the QCD partons manifest themselves under the strong interaction at the energy scale of the nucleon mass (GeV). In this paper we focus on the study of the Forward Tagger, a detector consisting of a calorimeter, scintillation hodoscope and tracking device, added to the standard equipment to detect the scattered electrons at low polar angles. Trigger efficiency analysis for the Forward Tagger, carried on in collaboration with INFN, will be briefly presented. Analysis on different data samples showed a good efficiency of the Triggering System. Further investigations are needed to understand the presence of some trigger inefficiency in the off-diagonal area. Graphs showing the detector efficiency are also presented.

Keywords: Hadronic Resonances, Low-Q2 electron scattering, CLAS12, JLAB.

Introduction

CLAS12 has been part of the energy-doubling project of Jefferson Lab's Continuous Electron Beam Accelerator Facility, funded by the United States Department of Energy. Fig.[1] An international collaboration of over 40 institutions contributed to the design and construction of detector hardware, developed the software packages for the simulation of complex event patterns, and commissioned the detector systems. CLAS12 is based on a dual-magnet system with a superconducting torus magnet that provides a largely azimuthal field distribution that covers the forward polar angle range up to 35 deg, and a solenoid magnet and detector covering the polar angles from 35 deg to 125 deg with full azimuthal coverage. Trajectory reconstruction in the forward direction using drift chambers and in the central direction using a vertex tracker results in momentum resolutions of $< 1\%$ and $< 3\%$, respectively. Cherenkov counters, time-of-flight scintillators, and electromagnetic calorimeters provide good particle identification. These capabilities are being used in a broad program to study the structure and interactions of nucleons, nuclei, and mesons, using polarized and unpolarized electron beams and targets for beam energies up to 11 GeV. In MesonEx a comprehensive study of the meson spectrum with precise determination of resonance masses and properties with a high statistics and high resolution experiment is proposed. The meson spectrum in the mass range $1.5 - 2.5$ GeV will be studied looking for rare $q\bar{q}$ states and unconventional mesons with exotic quantum numbers. The technique, electroscattering at very low Q^2 ($10^{-2} - 10^{-1}$ GeV^2) provides a high photon flux and a high degree of linear polarization and represents a competitive and complementary way to study the meson spectrum and production mechanisms with respect to real photoproduction experiments. A Forward Tagger (FT) consisting of a calorimeter, scintillation hodoscope and tracking device will be added to the standard equipment to detect the scattered electrons in the angular range $\theta_{e'} = 2.5° - 4.5°$ and energy range $E_{e'} = 0.5 - 4.5$ GeV. Events will be selected by the FT only when meeting strict conditions. To check if the machinery works properly we selected the $\vec{e} + p \rightarrow e + p + \pi^0$ channel of reaction, and the respective triggering condition: 2 energy cluster produced by the scintillator, both with $500 < E < 8000$ MeV and with a difference in detection time not higher than 20 ns.

Forward Tagger

The characteristics of the detector and the trigger conditions foreseen for the experiment - 11 GeV electron beam
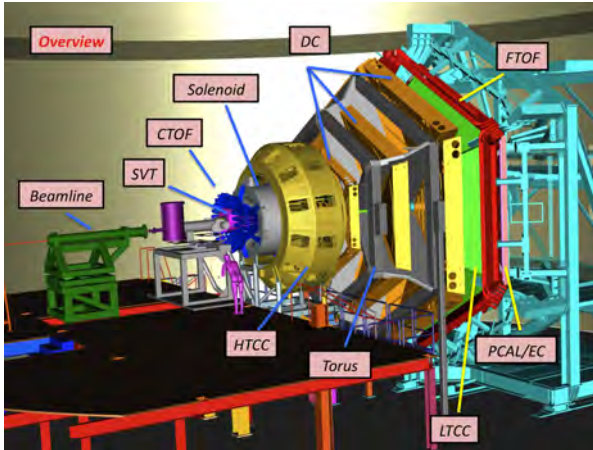
Figure 1: *Scheme of CLAS12 spectrometer. All the components of the system are here highlighted: Beamline, Silicon Vertex Tracker (SVT), Central Time-of-Flight (CTOF), Solenoid, High Threshold Cherenkov Counter (HTCC), Drift Chamber (DC), Torus, Forward Time-of-Flight (FTOF), Low Threshold Cherenkov Counter (LTCC), Preshower Calorimeter &x Electromagnetic Calorimeter (PCAL/EC).*

scattering on a 5cm long LH$_2$ target with multiple particles in the final state - will allow measurements of many final states simultaneously. While the hadrons will be detected in the CLAS12 spectrometer [1], the electron scattered at very small angles (2.5° to 4.5° in polar angle) and low four momentum transfer, Q^2, will be detected in the Forward Tagger (FT). The FT specifications were thus defined to have optimal electron detection in this angular range, compatible with the high rate of electromagnetic background. To reconstruct the quasi-real photon variables, it is necessary to measure the scattered electron three momentum. The relevant quantities are:

- The energy $E_{e'}$ since the photon energy is given by $E_\gamma = \nu = E_{beam} - E_{e'}$ and its linear polarization by $P_\gamma = \epsilon \sim (1 + \frac{\nu^2}{2E_{beam}E_{e'}})$;

- The azimuthal angle $\Phi_{e'}$ to determine the polarization plane,

- The polar angle $\theta_{e'}$ since:
  $Q^2 = 4_{Ebeam}E_{e'}sin^2(\theta_{e'}/2).$

The FT is composed of an electromagnetic calorimeter (FT-Cal) to identify the electron in the energy range $0.5 - 4.5$ GeV by measuring its electromagnetic shower energy and to provide a fast trigger signal, a Micromegas tracker (FT-Trk) to measure the scattering angles ($\theta_{e'}$ and $\Phi_{e'}$), and a scintillation counter (FT-Hodo) to provide e/γ separation. The FT-Cal and FT-Hodo also provide fast signals to trigger the data acquisition [2] in coincidence with signals from CLAS12. All of these components were designed to fit within a 5.5 deg cone around the beam axis to have minimal impact on the operation and acceptance of the CLAS12 equipment in the forward direction. Figure [2] shows a CAD rendering of the FT.

The Calorimeter (FT-Cal)

The FT-Cal has to fulfill demanding requirements in terms of: radiation hardness, light yield, shower containment (small radiation length and Moliere radius), scintillation decay time, and good energy and time resolution. The electron energy resolution is a crucial factor to determine precisely the photon energy and to ensure the exclusivity of the measured reaction via the missing mass technique. However, since we are interested in low-energy electrons and high-energy photons, the energy resolution on the latter is significantly better than the resolution of the electron. The FT-Cal should have a fast scintillation decay time ($\tau \sim 10$ ns) to sustain high rates with small pile-up effects and to provide the scattered electron interaction time with good accuracy (< 1 ns) in order to reject background and to identify the relevant signals via coincidence with CLAS12. Due to the expected high rate from electromagnetic background ($\sim$120 MHz at the nominal luminosity of 10^35 cm^{-2}s-1), the calorimeter should be highly segmented in the transverse direction. The size of each detection element should be comparable with the characteristic transverse size of the electromagnetic shower (Moliere radius) to contain the shower produced by incident electrons to a few readout cells, thus minimizing rates and pile-up. Finally, the photodetectors for the light read out should work in a sizable magnetic field and fit within the available space. Thus, standard photomultipliers (PMTs) cannot be used, while photodetectors based on semiconductors, e.g. avalanche photodiodes (APDs), have been shown to meet the required criteria. To match the necessary requirements, lead tungstate (PbWO$_4$) was chosen as the scintillating material and Large-Area APDs (LAAPDs) as the readout sensors. The FT-Cal is made from 332 15 × 15 × 200 mm^3 parallelepiped PbWO$_4$ Type-II crystals arranged around the beamline with full azimuthal angular coverage ($0° < \Phi < 360°$) and small forward angle acceptance ($2° < \theta < 5°$). The crystals are placed with their long side parallel to the beamline to form a ring.

The Hodoscope (FT-Hodo)

The primary aim of the FT-Hodo is to discriminate between photons and electrons that produce an electromagnetic shower in the calorimeter. Specifically, electrons are identified by hits in the hodoscope array that are correlated in both position and time with a cluster observed in the calorimeter. The FT-Hodo is comprised by an array of 232 plastic scintillator (Eljen-204) tiles segmented in two layers to suppress contributions from the splash-back of the electromagnetic shower created by events depositing energy in the FT-Cal. The scintillators provide fast timing and sufficient resistance to radiation damage for use in the high-rate and high-dose environment of the FT. The geometry and readout of the hodoscope are constrained by the surrounding apparatus. Specifically, the device is positioned upstream of the FT-Cal, fitting into a circular disk of diameter 330 mm and 42 mm depth. The readout is achieved using 3×3 mm^2
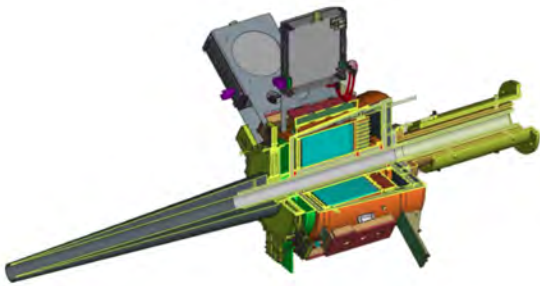
Figure 2: *CAD drawing of the Forward Tagger. The FT calorimeter shown in cyan is located at about 185 cm from the beam-target interaction point and is enclosed in a copper and Rohacell case to provide thermal insulation. The scintillation counter (green) and the tracker (yellow) are located in front of the calorimeter. A tungsten cone (gray) shields the FT from Møller electrons and other electromagnetic background (low-energy photons) created by the beam. The left side of this figure represents the upstream end of the detector.*

Hamamatsu S13360-3075PE SiPMs (50% photon detection efficiency for 450nm photons) coupled to 5-m-long clear optical fibers (Kuraray clear-PSM with attenuation length >10m), which are fusion spliced to ∼30-cm-long wavelength shifting (WLS) Kuraray Y11 fibers, embedded in the scintillator tiles. The splicing induces a photon losìs of less than 2%, where the use of optical fibers allows the captured light to be transported with a light loss of less than ∼ 40% over the 5-m path to the SiPM. This readout design of the FT-Hodo addresses the need to minimize material in the detector acceptance, to operate in regions of high magnetic fields produced by the CLAS12 solenoid and torus magnets, and to tolerate the high-background radiation environment. The FT-Hodo is comprised of two segmented plastic scintillator (Eljen-204) tile arrays, which are embedded with wavelength shifting (WLS) fibres. Read out is achieved using 3×3 mm^2 silicon photomultipliers (SiPM) via clear optical fibres. The plastic scintillators provide fast timing and sufficient resistance to ptva radiation damage for use in the high rate environments of the CLAS12 Forward Tagger.

The Micromegas Tracker (FT-Trk)

For a precise determination of the scattered electron angle, a tracker complements the FT-Cal and FTHodo detectors. The FT-Trk uses the same technology adopted by the CLAS12 central and forward Micromegas detectors. In this section we describe the specific design of the FT-Trk. Two double-layers of Micromegas detectors are located in front of the hodoscope, in the space between the FT and the HTCC [3]. The two detectors are indeed a good compromise to achieve an efficient background rejection and track reconstruction with a low material budget. Each layer is composed of a double-faced Micromegas disk built on a common printed circuit board

(PCB). Each side of the PCB displays strips, the downstream strips being perpendicularly oriented to the upstream strips. This particular geometry enables the determination of the (x;y) coordinates (perpendicular to the beam z -axis) of a track. To limit the number of electronics channels, the pitch chosen was 500 μm, which leads to a resolution better than 150 μm. A drift space of 5 mm, together with an amplification gap of 128 μm, provides good efficiency. The two double layers, centered on the beam axis, cover polar angles from 2.5 deg to 4.5 deg with an active area defined between a 70 mm inner radius and a 143 mm outer radius. The total number of channels is 3072. Figure 13 shows the CAD implementation of the detector. The FT-Trk read out uses the same data acquisition scheme adopted for the CLAS12 Barrel Micromegas Tracker (BMT) [4], which consists of a Front-End Unit (FEU) and a Back-End Unit (BEU). The front-end electronics are responsible for signal preamplification, shaping, buffering during the trigger generation process, data digitization, and compression. Due to the limited space available, the front-end electronics are designed to be placed off-detector. The back-end electronics are responsible for data concentration, providing the interface to the CLAS12 event building system and are the same units used for the BMT [4].

Data Analysis

Different analysis, using special runs data (runs from #004784 to #004789), were carried out to investigate trigger efficiency. In the special runs, of $\vec{e}+p \rightarrow e+p+\pi^0$ type, two different kind of trigger were used, which can be summarized as follow:

- Trigger Bit 26 (TB26): same strict conditions used in normal runs (at least two energy cluster with $500 < E < 8000$ MeV and with a difference in detection time not higher than 20 ns). This trigger is used for flagging the events with the right conditions.

- Trigger Bit 27 (TB27): wide conditions (at least one energy cluster with $E > 100$ MeV. This trigger were used for flagging the events and to start the data acquisition also. It has to be noticed that TB27 has no time conditions, needing just one energy cluster to be fired.

The analysis was carried out using *Clas12root*, an analysis tool based on Root (C++) and developed by CLAS12 collaboration. TB27 flagged data can be used as a comparison to investigate possible events losses, once filtered using both energy and time TB26 conditions. Histogram c) from Fig. [3] was produced using

$$\frac{\#Events_{TB26}(E_{EC1}; E_{EC2})}{\#Events_{TB27}(E_{EC1}; E_{EC2})},$$

where the numerator and denominator are the number of events, as the energy of the 2 energy clusters varies, which triggered the TB26 and TB27, respectively. During data analysis 543 events with ideal time and energy conditions, but without TB26 flag, were noticed. In the a) histogram from Fig. [3] the aforementioned events
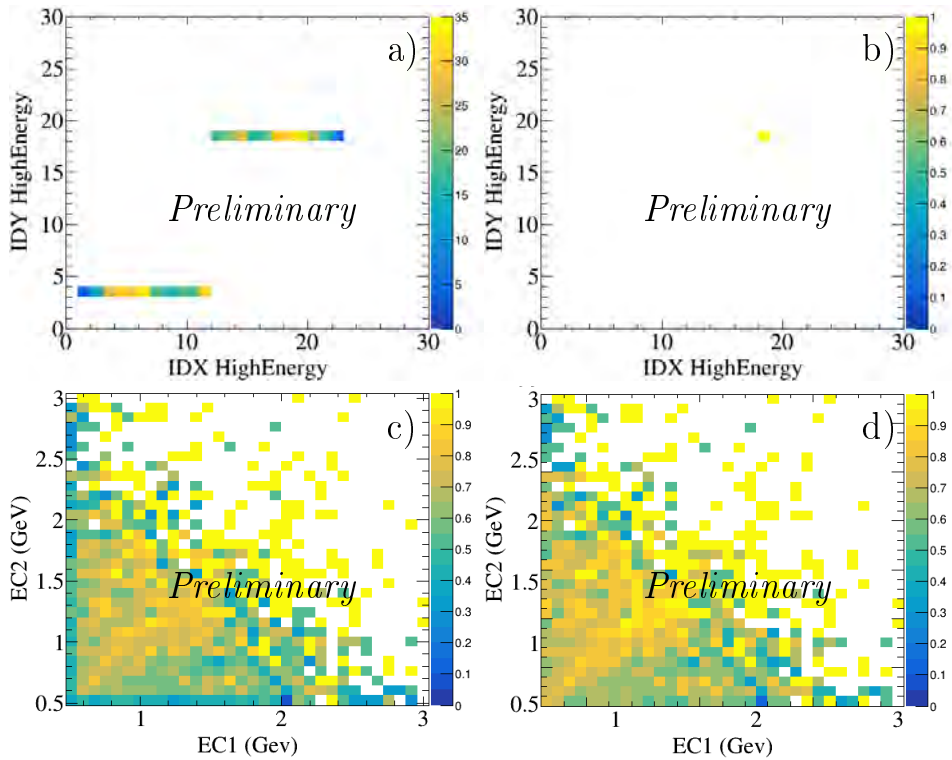
Figure 3: *Trigger efficiency studies: difference between before (panels a,c) and after(panels b,d) excluding the broken run events. The b panel, reproducing the detector APD surface, shows how, excluding the broken run, the bad events can be reduced to only one, versus the almost 500 of the panel a. As can be seen watching the c and d panel, Trigger Efficiency calculated by triggering events against valid events is shown as energy varies. The efficiency increases after removing the broken run, especially in the outer zone of the graph.*

are exposed, reporting the (x,y) coordinates of the hits of the energy clusters on the detector and showing a discrepancy with the expected result, awaiting an homogeneous distribution. All the events (except for one), as can be seen from b) histogram in Fig. [3], can be excluded cutting out one of the special run used for the analysis (#004787). Possible data corruption or incorrect data acquisition due to hardware problems is hypothesized. The trigger efficiency after the broken run exclusion is shown in d) histogram from Fig [3], showing good acquisition efficiency, especially in the diagonal area (the most interesting area for the ongoing studies).

Conclusion

In this paper trigger efficiency studies for forward tagger, used in MesonEx experiment for hadronic spectroscopy studies, were presented, giving an insight on CLAS12 and FT detectors structure. The analysis, carried out thanks to the Root-based software Class12root and made on special runs with two different type of trigger, show good results. The forward tagger trigger for π^0-production events works with a good efficiency. Further investigations are needed to understand the presence of trigger inefficiency in the off-diagonal area.

References

[1] V. D. Burkert, et al., The CLAS12 Spectrometer at Jefferson Laboratory, to be published in Nucl. Instrum. Meth. A, (2021).

[2] S. Boyarinov, et al., The CLAS12 data acquisition system, to be published in Nucl. Instrum. Meth. A, (2021).

[3] Y. G. Sharabian, et al., The CLAS12 high threshold Cerenkov counter, to be published in Nucl. Instrum. Meth. A, (2021).

[4] A. Acker, et al., The CLAS12 Micromegas vertex tracker, to be published in Nucl. Instrum. Meth. A, (2021).

Molecular Doping applied on silicon nanostructures: a review

G. Gallo[1], C. Bongiorno[2], F. Neri[1], E. Fazio[1], R. A. Puglisi[2]

[1]*Dipartimento Scienze Matematiche e Informatiche, Scienze Fisiche e Scienze della Terra (MIFT), Università degli Studi di Messina, Viale F. Stagno d'Alcontres, 31, 98166 Messina, Italy*

[2]*Istituto per la Microelettronica e Microsistemi, Consiglio Nazionale delle Ricerche, Strada VIII n.5, Zona Industriale, 95121 Catania, Italy*

*Corresponding Author email: ggallo@unime.it

Abstract

Semiconductor industry has been recently forced to move from planar to non-planar device architectures in order to maintain electron device scaling. Thus, it emerges the need to develop a radically new, non-destructive, conformal method for doping. Molecular doping (MD) is a promising surface-based technique, where organic molecules are covalently bound to the semiconductor surface at relatively low processing temperatures (from room temperature up to about $200°C$). A thermal treatment is then applied which releases the dopant atoms from the organic molecules, provides the energy for diffusion into the semiconductor substrate and subsequent activation. Very promising results have been achieved both on planar and nanostructured silicon substrates. However, there is still a need to understand the physical-chemical properties of the interface between the molecules and the nanostructured surfaces. In this contribution, the main literature results achieved on planar and nanostructured surface are reviewed, mainly focusing the attention on: dopant conformality, carbon contamination, dose control, dopant diffusion control and the rule of capping role.

Keywords: silicon nanowires, molecular doping, chemical interface.

Introduction

Over the last decades semiconductor nanostructures have attracted considerable scientific interest due to their peculiar properties, arising from the interplay between quantum confinement and surface related effects, which significantly alter the electronic behavior of these nanostructures [1]. Silicon nanostructures are particularly appealing for application in several fields like microelectronics, optoelectronics, and photovoltaics [2–4]. During the last century, impurity doping of Si was used to tailor the electronic properties of bulk silicon, forming metallurgical p/n junctions, used as building blocks of Si-based electronic devices [5–7]. As in the case of bulk semiconductors, the exploitation of silicon systems with reduced dimensionality like nanowires, as basic elements for the fabrication of complex microelectronic devices, requires the capability to effectively control their electronic properties by means of doping. Actually both p-type and n-type impurities have been successfully introduced in Si mainly by thermal diffusion or ion implantation [8–11]. These techniques show several issues when applied to nanostructures, such as the difficulty to achieve conformal and abrupt junctions and crystal damage induced by the implanted ions as well as the use of dangerous gas and high cost facilities. An alternative, low cost and promising approach to assure a controlled and conformal doping

at the nanoscale level is the molecular doping (MD) [12]. The MD is a method which exploits the Si crystalline nature and its surface properties on which a layer of self-assembled molecules is formed. It is a process based on the use of solutions containing the dopant molecules that follow the nanostructured surfaces, allowing a control of their density and surface distribution. These aspects together with the use of low cost and safe equipment are the main advantages of MD [12]. Nevertheless, a deep understanding of the processes involved in MD is not yet available [13]. In this contribution, first we briefly describe the doping procedure generally used for doping a planar silicon. Then, we focused the attention on the molecular doping approach applied to Si nanowires, reporting preliminary results on the chemical-physical characterization of the Si-molecule interface.

Molecular Doping on Planar Silicon

As introduced previously, silicon technology relies on the capability of tuning the electrical properties of the substrate through the controlled introduction of substitutional impurities (doping) in the crystal lattice of the Si host in order to tailor its electronic properties. Conventionally, this is carried out by *in situ* doping (i.e. dur-

ing epitaxial growth) or *ex situ* doping strategies, including ion, solid, liquid or gas [14]. However this technique present several limitations: they are very expensive, they use dangerous materials, they involve a stochastic distribution of the implanted atoms/ions, they do not guarantee conformality and above all some of them can damage the nanostructures. The MD approach represents a nondestructive method to introduce impurity atoms into Si. Molecules containing dopant atoms are designed, synthesized and chemically bound in self-limiting monolayers to the semiconductor surface; subsequent annealing enables diffusion of the dopant atom into the substrate [15].
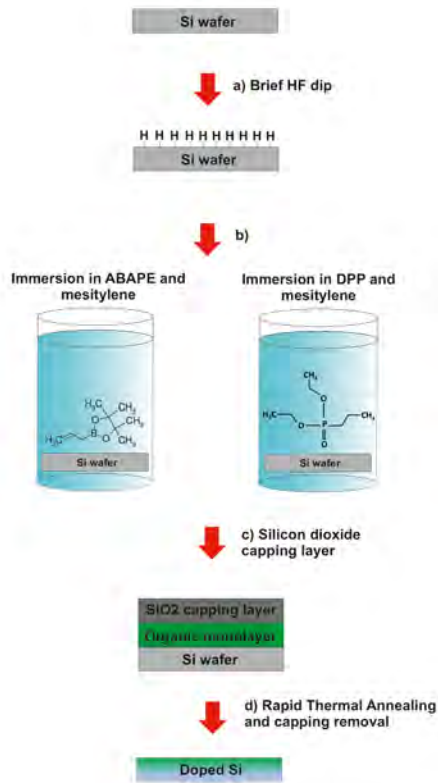

Figure 1: *(a) Wet etching of native SiO_2 with dilute aqueous HF yields the H-terminated silicon surface, (b) hydrosilylation grafts dopant as well as diluting molecules onto the H-terminated Si surface, (c) SiO_2 capping layer is sputtered onto the modified surface, and (d) high-temperature rapid annealing and removal of capping layer result in a surface junction with dopants.*

A typical scheme of a MD procedure applied on a planar Si is shown in Fig. 1 and reported in Ref. [16]. The first step consists in the immersion of the Si substrate into an aqueous HF solution, and then in a solution of diethyl 1-propylphosphonate and mesitylene at the boiling temperature (about $160°C$) for 2.5 h. This step creates a layer of phosphorus-containing molecules all over the sample surface. In case of p-type doping, a boron precursor, such as the allylboronic acid pinacol ester, always

dissolved in mesitylene is used at its boiling temperature of about $120°C$. In some procedures, a cap layer can be deposited over the molecular layer to protect the sample during the further processing steps. A furnace annealing at $1050°C$ for 500 s in N_2 is then performed to diffuse and activate the dopant. Doping levels of $1 \times 10^{19} cm^{-3}$ are controllably obtained without structural damage and hetero-interfaces creation. As mentioned above, the cap layer deposition can be included as an intermediate process step. The electrical properties are studied in the literature, by correlating the dopant diffusion inside the Si substrate in the presence or absence of a cap layer: specifically, a layer of SiO_2 deposited by spin-on-glass (SOG) or deposited in a chemical vapor deposition (CVD) chamber or a layer of oxidized silicon placed over and in contact with the samples to be doped. For the different capping conditions, a competition between the diffusion of the dopant toward the Si substrate and other loss processes occurring during the annealing step was observed. Specifically, electrical measurements have shown that the imperfect physical contact between the oxidized cap and phosphonate-covered Si samples causes the loss processes. In the CVD samples, dopant diffusion toward the Si substrate seems to be the preferred process, because the dopant loss mechanisms towards outside are limited by the density of the oxide cap [17]. The no cap samples are characterized by higher carrier dose than the external cap or SOG samples. The first result can be explained by the non-perfect physical contact between the cap layer and the external cap samples. The second result is due to the migration or capture of phosphonate layers in the liquid oxide before the annealing step in the SOG samples [17]. During the last years, recent studies have been addressed, on one hand, to design the molecule characteristics to increase the doping efficiency and, on the other hand, to investigate the chemical properties of the surface and their role on the electrical properties [17]. An alternative MD method is shown by Hazut et al. [18], the Monolayer contact doping (MLCD). The monolayer containing dopant atoms is formed on a donor substrate using precursor molecules. The donor substrate and the pristine i-Si substrate, which works as a target substrate, are brought to contact and annealed using rapid thermal anneal. During the annealing process, monolayer molecules thermally decompose and dopant atoms originate from dopant diffusion into both donor and target substrates. Multiple contact doping processes yield high doping levels with surface dopant concentration higher than $5 \times 10^{20} cm^{-3}$. Dopant profiles depths of 30-40 nm were demonstrated, and ultrashallow profiles of less than 10 nm are achievable using short anneal times [18]. However, there is still little understanding of the diffusion of dopants and of the other atoms forming the precursor molecules, such as C and O, in the first atomic layers by annealing [15]. Shimizu et al. [15] have proposed to use the spike annealing to diffuse the dopant, providing a viable approach for large scale production and demonstrated uniformity on 6-inches wafers. All these evidences demonstrate that MD is an efficient method to obtain p-n metallurgical junction in planar silicon. It is not yet deeply understood what happens when the method is ap-

plied to nanostructured silicon. In the next paragraph we will discuss all the concepts implied in this process.

Molecular Doping on Silicon nanostructures

Doping of nanostructures, such as Si nanowire, presents critical issues like structural damage, conformality and control of the dopant dose and junction depth at nanometric level. As previously evidenced on planar Silicon surface, the diethyl 1-propylphosphonate/Si combination is considered as a promising alternative to the conventional semiconductor n-type doping methods, thanks to its solution-based processing, which is damage-free and intrinsically conformal. Recently, MD applied to Si nanowires (prepared by CVD and catalyzed by gold nanoclusters) was proposed by Puglisi et al. [19], following a MD procedure analogous to ones already adopted for planar Si [16]. The SiNWs array used presents density of $2 \times 10^{10} cm^{-2}$, average length of 500 nm and diameters up to 70 nm. Also in this case, a furnace annealing at $900°C$ C for 500 s was performed to diffuse and activate the dopant. The results of this study show that the molecules undergo to a sequential decomposition and self-assembling mechanism, finally forming a chemical bond with the silicon atoms [13]. In particular, DPP molecules first lose the aliphatic chains, i.e. $CH_2 - CH_3$ groups (see Fig. 2). Right after the molecule deposition, the surface chemical characterization indicates that there is only one type of bond between O and P, presumably of tridentate type, due to rupture of the P=O double bond and to the simultaneous breakage of C–O–P bonds. After the coating, a C=O bond is found indicating that a partial pyrolysis of the molecule during the dip coating process takes place. The molecules then adsorb to the surface with three O-Si bonds.
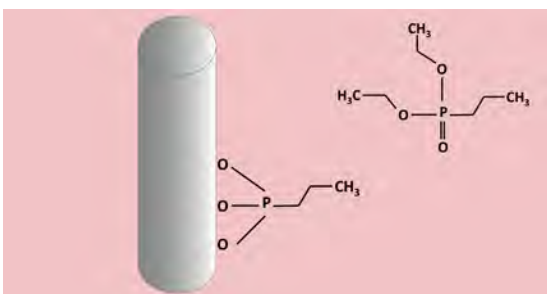

Figure 2: *Possible molecular decomposition mechanism: the aliphatic chains are lost and the DPP molecule attaches to the nanowire via the oxygen atoms.*

Single molecules arranged over the Si nanowire surface have been visualized by using Scanning Transmission Electron Microscopy (STEM). In Fig. 3 a,b representative STEM images of Silicon nanowires decorated with dyethyl-1 propylphosphonate (DPP) molecules are shown. The STEM profile demonstrates that the SiNW

core is covered by an oxygen shell, a phosphorous interlayer and a carbon external layer. This external layer evidences agglomerates to be ascribed to the single DPP molecules. The phosphorous signal is found in correspondence of the O-C interface (see Fig. 3b). This clearly indicates that the molecule undergoes to a modification of its structure upon grafting to the SiNWs, as supposed in figure 2. Similar scenarios have been obtained by the theoretical simulations. Thanks to this decomposition and rearrangement mechanism, the molecules density and relative distance are determined by their steric properties and can be controlled in a deterministic way.
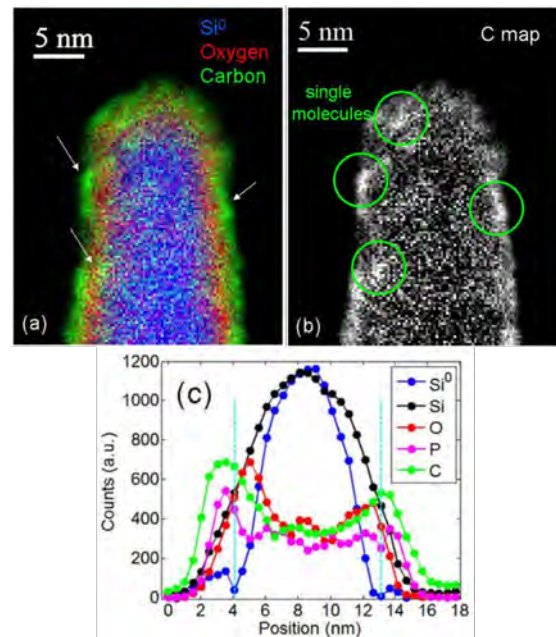

Figure 3: *Spectrum imaging in STEM mode of Si nanowires decorated by ester molecules. (a) RGB image showing the region of a NW close to the tip, composed by the superposition of the Si, O and C two-dimensional maps (blue, red and green respectively) extracted from the EELS spectrum image data-cube. (b) C map where the single molecules on the NW surface are indicated by the green circles. (c) Chemical profiles extracted by the spectrum image and by the EDX signal, referring to the distribution profiles of Si-Si bonds (blue data), total Si (black), oxygen (red), carbon (green) and phosphorous (magenta). The two dashed lines indicate the position of the C-O interface [Credits: Ref.[13]].*

The discovery of how many molecules can be grafted and how they attach themselves has a direct impact on the control of the NW doping and as a consequence on how to modulate its conductivity, once they are diffused inside the nanostructure. Therefore, in future, morphological-compositional characterization of the organic molecule interface - nanostructured silicon are still necessary to further study the chemical bonds between the molecule, containing the dopant atoms, and the Si nanostructure,

even when the process parameters vary.

Conclusion

One of the most challenging topics in the electronic field is trying to scale electronic devices to the nanometer size regime attaining control the doping of semiconductor materials with atomic accuracy. In this contribution, relevant results currently achieved are presented. We described in detail a new strategy, developed in the IMM-CNR Institute of Catania, in order to control nanoscale doping of silicon nanowires. This approach exploits the creation of highly uniform and covalently bonded monolayer dopant-containing molecules on the silicon nanostructures. To better address the characteristics of MD doped-Si nanostructures, we have first presented the results obtained on Si planar surface, showing that MD is an efficient method to obtain p-n metallurgical junction in planar silicon. Then, we discuss about MD applied to Si nanowires (prepared by CVD and catalyzed by gold nanoclusters). STEM, EDX and EELS analyses allowed to discover how organic molecules can be grafted on Si NW to predict how they will diffuse inside the nanostructure. The results achieved are interesting in view of energetic applications using optically performing SiNWs. Nevertheless in future, further studies are needed in order to understand more deeply the interface between the organic molecules and the Si nanostructured interface in order to control and optimize the electrical performances.

Acknowledgments

References

[1] Lundstrom M.: *Moore's law forever?* Science, vol. 299, no. 5604, pp. 210-211, 2013.

[2] Yoo et al.: *Scalable fabrication of silicon nanotubes and their application to energy storage.* Advanced Materials, vol. 24, no. 40, pp. 5452–5456, 2012.

[3] Liu et al.: *Silicon nanostructures for solar-driven catalytic applications.* Nano Today, vol. 17, pp. 96–116, 2017.

[4] Li et al.: *Light harvesting of silicon nanostructure for solar cells application.* Optics Express, vol. 24, no. 14, pp. A1075-A1082, 2016.

[5] Nakane et al.: *Preparation and characterization of ferromagnetic D O3 -phase Fe3 Si thin films on silicon-on-insulator substrates for Si-based spin-electronic device applications.* Applied physics letters, vo.. 89, no. 19, pp. 1-4, 2006.

[6] Buchal et al.: *Silicon-based optoelectronics.* MRS Online Proceedings Library Archive, vol. 486, no. 12, pp. 3-19, 1998.

[7] Altug et al.: *Introduction to the issue on nanoplasmonics.* IEEE Journal of Selected Topics in Quantum Electronics, vol. 19, no. 3, pp. 897–898, 2013.

[8] Fair et al.: *Modeling Rapid Thermal Diffusion of Arsenic and Boron in Silicon.* Journal of the Electrochemical Society, vol. 131, no. 10, pp. 2387-2394, 1984.

[9] Kim et al.: *The effect of ion-implantation damage on dopant diffusion in silicon during shallow-junction formation.* Journal of electronic materials, vol. 18, no. 2, pp. 143-150, 1989.

[10] Large et al.: *Ion-implantation doping of semiconductors.* Journal of Materials Science, vol. 2, no. 6, pp. 589-609, 1967.

[11] Zagozdzon-Wosik et al.: *Silicon doping from phosphorus spin-on dopant sources in proximity rapid thermal diffusion.* Journal of applied physics, vol. 75, no. 1, pp. 337-344, 1994.

[12] Ho et al.: *Controlled nanoscale doping of semiconductors via molecular monolayers.* Nature materials, vol. 7, no. 1, pp. 62-67, 2008.

[13] Puglisi et al.: *Direct observation of single organic molecules grafted on the surface of a silicon nanowire.* Scientific reports, vol. 9, no. 1, pp. 1-8, 2019.

[14] Duffy et al.: *Diagnosis of phosphorus monolayer doping in silicon based on nanowire electrical characterisation.* Journal of applied physics, vol. 123, no. 12, 2018.

[15] Long et al.: *Molecular Layer Doping: Non-destructive doping of silicon and germanium.* In 2014 20th International Conference on Ion Implantation Technology (IIT) IEEE., (pp. 1-4), 2014.

[16] Caccamo et al.: *Silicon doped by molecular doping technique: Role of the surface layers of doped Si on the electrical characteristics.* Materials Science in Semiconductor Processing, vol. 42, pp. 200-203, 2016.

[17] Caccamo et al.: *Advanced Organic Molecular Doping Applied to Si: Influence of the Processing Conditions on the Electrical Properties.* Physica Status Solidi - Applications and material science, vol. 215, no. 14, pp. 1-5, 2018.

[18] Hazut et al.: *Contact doping of silicon wafers and nanostructures with phosphine oxide monolayers.* ACS Nano, vol. 6, no. 11, pp. 10311-10318, 2012.

[19] Puglisi et al.: *Molecular doping applied to Si nanowires array based solar cells.* Solar Energy Materials and Solar Cells, vol. 132, pp. 118-122, 2015.

Integration between neurons and astrocytes Computational models and methods to describe the complexity of the brain

R. Musotto[1−3,*], U. Wanderling[1], M. De Pittà[2], G. Pioggia[3]

[1] *University of Messina, Department of Physics, Messina, Italy*

[2] *University of the Basque Country, Basque center for applied mathematics, Bilbao, Spain.*

[3] *National Research Council of Italy (CNR), Institute for Biomedical Research and Innovation (IRIB), Messina, Italy*

[*]Corresponding Author email: romusotto@unime.it

Abstract

This work presents an overview of the main models used to describe the behavior of biological neuronal networks. In particular, the pioneering work of A.L. Hodgkin and A.F. Huxley on the modeling of neuron physiology and the developments of E.M. Izhikevich for the description of neuronal networks that are affordable from a computational point of view, will be commented. We will also illustrates the role recently assumed by astrocyte cells. Astrocytes not only play a supporting role in correct neuronal function, but also show communication activity, through Ca^{2+} waves, between themselves and with neurons. Furthermore, this kind of signalling is essential for the proper functioning of the neuronal activity of the human brain, for example, in memory and learning.

Keywords: Astrocyte-neuron signaling, intracellular calcium, calcium waves, synaptic activity.

Introduction

Neurons and glia cells are building blocks of the human brain. Neurons are defined based on their ability to produce action potentials; the other cells in the human brain, which do not support this ability, are called glia cells. By the early 1990s, it was widely believed that glia cells only performed passive functions, such as providing nutrition and removing waste. In 1999, for the first time, the term "tripartite synapse" was introduced to describe the bidirectional communication between neurons and astrocytes. In this article we will consider the close interactions between synaptic terminals and surrounding astrocytic processes through the use of biophysical models. Calcium signaling is the most commonly measured readout of astrocyte activity in response to stimulation, be it by synaptic activity, by neuromodulators diffusing in the extracellular milieu, or by exogenous chemical, mechanical, or optical stimuli. In this perspective, the individual astrocytic Ca^{2+} transient is thought, to some extent, as an integration of the triggering stimulus [1] and it is thus regarded as an encoding or decoding of this stimulus, depending on the point of view [2] [3]. Multiple and varied are the spatiotemporal patterns of Ca^{2+} elevations recorded from astrocytes in response to stimulation, each possibly carrying its own encoding[4]. Insofar as different encoding modes could correspond to different downstream signaling, including gliotransmission and thereby regulation of synaptic function, understanding the bio-

physical mechanisms underlying rich Ca^{2+} dynamics in astrocytes is crucial. Intracellular calcium (Ca^{2+}) is a second key messenger in living cells . It controls various physiological processes by encoding information on external stimuli in the amplitude or frequency of its oscillation [5]. The finding that calcium fluctuations occur in astrocytes along with their ability to release gliotransmitters, confirms that astrocytes active participation in information processing in the brain [6]. Since astrocytes are unable to create action potentials, they respond to neuronal activity by increasing the level of cytosolic calcium. In fact, when an astrocyte is activated by its agonist (such as glutamate), a series of reactions is triggered, which leads to the production of IP_3 (inositol 1, 4, 5-triphosphate). As a result, astrocytes participate in neural transmission and respond by releasing various glyotransmitters, such as glutamate, adenosine triphosphate (ATP) and other neuroactive materials [7] becoming active partners in synapses.

The Hodgkin–Huxley model

With a series of articles published starting in 1952, A.C. Hodgkin and A.F. Huxley have opened the door to a detailed understanding of how electro-physiological signals are transmitted within the nervous system. It was from these works that the description of the potential for action was born[8]. The Hodgkin and Huxley model expresses the electrical behavior of a nerve cell, describing the total

membrane current I as a function of time and membrane depolarization voltage V. Defining: E_r the absolute value of the resting potential, V_{Na}, V_L, V_K the voltage drops on each channel (direct measurement of the deviation from the rest potential), and C_m the membrane capacity per unit area, we have:

$$I = C_m \frac{dV}{dt} + g_k(V - V_k) + g_{Na}(V - V_{Na}) + \overline{g}_L(V - V_L)$$

where $V = E - E_r$ $V_{Na} = E_{Na} - E_r$ $V_L = E_L - E_r$

However the model is extremely expensive to implement. It takes 120 floating point operations to evaluate 0.1 ms of model time (assuming that each exponent takes only ten operations), hence, 1200 operations/ms. Thus, one can use the Hodgkin–Huxley formalism only to simulate a small number of neurons or when simulation time is not an issue. Having a network of computationally efficient and biologically plausible cortical spiking neurons interconnected according to the principles of known anatomy of the neocortex should be the goal of every scientist exploring information processing in the mammalian brain. In this regard we have chosen to use the Izhikevich model. Starting from the theory of bifurcations, it is able to simplify models difficult to compute, such as the Hodgkin-Huxley.

The Izihkevich Model

The Izihkevich model [9] consists of a system of two first order non-linear differential equations:

$$V'_m = 0.04V_m^2 + 0.05V_m + 140 - u + I \qquad (1)$$
$$u' = a(bV_m - u)$$

Where u and v are dimensionless variables, I is the input to the system and a and b are dimensionless parameters which are manipulated to describe different firing patterns. The variable v is of most interest as it represents the membrane potential of the neuron in microvolts (mV) and u represents a membrane recovery variable, which accounts for the activation of K^+ ionic currents and inactivation of Na^+ ionic currents, and it provides negative feedback to v. After the spike reaches its apex (30 mV), the membrane voltage and the recovery variable are set according to the following rule:
if v $\geq$ 30mV then
$V_m = c$ AND $u = u + d$
Parameters of the model
By changing parameters a, b, c and d different firing patterns can be simulated. Each parameter corresponds to different aspects of neural behaviour:

- The parameter a describes the time scale of the recovery variable u. Smaller values result in slower recovery time.
- The parameter b describes the sensitivity of the recovery variable to the sub threshold fluctuations of the membrane potential v.
- The parameter c describes the after-spike reset value of the membrane potential v caused by the fast high-threshold K^+ conductances.

- The parameter d describes after-spike reset of the recovery variable u caused by slowhigh-threshold Na^+ and K^+ conductances.

Regular Spiking Neurons
Neocortical neurons in the mammalian brain can be classified into several types according to the pattern of spiking and bursting seen in intracellular recordings. For our work we will use the Regular Spiking type.[10] RS (regular spiking) neurons are the most typical neurons in the cortex. When presented with a prolonged stimulus the neurons fire a few spikes with short inter spike period and then the period increases. This is called the spike frequency adaptation. Increasing the strength of the injected dc-current increases the inter spike frequency, though it never becomes too fast because of large spike-after hyperpolarizations. In the model, this corresponds to $c = 65$ mV (deep voltage reset) and $d = 8$ (large after-spike jump of u).
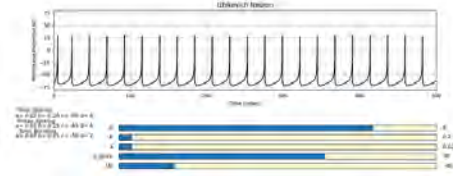

Figure 2: *Python simulation of the Izhikevich model for Regular Spiking neurons*
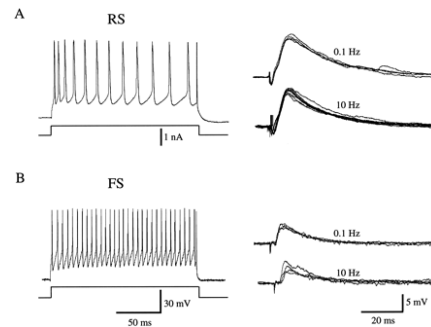
Figure 3: *Spike discharge pattern of RS neuron of rat in layer 2/3 of area 17 during injection of depolarizing current pulse (200 msec, 0.5 nA)*
[11]

A neuron can be stimulated by injecting pulses of direct current through an electrode. We record the membrane potential response. When a stepped input current is used to stimulate a neuron, the cell continues to fire a sequence of spikes called spike trains. The goal of the Izhikevich model used is to reproduce these models using computational computation.
Authors implemented the Izhikevich model for Regular Spiking neurons, Fig.2. It is worth mentioning how our neuro-computational implementation responds analogously to the patterns of the biological RS neurons of rat Fig.3.

A model for astrocytes

Experimental evidence shows that astrocytes play an active role in processing information on the brain, although it is not yet understood how these cells can encode synaptic stimuli and influence neuronal spiking activity. Although astrocytes are not electrically excitable cells, in particular they cannot generate action potentials, they possess a form of chemical excitability based on changes in their intracellular calcium concentration. From a physiological point of view, astrocytes regulate the current of the synaptic signal between two neurons by modulating the amount of neurotransmitters in the synaptic cleft through the dynamics of inter and intracellular calcium. These Ca^{2+} changes can be transient or oscillatory and can occur spontaneously or be induced by different means such as mechanical, electrical or chemical stimulation. In particular, the increase in astrocytic Ca^{2+} can be elicited in response to a series of neurotransmitters and factors including glutamate, GABA, adrenaline, ATP, serotonin, acetylcholine, dopamine, nitric oxide (Bergmann glia) and BDNF1. This response is mediated by several receptors located on the plasma membrane of astrocytes and is generally consistent with the mobilization of Ca^{2+} from the intracellular deposits of the endoplasmic reticulum. The presence of receptors on astrocytes could be seen as the teleological evidence of the neuron-glia signal [12]. Of the possible glial codes, the calcium signal is the most studied, probably due to the availability of markers to monitor intracellular Ca^{2+} and its recognized intracellular messenger function in a multitude of other cells. In detail, calcium dynamics are controlled by the calcium-induced calcium release interaction (CIRC), a non-linear amplification method that initiates the modulation of pre-synaptic and post-synaptic neural activities and promotes depolarizing currents in neurons. For the study and simulation of these dynamics, a minimum two-variable model was used: the Li-Rinzel model [13]. The two dynamic variables of the LR model are the concentration of free cytosolic Ca^{2+} (C) and the fraction of the open inositol triphosphate receptor subunits (IP_3), h.

$$C = J_{Chan}(C, I) + J_{leak} - J_{pump}(C) \qquad (2)$$

With $h = h_\infty h / t_h$. The dynamics of C is controlled by three flux, corresponding to:
- a passive loss of Ca^{2+} from the endoplasmic reticulum (ER) of the cell to the cytosol ($Jleak$);
- an active absorption of Ca^{2+} in ER ($Jpump$) due to the action of the pumps;
- a release of Ca^{2+} ($JChan$) which is mutually controlled by Ca^{2+} and by the concentration of Inositol Triphosphate (IP_3)

$$J_{leak}(C) = v_2[C_0 - (1 + C_1)C] \qquad (3)$$
$$J_{pump}(C) = \frac{V_3 C^2}{K_3^2 + C}$$
$$J_{chan}(C) = v_1 m_3 h^3 [C_0 - (1 + C_1)C]$$

Along with the gating variables:

$$m_\infty = \frac{I}{I + d_1} \frac{C}{C + d_5} \qquad h_\infty = \frac{Q_2}{Q_2 + C}$$
$$T_h = \frac{1}{a_2(Q_2 + C)} \qquad Q_2 = \frac{I + d_1}{I + d_3} d_2$$

Therefore, the level of IP_3 is directly controlled by the signals affecting the cell from its external environment. In turn, the level of IP_3 determines the dynamic behavior of the LR model. The calcium signal can therefore be considered as coded information relating to the level of IP_3. V_1 denotes the maximum CICR rate, the total cytosolic concentration of free Ca^{2+} is denoted by c_0, c_1 denotes the ER/cytoplasmic volume ratio, the IP_3 -induced calcium release channels (IICR) and CICR are represented by m and n, respectively. v_3 is the maximum absorption rate for the SERCA pump (Sarco-Endoplasmic-Reticulum Ca^{2+} -ATPase), v_2 is the calcium loss rate and K_3 is the activation constant of the SERCA pump. We have explored, through simulations using the Python program, the range of biophysical parameters for which the LR system can exhibit a change in frequency modulation (FM) with the level of IP_3 (I) as a control parameter. We found that K_3 (the active SERCA pump affinity), d_5 (the receptor affinity for IP_3), and C_0 (total cytosolic concentration of free Ca^{2+}) can all regulate the transition between AM and FM coding dynamics.
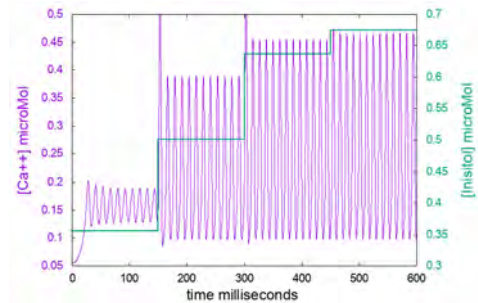

Figure 4: *The original LR parameters (table I) provide amplitude variability of oscillations that occur at almost fixed frequency. IP_3=0.355; 0.5; 0.637; 0.675*
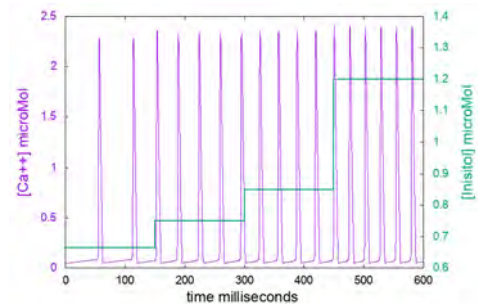

Figure 5: *A higher SERCA pump **Ca²⁺** affinity (K_3 = 0.051 μM) is responsible for oscillations with variable frequency but nearly constant amplitude. IP_3=0.6634; 0.75; 0.85; 1.2*

v$_1$	6 sec^{-1}	d$_1$	0.13μM
v_2	0.11sec^{-1}	d$_2$	1.049μM
v_3	0.9 μM sec-$^{-1}$	d$_3$	0.9434μM
C_1	0.185	a$_2$	0.2 μM^{-1}sec^{-1}
C_0	2.0μM – [4.0]	d$_5$	0.08234μM – [0.2]
K_3	0.1 – [0.051]	-	-

Table 1: *Biophysical parameters for the modulation of Ca^{2+} oscillations in AM. Parameters for FM are in square brackets*

Discussion and Conclusions

When the variations of IP_3 modulate both the amplitude and the frequency of the oscillations we will have an AFM dynamics. According to our analysis, AFM encoding can be found in many cases, most typically for higher C_0 or lower values of v_3. In terms of Ca^{2+} fluxes at higher calcium levels, amplitude modulation can coexist with frequency modulation. We found that AFM dynamics can also be reproduced from a minimal model for a particular range of model parameters. These results suggest that by activating intracellular mechanisms that control the values of physiological parameters to which model parameters C_0 or v_2, K_3 and v_3 for SERCA pumps or d_5 for IP_3R correspond, the type of information encoding can be regulated. These results are important because in AM, Ca^{2+} peaks encode information; in FM, variations inIP_3 trigger bursts of Ca^{2+} spikes with information encoded in the interspike intervals. In mixed AFM mode, both functions carry information. The above can be very relevant for the regulation of synaptic information transfer by astrocytes. Astrocytes, in fact, respond to synaptic activity through the dynamics of intracellular Ca^{2+} which in turn are transmitted to neurons by activating the release of gliotransmitters. We might expect that the short-term effectors most sensitive to the number of pulses scale are involved in feedback at the local synapse while the long-scale ones integrate the total coordinates of the signal information with the other astrocytes via intercellular signaling. This mechanism can in principle be implemented in new types of electronic systems and is particularly suitable for those systems that require particular coordination constraints of information input from multiple channels.

References

[1] G. Perea and A. Araque, *Synaptic regulation of the astrocyte calcium signal*, J Neural Transm,**112** (2005), p. 127–135.

[2] G. Carmignoto, *Reciprocal communication systems between astrocytes and neurones*, Progress in Neurobiology, **62** (2000), pp. 561 – 581.

[3] D. Pitta et al., *Computational quest for understanding the role of astrocyte signaling in synaptic transmission and plasticity*, Front Comput Neurosci,**6** (2012), p. 98.

[4] E. Bindocci, I. Savtchouk, N. Liaudet, D. Becker, G. Carriero, and A. Volterra, *Three dimensional ca^{2+} imaging advances understanding of astrocyte biology*, Science, (2017).

[5] L. Aguilera, F. T. Bergmann, G. Dalmasso, S. Elmas, T. Elsässer, R. Grosseholz, P. Holzheu, P. Kalra, U. Kummer, S. Sahle, and N. Veith, *Robustness of frequency vs. amplitude coding of calcium oscillations during changing temperatures*, Biophysical Chemistry, **245** (2019), pp. 17 – 24.

[6] R. CR and K. C, *Two sides of the same coin: sodium homeostasis and signaling in astrocytes under physiological and pathophysiological conditions*, National Library of Medicine, **61** (2013), pp. 1191–205.

[7] R. Min, M. Santello, and T. Nevian, *The computational power of astrocyte mediated synaptic plasticity*, Frontiers in Computational Neuroscience,**6** (2012), p. 93.

[8] A. L. Hodgkin and A. F. Huxley, *A quantitative description of membrane current and its application to conduction and excitation in nerve*, The Journal of Physiology, **117** (1952), pp. 500–544.

[9] E. M. Izhikevich, *Chattering cells: superficial pyramidal neurons contributing to the generation of synchronous oscillations in the visual cortex*, Science, **274** (2003), p. 109.

[10] D. A. M. C M Gray, *Simple model of spiking neurons*, IEEE Transactions on Neural Networks, **14** (1996), pp. 1569–1572.

[11] A. B. Zhengwei Shao, *Different balance of excitation and inhibition in forward and feedback circuits of rat visual cortex*, JNeurosci, **16** (1996), pp. 7353–7365.

[12] H. B. e. Maurizio De Pittà, *Computational glioscience*, Springer Series in Computational Neuroscience, (2019).

[13] J. R. Y X Li, *Equations for insp3 receptor-mediated [ca2+]i oscillations derived from a detailed kinetic model: a hodgkin-huxley like formalism*, J Theor Biol, **166** (1994), pp. 461–73.

K*(892)± Resonance Production in proton-proton Collisions at $\sqrt{s} = 13$ TeV as a Function of Charged Particle Multiplicity

A. Rosano[1,2*] and G. Mandaglio[1,2]

[1] MIFT Department, University of Messina, Messina, Italy
[2] INFN Sezione di Catania, Catania, Italy

*Corresponding Author email: arosano@unime.it

Abstract

Hadronic resonances are perfect probes to investigate the evolution of the fireball created in ultra-relativistic heavy-ion collisions. Resonances with lifetime comparable to the fireball one, like K*(892)±, may be sensitive to re-scattering and regeneration competing mechanisms. According to recent measurements, even pp and p-Pb collisions show typical features of heavy-ion collisions, like collective behaviour and suppression of short-lived resonances (like ρ^0 and K*^{0}). Multiplicity dependent studies of K*(892)± production in pp collisions at $\sqrt{s} = 13$ TeV can provide further evidences to confirm the observed trend, and the preliminary results are shown in this work. K*(892)± data are also compared to K*(892)^0 results.

Keywords: hadronic resonances, heavy-ion collisions, resonance production, ALICE, QGP, hadronic phase.

Introduction

ALICE (A Large Ion Collider Experiment [1]) is one of the largest experiments hosted at CERN. The detector is mainly designed to study ultra-relativistic heavy-ion collisions in order to investigate the physics of strongly interacting matter at extreme energy densities, where the Quark Gluon Plasma (QGP) formation is expected [2]. Short-lived resonances, like K*(892)± (in the following simply K*±), are perfect probes to investigate the properties of the hadronic medium, as they have lifetime comparable to the fireball one (~ 10 fm/c). If the hadronic phase lasts enough, resonances may decay inside the medium and their decay products can interact with the other particles. This would result in a suppression of the resonances measured yields, since they are reconstructed through their decay daughters. The process just described is known as re-scattering. In another way a competing mechanism, known as regeneration, can also occurred. Resonances can be regenerated in pseudo-elastic collision of the medium particles and, as a consequence, the measured yield will be enhanced [3]. In proton-proton (pp) and proton-lead (p-Pb) collisions QGP formation is not expected since the critical values of temperature and energy density should not be reached. For this reason pp and p-Pb collisions are normally used as baseline for nucleus-nucleus (A-A) collisions. However, recent measurements of resonances production in high multiplicity pp and p-Pb collisions have also shown the onset of QGP-like properties, like the hardening of

p_T spectra with increasing multiplicity, that should be related to collective expansion of the fireball [4, 5] and the suppression of short-lived resonances, due to daughters re-scattering in the medium [6]. These evidences seem to suggest the presence of a hadronic phase and the formation of QGP droplets even in smaller collision systems. Therefore a closer look to pp collisions is needed, especially in high-multiplicity events.

K*(892)± analysis

Data-set and Event Selection

The preliminary results of charged mesons K*± analysis, produced at mid-rapidity ($|y| \leq 0.5$) in pp collisions at $\sqrt{s} = 13$ TeV as a function of charged-particle multiplicity are briefly described. K*± is a strange resonance ($u\bar{s}$, $\bar{u}s$) with a very short lifetime ($\tau = 3.6$ fm/c), therefore is a good candidate for probing the existence of a hadronic phase in high multiplicity pp collisions. The analysis has been carried out on ALICE data collected during Run 2 and the corresponding Monte Carlo sample for reconstruction efficiency and signal-loss correction factor estimation. K*± is reconstructed via its hadronic decay channel K*± → $\pi^{\pm}$+ K^0_S (B.R. 33.3% [7]) and K^0_S is reconstructed via K^0_S → $\pi^+ + \pi^-$ (B.R. 69.2% [7]). Primary pions (coming from K*± decay) are identified by energy loss measurements while K^0_S is identified by applying topological cuts on the daughters tracks (secondary pions). The ALICE sub-detectors involved in the
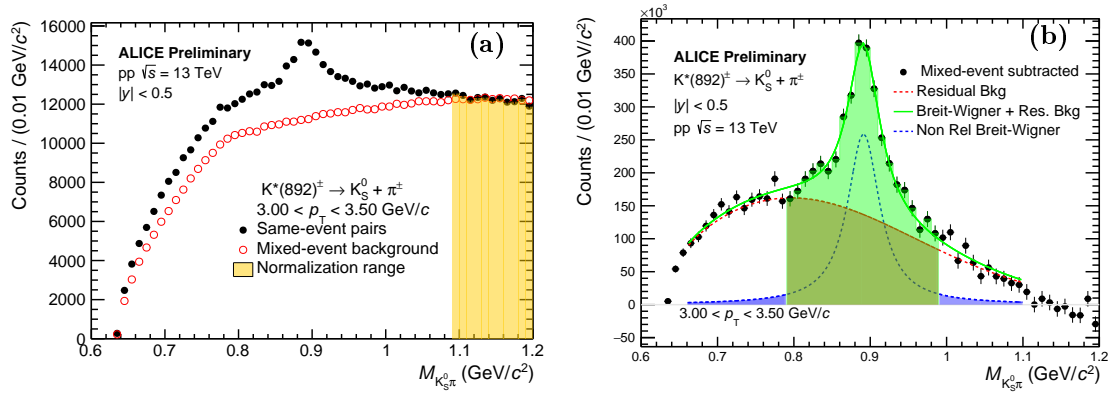
Figure 1: $K_S^0\pi^\pm$ invariant mass distribution: the background shape, evaluated via event mixing technique, (red open circle) and the normalization region (yellow-filled area), are also shown **(a)**. Invariant mass distribution obtained after background subtraction: the solid green curve is the result of the final fit. The dashed red line describes the residual background, while the blue one is the non relativistic Breit-Wigner function. Colored regions show the areas interested in the bin counting method **(b)**.

reconstruction are:

- ITS (Inner Tracking System), TPC (Time Projection Chamber), and TOF (Time Of Flight) for vertexing, tracking, and particle identification.

- V0 scintillators (V0A and V0C) for triggering and charged-particle multiplicity estimation at forward rapidities.

More details about the ALICE apparatus can be found in Ref. [1]. The events are selected with the minimum bias trigger ("kINT7", logical AND between V0A and V0C). The multiplicity dependent analysis can be performed thank to the "INEL > 0" class, defined as the set of inelastic collisions with at least one charged particle in the pseudo-rapidity range $|\eta| < 1$. The event sample belonging to INEL > 0, refers to the total charge deposited in both V0 detectors, and can be divided into several multiplicity classes [8]. The average charged-particle multiplicity densities corresponding to the different multiplicity classes are indicated in Tab. 1. The first class is related to the most central collisions (higher multiplicity), while the last one refers to the most peripheral collisions (lower multiplicity).

Multiplicity class (%)	$\langle dN_{ch}/d\eta \rangle$
0-1	25.75
1-5	19.83
5-10	16.12
10-20	12.91
20-30	10.11
30-40	8.07
40-50	6.48
50-70	4.64
70-100	2.52

Table 1: *Average charged-particle multiplicity densities at midrapidity for each multiplicity class.*

Signal Extraction

$K^{*\pm}$ raw yields are estimated via the invariant mass distribution of $K_S^0\pi^\pm$ pairs binned in 12 p_T intervals for the

0-1 multiplicity class (first class) and in 14 p_T intervals for the other classes. The distribution obtained is a peak over a large combinatorial background whose shape has been estimated via the event-mixing technique. An example of the spectra obtained before (a) and after (b) the combinatorial background subtraction is shown in Fig. 1. Signal and residual background have been fitted with the following function:

$$\frac{D}{2\pi}\frac{\Gamma_0}{(M_{K\pi} - M_0)^2 + \frac{\Gamma_0^2}{4}} + F_{BG}(M_{K\pi}) \qquad (1)$$

$$F_{BG}(M_{K\pi}) = \\ = [M_{K\pi} - (m_\pi + m_K)]^n\, e^{(A + BM_{K\pi} + CM_{K\pi}^2)} \qquad (2)$$

The first term of Eq. 1 is a non-relativistic Breit-Wigner function, to identify the resonance peak, while the second term is the function used for fitting the residual background, expressed in Eq. 2. D is the integral of the peak function from 0 to ∞, while M_0 and Γ_0 are the mass and the width of $K^{*\pm}$. To have a good fit the width was fixed to PDG value [7]. Referring to Eq. 2 $m_\pi = 139.57\,GeV/c^2$ [7] and $m_K = 497.61\,GeV/c^2$ [7] are the pion and K_S^0 masses, while n, A, B and C are fit parameters. The raw yields of $K^{*\pm}$ have been extracted using the bin counting method (figure 1.b). It consists in:

- integrating the invariant mass histogram over the region $M_0 - 2\Gamma_0 < M_{K\pi} < M_0 + 2\Gamma_0$;

- subtracting the residual background integral over the same interval;

- adding the integral of the tails of the non-relativistic Breit-Wigner at both ends.

Corrected Yields

Starting from row counts some corrective factors have to be considered in the final equation for $K^{*\pm}$ yields reconstruction (eq. 3). They are:

- **BR**: the decay Branching ratio for $K^{*\pm} \to \pi^\pm K_S^0$ (BR = 33.3%);

- ϵ_{rec}: reconstruction acceptance $\times$ efficiencies, computed with the Monte-Carlo data sample. It is given by the ratio between the number of the generated and reconstructed $K^{*\pm} \to \pi^\pm K^0_S$;

- f_{SL}: signal-loss factors, determined with the same Monte-Carlo sample used for ϵ_{rec}. It is necessary to estimate the loss of $K^{*\pm}$ due to trigger and event-selection cuts.

- f_{norm}: factors for taking into account the efficiency of trigger selection for inelastic pp collisions. They are tabulated values [9].

In addition a one-half factor has been considered because both K^{*+} and K^{*-} are taken into account. Therefore the corrected p_T spectra have been obtained as:

$$\frac{d^2N}{dp_T dy} = \frac{1}{2} \frac{d^2N_{raw}}{dp_T dy} \frac{f_{SL} \times f_{norm}}{BR \times \epsilon_{rec}} \quad (3)$$

where:

$$\frac{d^2N_{raw}}{dp_T dy} = \frac{RawCounts}{N_{evt} \times \Delta p_T \ times \Delta y} \quad (4)$$

are the raw counts normalized to the number of accepted events (N_{evt}) in the specific p_T bin and multiplicity class, and divided for the transverse momentum step (Δp_T) and rapidity interval ($\Delta y = 1.0$, since $|y| < 0.5$).

Systematic Uncertainties

In this section is described the procedure for estimating the systematic uncertainties related to $K^{*\pm}$ yields evaluation. The same yield have been computed many times with different analysis parameters. In particular the systematic sources considered until now are: primary pions selection, secondary tracks selection, vertex identification, and signal extraction procedure.

One, two or more variations from each default selection criteria have been considered, applying them one by one. A total of 35+1 variations have been used with 11+1 different procedures of signal extraction (+1 is referred to default cuts and standard procedure of signal extraction). Therefore for each cut 12 different (11 variations + 1 standard) $K^{*\pm}$ p_T spectra have been estimated. The complete process to estimate the systematic uncertainties is fully described in Ref. [10] and follows several steps:

1. for each cut (index j) in a specific group a weighted mean of the 12 different spectra is calculated using the probability of the fit as weight:

$$V_{mean\,j} = \frac{\sum_i V_i p_i}{\sum_i p_i} \qquad i = 1 - 12 \quad (5)$$

where V_i and p_i are respectively the efficiency corrected yield and the fit probability from the 12 different configurations of signal extraction.

2. The systematic uncertainty for each cut ($U_{SX\,j}$) is given by the RMS of $V_{mean\,j} - V_i$.

3. A Barlow check is done for all 12 variations of signal extraction of each cut compared to the standard cut. The cuts which pass the Barlow check are not considered in the final systematic uncertainties.

4. For each group a weighted mean of spectra estimated with the standard cut and with the cuts which fail the Barlow check is calculated as:

$$V_{MEAN} = \frac{\sum_j V_{mean\,j} p_{mean\,j}}{\sum_j p_{mean\,j}} \quad (6)$$

where $p_{mean\,j} = <p_i>$.

5. The systematic uncertainty for each group (U_{RSX}) is given by the RMS of $V_{MEAN} - V_{mean\,j}$.

6. The systematic uncertainty connected to the signal extraction procedure (U_{MSX}) is estimated by a weighted mean of the systematic uncertainties of all the cuts which fail the Barlow check:

$$U_{MSX} = \frac{\sum_j U_{SX\,j} p_{mean\,j}}{\sum_j p_{mean\,j}} \quad (7)$$

This approach has to be performed for each multiplicity class. In Fig. 2 is shown the p_T distributions of the systematic uncertainties of the sources previously described, for the class 1-5. Similar spectra have been obtained also for the other multiplicity classes. The procedure just described is still ongoing therefore the uncertainties in the p_T spectra shown in this work are only statistical. As next step, additional sources that will be considered in further analysis are material budget, hadronic interaction, and global tracking.

Then systematic uncertainties from the different sources will be added in quadrature to obtain the total systematic uncertainty at each multiplicity class.
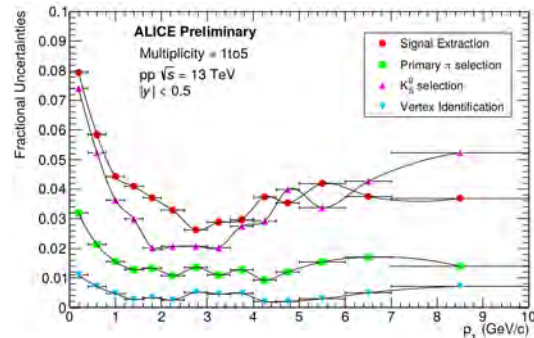

Figure 2: *The p_T spectra of the systematic uncertainty from the different sources in the multiplicity class 1-5.*

Results and Conclusions

The preliminary results of $K^{*\pm}$ resonance production at mid-rapidity in pp collisions at $\sqrt{s} = 13$ TeV for different charged-particle multiplicity classes has been reported in this work. Figure 3 shows the p_T spectra and the ratios of p_T spectra to the INEL>0 class (the class corresponding to the whole multiplicity 0-100) of $K^{*\pm}$ compared to K^{*0} at the same collision system and energy. The yields of both $K^{*\pm}$ and K^{*0} have been calculated in the same p_T bins and multiplicity classes. A good agreement, within the statistical uncertainties, may be noticed between the
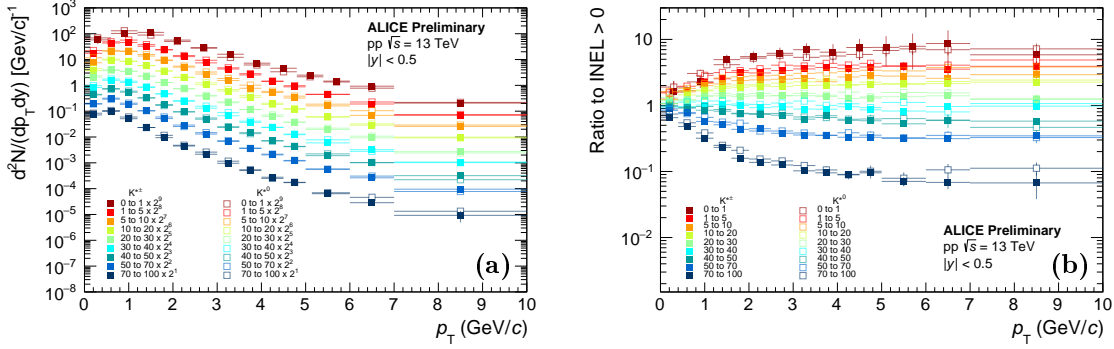
Figure 3: $K^{*\pm}$ and K^{*0} p_T spectra for different multiplicity classes, scaled by the indicated factors **(a)**. Ratios of $K^{*\pm}$ and K^{*0} p_T spectra to INEL>0 **(b)**.

two data samples. In Fig. 3.a as for K*0, the p_T spectra get harder from peripheral to central collisions, typical feature of A-A collisions. This is much more evident looking at figure 3.b, where the slopes of p_T spectra increase with increasing multiplicity for $p_T < 5$ GeV/c while for $p_T > 5$ GeV/c the shapes are the same for all multiplicity classes. This behaviour is qualitatively similar to the trend observed in heavy-ion collision, where this effect is due to collective radial expansion of the fireball. However, in small collision systems, color reconnection mechanism can mimic flow-like effects [11]. Since the results achieved are consistent with those reported for other hadron species [6], the multiplicity-dependent analysis of K*± production in pp collisions at $\sqrt{s} = 13$ TeV appears promising to corroborate the hypothesis of the presence of a hadronic phase even in small systems. Prospects for the prosecution of the present analysis are the completion and improvement of the procedure for systematic uncertainties estimation, and the calculation of K*± p_T-integrated yields (dN/dy) and of the mean transverse momentum ($\langle p_T \rangle$) at each multiplicity. This would permit the evaluation of the ratios to long-lived K mesons (K*±/K) and possibly reproduce the hint of suppression already remarked for K*0 in pp collisions at $\sqrt{s} = 13$ TeV, suggesting the presence of re-scattering effects in high multiplicity pp collisions.

References

[1] ALICE Collaboration: Aamodt, K. et al.: *The ALICE experiment at the CERN LHC.* Journal of Instrumentation 3.08, S08002, (2008).

[2] Bazavov, A. et al.: *Chiral and deconfinement aspects of the qcd transition.* Physical Review D 85, 054503, (2012).

[3] Sahu, D. et al.: *Role of event multiplicity on hadronic phase lifetime and QCD phase boundary in ultrarelativistic collisions at energies available at the BNL Relativistic Heavy Ion Collider and CERN Large Hadron Collider.* Physical Review C 101, 014902 (2020).

[4] ALICE Collaboration: Acharya, S. et al.: *Multiplicity dependence of $K^*(892)^0$ and $\Phi(1020)$ production in pp collisions at $\sqrt{s} = 13$ TeV.* Physics Letters B 807, 135501 (2020).

[5] ALICE Collaboration: Acharya, S. et al: *Investigations of anisotropic flow using multi-particle azimuthal correlations in pp, p-Pb, Xe-Xe, and Pb-Pb collisions at the LHC* Phys. Rev. Lett. 123 142301 (2019).

[6] Khuntia, A. for the ALICE Collaboration: *Latest results on the production of hadronic resonances in ALICE at the LHC.* arXiv:2001.09023 [hep-ex].

[7] Particle Data Group Collaboration: Zyla, P.A. et al: *The Review of Particle Physiscs.* Prog. Theor. Exp. Phys. 083C01 (2020).

[8] ALICE Collaboration: Acharya, S. et al: *Multiplicity dependence of (multi)-strange hardron production in proton-proton collisions at $\sqrt{s} = 13 TeV$.* Eur. Phys. J. Phys. C80, 167 (2020).

[9] Lim, B.H.: *Production of $\Xi(1530)^0$ in pp collisions at $\sqrt{s} = 13 TeV$, ANA-886.* https://alice-notes.web.cern.ch/node/886.

[10] Garg, K. and Badalà, A.: *K(892)*± resonance production in pp collisions at $\sqrt{s} = 13$ TeV* https://alice-notes.web.cern.ch/system/files/notes/analysis/631.

[11] Ortiz Velasquez, A. et al.: *Color reconnection and fow-like patterns in pp collisions* Phys. Rev. Lett. 111, 042001 (2013).

PhD in Physics 2019-2020 Activities report 1st year PhD (XXXV Cycle)

Abir Saidi[1], Tutor: Prof. Rosalba Saija[1]

[1]*Dipartimento di Scienze matematiche e informatiche, scienze fisiche e scienze della terra,University of Messina, Messina, Italy*

*Corresponding Author email: asidi@unime.it,rsaija@unime.it

Abstract

My research thesis is about the modeling of optical forces on particulate matter in specific atmospheric and planetary environments. My work moves into the modeling of electromagnetic scattering at the nanoscale. The main calculation tool that we use is based on the formalism of the Transition Matrix or T-matrix. The transition matrix formalism was derived starting from the integral equation formulation of electromagnetic scattering to solve the scattering problem.The previous project is about astrophysics dustgrains but this year we use the theory of scattering applied on silver and gold nanoparticles to some measurements that have been made at the University of Messina with Professor Fasio and Professor Neri together with Professor Ossi at the University of Milano. As a first step we study the Optical Properties of *Ag-Au* Colloidal Alloys Pulsed Laser Ablated in Liquid: Experiments and Theory.

Keywords: electromagnetic scattering, Transition Matrix, dustgrains, Optical Properties of Ag-Au
.

Introduction

In this work, we simulated the extinction spectra of *Ag-Au* alloyed *nanoparticles* produced by pulsed laser ablation in a liquid of elemental targets followed by re-irradiation of suitable mixtures of the obtained colloidal suspensions. When we make use of the optical constants of *Ag-Au* alloys, our theoretical approach, developed in the framework of the *T-matrix* formalism, accurately reproduces the experimental features of the extinction spectra of laser-produced *nanoalloys* with compositions that span the entire composition range (*Ag25Au75, Ag50Au50, and Ag75Au25*).

Results

We investigate the extinction spectra of elemental samples as prepared. The first curve is the extinction spectra of elemental silver as Figure (1) and (2) and the second one is for elemental gold as prepared as Figure (2) and (4) which in both the red curve refers to experimental data done in a collaborated experimental lab and the blue curve refers to the best fit from theory. The optical constants for both gold *NP* and silver *NP* are those derived from the work of Johnson and Christy. Since e-silver and *e-Au* are *polydispersed* in size as we can see we are confident that the optical properties of both elemental colloids can be determined through a weighted average of particles sizes, from *rmin = 1 nm* to *rmax = 300 nm*, of single-particle extinction and scattering cross-sections

calculated As suggested by the sampling in size, we choose a simple analytical function of the *lognormal* to fit the experimental data. So the blue curves show the comparison between the experimental normalized *UV-Vis* spectra for as-prepared silver and *NPs* and the best fit obtained as Figure (7).

Then we present the extinction spectra of the re-irradiated particles of silver and gold as Figure (5) and (6), the *1st* curve refers to silver re-irradiated extinction spectra and the second one refers to the gold after laser re-irradiation. In this table as Figure (7), we report the best-fit parameters obtained. And we can see that our best fits are in good agreement with the experimental data for all elemental samples, so we can conclude that in this case, the re-irradiation create more small particles, it changes for *Ag* from *30 nm* to *25 nm*, and for *Au*, it changes from *30 nm* particles to *15 nm* particles.

We report the extinction spectra of *e-Ag* and *e-Au* colloids mixed in selected proportions as Figure (8). We have simulated these interactions considering a dimer consisting of one sphere of Au and one sphere of Ag and the distance between the two spheres goes from *5 to 15 nm*. We notice that the intensity of the peak at about *400 nm*, associated with silver *NPs*, increases on increasing silver content. The same peak also undergoes a gradual red shift from *396 nm* to *406 nm*. But *Au NP* feature shifts progressively from *515 nm to 507 nm* on lowering the Au content. These shifts are theoretically justified by supposing that upon mixing there is a weak interaction between the particles that make up the mixture.

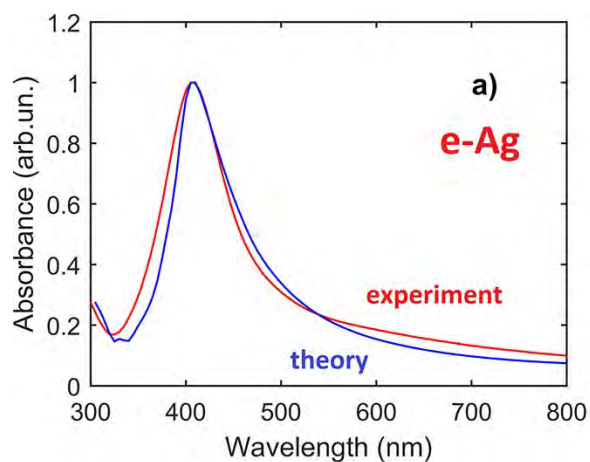Figure 1: *extinction spectra of elemental Ag as prepared*

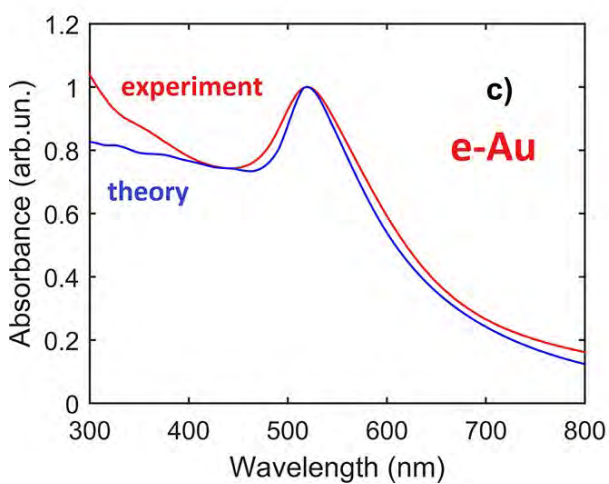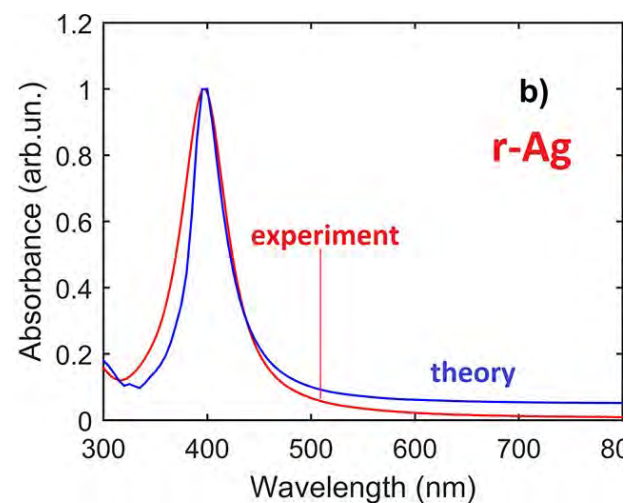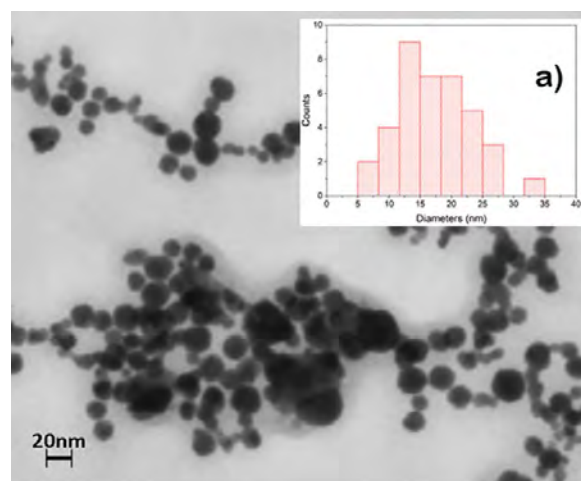Figure 2: *extinction spectra of elemental Au as prepared*
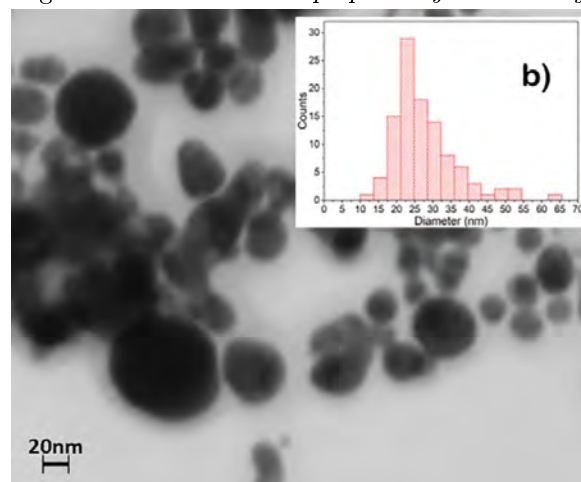

Figure 3: *Elemental NPs prepared by PLAL e-Ag*

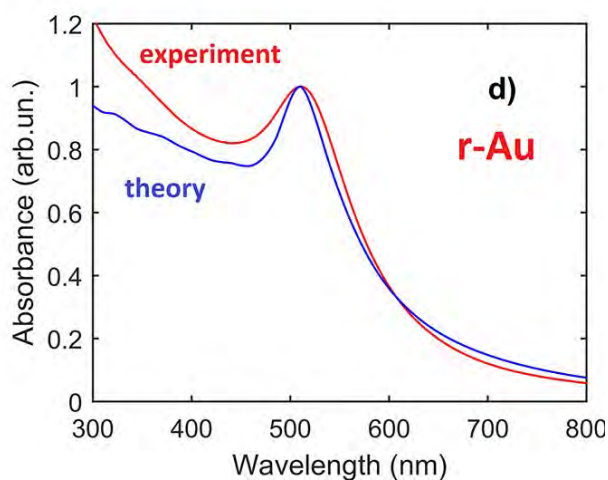Figure 4: *Elemental NPs prepared by PLAL e-Au*

Figure 5: *extinction spectra of the re-irradiated Ag*

Figure 6: *extinction spectra of the re-irradiated Au*

	r_{av} (nm)	σ	r_{min} (nm)	r_{max} (nm)
e-Ag	30	1.5	1	300
irr. e-Ag	25	1.3	1	300
e-Au	30	2	1	100
irr. e-Au	15	2	1	100

Figure 7: *Values of the Parameters Obtained through the Best Fit Procedure of the Experimental Data*

Then we presented the simulations obtained for the re-irradiated samples made by mixing e-Au and e-Ag colloids as Figure (5) and (6), where the fraction of *Ag NPs* ranges from *25% to 75%* as Figure (9). From the analysis of the experimental data, we observe that by re-irradiating the mechanically mixed colloids the lowest frequency peak we previously assigned to *AgNPs* disappears.

To understand if it is a core-shell NP or a new kind of particles are formed as Figure (10). The curves are obtained for a core-shell spherical NP, for homogeneous spheres using both Bruggeman's *Eff Med App* and dielectric optical constant coming from the analytic model. We simulate the extinction spectra for Ag50Au50, from different models: *Au-Ag core-shell, Au shell, 4.12 nm* (red line); *Au-Ag core-shell, Ag shell, 4.12 nm* (black dashed line); *Ag50Au50* with dielectric optical constant coming from Bruggeman's mixing rule (green line); *Ag50Au50* with dielectric optical constant coming from the analytic model (red dashed line); the blue line refers to experimental extinction spectrum of the same r-irradiate colloids. By analyzing that curve (10) we can notice that the absorption spectra for the model (1; red and black dashed curves), (2; green curve), and (3: red dashed curve) are very far from experimental data. As expected, in the first case the layered structure introduces a further peak due to the presence of the core that marks the optical behavior. We can see that Bruggeman's model gives an absorption spectrum whose behavior is, as was to be expected, an intermediate result between the two spectra core-shell.
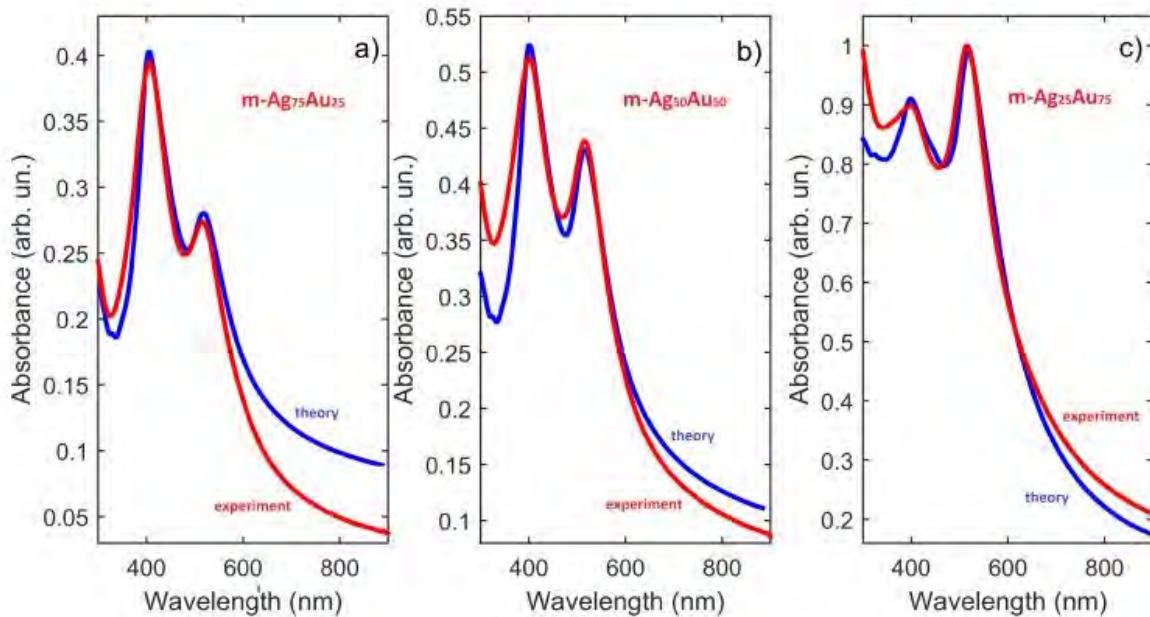
Figure 8: *Extinction spectra from experiment (red line) and simulation (blue line) for three m-AgxAu100x mixed colloids of different stoichiometry, spanning the composition range: (a)m-Ag75Au2575Au25; (b)m-Ag50Au50; (c)m-Ag25Au75.*

Also, the result obtained by Rioux's analytic model (red dashed curve) presented is far from experimental data. All such unsatisfactory results indicate that the experimental re-irradiation of the sample produces colloidal solutions of *NPs* with optical properties that can no longer be described through the dielectric functions that make use of a mixing rule.

For these reasons, we resort to the optical constant for real *Ag-Au* alloys obtained experimentally using the results of Penea Rodreguez. In figure a and c, we present the values of the real part *(n)* and imaginary part *(k)* of the refractive index corresponding to the *Ag-Au* alloys prepared in the laboratory re-irradiating mixtures of the three proportions. together with the real and imaginary. For comparison in Figure, we show the values of *n* and *K* obtained with the Bruggeman's mixing rule (11).

Figure 9: *Experimental (red line) and calculated (blue line) normalized extinction spectra of re-irradiated colloids of different compositions: (a) r-Ag75Au25; (b) r-Ag50Au50; (c) r-Ag25Au75.*

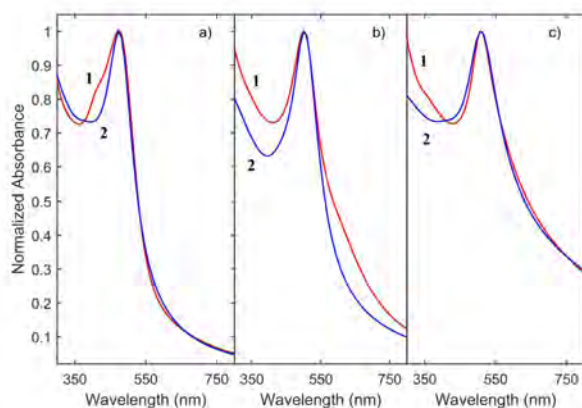We can notice that we have new material by analyzing these curves because as we can see there is a difference between the refractive index of Ruggman Andof Penea Rodreguez. This difference indicates that there is a formation of new material. So now we can report the normalized experimental UV-Vis absorbance in good agreement with the calculated values for the re-irradiated mixtures with different compositions. For the simulated absorbance we adopted the previously discussed model for the dielectric constant of the alloy and, even in this case, we considered a log-normal distribution in size (9)(12).

We introduced a model that nicely describes light absorption in $AgAu$ alloyedNPs. This model was tested by analyzing the extinction spectra collected from colloids synthesized by $PLAL$, covering a broad composition range. Provided the model can be fed with the optical constants of other alloys over the compositional range of interest.
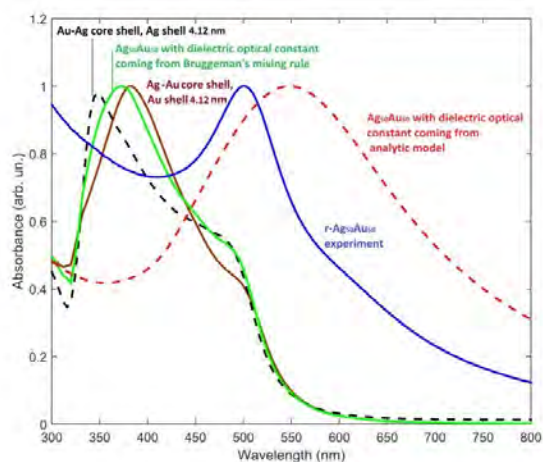
Figure 10: *Extinction spectra for Ag50Au50, from different models*
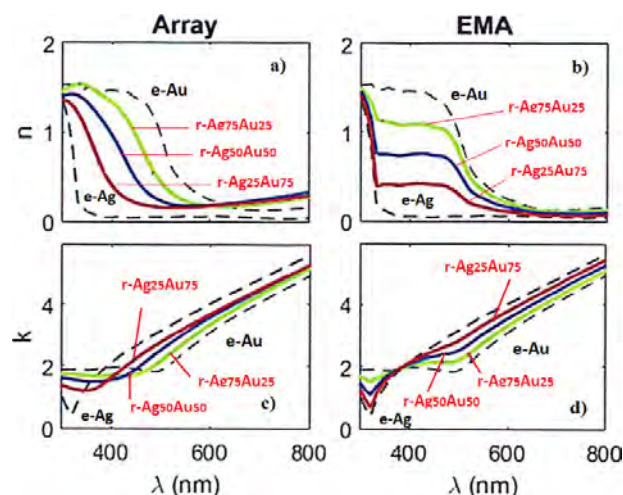
Figure 11: *Real (n, panel (a)) and imaginary (k, panel (c)) parts of the refractive index as functions of the wavelength for re-irradiated r-Ag-Au colloids of different compositions.*

	r_{av} (nm)	σ	r_{min} (nm)	r_{max} (nm)
25%Au-75%Ag	10	2	1	100
50%Au-50%Ag	10	2	1	100
75%Au-25%Ag	10	2.5	1	100

Figure 12: *Values of the Parameters Obtained through the Best Fit Procedure of the Experimental Data Shown in Figure (9)*

Projects

1. ASI-INAF "Space Tweezers" (4 February 2019 – in course)
2. Prin 2020 (22 January 2020– in course)

Seminars

- 8 May 09:00-11:00: webinar MATLAB Campus Wide all'Università di Messina
- 14 May 15:00-17:00: webinar Laboratorio C.O.P. Power You Digital - Allena le tue competenze
- 15 May 10:00-11:00: webinar NanoLab Talk "Laser synthesis of plasmonic platforms for SERS-based therapeutic drug monitoring
- 8 May 15:00-17:00: Laboratorio C.O.P. Il curriculum Vitae
- 4 June 16-17: Webinar "Midinfrared Discussions Webinar Series"
- 10 June 15-17: Webinar "Cop Il Colloquio Di Lavori"
- 11-18-25 June 16-17: Webinar «Midinfrared Discussions Webinar Series"

- 26 June 14-15: Webinar "Cultural Heritage At The Esrf: From The Discovery Of Masters' Secrets To The Conservation Of Artworks" – Marine Cotte, Esrf Scientist
- 20 July 10:00-13:00: Fisica Dei Sistemi Disordinati, Polimeri E Biofisica (C. Branca – U. Wanderlingh)
- 20 July 13:00-17:00: Webinar Dr. Iatì
- 01-06-16-21-07-2020, 24-06-2020: Serie di seminari Webinar in collaborazione con Area Science Park

References

[1] Fazio, E., Saija, R., Santoro, M., Abir, S., Neri, F., Tommasini, M., Ossi, P. M.: *On the Optical Properties of Ag–Au Colloidal Alloys Pulsed Laser Ablated in Liquid: Experiments and Theory.* . In: The Journal of Physical Chemistry C, 124(45), 24930-24939 (2020).

REPORTS

STUDENTI DI DOTTORATO DI RICERCA

CICLO XXXVI

Simulations and performance study of EEE telescopes and their possible integration with portable detectors

S. Grazzi[1,3*], G. Mandaglio[1,2], M. Battaglieri[3,4]

[1] *MIFT Department, University of Messina, Messina, Italy*
[2] *INFN Sezione di Catania, Catania, Italy*
[3] *INFN Sezione di Genova, Genova, Italy*
[4] *Thomas Jefferson National Accelerator Facility (Jefferson Lab, JLab), Newport News, VA 23606, USA*

[*]Corresponding Author email: stafano.grazi@unime.it

Abstract

The muon telescopes of the Extreme Energy Events (EEE) Project [1, 2] are based on Multigap Resistive Plate Chamber (MRPC) technology. The EEE array is composed, so far, of 60 telescopes, organized in clusters and single telescope stations distributed all over the Italian territory and installed in High Schools, spanning more than 10 degrees in latitude and 11 in longitude, . The study of Extensive Air Showers (EAS) requires excellent performance and a good understanding of detector response. A investigation of several EEE telescopes has been performed and result are use to build a calibrated simulation Framework. The response of a single MRPC and the of telescope have been implemented in a GEANT4-based framework (GEMC) to study the telescope response. The detector geometry, as well as details about the surrounding materials and the location of the telescopes have been included in the simulations in order to realistically reproduce the experimental set-up of each telescope. With same simulation tool has been study the response of a portable portable cosmic muon detector (AstrO) developed at the National Institute of Nuclear Physics, Genoa section (INFN-GE), designed for both educational and scientific purposes. Astro can be easy interfaced with other cosmic muon telescope to provide additional and complementary information respect static detectors, thanks to its portability.

Keywords: cosmic rays, cosmic muons, MRPC, GEANT4, scintillator, Streaming Readout.

EEE Project

The EEE network precisely measuring cosmic muon rates and arrival time, looks at the sky in a complementary way than traditional optic telescopes. The EEE main goal is to study high-energy cosmic rays. Some recent results, published by the EEE Collaboration, include: observation of the Forbush effect [3], searches for anisotropies in cosmic ray intensity [4], and long distance correlation in secondary muons [2]. Each station of the EEE network, that defines a "telescope" for Cosmic Rays (mainly muons), is made of three Multigap Resistive Plate Chambers (MRPC) [5], synchronized with GPS, specifically designed to achieve good tracking and timing capability, low construction costs, and an easy assembly procedure (major detail can be found in [6]. Each MRPC consists of 6 gas gaps obtained by stacking glass sheets separated from each other by fishing line spacers, placed inside a gastight aluminum box and flushed with a mixture made of $C_2H_2F_4$ and SF_4 in 98/2 proportions. The active area of each chamber is 158 cm $\times$ 82 cm, and the readout panel is split in 24 copper strips, 158 $\times$ 2.5 cm (separated one from another by 7 mm of space), each connected to a readout channel of the Front-End Amplifier Boards (FEA).

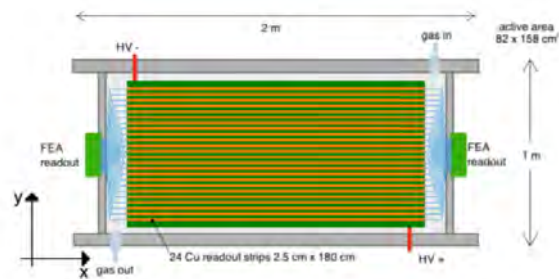Figure 1: *Top view of an EEE MRPC chamber.*

A quantitative understanding of these effects can be obtained by a precise measurement of the cosmic muon rates and arrival time (at ns level). To do so a sophisticated detector, a good understanding of the experimental conditions, good performance and an excellent synchronization of data coming from different telescopes in the EEE grid is mandatory.

Performance

Using data taken during coordinated runs has been possible to evaluated the performance of whole network such: efficiency, time and spatial resolution of the detectors and also the stability of operation of each single telescope. The study is performed at different voltages monitoring also pressure and temperature and correcting for their variations. The mean efficiency evaluated using data from 31 telescopes chamber is 93% and has been checked to be stable by considering the stability of the rate of muons which is strongly affected by efficiency variation. Performing a comparison of the hit information s on the central chamber with the ones on the external chambers, so that the width of the obtained distribution Δs is used to estimate the (time/longitudinal spatial/transverse spatial) resolution (σ_t, σ_x, σ_y) of the telescope. Time (spatial) residuals used for the measurement of the time (spatial) resolution are defined as $\Delta s = (s_{top} + s_{bot})/2 - s_{mid}$, where stop, s_{mid}, s_{bot} are the time (spatial) values for single or clustered hits and s represents t, x, or y depending on the considered case. More details can be found in [6]. Concerning the transverse and longitudinal spatial resolution (σ_y and σ_x) in all run, we obtained 0.92±0.01 cm and 1.48±0.04 cm along Y and X respectively. The NINO ASIC [7] based Front End cards together with the use of MultiHit TDCs provides time and charge (TOT, Time Over Threshold) measurements of the signals. Using the TOT information we measured the time resolution of the detectors, applying time slewing corrections, and obtained a mean value is 238 ± 40 ps.

Simulation

The response of a single MRPC and the combination of three chambers have been implemented in a GEANT4-based framework to study the telescope response. The model described in Ref. [8] has been used to generate the single-muon distribution. The azimuthal distribution of muons is considered to be uniform, while the polar angle distribution (angle with respect to the Zenith)) is taken from an improved Gaisser-like parametrization (see Ref. [9, 10]) that includes Earth curvature at all latitudes and low energy muons ($E_\mu < 100$ GeV/c). The flux, as a function of muon energy E_μ and θ_μ is given by:

$$\frac{dI_\mu}{dE\mu} = 0.14 \left[\frac{E_\mu}{GeV}(1 + \frac{3.64\,GeV}{E_\mu(cos(\theta^*)^{1.29}}) \right]^{-2.7}$$
$$\left[\frac{1}{1 + \frac{1.1\,E_\mu\,cos\theta^*}{115\,GeV}} \right] + \left[\frac{0.054}{1 + \frac{1.1\,E_\mu\,cos\theta^*}{850\,GeV}} \right] \quad (1)$$

where

$$cos\theta^* = 0.14\sqrt{\frac{(cos\theta)^2 + P_1^2 + P_2(cos\theta)^{P_3} + P_4(cos\theta)^{P_5}}{1 + P_1^2 + P_2 + P_4}}$$
$$(2)$$

and the used parameters P_1 - P_5 are 0.102573, -0.068287, 0.958633, 0.040725, 0.817285, respectively. The absolute muon flux normalization of 1.06 cm^{-2} min^{-1}, used in the simulation, is the one reported in the PDG [11].

Finally, the generated muons were processed by GEMC to record the simulated interaction with the EEE telescope and to derive the expected angular distribution of single-track events and the absolute rate. This simulation tool is based on the GEMC [12] framework providing user-defined geometry and hit description. Detector and building structures are implemented by using the standard GEANT volume description. The program handles multiple input/output format and provides a graphical interface to visualize the detector and the hits in active and passive volumes.
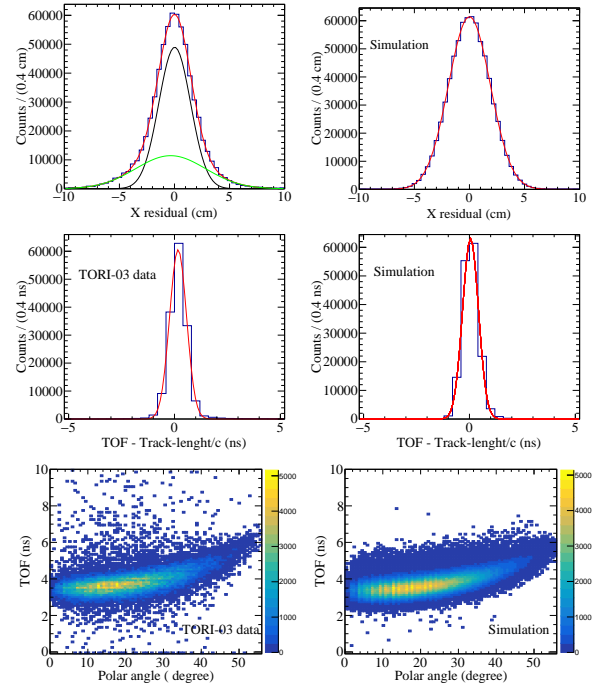
Figure 2: *Comparison of microscopic quantities between experimental data and Simulation. On left, telescope track X coordinate residual (top), Time-of-Flight - track length over C (with respect to the speed of light) (middle), correlation between tracks Time-of-Flight and polar angle (bottom). In the top (middle) panel, the distribution is fit to a double (single) Gaussian, shown as a red curve. The standard deviation of the narrow Gaussian in the top panel is $\sigma_X = 1.44 \pm 0.3$ cm. The fit mean value and Std in the time distribution (middle panel) are 0.16 ± 0.04 ns and 0.37 ± 0.03 ns, respectively. On Right, telescope simulation. Same observables. Std of the Gaussian fits are: $\sigma_X = 1.898 \pm 0.15$ cm, $\sigma_{TOF-TrL} = 0.40 \pm 0.05$ ns, respectively; the mean value of the Gaussian fit of the time distribution (middle panel) results 0.10 ± 0.03. ns*

The MRPC response was parametrized mimics the avalanche propagation in the gas that is effectively described by a cone with the vertex generated by the particle interaction in the upper layer of the chamber and that develops downwards. Using data from detector per-

formance analysis, the size of the cone in the transverse plane (with respect to the track propagation) is assumed to be the cluster size σ_x=9.2 mm and σ_y = 15 mm as referred previously. To reproduce the measured speed and time resolution, the signal propagation time along the strip is assumed to be 15.8 ns/cm, smeared to take into account the measured experimental resolution of σ_t = 238 ps. In the simulation, the three chambers in the most common configuration are placed in a concrete wall box with variable thickness mimicking the room where the real telescope is located. Of course, more complicated geometries of the surrounding space can be implemented. The information generated by GEMC and necessary to reconstruct the muon track are: the total number of hits for each chamber (at least one); the coordinates of the strips that give signals; the signal time from the generation point to the edge of the chamber. This information has been processed with the same reconstruction algorithm used on experimental data. In this way is easily compared results from simulation with real data.
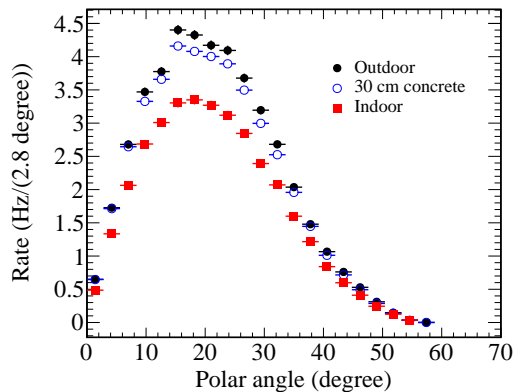

Figure 3: *Comparison of absolute single muon rates as a function of tracks polar angle in different simulation environmental conditions.*

In order to compare the simulated and experimental data, is necessary calculate with precision the efficiency on surface of each MRPC of a telescope of the network. We mapped each chamber by dividing it in 24×20 (X×Y directions) sectors. We define the tracking efficiency as the ratio between the map of the missing hits (geometrical position belonging to a sector of a chamber crossed by a track reconstructed by using the information provided by the other two chambers) and the map of the good hits (hits belonging to sectors of chambers crossed by tracks reconstructed by using information of all chambers). The framework has been validated [13] by a detailed comparison to single-muon rates (angular and integrated) recorded by some selected EEE telescopes. The agreement between experimental data and simulated data at few percent on several observables (absolute cosmic rate, angular distributions, resolution, ...), gives us confidence on the validity of our implementation. Simulations can be used also to compare and correct the response of different detectors in the EEE network in order to achieve the systematic precision requested by the study.

As already mentioned, the EEE telescopes are often placed in rooms with variable thickness of concrete walls and roof. Moreover, detailed drawings of the building (schools, university labs, ...) are not always available for a thorough assessment of the experimental conditions. For a correct comparison of different telescopes it is therefore important to evaluate the effect of the location.
We studied different experimental setups, common to the EEE network, with an increasing complexity of the environmental conditions. We started by comparing the results obtained simulating an outdoor and an indoor (30 cm walls and a 70 cm roof, concrete) telescope.

AStrO

AstrO is a portable cosmic muon detector developed at the National Institute of Nuclear Physics, Genoa section (INFN-GE), designed for both educational and scientific purposes. The detector is made of eight plastic scintillator bars arranged in two parallel planes. Two long bars (60 x 8 x 2.5 cm^3) and two short ones (18 x 8 x 2.5 cm^3), placed perpendicularly below the long ones to form a grid, define two identical sets of hodoscopes. The detector layout and more detail can be find in [14].
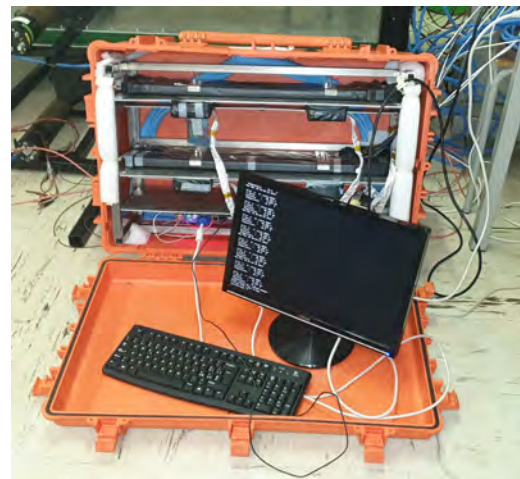
Figure 4: *AstrO detector inside the trolley.*

The acquisition is controlled by a microprocessor (FPGA) that can identify the coincidences between two or more scintillators. Portability, robustness, stability are the main features of the AstrO telescope. With this features, it is capable of measuring the integral intensity of vertical muons (integrated over the detector acceptance) with the sensitivity of spotting variations due to solar activity (Forbush effect) or related to altitude or latitude change of the detector location; by comparing indoor to outdoor rates it provides the muon absorption factor due to the presence of surrounding materials in buildings, mines or caves; by changing the bars set-up it can measure the angular distribution of cosmic muons. Using a proper GPS system it is also able to do measurement that can be easily compare with other Cosmic Rays detector such EEE telescope or Oulu Neutron monitor.
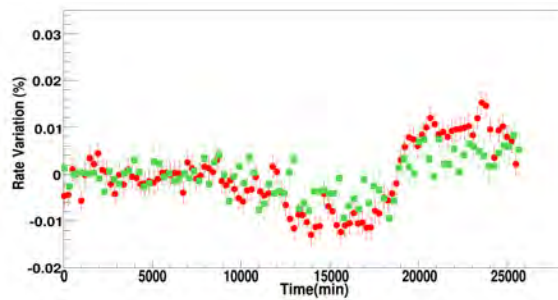
Figure 5: *AstrO absolute muon rate measured from November 22 to December 10 2019 (green) superimposed to Oulu measurement in same period (red).*

The response of the AstrO detector to cosmic muons has been simulated using the GEMC simulation tool in similar way of EEE Telescope (same parameterization but different geometry and detector type). This permit to easy understood the behavior of surrounded material as well different geometry.

Future

The Simulation framework is a valuable tool to study the detector performance, it can be used to compare and correct the response of different detectors in the EEE network in order to achieve the systematic precision requested by the study of small effects such as the variation of the cosmic ray flux due to the Forbush effect. Finally, the EEE simulation framework can be used to investigate new directions, such as the use of cosmic muons for building tomography, extending the current scope of the EEE Collaboration.

A new version of the AstrO detector (AstrOPlano), is currently under construction. This new detector has the same number of scintillators and the same geometry as AstrO, with some differences and improvements: newer and better performing SiPMs, thinner bars with better optical coupling, different electronics with the FPGA replaced by a Raspberry Pi , an ad hoc card capable of continuously acquiring data (Streaming Readout) and which allows you to sample the shapes of the impulses of events and charge, a new, more performing GPS. As Astro, Astroplano can used to making coordinate measure with other detector such EEE, and also try some improvement such the possibility to displace several detector around static one to better study particles shower distribution. It is also can be investigate the possibility to applied streaming Readout technique to EEE telescope acquisition.

References

[1] M. Abbrescia et al. (EEE Collaboration), The EEE experiment project: status and first physics results, Eur. Phys. J. Plus **128**, 86 (2013).

[2] M. Abbrescia et al. (EEE Collaboration), Search for long distance correlations between extensive air showers detected by the EEE network, Eur. Phys. J. Plus **133**, 34 (2018).

[3] M. Abbrescia et al. (EEE Collaboration), Observation of the February 2011 Forbush decrease by the EEE telescopes, Eur. Phys. J. Plus (2011) **126**, 61.

[4] M. Abbrescia et al. (EEE Collaboration), Looking at the sub-TeV sky with cosmic muons detected in the EEE MRPC telescopes, Eur. Phys. J. Plus **130** (2015) 187.

[5] An S. et al. (EEE Collaboration), Multigap resistive plate chambers for EAS study in the EEE Project, Nucl. Instrum. Meth. A **581**, 209 (2007).

[6] EEE Collaboration, The Extreme Energy Events experiment: an overview of the telescopes performance, Published by IOP Publishing for Sissa Medialab, JINST 13 (2018) 08, P08026.

[7] F. Anghinolfi, P. Jarron, A.N. Martemyanov, E. Usenko, H. Wenninger, M.C.S. Williams et al., NINO: An ultra-fast and low-power front-end amplifier/discriminator ASIC designed for the multigap resistive plate chamber, Nucl. Instrum. Meth. A **533**, 183 (2004).

[8] H. M. Kluck, Measurement of the Cosmic-Induced Neutron Yield at the Modane Underground Laboratory, Ph.D. thesis, KIT, Karlsruhe (2013). doi:10.1007/978-3-319-18527-9. URL http://nbn-resolving.org/urn:nbn:de:swb: 90-398379

[9] M. Guan, M. C. Chu, J. Cao, K. B. Luk, C. Yang, A parametrization of the cosmic-ray muon flux at sea-level, arXiv e-prints (2015) arXiv:1509.06176arXiv:1509.06176.

[10] T. Gaisser, T. Stanev, Cosmic Rays in Review of Particle Physics, Physics Letters B 592 (2018). URL http://pdg.lbl.gov

[11] M. Tanabashi, et al., Review of Particle Physics, Phys. Rev. D **98** (3), 030001 (2018).

[12] GEMC, GEant4 Monte-Carlo (version 2.6): https://gemc.jlab.org/gemc/html/index.html/

[13] M. Abbrescia et al. (EEE Collaboration), The cosmic-muon and detector simulation framework of the Extreme Energy Events (EEE) experiment, Eur. Phys. J. C, submitted for publication

[14] S. Grazzi, M. Battaglieri, F. Fontanelli, et al. (2020). AstrO: A portable cosmic ray telescope. Nuclear Instruments and Methods in Physics Research Section A: Accelerators, Spectrometers, Detectors and Associated Equipment. 976. 164275. 10.1016/j.nima.2020.164275.

Probabilistic Computing for Factorization Problems

A. Grimaldi[1,*], L. Sanchez-Tejerina[1,2], M. Carpentieri[3], K. Y Camsari[4], G. Finocchio[1]

[1] *Dipartimento di Scienze Matematiche e Informatiche, Scienze Fisiche e Scienze della Terra, Università degli Studi di Messina, Messina, Italy*

[2] *Department of Biomedical, Dental, Morphological and Functional Imaging Sciences, Università degli Studi di Messina, Messina, Sicilia, Italy*

[3] *Dipartimento di Ingegneria Elettrica e dell'Informazione, Politecnico di Bari, Bari, Puglia, Italy.*

[4] *Department of Electrical and Computer Engineering, University of California Santa Barbara, Santa Barbara, CA, United States.*

[*]Corresponding Author email: angrimaldi@unime.it

Abstract

With the growing number of relevant computational problems that require exponentially growing resources (NP-hard problems), the interest toward alternative computational frameworks has been increasing. The ideal new technology needs to combine computational power and efficiency, requiring a low energy cost while being CMOS-compatible. Probabilistic computing implemented through spintronic components satisfies these requirements.

The novelty approach of probabilistic spin logic circuits (PSL) lies in their bidirectionality. While a standard circuit can only be operated in one direction, PSL circuits allow themselves to be run in reverse, by selecting an output and obtaining an input that is compatible with the set result. This framework has many applications to NP-hard problems such as factorization, where it allows to factorize a number by using a standard multiplication circuit and clamping the output bits to those of the number to factorize.

Keywords: probabilistic computing, MTJ, spintronics, unconventional computing, factorization.

Introduction

Standard computing is based on deterministic transistors and logic gates. A circuit can be operated only in its intended direction, from input to output, with a great precision. Many problems can be solved in a very short time using this algorithmic approach. However, some problems, known as NP-complete, have a computational cost that scales exponentially even with the fastest algorithms. Many of these problems, such as factorization, Max-SAT problems, traveling salesman problems, have a great relevance in today's world.

In order to find a novel approach that could decrease the complexity of these problems, many kinds of unconventional computing frameworks are being developed. While the advancements in the field of quantum computing are promising [1, 2], the current hardships of scaling that technology has brought some new ideas that use the same hardware as standard computing but take on a non-deterministic approach, such as memcomputing [3] and probabilistic computing [4].

For the sake of efficiency, the ideal approach would be to have a new computational framework that uses CMOS-compatible components with low energy requirements. The basic building block of probabilistic computing is the p-bit, which is shown to be easily implementable with MTJs [5, 6], simple yet very efficient spintronic devices that are CMOS-compatible [7].

The combination of probabilistic computing and spintronics has already been implemented in hardware with good results [8]. Relevant NP-complete and NP-hard problems, such as factorization, have been tested with promising results. The unconventional approach of probabilistic spin logic (PSL) circuits derives from the fact that they can be operated both in the standard, "direct" mode and in reverse. While in direct mode, the input p-bits are clamped, and the output p-bits take on the correct value. In reverse mode, the output is clamped, and the circuit p-bits fluctuate between states that are compatible with the set result [4]. This feature has potential applications in a wide range of computational problems, such as the before mentioned factorization, Max-SAT problems, combinatorial problems, and many other optimization problems.

PSL circuits can be implemented on a deterministic Turing machine with the use of any kind of random signal generator. The base unit of such a circuit is an element that receives an input signal and outputs the state of the p-bit according to a function that has a random component and a deterministic one. Thus, a polarized input signal will still get close to deterministic results while a non-polarized one will have a more uncertain outcome.

To determine the input signal of each p-bit a matrix notation is used, where off-diagonal elements represent the interaction between p-bits.

Positively interacting bits will increase or decrease the input signal to enhance the probability of being in the same state, while negatively interacting p-bits will do the opposite and strive to be in different states. A pseudo-temperature coefficient scales the input signal, effectively dampening or heightening the interactions, allowing thus to control the mobility of the system. The evolution algorithm is asynchronous in nature and requires the update order to be random and sequential.

Aims

The goal of the research is to build a new computing framework capable of handling NP-hard problems unsolvable for standard computation. In particular, the work here presented aims to create a factorization algorithm with a cost that does not scale exponentially with the number of input bits and, therefore, has the potential of being refined to handle numbers that are currently impossible to factorize. The state of the art for a general form number is 829 bits. In this work we managed to factorize correctly a 12 bits number with a probabilistic approach.

Methods

The base unit of a probabilistic computing circuit is any random signal generator whose output can be tuned with an input signal.

$$m_i(t) = \text{sgn}\left(\text{rand}(-1, +1) + \tanh(I_i(t))\right) , \quad (1)$$

where I_i is the input signal, $\text{rand}(-1, +1)$ is a random real number between -1 and $+1$ and m_i is magnetization of the unit, which is the state of the p-bit.

In this ideal configuration each p-bit can only assume a value of -1 or $+1$, which correspond to the logic 0 and 1. In Figure 1a the behavior of such a unit is presented. As one can see from Figure 1b, if the input signal is negative the p-bit will most likely assume the -1 state, if it is positive the $+1$ state, If the input signal is small, the result will be random.

The input signal of each unit depends on the relations between the circuit's p-bits and their state at the time of updating. The equation that controls this process is

$$I_i(t) = I_0\left(h_i(t) + \sum_j J_{ij}m_j(t)\right) , \quad (2)$$

where I_0 is scaling coefficient that establishes the overall strength of the interactions and acts as an inverse temperature, h_i is the bias of p-bit i and J_{ij} is the interaction between p-bit j and p-bit i. Each circuit has its own J interaction matrix and h bias vector that characterize the evolution of the state of the system. The update algorithm is asynchronous, meaning that p-bits will be updated randomly and sequentially, each time using the

updated m state vector in the calculation of the new input signal through the use of Eq. 2.
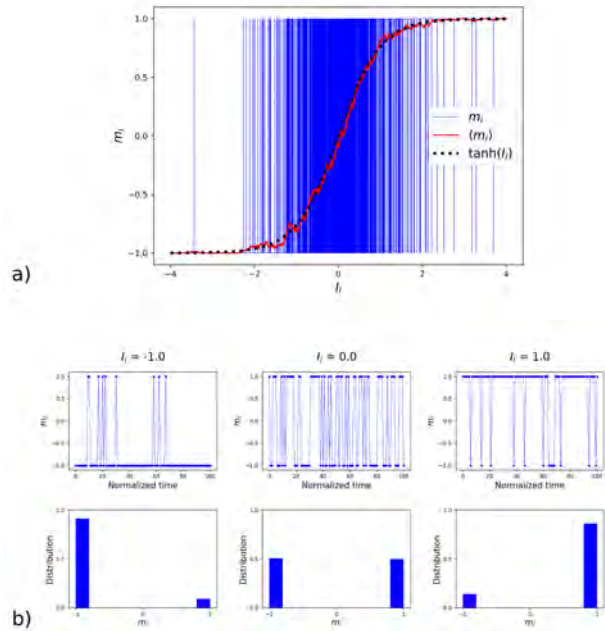
Figure 1: *Behavior of a p-bit state as a function of the input signal; in a) it is shown how the averaged value of this base unit is almost identical to an hyperbolic tangent; in b) the state of the p-bit is shown as a function of time with various values of the input signal, with an histogram that shows the probability distribution of the state*

Invertible AND gate

To show a minimal example of probabilistic computing novel features, it is useful to consider a standard logic gate implemented in PSL logic. The interaction matrix J and the bias vector h of an AND gate ($A \wedge B = C$) are the following:

$$J_{AND} = \begin{bmatrix} 0 & -1 & +2 \\ -1 & 0 & +2 \\ +2 & +2 & 0 \end{bmatrix} , \quad h_{AND} = \begin{bmatrix} +1 \\ +1 \\ -2 \end{bmatrix} . \quad (3)$$

It is interesting to highlight how all the elements of the main diagonal of the matrix are 0. This is because those elements would represent self-interactions and, as such, would have a constant energy contribution to the total energy and can be simplified out of the equation. In Figure 2 the behavior of the AND gate with different bits clamped is shown. While clamping the input bits, the system behaves identically to a normal logic gate, whereas, with the output clamped instead, the input bits explore all the states compatible with that output with equal probability while neglecting the ones that don't.

Figure 2: *Reversible AND gate operated in reverse mode; in a) the output bit clamped to 0, so the corresponding p-bit has $m = -1$; the compatible states (00, 01 and 10) are equally probable, the non-compatible is less represented; it sho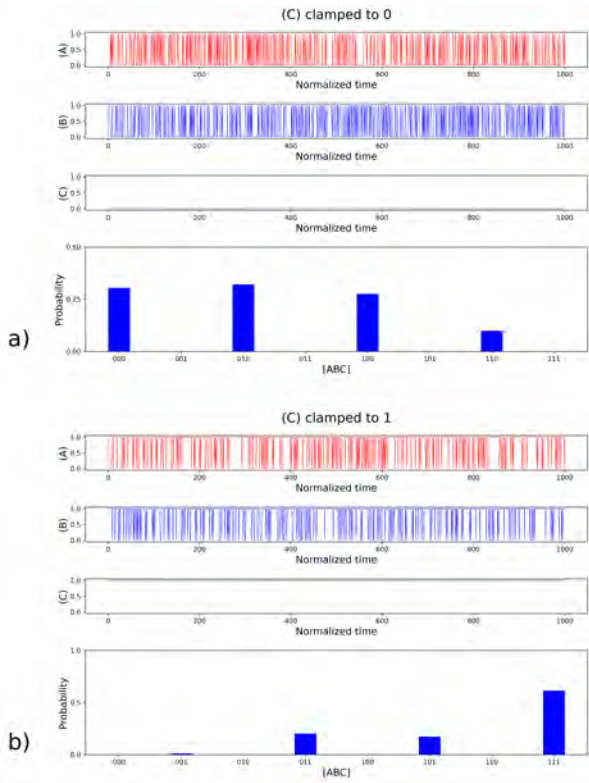uld be noted that with a higher I_0 the incompatible state would be even less probable; in b) the same gate has its output bit clamped to 1; in this case, the only compatible state is 11, which is by far the one more frequently explored*

Connection of circuital components

A PSL circuit has a single interaction matrix that represents how the p-bits of the whole system interact with each other, meaning that even in presence of more that one circuital component there is still only one interaction matrix.
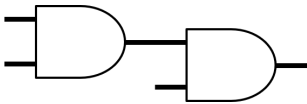

Figure 3: *Two AND gates connected; the output C of the left gate and the input A of the right gate are the same bit*

The way connection are represented can be clarified with and example: let us consider a simple circuit as the one shown in Figure 3. Each AND gate has an interaction matrix and bias vector identical to Eq.3. In addition to that, the C output bit of the first AND gate is strongly correlated to the A input bit of the second. In fact, they are the same bit. That can be thought as an interaction with infinite strength, obtaining

$$
\begin{aligned}
J_{tot} &= \begin{bmatrix}
0 & -1 & +2 & 0 & 0 & 0 \\
-1 & 0 & +2 & 0 & 0 & 0 \\
+2 & +2 & 0 & J_{link} & 0 & 0 \\
0 & 0 & J_{link} & 0 & -1 & +2 \\
0 & 0 & 0 & -1 & 0 & +2 \\
0 & 0 & 0 & +2 & +2 & 0
\end{bmatrix} \\
&= \begin{bmatrix}
0 & -1 & +2 & 0 & 0 \\
-1 & 0 & +2 & 0 & 0 \\
+2 & +2 & 0 & -1 & +2 \\
0 & 0 & -1 & 0 & +2 \\
0 & 0 & +2 & +2 & 0
\end{bmatrix} \, ,
\end{aligned}
\tag{4}
$$

where the columns and rows of the connected bits were added together and the interaction J_{link} is removed. This is justified by the fact that, because those bits represent the same logical bit, the interaction can be thought as a self-interaction, which would be a constant term and can thus be neglected.

Results and Discussion

The implementation of factorization circuit in PSL is a simple multiplier circuit operated in reverse. In Figure 4a, the circuit scheme for a 4-bit multiplier is shown. In Figure 4b the J matrix of such a system is shown graphically. As one can see, the matrix is very sparse as most p-bits interact with only a handful of close p-bits.

To operate the circuit, the output bits need to be clamped to represent the number to factorize, for example 35, a co-prime whose factor are 5 and 7. Then, the system is evolved with an increasing value of the inverse temperature coefficient I_0, in a process called annealing, shown in Figure 4c.

When I_0 is close to 0, that is when the temperature is very high, the system explore all the states with equal probability, completely disregarding interactions and bias. The system exhibit gas-like or liquid-like behavior. When I_0 increases, meaning that the temperature is lowering, the system undergoes a process that resembles phase transition, in particular crystallization. The interactions become stronger and constrain the state of the system to only explore states compatible to the circuit logic. In the case of factorization, the only allowed states are the one that result in the input bits representing the factors of the number to factorize.

This method manages to consistently guess the correct solution up to 3901 and, with the use of different annealing regimes or other evolution algorithms that mainly act on the I_0 parameter, it can be further improved.
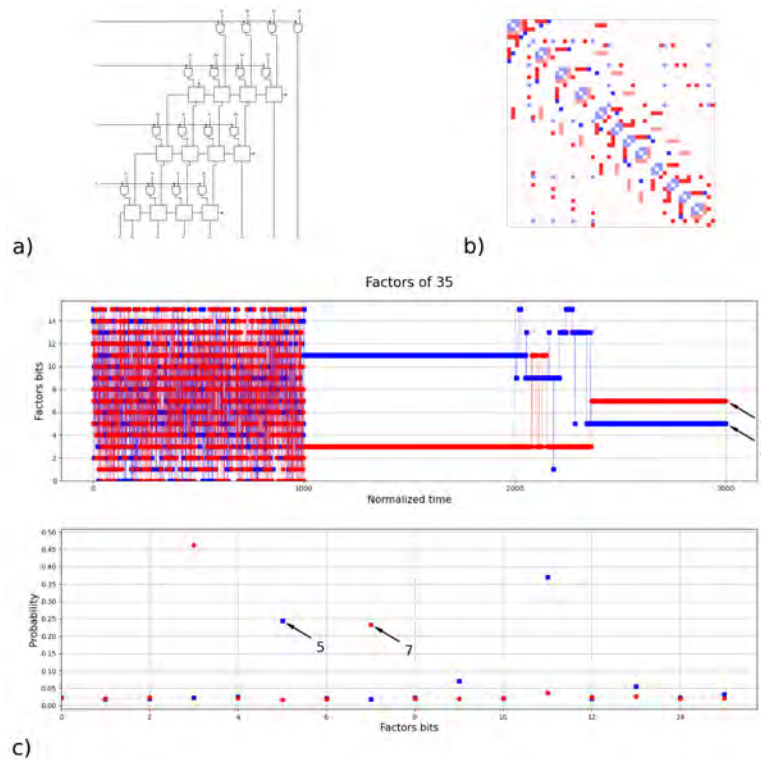
Figure 4: *4-bit multiplier/factorization; in a) the scheme of the circuit is shown; the square elements are full adders while the semi-circular ones are AND gates; in b) the J interaction matrix of the circuit is pictorially represented; red elements are positive while blue ones are negative; c) the factorization annealing process of 35 is shown; the system starts at a high temperature, exploring all states with equal probability; while cooling it falls into a plausible local minima ($3 \times 11 = 33$, which is rather close to 35) and finally, when the low temperature causes the system to be unstable in its current configuration, the state jumps to the correct solution*

Conclusions

Probabilistic computing, along with PSL, is a promising field that has the potential to be applied to many computational problems. A micro-magnetic dynamics approach to the same problem is currently in development and could potentially increase the maximum solvable number while also allowing the use of parallelization to speed up the calculation.

References

[1] W. M. Kaminsky and S. Lloyd: *Scalable Architecture for Adiabatic Quantum Computing of Np-Hard Problems*. in "Quantum Computing and Quantum Bits in Mesoscopic Systems", 229–236, 2004.

[2] G. Finocchio et al.: *The promise of spintronics for unconventional computing*. Journal of Magnetism and Magnetic Materials, **521**, 167506 (2021).

[3] F. L. Traversa and M. Di Ventra: *Polynomial-time solution of prime factorization and NP-complete problems with digital memcomputing machines*. Chaos, **27**, 023107 (2017).

[4] K. Y. Camsari et al.: *Stochastic p-bits for invertible logic*. Physical Review X, **7**, 031014 (2017).

[5] R. Faria, K. Y. Camsari, and S. Datta: *Low-Barrier Nanomagnets as p-Bits for Spin Logic*. IEEE Magnetics Letters, **8**, 1-5 (2017).

[6] K. Y. Camsari, S. Salahuddin, and S. Datta: *Implementing p-bits with Embedded MTJ*. IEEE Electron Device Letters, **38**, 1767–1770 (2017).

[7] J. Cai et al.: *Voltage-Controlled Spintronic Stochastic Neuron Based on a Magnetic Tunnel Junction*. Physical Review Applied, **11**, 034015 (2019).

[8] W. A. Borders et al.: *Integer factorization using stochastic magnetic tunnel junctions*. Nature, **573**, 390–393 (2019).

Metal-Oxide-Metal (MOM) Capacitors for Integrated Circuits (ICs) in BCD Technology: an Overview

G. Malta[1−2*], F. Gabriele Campisi[2], G. Romano[2], S. Patanè[1]

[1] *Dipartimento di Scienze Matematiche e Informatiche, Scienze Fisiche e Scienze della Terra,*
 Università degli Studi di Messina, Messina, Italia
[2] *ST Microelectronics S.r.l., Stradale Primosole, 50, 95125 Catania*

[*]Corresponding Author email: giumalta@unime.it

Abstract

In this work an overview of the current methodologies used for the detection and characterization of defects in Metal-Oxide-Metal (MOM) capacitors, for Integrated Circuits (ICs) applications, is presented. Structural characteristics and electrical performances exhibited by MOM structures will be first addressed, together with a brief description of the architectural geometries currently available. In particular, optical tecniques aimed at achiving a first evaluation of position of such inhomogeneities are first discussed. After that, well-established approaches for their elemental characterization will be taken into account. Since the presence of impurities usually causes reliability rejects of the final product, the manufacturing of high-performance power semiconductor devices is of paramount importance. However, no electrical test able to highlight the presence of inhomogeneities is currently available. In this sense, the potentiality of the scanning acoustic microscopy (SAM) as novel approach for the detection of in-depth defectes, otherwise impossible to reveal, will be proposed.

Keywords: Metal-oxide-metal (MOM) capacitors, Integrated circuits, Capacitors, Impurities, Elemental characterization, Scanning acoustic microscopy (SAM).

Introduction

Integrated circuits (ICs) are high-density devices composed of active (transistors, diodes, etc.) and passive elements (resistors, capacitors, etc.) spatially-arranged in a single layer of silicon semiconductor (*wafer*). The first prototype of IC was developed in 1958 by Jack St. Clair Kilby, for which he was awarded with the Nobel Prize in 2000. Nowadays, analog integrated circuits (AICs) employ three different types of capacitors based on MOS (p-n junction), MIM (metal-insulator-metal) and MOM (metal-oxide-metal) structures. Although characterized by high capacitance density per unit area, MOS junctions are not suitable for all ICs applications, due to their low breakdown voltage and non-linear response. Hence, many efforts have been devoted to the optimization of MOM and MIM structures, with the aim to overcome the aforementioned MOS issues [1, 2].

However, due to lower production costs and higher capacitance density with respect to MIM components, MOM capacitors became popular for the manufacturing of power semiconductor devices. In this work we report the state-of-art about MOM capacitors, together with a description of some of their known applications in Bipolar-Cmos-Dmos (BCD) technology.

MOM capacitor consists of multiple lateral capacitive units made up of metal layers (MT) separated from each other by oxide layers (OL). Each MTs are put in contact through tungsten *vias*, forming the so-called *strips* (see Fig. 1).
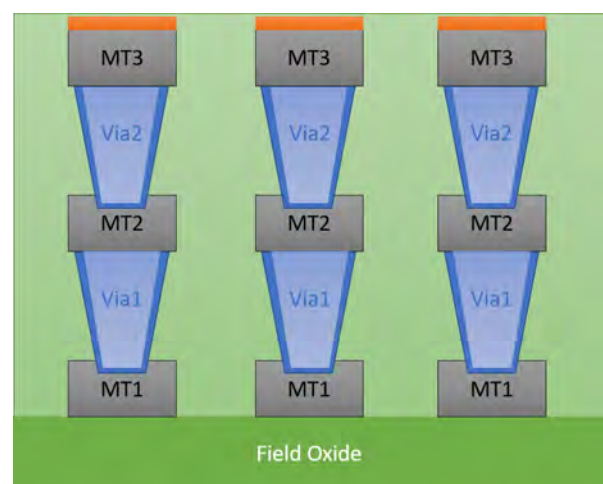

Figure 1: *Frontal view of a MOM capacitor. Dark grey boxes (MT1, MT2,...) account for metal layers separated from each other by oxide layers (green area). Metal layers are contacted by means of tungsten vias (Via1, Via2,...).*

The lateral intra-layer coupling furnishes better matching properties than vertical geometries, thanks to the enhanced processing control of lateral dimensions. In order to optimize the capacitance per unit area, a minimum spacing between each conductive layer must be achieved. In this sense, different types of MOM architectures have been developed (parallel stacked wires, interdigitated parallel wires, woven and vertical bars MOMs, see Fig. 2 for details) in order to obtain high capacitance density (up to ∼2 fF/μm^2) and low parasitic capacitance with a relatively low production cost [3, 4].
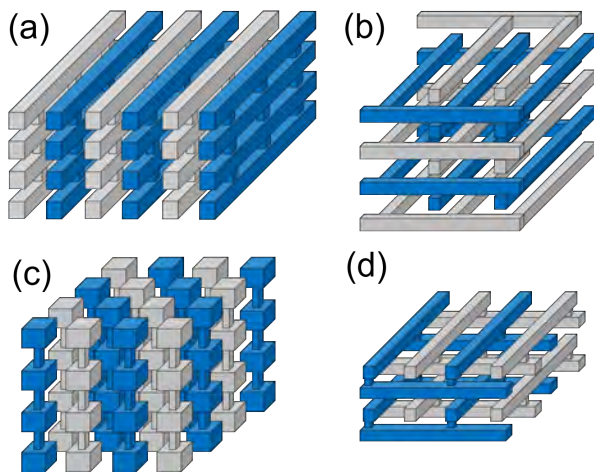

Figure 2: *Schematic representation of the parallel stacked wires (a), interdigitated parallel wires (b), woven (c) and vertical bars (d) MOM architecture. Blue and grey strips account for positive and negative conductors, respectively.*

In the emerging field of ICs, MOM structures represent a fundamental building-block for the engineering of devices built on silicon substrates. However, because of their extremely small size, the presence of defects included during a specific step of the production flow can lead to electric failures. Generally, although most of them can be properly screened through parametric tests and *electrical wafer sorting* (EWS), some of these elude such standard electrical tests, causing unwanted reliability failures. In this framework, the development of novel approaches (based on electrical, optical, and spectroscopic techniques) able to properly detect the presence of impurities such us metal flakes, polymeric residues and structural inhomogeneities, represents a key point for the enhancing of the final device reliability. In this work, a brief overview of the existing methodologies adopted for the investigation of MOM structures will be addressed, with particular regard to the current techniques used for the detection and characterization of top, bottom and inter-strip defects.

Current methodologies for MOM analysis

Optical and electron-based techniques

Generally speaking, optical and scanning electron microscopy (OM and SEM, respectively) represent well-established approaches for the evaluation of defect localization in semiconductor devices. In this frame the OM allows to detect the defects on the metal surface. Buried defects can be observed too but only inside the oxide layers as in these the light can travel inside. In any case, the OM resolution is intrinsically limited due to the diffraction of visible light if no special trick are used. Being defects of interest (DOI) in MOM capacitors of the order of 1-2 μm, shape and conformation cannot be easily determined through OM analyses, due to intrinsic limitations of the used probe.

High-resolution images can be obtained by using SEM, allowing the observation of defects/particles having dimensions down to tens of nanometres. A common SEM inspection system for ICs applications is developed in such a way to review and classify defects on a processed silicon wafer. Undesirable metallic or polymeric components are magnified thanks to a post-processing analysis which involves the use of at least two different images, one associated to the defect-containing die and one used as reference. This approach become mandatory since defect locations in semiconductor devices can not always be accomplished by using the image position information alone, due to different errors affecting each measurements (see Fig. 3).
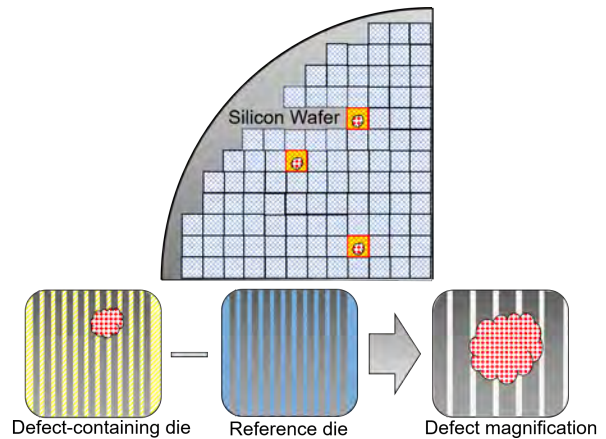
Figure 3: *Example of defect magnification obtained by post-processing analysis involving the use of two die with and without a defect.*

The main limitation of such technique relies in the fact that information are limited to the superficial layer of the investigated material. Hence, small impurities located at the bottom of the metal layer and/or embedded within the strips of the MOM capacitor are extremely difficult to detect/characterize. However, depending on their dimension, such in-depth impurities can affect the overlying

surface, resulting in a detectable superficial inhomogeneity. Moreover, underlying defects, having dimension less than the distance between two adjacent strips, and localized at different focal planes, do not provide sufficient optical signal to be revealed. In this case, such impurities can still be sceened through electrical tests. For this purpose, EWS and *burn-in* are usually accomplished with the aim to induce, under controlled conditions, preventive failure allowing to properly distinguish damaged components.

The increasing miniaturization of electronic devices, however, demanded the development of analytical tools having higher resolutions. In this framework, once defects are localized by means of the aforementioned techniques, more detailed analyses are usually assessed. Specifically, Transmission Electron Microscopy (TEM) on ultrathin sections of wafers can be used to reveal the exact position where DOIs develop. Accordingly, sample is positioned along an electron beam which is produced, accelerated and focused by means of electromagnetic lenses. The reduced thickness of the specimen allows electrons to pass through the surface following electron/sample interactions. Then, transmitted electrons are focused on an imaging device, such as fluorescent screens or charge-coupled devices (CCD), producing a magnified image. In this way it is possible to highlight the specific phase of the industrial flow which causes the injection of unwanted components.

Scanning Acoustic Microscopy (SAM)

Nowadays, the evaluation of structural cracks, delamination and voids in ICs semiconductor devices can be also accomplished by the Scanning Acoustic Microscopy (SAM) technique. Generally speaking, SAM microscopes utilize acoustic waves as probe in order to achieve information about material structural properties. With the aim to determine positions of unknown defects (organic or inorganic) placed between strips or at the bottom of metal layers, SAM tools can be employed by setting up suitable work conditions. SAM exploits the interaction of a specimen with a focused ultrasonic wave, which during its propagation through the sample undergo attenuation (absorption) and scattering phenomena due to the presence of acoustic impedance Z discontinuities ($Z = \rho c$, with ρ and c equal to the density of the medium and the acoustic wave speed, respectively). When an high-frequency acoustic wave encounters an interface between layers characterized by different Z (Z_1 and Z_2, for example), partial transmission/reflection is also likely to occur. The exact portion of the back-reflected amplitude can be calculated by the reflection coefficient, R, equal to:

$$R = \frac{|Z_2 - Z_1|}{Z_2 + Z_1} \qquad (1)$$

The higher is the difference between the Z values at the interface, the higher the intensity of the scattered signal will be. In addition, the time needed by the wave to travel back and forth is also an important parameter in order to correctly evaluate the depth d (location) of a specific defect in the bulk. Besides measuring the intensity

of the reflected sound wave, the time needed for the detection of the back-reflected wave (echo) is also captured and displayed in the so-called *A-scan*. Then, information about the depth (location), d, of a potential defect in the material bulk can be found as:

$$d = \frac{t^* c}{2} \qquad (2)$$

where t^* and c are the measurable time of flight and sound speed, respectively (see Fig. 4 for details). The division by 2 accounts for the back and forth path of the sound wave from and to the SAM transducer.
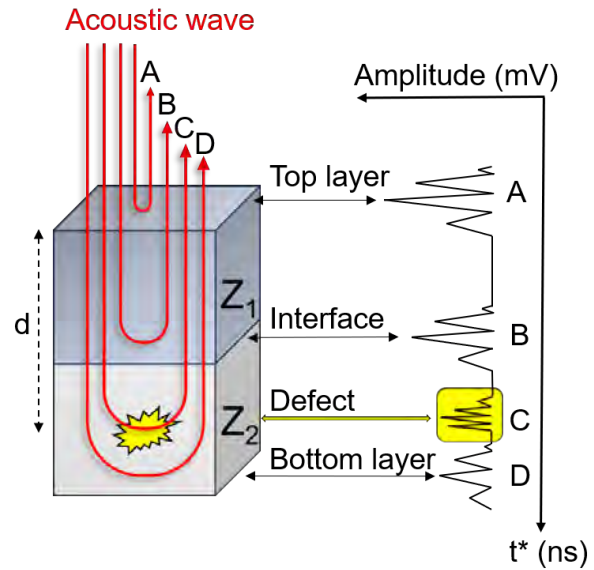
Figure 4: *Schematic representation of an A-scan on a double-phases (Z_1 and Z_2) defect-containing material. The high-frequency acoustic wave travels (red line) through the investigated sample and partial back-scattered reflections (echoes) due to the presence of interfaces occur (A, B, C and D).*

Since the spatial resolution of such instrument is related to the frequency of the incoming acoustic wave, the detection of defects having dimension of the order of 1-2 μm requires the employment of GHz-waves. However, the use of GHz-waves strongly reduces the probe-sample working distance down to 60 μm, thus representing a first important limitation due to the fact that samples must always be immersed within a liquid medium.

The next step of a MOM failure analysis involves the chemical characterization of the detected impurities. In this context, Energy Dispersive X-ray (EDX) analysis and Scanning *Auger* Electron spectrometry (AES) are usually applied with the aim to determine the elemental composition of unwanted components. in the next section, a brief overview of the aforementioned techniques is addressed.

Chemical techniques

The Energy Dispersive X-ray (EDX) analysis is a powerful technique for the evaluation of the elemental compo-

sition in specimens (in our case the defect). It is usually coupled with electron microscopy and it is based on the generation of characteristic X-rays following primary/atomic electron interactions occurring within the first 1-3 μm from the topmost layer.

Such methodology allows to distinguish inorganic/organic components starting from the evaluation of their characteristic elements providing, at the same time, information on their origin and cause [5]. In Fig. 5 a SEM-EDX analysis of a defect located on a wafer used in BCD technology is reported, as example.

Figure 5: *SEM-EDX spectrum of a detected impurity (yellow filled area) on a silicon-based wafer. The aforementioned profile is superimposed to a reference one (red line) collected on the die. In the inset, a SEM image displaying both the defect (yellow filled dot) and substrate (red filled dot) is also shown [5].*
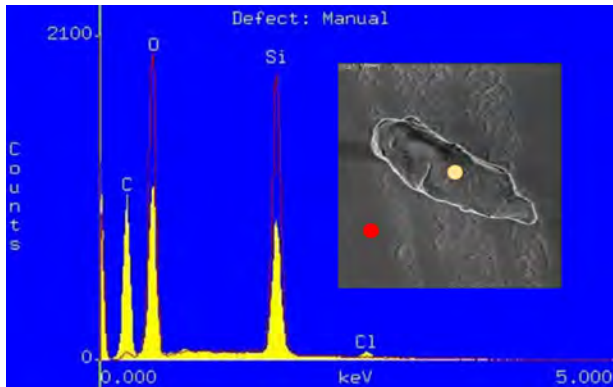
A comparison between the defect/substrate EDX spectra (yellow area and red line of Fig. 5, respectively) reveals a significant difference in carbon (C), oxygen (O) and silicon (Si) content. In particular, in the defect spectrum, a remarkable increase of C can be clearly observed, in conjunction with a reduction of both O and Si amount. This occurrence highlight the presence of an organic carbon-based impurity located at the top of the MOM layer. In addition, the presence of small amount of chlorine (Cl), as revealed by the low-intensity signal at ~2.6 keV, can furnish useful indication of the specific productive phase responsible of the impurity addition.

Similar information can be obtained by means of Scanning *Auger* Electron spectrometry (AES). In this case, a focused electron beam (3-20 keV) scans across the sample ($\leq$0.1 μm) thus ionizing atoms embedded within the first five atomic monolayers of the material. Metastable species occur, which immediately relax through *Auger* processes. *Auger* electrons are pulled off from the surface and revealed by the spectrometer which measure their kinetic energy distribution. The average depth of analysis for an AES measurement is approximately 5×10^{-3} μm. As shown in Fig. 6, depending on the energy and type of probe/sample interaction, the aforementioned techniques provide the elemental identification of defect located at different depth below the topmost MOM layer.
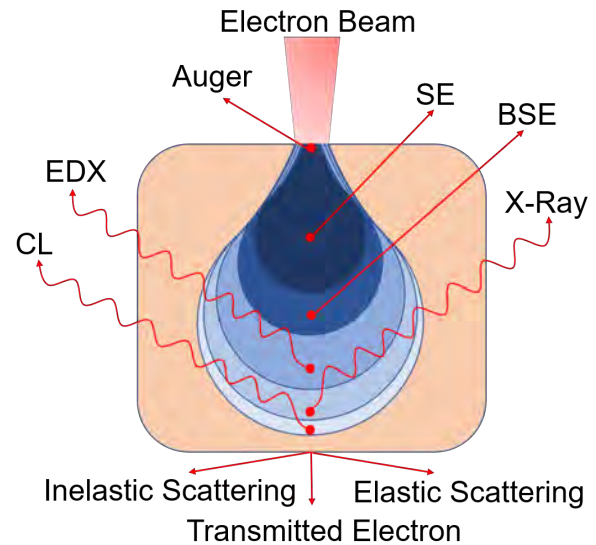
Figure 6: *Representation of the possible outcomes following electron/sample interactions. Moving towards deeper sample depths Auger electrons (surface sensitive), secondary electrons (SE), back-scattered electrons (BSE), EDX, X-rays and cathodoluminescence (CL), can be observed.*

Optimization of both EDX and AES is achieved by cutting in half the defect by means of the Focused Ion Beam (FIB) methodology. FIB instruments, generally coupled with a SEM microscope, produce a focused beam of ions (usually gallium) that can be operated at both low and high beam currents for imaging and/or site specific sputtering (or milling), respectively. For MOM defect analysis, the FIB process allows the etching of the first atom layer in such a way to keep the underlying ones unaltered. In this way, embedded impurities below 5 μm from the top layer can be characterized, despite both EDX and AES are two surface techniques.

Conclusions

In this work, an overview of the current techniques used for the evaluation of locations and elemental composition of defects in MOM structures, is presented. Nowadays, the fast and accurate detection and characterization of spurious components represent a hot-topic in the field of integrated circuits. The general aim is to reduce the amount of DOI within MOM capacitors in order to enhance the final device reliability, and suggest new methodologies for defects screening based on their elemental/molecular composition. Finally, it is worth underlying that the development of novel software based on the "machine-learning" algorithms capable to classifying defects automatically represents also a step forward for a fast and reliable analysis of in-line failures.

References

[1] Hu, H., Zhu, C., Lu, Y., Li, M., Cho, B., Choi, W.: *A high performance MIM capacitor sing HfO2 dielectrics*. IEEE Electr. Dev. Lett., **23**(9), 514-516 (2002).

[2] Kim, J., Plouchart, J., Zamdmer, N., Sherony, M., Lu, L.-H., Tan, Y., Yoon, M., Jenkins, K., Kumar, M., Ray, A., Wagner, L.: *3-dimensional vertical parallel plate capacitors in an SOI CMOS technology for integrated RF circuits*. VLSI Circuits Dig. Tech. Papers, 29–32 (2003).

[3] Liu, C. C., Chang, S. J., Huang, G. Y., Lin, Y. Z.: *A 10-bit 50-MS/s SAR ADC with a monotonic capacitor switching procedure*. IEEE JSSC, **45**(4), 731–740 (2010).

[4] Chen, N.-C., Chou, P.-Y., Graeb, H., Lin, M. P.-H.: *High-Density MOM Capacitor Array with Novel Mortise-Tenon Structure for Low-Power SAR ADC*. IEEE Design, Automation & Test in Europe Conference & Exhibition, 1757–1762 (2017).

[5] Porat, R., Dotan, K., Hemar, S., Levin, L., Li, K., Sung, G., Lin, C.-T., Lin, S.-K., Wang, H.-I.: *SEM-based methodology for root cause analysis of wafer edge and bevel defects*. IEEE/SEMI Advanced Semiconductor Manufacturing Conference, 11–14 (2008).

Dynamical detection of ultrastrong light-matter interaction: an open quantum system approach

F. Mauceri[1,2,*]

[1]*Dipartimento di Scienze Matematiche e Informatiche, Scienze Fisiche e Scienze della Terra, Università di Messina, Messina, Italy.*

[2]*Centro Siciliano di Fisica Nucleare e Struttura della Materia, Viale A. Doria 6, 95125 Catania, Italy.*

*Corresponding Author email: fabio.mauceri@unime.it

Abstract

The aim of this work was to prove that a dynamical detection of Ultra Strong Coupling (USC) regime is possible through STIRAP. This would offer some advantages over traditional protocols: for example compared to traditional spectroscopy, STIRAP manages to transfer population in a highly efficient and selective way, which is very useful for USC systems. However, the evolution of the system is complicated by the interaction with the environment. The formalism of the density matrix is then used to study its dynamics, solving a master equation (ME).

Keywords: USC, Cavity-QED, STIRAP, Master Equation.

Background

The strength of the light-matter interaction is fixed by nature through the fine structure constant α. In 1946, Purcell [1] discovered that the interaction strength of an oscillator with light can be increased or decreased by changing the electromagnetic conditions of the environment in which it is located. From this discovery, a whole field of research was born called cavity quantum electrodynamics (Cavity-QED), where the natural coupling constant is replaced by a coupling constant g that quantifies the strength of interaction between light and matter. An important regime is the Strong Coupling (SC) obtained when the coupling strength is bigger than the losses of the system. Dividing g by the cavity frequency ω_c, the dimensionless parameter $\eta = g/\omega_c$ is obtained, and it is commonly stated that the Ultra Strong Coupling (USC), another regime of light-matter interaction, is achieved when $0.1 < \eta < 1$. The parameter η allows us to determine if the perturbation theory can be used and which approximation can be made in the light-matter interaction. In particular, the SC regime can be described through the Jaynes-Cummings model, while the USC by the Rabi model. An interesting property of the USC is that the ground state does not conserve the number of excitations and it contains virtual excitations. This means that the ground state is a superposition of states with different number of excitations.

Fig. 1 shows a microwave spectroscopy of a system with a superconducting flux qubit coupled to a coplanar-waveguide resonator [2]. The system displays a normalized coupling strength $\eta = g/\omega_c = 0.12$. The plot shows the cavity transmission as a function of probe frequency ω_{probe} and flux offset, which tunes the qubit frequency. The avoided level crossing indicates a coupling between states with different numbers of excitations (one state has a single photon in the third resonator mode; the other state has one qubit excitation and one photon in the first resonator mode). Such a coupling requires the so called counter-rotating terms and is not reproduced by the Jaynes-Cummings approximation. The USC regime can improve the performance of already existing devices built in the SC regime [3], and even open new areas of research since some effects cannot be seen outside of this regime. This allows for suitable applications, such as the realization of new kind of quantum gates on specific short life time system [4][5][6], to some theoretical one as the emergence of new phenomena, such as quantum phase transition.
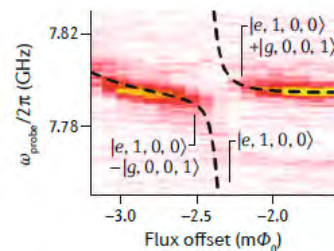

Figure 1: *Avoided level crossing typical of USC.*

Coherent amplification

SEP - Spontaneous Emission Pumping

Spontaneous Emission Pumping (SEP) represents the easiest way to probe the light-matter interaction. For instance, by exciting the interacting systems with a co-

herent probe at a given frequency, it is possible to detect output signals also at different frequencies, certifying the existence of an interaction channel responsible for such a transition. In particular, such a channel can be a benchmark for the existence of USC regime.
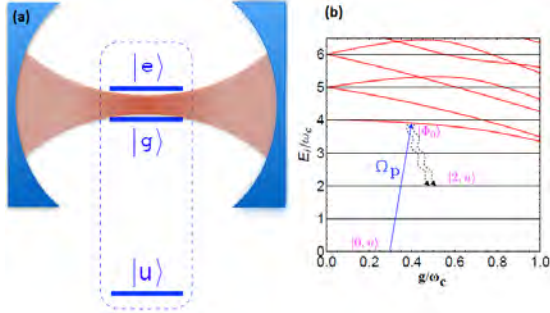

Figure 2: *(a) Schematic representation of a three level atom interacting with an optically confined mode. (b) Level scheme of H_{sys} as function of g/ω_c, for $\omega_c = \omega_{\text{eg}}$ and $\omega_{\text{gu}} = 4\omega_{\text{eg}}$. The blue arrow represents the drive frequency ω_p, resonant with the transition $|0, u\rangle \rightarrow |\Phi_0\rangle$. In USC the state $|\Phi_0\rangle$ has a component on the state $|2, u\rangle$, thus a detection of two photons is a benchmark of the USC itself. Such a photon pair detection is allowed via decay from the optical mode.*

In [7] it was proposed that population pumped from $|0, u\rangle$ to $|\Phi_0\rangle$ may decay in $|2, u\rangle$, due to the finite overlap $c_{02} := \langle 2, u | \Phi_0 \rangle \neq 0$, with $c_{02}(g)$ coefficient of the Rabi eigenstate

$$|\Phi_0\rangle = \sum_{n=0}^{\infty} [c_{0,2n}|2n, g\rangle + d_{0,2n+1}|2n+1, e\rangle] \qquad (1)$$

The process is forbidden in the Jaynes-Cummings limit, hence detection of this channel, uniquely leaving two photons in the mode, unveils USC, as shown in [7]. However SEP would have very low yield, since in most of the present implementations of USC architectures c_{02} is not large enough. Therefore, is introduced a coherent drive able to populate efficiently the final states, see Fig. 2 (b). Additionally, if a finite temperature is considered, the relevant states might be occupied from the thermal excitation, generating noise that can be comparable with the signal.
The Hamiltonian of a three levels atom coupled to an electromagnetic field in a cavity (Fig. 2 (a)), as given by the Rabi model, is:

$$H_{\text{sys}} = H_0 + g(a + a^\dagger)(|g\rangle\langle e| + |e\rangle\langle g|) \qquad (2)$$

where $H_0 = \omega_c a^\dagger a + \omega_u |u\rangle\langle u| + \omega_g |g\rangle\langle g| + \omega_e |e\rangle\langle e|$ is the Hamiltonian of the uncoupled subsystems, $|u\rangle, |g\rangle$ and $|e\rangle$ are the atomic levels of the uncoupled atom, $a^\dagger$ and a are the creation and annihilation operator for the cavity field, while $|n\rangle\langle m|$, are the atomic transition operators. For sake of simplicity, we define $\omega_u = 0$, $\omega_{\text{gu}} = \omega_g - \omega_u = \omega_g$

and $\omega_c = \omega_e - \omega_g$, meaning that the $|e\rangle \rightarrow |g\rangle$ transition is resonant with the cavity mode.
By adding to H_{sys} the driving term $H_{drive} = \Omega_0 \cos(\omega_p t)(|g\rangle\langle u| + |u\rangle\langle g|)$, we can bring excitations from $|0, u\rangle$ to $|\Phi_0\rangle$. Being $\gamma_{1,5}$ the decay rate between states $|0, u\rangle$ and $|\Phi_0\rangle$, and considering the case of weak pumping regime, i.e. $\Omega_0 \ll \gamma_{1,5} \ll \omega_{\text{gu}}$, we can calculate analytically the population of state $|\Phi_0\rangle$, $P_{|\Phi_0\rangle} = (\Omega_0/\gamma_{1,5})^2$. From this result, it is straightforward to find the population (see [5]) of the state $|2, u\rangle$, namely $P_{|2,u\rangle}$.

$$P_{|2,u\rangle} = \frac{\gamma_{3,5}^{(0)}}{2\kappa} |c_{02}(g)|^2 (\Omega_0/\gamma_{1,5})^2 \qquad (3)$$

with κ cavity losses. We can define the SEP efficiency as the population brought from $|\Phi_0\rangle$ to $|2, u\rangle$, i.e.

$$\eta_{SEP} = \frac{P_{|2,u\rangle}}{P_{|\Phi_0\rangle}} = \frac{\gamma_{3,5}^{(0)}}{2\kappa} |c_{02}(g)|^2 \qquad (4)$$

It is also possible to obtain these results from a rate equation derived from the Master Equation (M.E.).
Restricting the subspace of the optical mode to the first three Fock states, we can calculate the mean photon number as $\langle a^\dagger a \rangle = \text{Tr}[a^\dagger a \rho_{ss}]$, and we easily get $\langle a^\dagger a \rangle = \rho_{2,2} + 2\rho_{3,3}$, where $\rho_{3,3}$ is nothing but the equation (3), and at the steady-state $\rho_{2,2} = 2\rho_{3,3}$. Finally, we obtain

$$\langle a^\dagger a \rangle = \frac{2\gamma_{3,5}^{(0)}}{\kappa} |c_{02}(g)|^2 (\Omega_0/\gamma_{1,5})^2 \qquad (5)$$

From equation (3), we can calculate the output photon flux, by applying the input-output theory [9] to the optical mode channel, obtaining:

$$\langle n \rangle_{\text{out}} = \kappa \times \langle a^\dagger a \rangle = 2\gamma_{3,5}^{(0)} |c_{02}(g)|^2 (\Omega_0/\gamma_{1,5})^2 \qquad (6)$$

In order to evaluate the maximal photon flux ($\langle n \rangle_{\text{out}}$) for SEP, we impose that the transition $|0, u\rangle \rightarrow |\Phi_0\rangle$ is saturated, i.e. $(\Omega_0/\gamma_{1,5})^2 = 1/2$, and we put $\gamma_{3,5}^{(0)} = \gamma_{1,5} = 10^{-4} \times \omega_c$, $\kappa = 10^{-4} \times \omega_c$, $g = 0.5 \times \omega_c$, and $\omega_c = 6\,\text{GHz}$, quite a reasonable set of physical parameters for state-of-art circuit QED. Although we imposed a regime of saturation in order to maximize the effect of SEP, we obtain (at T=0 k) $\langle n \rangle_{\text{out}} \simeq 5.2 \times 10^3$ photons per second, that is a quite disappointing result.
By increasing Ω_0 we can enhance the number of photons emitted per second, but we lose the ability to solve the system analytically.

STIRAP amplification

A protocol based on STIRAP [8] can increase the number of emitted photons, allowing a reliable detection method even with thermal noise, since it can selectively addresses the target state with $\sim 100\%$ efficiency. A key issue is that STIRAP requires g large enough to guarantee adiabaticity for the Stokes pulse, as shown in [5], where the authors found that this (soft) threshold depends linearly on $c_{02}(g)$, whereas the efficiency in SEP is much smaller, depending on $|c_{02}(g)|^2$ ($\propto g^4$ for small g). The idea is to exploit such a method to detect the USC regime in a three level atom (the minimal model for STIRAP) coupled to a single mode optical resonator.

STIRAP uses pulses to bring the population to its target state ($|2, u\rangle$), then the lossy cavity will bring photons outside, allowing photodetection, so that the state at the end of the protocol will be the ground state ($|0, u\rangle$). Thus the maximum photons output that a single STIRAP cycle can achieve is 2 (excluding thermal photons). So, to get a efficient photon current, one needs to repeat the protocol many times. In other words, we expect to create a target state, then wait until the system decays reaching its equilibrium, and after this reset, we start again. The cycle time, $t_f - t_i$, takes into account the temporal length of STIRAP plus the relaxation time.

However, there is a tradeoff, because if we increase the decay rate for the optical mode, we get more photons per second, but on the other side we reduce the efficiency of STIRAP, as part of the population gets lost during the protocol before it reaches the target state.

Since ideal STIRAP does not populate $|\Phi_0\rangle$, we need to modify the definition of the efficiency η from (4). For STIRAP the efficiency is the population brought to $|2, u\rangle$:

$$\eta_{STIRAP} = P_{|2,u\rangle} \tag{7}$$

Analysis for an ideal system at temperature $T = 0$ K, without losses, shows that for coupling strength $g/\omega_c \leqslant 0.5$ the ideal efficiency for STIRAP is at least 2 order of magnitude larger than the SEP's. However, it has to be stressed that this is just the efficiency in creating the target state $|2, u\rangle$ for a system without losses. Since we are interested in the photons output of the system, we need to introduce losses and that can decrease the STIRAP efficiency up to the point that it will no longer work, because we have lost adiabaticity.

We discuss photodetection in this system, based on the simplest scheme of measuring photons leaking from the cavity. It is a destructive measurement, reliable in the case where an open quantum system has a non-negligible leakage into the external detection channel, namely the cavity quality factor is not too large, but this reduces the coherent amplification effect, thus we have a trade off.

Dynamics and second order correlation function

Since we are interested in measuring the photons leaking the cavity, we need to analyze an open system. This can be problematic since we also have to follow the dynamics of the environment. To solve this problem we use a density matrix approach, that allows us to ignore the infinite degrees of freedom of the environment with a procedure called "tracing out". We follow the dynamics of the system with a master equation, in particular the Redfield form:

$$\begin{aligned} \dot{\rho}(t) = {}& -i[H, \rho(t)] \\ & + \sum_{j,k>j} \Gamma^{jk} N(\epsilon_j, \epsilon_k, T) \mathcal{D}[|k\rangle\langle j|]\rho(t) \\ & + \sum_{j,k>j} \Gamma^{jk} \left(1 + N(\epsilon_j, \epsilon_k, T)\right) \mathcal{D}[|j\rangle\langle k|]\rho(t), \end{aligned} \tag{8}$$

with ϵ_n energy of the system eigenvector $|n\rangle$, $\Gamma^{jk} = \Gamma|\epsilon_j - \epsilon_k| * |\langle j|\hat{A} + \hat{A}^\dagger|k\rangle|^2$, $\mathcal{D}[\hat{O}]\rho = \frac{1}{2}\left(2\hat{O}\rho\hat{O}^\dagger - \rho\hat{O}^\dagger\hat{O} - O^\dagger O\rho\right)$, $N(\epsilon_j, \epsilon_k, T) = 1/\exp[\hbar(\epsilon_j - \epsilon_k)/k_B T] - 1$ and where we have called $\hat{A}$ the system operators and Γ the losses (either cavity or atomic).

Proper pulses allow to bring the population from $|u, 0\rangle$ to $|u, 2\rangle$ in a very short time window giving an high burst of photons. We are motivated to analyze the statistical properties of output photons in order to certify the realization of the target state. Indeed, a measurement of two photons, by itself could be not enough to demonstrate the success of the protocol, as the detection of two photons can be realized also with a mixed state (like thermal photons).

The general formula to calculate the second order correlation function [9], at zero delay time, reads

$$g^{(2)}(t, t) = \frac{\langle a^\dagger(t)a^\dagger(t)a(t)a(t)\rangle_{\text{out}}}{\langle a^\dagger(t)a(t)\rangle_{\text{out}}^2} \tag{9}$$

This definition is equivalent to the ratio of the probability to detect a second photon at a detector 2 once that a first photon triggered the detection at detector 1, that's why in general, such a definition involves a quantum object depending on two times (chronologically ordered) t_2 and t_1, i.e. $g^{(2)}(t_1, t_2) = \langle a^\dagger(t_1)a^\dagger(t_2)a(t_2)a(t_1)\rangle/(\langle a^\dagger(t_1)a(t_1)\rangle\langle a^\dagger(t_2)a(t_2)\rangle)$. As $t_2 \to t_1$ we recover the $g^{(2)}(t, t)$, mostly known as $g^{(2)}(0)$, since there is no delay between t_1 and t_2. The statistical properties of the emitted photons are well described by the possible values of $g^{(2)}(0)$, and in particular, $g^{(2)}(0) < 1$ refers to quantum light, i.e. there is no correspondence with classical description. This result is known as photon antibunching, and it is typical of light emitted by spontaneous decay of a two level atom. Indeed, the detection of a second photon cannot happen since we have to wait the reload of the atomic transition. Also a pure Fock states of an optical mode have genuine quantumness, as it is easy to demonstrate that the Fock state for $n = 2$ has $g^{(2)}(0) = 1/2$, since

$$g^{(2)}(0) = \frac{\langle n|a^\dagger a^\dagger a a|n\rangle}{|\langle n|a^\dagger a|n\rangle|^2} = \frac{n(n-1)}{n} = 1 - \frac{1}{n} \tag{10}$$

Our aim is to create the Fock state $|2, u\rangle$ and we expect to see, at the end of the protocol, a 2 photon state and the corresponding $g^{(2)}(0) = 1/2$.

Preliminary work, with parameters already obtained in experiments, shows how the STIRAP protocol greatly enhances the photon flux, making it a viable method of detection. Additionally, the photons flux with SEP is comparable to the thermal noise, so in order to reliably utilize it as a detection method, some sort of post processing might be needed to filter out the noise, while STIRAP amplification allows to skip this passage.

It remains to be seen the robustness of the protocol for low cavity quality-factor, and in particular a lower limit for the adiabaticity needed for the STIRAP.

Conclusions

STIRAP seems a promising method of revelation for the USC. Further works needs to be done for different values of the parameters (losses of the system, value of the coupling strength and time of the protocol) to see when is possible to obtain an actual advantage over other protocols.

Acknowledgment

I thank professor A. Ridolfo for following me in this thesis work and professor S. Savasta for corrections to this report. This research was founded by the Centro Siciliano di Fisica Nucleare e Struttura della Materia.

References

[1] E. M. Purcell, "Spontaneous emission probabilities at radio frequencies", Phys. Rev. 69, 681 (1946)

[2] T. Niemczyk et al., "Circuit quantum electrodynamics in the ultrastrong coupling regime", Nat. Phys. 6, 772(2010)

[3] A. F. Kockum et al., "Frequency conversion in ultrastrong cavity QED", Sci. Rep. 7, 5313 (2017)

[4] G. Romero et al., "Ultrafast Quantum Gates in Circuit QED", Phys. Rev. Lett. 108, 120501

[5] G. Falci et al., "Ultrastrong coupling probed by Coherent Population Transfer", Sci Rep 9, 9249 (2019)

[6] G. Falci et al., Fortschr. Phys., 1–10 (2016)

[7] R. Stassi et al., "Spontaneous conversion from virtual to real photons in the ultrastrong-coupling regime", Phys. Rev. Lett. 110, 243601

[8] N. Vitanov et al., "Coherent manipulation of atoms and molecules by sequential laser pulses", Adv. in At. Mol. and Opt. Phys. 46, 55–190, (2001)

[9] A. Ridolfo et al., "Photon blockade in the ultrastrong coupling regime", Phys. Rev. Lett. 109, 193602, 2012

[10] Howard J. Carmichael , "Statistical Methods in Quantum Optics 1, Master Equations and Fokker-Planck Equations", 1999, Springer-Verlag Berlin Heidelberg

Calculation of Emission Spectra in Ultrastrong Coupling Regime under Incoherent Excitation

A. Mercurio[1*], V. Macrì[1,2], S. Savasta[1,2]

[1]*Dipartimento di Scienze Matematiche e Informatiche, Scienze Fisiche e Scienze della Terra, Università di Messina, I-98166 Messina, Italy*

[2]*Theoretical Quantum Physics Laboratory, RIKEN, Wako-shi, Saitama 351-0198, Japan*

*Corresponding Author email: alberto.mercurio@unime.it

Abstract

The interaction between a two-level atom and a quantized single-mode electromagnetic field is described by the quantum Rabi model. Depending on the coupling strength, the system can show different properties. Furthermore, several issues may prevent to describe correctly the physics of the quantum Rabi model when it approaches the Ultrastrong coupling regime. Indeed, without taking into account gauge invariant issue and the dressed description of the light-matter interaction, photondetection predicts nonphysical results. Here, we study the emission spectra of the Rabi model under incoherent excitation of the two-level system, described by an effective qubit temperature. The resulting, gauge-invariant spectra strongly depend on the coupling strength.

Keywords: Rabi model, Cavity QED, quantum optics, emission spectra.

Introduction

Light-matter interaction is one of the most common phenomena in nature. Two-level atom (qubit) interacting with a quantized single-mode electromagnetic field, is well described by the quantum Rabi model [1] which remains valid and gauge invariant [2], when the detuning between additional atomic transitions and the cavity mode is much larger then the light-matter coupling rate. When the interaction rate increases, a multilevel matter system can be still approximated by a qubit for sufficiently high degree of anharmonicity.

The quantized single-mode electromagnetic field can be obtained by an optical cavity whose resonance frequency is rather close to that of the qubit and with the additional modes sufficiently separated in frequency.

Depending on the system engineering, the coupling strength g can be smaller (weak coupling) or greater (strong coupling) than the losses. In the weak regime, the excitation spreads outside the system before it can be exchanged between the two subsystems, while in the strong regime the cavity and the qubit can exchange excitation several times before it is lost into the environment. The system dynamics in these regimes can be described neglecting the counter rotating terms in the Rabi Hamiltonian, applying the so-called rotating wave approximation (RWA). The resulting Hamiltonian is referred as the Jaynes-Cummings (JC) model.

When the coupling strength becomes comparable to the bare excitations of the system, a new regime emerges, known as the ultrastrong coupling regime (USC) [3]. Furthermore, the deep strong coupling regime (DSC) can be achieved when the coupling strength exceeds the frequency of the bare excitations of the system. The largest light-matter coupling strengths have been obtained with Landau polaritons in semiconductor systems [4], using superconducting circuits [5], and in plasmonic nanoparticle crystals [6].

In particularly in superconducting circuits, electrical circuits with Josephson junctions, operating at GHz frequencies, function as artificial atoms, acquiring a level structure similar to that of natural atoms. These artificial atoms are then coupled to photons in LC or transmission-line resonators. Superconducting circuits are a powerful platform for exploring atomic physics and quantum optics [3].

The USC regime is as fascinating as deceptive, and it can give rise to several interesting physical effects [7–9]. Due to the presence of the counter rotating terms, the total number of excitations is no more conserved, moreover, a clear difference between USC systems and those with lower coupling strength is the presence of light and matter excitations in the ground state and in all excited states.

A dressed description of the light-matter interaction is needed if we want to correctly describe photondetection. Moreover, a gauge-invariant issue has been questioned due to the apparent gauge-dependence of the Rabi Hamiltonian.

Indeed, while in the dipole gauge the quantum Rabi model is described correctly, the Coulomb gauge was considered not able to describe it for very large coupling strength. [10]. Recently, these gauge ambiguities have been resolved [2].
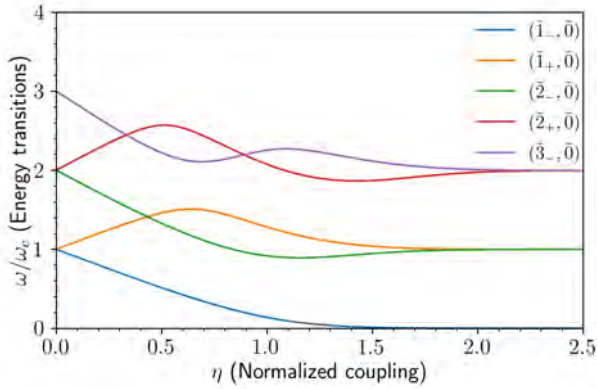
Figure 1: *First energy transitions of the Rabi Hamiltonian in reference to the ground state. Like any gauge invariant theory, they must be equal to both Equation 1 and Equation 2. The eigenstates are written in the Jaynes-Cummings form, with a tilde hat, indicating the dressed behaviour above the ultrastrong coupling regime.*

It was caused by the Hilbert space truncation of the matter systems (reduced to a qubit), which needs to be mathematically truncated to be considered as a two-level system. Such truncation generates a sort of non-locality in the potential, which can be fixed introducing the light-matter interaction by applying a specific unitary transformation into the description. This transformation is able to fix the gauge problem in a truncated Hilbert space.

Beyond the USC regime, still increasing the coupling strength, one enters the DSC regime. In this case, the light-matter interaction becomes so intense that the two subsystems do not exchange energy anymore. This phenomenon is called decoupling [9].

As mentioned above, it is necessary to take into account the dressed nature of the eigenstates, in order to write down correctly the operators describing photondetection and interaction with the environment. Following the input-output theory, it is possible to obtain the dressed operators[11], preventing the risk to get unphysical results.

Here, we study the emission spectra of this system under incoherent excitation, described by considering a qubit at an effective temperature $T \neq 0$, while the cavity is at $T = 0$. Both subsystems are weakly coupled to an ohmic reservoir with damping factors γ_q and γ_c for the qubit and the cavity, respectively.

Usually, the interaction between the subsystems is neglected in a Lindblad master equation approach [1, 7]. In presence of intense light-matter coupling, the dynamics has to be described by a generalized master equation [12] in terms of dressed operators. This generalization capture correctly the physics of the quantum Rabi model for the whole coupling range, which is from the weak to the deep strong.

Theoretical Model

The Hamiltonian in the dipole gauge is ($\hbar = 1$)

$$\hat{\mathcal{H}}_D = \omega_c \hat{a}^\dagger \hat{a} + \frac{\omega_q}{2} \hat{\sigma}_z + i\eta\omega_c \left(\hat{a}^\dagger - \hat{a} \right) \hat{\sigma}_x \qquad (1)$$

where $\hat{a}$ ($\hat{a}^\dagger$) is the destruction (creation) cavity operator, $\sigma_{x,y,z}$ are the Pauli matrices, ω_c and ω_q are the cavity and the qubit resonance frequencies respectively, and $\eta = g/\omega_c$ is the normalized light-matter coupling. Furthermore, according to Ref. [2] the Rabi Hamiltonian in Coulomb gauge is

$$
\begin{aligned}
\hat{\mathcal{H}}_C &= \omega_c \hat{a}^\dagger \hat{a} + \frac{\omega_q}{2} \left\{ \hat{\sigma}_z \cos \left[2\eta(\hat{a} + \hat{a}^\dagger) \right] \right. \\
&+ \left. \hat{\sigma}_y \sin \left[2\eta(\hat{a} + \hat{a}^\dagger) \right] \right\}
\end{aligned}
\qquad (2)
$$

which can be derived from Equation 1 making a unitary trasformation $\hat{\mathcal{H}}_C = \hat{\mathcal{U}}\hat{\mathcal{H}}_D\hat{\mathcal{U}}^\dagger$, where $\hat{\mathcal{U}} = \exp\left[i\eta\sigma_x(\hat{a} + \hat{a}^\dagger) \right]$. For the whole paper we will use the Hamiltonian in Coulomb gauge.

The system evolves according to the generalized master equation [12]

$$\dot{\hat{\rho}} = -i \left[\hat{\mathcal{H}}_C, \hat{\rho} \right] + \mathcal{L}_{\text{gme}}\hat{\rho},$$
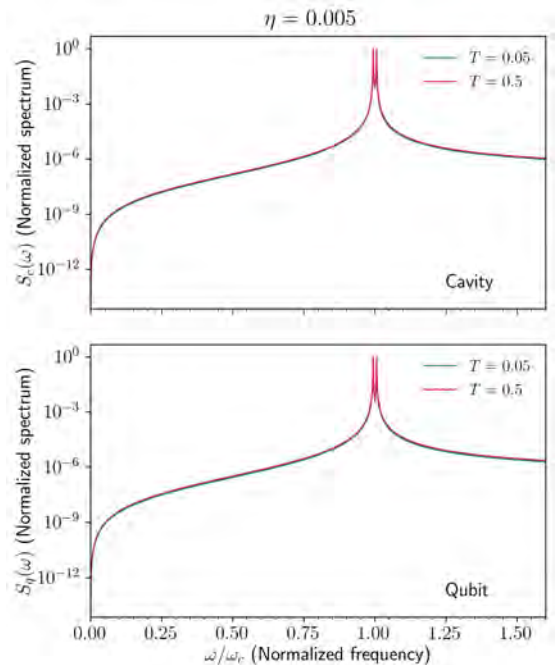

Figure 2: *Normalized power spectrum of both the cavity and the qubit, in the strong coupling regime. It is already possible to notice the splitting between the two lowest energy excited levels. In this case the shape of the low and high temperature spectra are the same.*
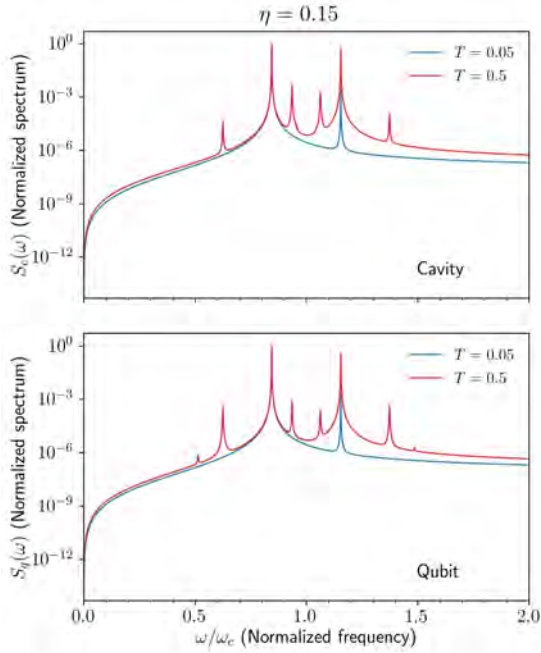
Figure 3: *Normalized power spectrum of both the cavity and the qubit, in the ultrastrong coupling regime. At low temperature, only the first lower and upper polariton transitions are eligible. The $(\tilde{1}_+, \tilde{0})$ is less intense than the $(\tilde{1}_-, \tilde{0})$ transition, as can be derived from Figure 1. At high temperature, new secondary transitions emerge, showing the full activity of the system at this coupling.*

where $\hat{\rho}$ is the density matrix and $\mathcal{L}_{\mathrm{gme}}$ is the generalized superoperator, which has not the standard Lidbladian form.

As expressed in Ref. [11], the detection operators are very different from those involved in the dynamics. As an example, for the cavity it is often used $\langle \hat{a}^\dagger \hat{a} \rangle$ to calculate the mean number of photons to be detected. However, when reaching the USC regime all the states become dressed and it can give rise to nonphysical results, such as a ground state photon number different from zero. The $\langle \hat{\mathcal{A}}^- \hat{\mathcal{A}}^+ \rangle$ and $\langle \hat{\Sigma}^- \hat{\Sigma}^+ \rangle$ operators should be used instead for the cavity and the qubit respectively [8, 12]. We use for now on, the parameters $\gamma_q = 10^{-4}\omega_c$ and $\gamma_c = 10^{-3}\omega_c$, while $\omega_q/\omega_c = 1$. The numerical calculations are performed with QuTip under Python [13].

Results

Before starting to show the numerical results, it is useful to define the eigenstates of the system. In the JC model, when the coupling is below strong coupling regime, the eigenstates can be written as $|n_\pm\rangle = |n, g\rangle \pm |n, e\rangle$, where $|n\rangle$ is the photon state, while $|g\rangle, |e\rangle$ are the two states of the qubit. As an example, the $|1_-\rangle$ and $|1_+\rangle$ states are called first lower and upper polariton respectively. The eigenstates of the quantum Rabi model, beyond the strong coupling regime do not display the same simple

structure. Here we indicate them by generalizing the above JC notation introducing a tilde. With this notation, the state $|\tilde{n}_\pm\rangle$ describes the eigenstate of the quantum Rabi Hamiltonian, which tends to the corresponding state $|n_\pm\rangle$ for $\eta \ll 1$ (see Figure 1).

Figure 1 shows the energy transitions in reference to the ground state of the two Rabi Hamiltonians Equation 1 and Equation 2. Since we are using a gauge invariant model, the two Hamiltonians return the same values.

Figure 2 shows the power spectrum of both the cavity and the qubit, in the SC regime. It is already possible to notice the separation between the first lower and upper polariton transitions. At this coupling regime and at these temperatures, this is the only (splitted) emisison line, corresponding to the lowest-energy transitions of the system. In this case the shapes are the same at both low and higher temperatures. However, their intensity (not shown here owing to the adopted normalization of the spectra), is rather different.

At low temperature and increasing the coupling strength, the transition frequency $(\tilde{1}_+, \tilde{0})$ reduces. This behaviour can be observed in Figure 3. However, increasing the temperature, additional lines emerge, showing the full activity of the system at this coupling.

Studying all the eligible transitions from Figure 1, we can list the six transitions showed in the cavity spectrum. From left to right they are: $(\tilde{2}_-, \tilde{1}_+)$, $(\tilde{1}_-, \tilde{0})$, $(\tilde{2}_-, \tilde{1}_-)$, $(\tilde{2}_+, \tilde{1}_+)$, $(\tilde{1}_+, \tilde{0})$ and $(\tilde{2}_+, \tilde{1}_-)$.
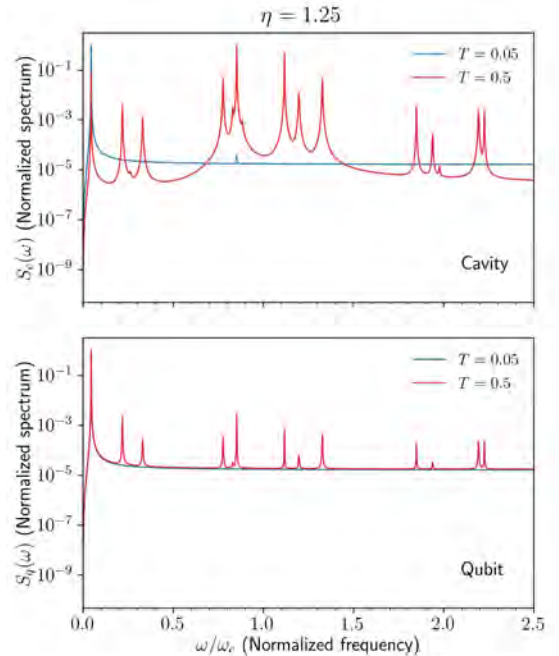

Figure 4: *Normalized power spectrum of both the cavity and the qubit, in the deep coupling regime. At low temperature there is still the $(\tilde{1}_-, \tilde{0})$ transition, while the first upper polariton has practically disappeared. Increasing the temperature, the shape difference between the cavity and the qubit becomes more relevant.*

Figure 4 shows the normalized spectrum of both the cavity and the qubit in the DSC regime. Here the spectrum shapes of the two subsystems are very different, and at low temperature only the line from the lowest energy transition survives.

Conclusions

In this work we have analyzed the interaction between a qubit and a single mode cavity under an incoherent excitation, described by an effective temperature $T \neq 0$ of the qubit reservoir. The system is in weak interaction with an ohmic bath, with the cavity at zero temperature. We have numerically calculated the cavity and qubit emission spectra, which provide information on the interaction dynamics and on all the eligible transitions. The number of such transitions increases with the temperature, as expected.

We used a complete gauge invariant model using dressed output operators and a gauge invariant master equation in the dressed basis.

The quantum Rabi Hamiltonian is one of the most simple and fundamental models in quantum optics. However, despite its simplicity, it still remain one of the most fundamental models to study the light-matter interaction. Moreover, the dynamics of an open quantum system described by the quantum Rabi model beyond the SC regime, can be rather complex and requires to go beyond the standard methods used in quantum optics.

References

[1] Lambropoulos, Peter, and David Petrosyan: *Fundamentals of quantum optics and quantum information.* Vol. 23. Berlin: Springer, 2007.

[2] O. Di Stefano, A. Settineri, V. Macrì, L. Garziano,R. Stassi, S. Savasta, and F. Nori: *Resolution of gauge ambiguities in ultrastrong-coupling cavity quantum elec-trodynamics.* Phys. Rev. Lett.116,113601 (2016).

[3] A. F. Kockum, A. Miranowicz, S. De Liberato, S. Savasta, and F. Nori: *Ultrastrong coupling between lightand matter.* Nat. Rev. Phys.1, 19 (2019).

[4] A. Bayer, M. Pozimski, S. Schambeck, D. Schuh, R. Huber, D. Bougeard, and C. Lange: *Terahertz light-matter interaction beyond unity coupling strength.* Nano Lett. 17, 6340 (2017).

[5] F. Yoshihara, T. Fuse, S. Ashhab, K. Kakuyanagi, S. Saito, and K. Semba: *Superconducting qubit-oscillator circuit beyond the ultrastrong-coupling regime.* Nat. Phys. 13, 44–47 (2017).

[6] Mueller, Niclas S., et al.: *Deep strong light–matter coupling in plasmonic nanoparticle crystals..* Nature 583.7818 (2020): 780-784.

[7] F. Beaudoin, J. Gambetta, and A. Blais: *Dissipation andultrastrong coupling in circuit QED.* Phys. Rev. A84,043832 (2011).

[8] A. Ridolfo, M. Leib, S. Savasta, and M. J. Hartmann: *Photon Blockade in the Ultrastrong Coupling Regime.* Phys. Rev. Lett.109, 193602 (2012).

[9] S. De Liberato: *Light-Matter Decoupling in the DeepStrong Coupling Regime: The Breakdown of the PurcellEffect.* Phys. Rev. Lett.112, 016401 (2014)

[10] De Bernardis, Daniele, et al.: *Breakdown of gauge invariance in ultrastrong-coupling cavity QED..* Physical Review A 98.5 (2018).

[11] A. Settineri, O. D. Stefano, D. Zueco, S. Hughes,S. Savasta, and F. Nori: *Gauge freedom, quantum measurements, and time-dependent interactions in cavity andcircuit QED.* arXiv:1912.08548 [quant-ph].

[12] A. Settineri, V. Macrì, A. Ridolfo, O. Di Stefano, A. F.Kockum, F. Nori, and S. Savasta: *Dissipation and ther-mal noise in hybrid quantum systems in the ultrastrong-coupling regime.* Phys. Rev. A98, 053834 (2018).

[13] J. Johansson, P. Nation, and F. Nori: *QuTiP: An open-source Python framework for the dynamics of open quantum systems.* Computer Physics Communications183,1760 (2012).

Evaluation of failure modes in 4H-SiC powermosfets using Raman Spectroscopy

G. G. Piccione[1,*], M. Calabretta[2], S. Patanè[1]

[1]*Department of Mathematical and Informatics Sciences, Physical Sciences and Earth Sciences of Messina University, Viale Ferdinando Stagno D Alcontres 31, 98166 Messina, Italy*

[2]*STMicroelectronics srl, Stradale Primosole, 95121 Catania, Italy*

[*]Corresponding Author email: giupiccione@unime.it

Abstract

The goal of this paper is to characterize the failure mechanisms related to mechanical aspects of SiC-based devices, defining the upper limit for which, by applying a constant deformation using tensile tests, the material breaks. More specifically, the study concerns the dependence of phononic modes with respect to mechanical stress in a silicon carbide crystal in 4H polytype. The logical link between this study and the problems concerning reliability becomes immediately clear when we consider that a current pulse that crosses the active region of the device gives rise to a sudden increase in temperature which, in turn, produces a mechanical deformation easily measurable with optical interferometry techniques. The frequency of the Raman modes of the material depends on the mechanical stress and on the temperature; so it is therefore evident how the study of the Raman response of the material can easily provide valuable information about the behavior of the semiconductor in operating conditions and represents a considerable support for the definition of a possible model of reliability.

Keywords: Silicon Carbide, Raman Spectroscopy, Powermosfet.

Introduction

Today Silicon carbide (SiC) represents one of the emerging materials in the semiconductor device market which it has only joined in recent years. In this sense, technology is not yet mature and it faces many challenges in terms of manufactoring until today. Neverteless, Despite these difficulties, interest in this semiconductor is great as it largely allows to overcome the old silicon technology. SiC has superior material properties for certain applications than more conventional materials like Si or gallium arsenide (GaAs)(Tab. 1) [1].

The small intrinsic carrier concentration due to the wide bandgap (e.g. 3:3 eV in 4H-SiC) paired with the high thermal conductivity makes it suitable for high temperature applications. The high breakdown field allows to blocking voltages exceeding 1200V with low on-resistance, which makes SiC an ideal material for power devices. Additionally, SiC can withstand harsh environments, as it has a high thermal stability, chemical inertness and radiation resistance [2].

Power devices are operated in a wide range of temperatures and exposed to extreme environments such as high temperature and high humidity. The residual stresses in these extreme environments may cause unintended effects by producing cracks, defects, delamination, etc.

Proprietà	4H-SiC	Si	GaAs	GaN
Bandgap energy (eV)	3.26	1.12	1.43	3.45
Thermal conductivity $(Wcm^{-1}K^{-1})$	4.9	1.5	0.46	1.3
Breakdown field (x $10^5 Vcm^{-1}$)	32	3	4	30
Electron mobility $(cm^2 V^{-1}s^{-1})$	700-1200	1500	8500	900-1250
Sat. electron drift velocity (x $10^7 cms^{-1}$)	2.2	1.0	1.0	2.2

Table 1: *Material properties of 4H-SiC compared to other semiconductors.*

Moreover, it is not easy to measure the internal local stress nondestructively. Raman spectroscopy is one of the most effective techniques for evaluating the local stress in semiconductors.

This technique is particularly effective in silicon carbide devices since the applied stress deform the crystal changing the phonon frequents, and so induce a local variation

of the polarizability; moreover, SiC is characterized by strong covalent bonds and the Raman spectrum is therefore particularly intense and gives rise to good reliable measurements. In this paper, we first discuss the properties of the phonons in the 4H polytype and investigate the dependencies of the peak frequencies on the uniaxial stress using three-point bending tests. Then, we apply cross-sectional Raman measurements to 4H-SiC MOSFETs and determine the stress components on the basis of the fundamental uniaxial stress tests.
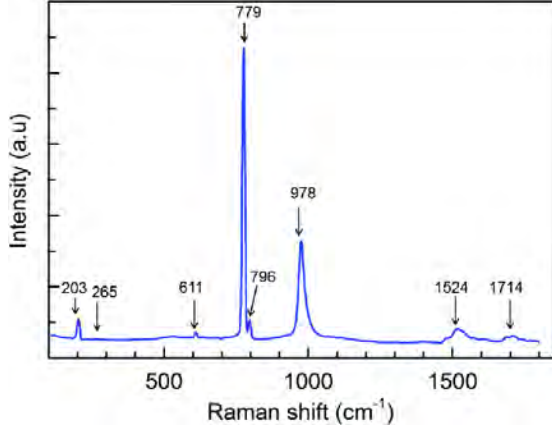

Figure 1: *Spettro Raman 4H-SiC*

Theory

The 4H polytype belongs to the C_{6v}^4 space group and it has eight atoms per unit cell. SiC is composed of Si and C, both elements are in 1:1 stoichiometric relationship where every Si atom is strongly covalently bonded to four C nearest neighbors and vice versa. However, SiC can exist in many different crystal structures, all with different electrical properties. More than 250 of polytypes are known. The normal modes in the longwavelength limit are 4 (A_1 + B_1 + E_1 + E_2), where the B_1 modes are Raman inactive, and the A_1 and E_1 modes are acoustic. The $3A_1$, $3E_1$, and $4E_2$ modes are observable. For $\theta = 0°$, the long-range electric field in the crystal changes the A_1 mode to the longitudinal optical mode $A_1(LO)$ and the E_1 mode to the transversal optical mode $E_1(TO)$. For $\theta = 90°$, the E_1 mode splits into the $E_1(LO)$ and the $E_1(TO)$ modes and the A_1 mode becomes the $A_1(TO)$ mode. The E_2 modes are nonpolar, and there is no dependency on the propagation angle. For an intermediate angle $\theta \neq 0°$ and $\theta \neq 90°$, the LO and TO modes have the mixed symmetry of the A_1 and E_1 modes [2, 3]. According to theory proposed by Briggs and Ramdas, the shifts in the phonon frequencies can be recaveted by the following equations

$$\Delta\omega_{A1} = a'_{A1}(\sigma_{11} + \sigma_{22}) + b'_{A1}\sigma_{33}$$

$$\Delta\omega_{E1} = a'_{E1}(\sigma_{11} + \sigma_{22}) + b'_{E1}\sigma_{33} \pm c'_{E1}(\sigma_{11} - \sigma_{22}) \quad (1)$$

$$\Delta\omega_{E2} = a'_{E2}(\sigma_{11} + \sigma_{22}) + b'_{E2}\sigma_{33} \pm c'_{E2}(\sigma_{11} - \sigma_{22})$$

Equation (1) is a set of simultaneous linear equations, where the stress components σ_{11}, σ_{22}, and σ_{33} can be derived from the phonon shifts $\Delta\omega A_1$, $\Delta\omega E_1$, $\Delta\omega E_1$ [4, 5]. The stress exerted on the sample causes a change in the volume and size of the solid, as the lattice atoms move out of their equilibrium position giving rise to an elastic force that tries to counterbalance the external force applied. The Young modulus is given by:

$$Y = \frac{k}{x_0} = \frac{k_c l_0}{A} \quad (2)$$

The measurements were carried out using a micrometer and not a dynamometer, so it was possible to measure the deformation and not the force. It is therefore necessary to relate the deformation (which was induced by the micrometer) with the applied force. Considering that the average properties of SiC are almost the same in the sample used, the error induced by this approximation can be considered more than negligible since thin films are homocrystalline. With the above we find:

$$\bar{F} = k \cdot \Delta x = 410 \ GPa \cdot 1 \times 10^{-6} = 2,46 \times 10^{-3} \ GPa \quad (3)$$

Then a force of $2.46 \times 10^{-3} \ GPa$ per micron of deformation was applied. The procedure was repeated up to the breaking load which for our samples exceed 350 μm.
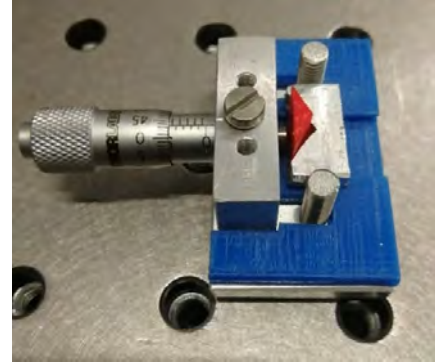
Figure 2: *Micrometer used to measure the deformation of the sample*

Experimental

In order to evaluate the threshold value beyond which a 4H-SiC film breaks, three-point bending tests were performed. We have created a system in which a "beam resting on two points" is subjected to a force in its central part. Referring to Fig. 5 it is evident that the structure under study will be subjected to a compressive stress at the point of support of the force and tensile stress on the opposite side.

Fig. 2 shows the mechanical system implemented to obtain controlled deformation. As you can see, it is a very simple system consisting of a micrometer equipped with a vernier and a support that holds two vertical axes consisting of two steel screws. The micrometer acts on a

wedge of rigid material and in doing it so applies a measurable deformation through the vernier to the specimen which rests on the two vertical axes. The whole system is miniaturized so that it can be inserted in the operating range of the Raman spectrometer.

The sample was subjected to a stress along the crystallographic axis c positioning it so that the epitaxial layers are on the opposite side to the point of support of the force, therefore the stress induced on the layers is of the tensile type while on the substrate it will be of the compressive. The force exerted can be related to the stress induced through the relationship:

$$\sigma = \frac{3FL}{2bd^2} \tag{4}$$

Where F is the force, b is the thickness of the sample, L is its length and d its thickness.

The Raman system used is schematically described in Fig. 3
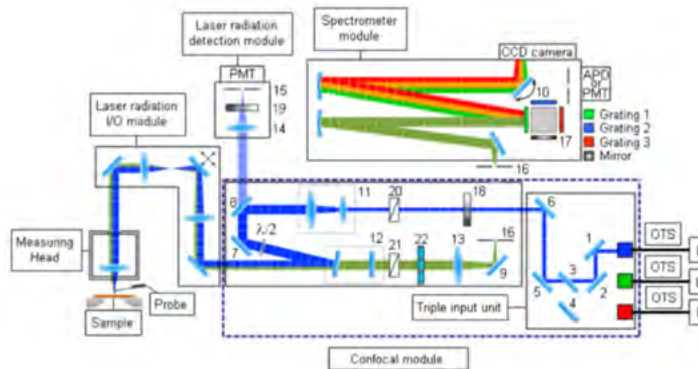
Figure 3: *Instrumental set-up of the Raman spectroscope*

We used an integrated system with an AFM head, suitable for performing TERS and AFM Raman measurements (Fig. 4). The system is equipped with three solid state laser sources (DPSS: Diode pumped Solid State Laser) operating at 532nm and 473nm, and a gas source at 632.6nm (HeNe laser); We use the one at 532 nm.

The acquisition software controls all the operating parameters, including the laser power and the operating temperature of the device and the Andor IDUS camera which is responsible for detecting the RAMAN signal. The operating temperature of the camera has been set at −65° C.
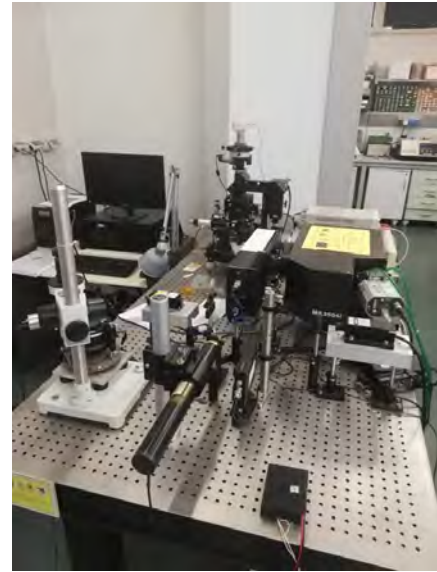
Figure 4: *Experimental setup used in laboratory*

Measurements were made by changing the deformation produced by stepping the micrometer by 5 μm at a time, this value was chosen to ensure repeatability and accuracy of the measurement, since the vernier of the micrometer allows us to appreciate a maximum of 2.5 μm.
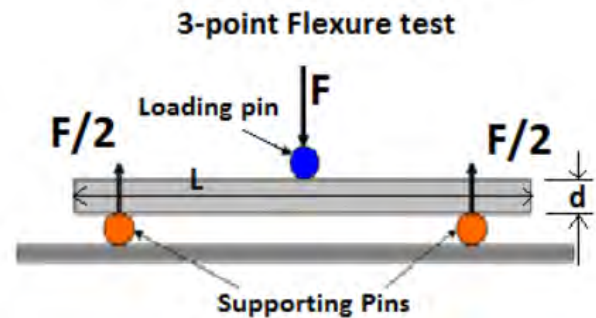
Figure 5: *Rappresentation of beam resting on two points*

Results and discussion

Fig. 6 shows one of the spectra obtained during the measurement campaign.
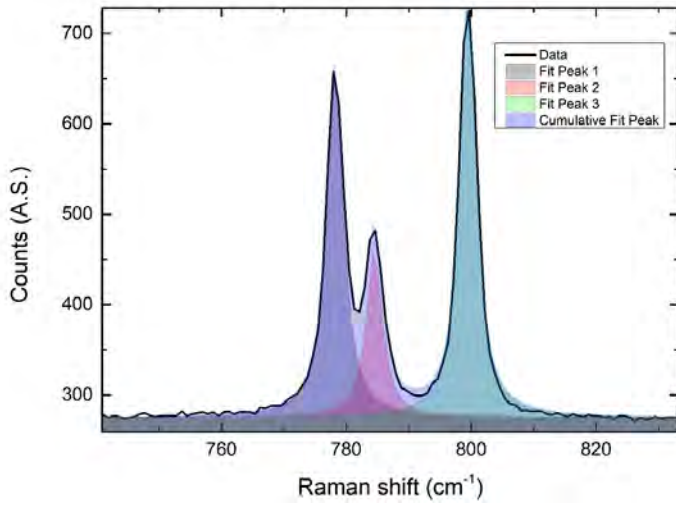
Figure 6: *Raman spectrum obtained under zero stress conditions and fit of the experimental data.*

The spectrum refers to the case of zero applied stress and the analysis is limited only to the peaks relating to modes $A_1(TO)$, $E_1(LO)$ and $E_1(TO)$. For convenience, just this spectrum is reported as the others are all obviously similar. For each of the measures the best fit of the experimental data was calculated using the least squares minimization method with an iterative Levenberg-Marquardt algorithm. For this purpose, the Raman spectrum was imagined as composed of 3 peaks with Lorenzian character, a rather plausible hypothesis considering the crystallinity characteristics of the material.

Observing values of X^2 and the error on the individual parameters (which are very good) it can be concluded that the confidence level of the fit is excellent (Fig. 7).

Fig. 8, Fig. 9 and Fig. 10 show the trend of the position of the Raman peaks when the applied deformation varies. As expected the position of the peaks depends on the tensile stress applied to the material. It is interesting to observe that the experimental data seem to indicate a different behavior depending on the observed phononic mode. This result is in good agreement with some experimental results already present in the recent literature.
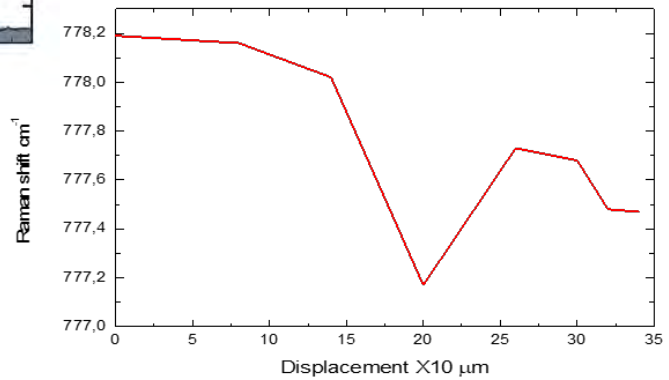
Figure 8: *Trend of Raman peaks position as the applied deformation varies from $770,0 cm^{-1}$ to $778,2 cm^{-1}$*

		Value	Standard Error
1	Model	Lorentz	
2	Equation	$y = y_0 + (2*A/PI)*(w/(4*(x-x_c)^2 + w^2))$	
3	Reduced Chi-Sqr	25.01329	
4	Adj. R-Square	0.98	
5			Value	Standard Error
6	Peak1(B)	y_0	274.68297	0.16009
7	Peak1(B)	x_c	778.19649	0.01771
8	Peak1(B)	w	3.2313	0.05598
9	Peak1(B)	A	1939.73409	25.96836
10	Peak1(B)	H	382.16026	4.08635
11	Peak2(B)	y_0	274.68297	0.16009
12	Peak2(B)	x_c	784.46812	0.03573
13	Peak2(B)	w	3.18336	0.11283
14	Peak2(B)	A	941.90765	25.93211
15	Peak2(B)	H	188.36634	4.10185
16	Peak3(B)	y_0	274.68297	0.16009
17	Peak3(B)	x_c	799.47756	0.01361
18	Peak3(B)	w	3.11751	0.03883
19	Peak3(B)	A	2319.37356	20.64143
20	Peak3(B)	H	473.63382	4.11952

Figure 7: *summary table of the fit results*

Figure 9: *Trend of Raman peaks position as the applied deformation varies from $784,0 cm^{-1}$ to $784,4 cm^{-1}$*
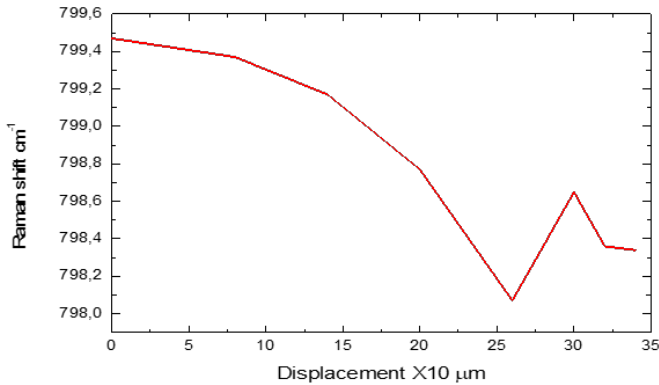
Figure 10: *Trend of Raman peaks position as the applied deformation varies from* $798,0 cm^{-1}$ *to* $799,6 cm^{-1}$

Conclusions

This work represents a first step towards the realization of an operational protocol for the improvement of the performances of the new power devices based on Silicon Carbide. The idea consists in evaluating the mechanical stress of the material by studying the properties of its Raman spectrum with the aim of providing operational support to designers. For this purpose, a 4H-SiC sample was studied by imposing a known deformation, defining

the breaking point by means of uniaxial tensile tests and comparing the results obtained with the literature.

The measurements have clearly highlighted a measurable dependence of the phononic modes with respect to the mechanical stress induced by the applied deformation and in particular the modes $A_1(TO)$, $E_1(LO)$ and $E_1(TO)$ have been studied. A realistic assessment of intrinsic stress would allow to propose a modification of the device layout that could be designed with an opposite pre-stressed structure.

References

[1] Sugie R., Uchida, T.: *Determination of stress components in 4H-SiC power devices via Raman spectroscopy.* Journal of Applied Physics, Vol. 6, No. 1 2017.

[2] Tsunenobu K., J. A. Cooper: *Fundamentals of Silicon Carbide Technology* Wiley-IEEE Press, 2018.

[3] Götz W.,et al.: *Nitrogen donors in 4H-silicon carbide* Journal of Applied Physics , Vol. 73, No. 7 , 1993.

[4] Dobson, P.: *Physical Properties of Crystals – Their Representation by Tensors and Matrices* Physics Bulletin , Vol. 36.

[5] Briggs, R. J., Ramdas, A. K.: *Piezospectroscopic study of the Raman spectrum of cadmium sulfide* Physical Review B , Vol. 13, No. 12, 1976.

Production of Radioactive Ion Beams by Means of the In-Flight Technique at LNS@INFN: Status and Perspectives

F. Risitano[1,2,*]
[1] *Dipartimento MIFT, Università di Messina, Messina, Italy*
[2] *INFN-Sezione di Catania, Catania, Italy*

[*]Corresponding Author email: fabio.risitano@unime.it

Abstract

For an in-depth study of interesting thematics in nuclear physics it is necessary to produce collisions of heavy radioactive ions with high isospin asymmetry, which could show peculiar structures and phenomena. The In-Flight method of RIBs (**R**adioactive **I**on **B**eams) production will be presented, with particular care on the facility *FRIBs@LNS* (*In-**F**light **R**adioactive **I**on **B**eams at **L**aboratori **N**azionali del **S**ud*). Moreover, the future fragment separator *FRAISE* (***FRA**gment **I**n-Flight **S**eparator*), currently under construction at LNS, will be discussed. Several RIBs production simulations have been developed, which show its improvements in intensity and variety of beams that can be produced, far superior to current system FRIBs.

Keywords: radioactive ion beams, In-Flight, fragment separator.

Introduction

In the last decades, several facilities aimed to the production of RIBs have been developed. Among the production methods, the *In-Flight* technique [1] is currently used at LNS (INFN) to produce RIBs for research purposes.

In the In-Flight technique, a stable heavy ion beam is fragmented on a thin target, producing a wide variety of ion species, a "cocktail" beam, including radioactive ions of interest. Cocktail beam ions are transmitted through the fragmentation target without being stopped and then sent in a *fragment separator*, a spectrometer which separates the ions of the cocktail beam through magnetic fields, transmitting only the wanted species.

To improve the quality of the produced beam, many devices can be used, such as focusing quadrupoles or multipoles, slits to stop impurities and degraders, materials which slow down ions depending on their mass, charge and velocity, contributing to improve the purity of the wanted beam.

At LNS in Catania, it is possible to produce RIBs with energy between 10 and 100 MeV/u, using stable beams accelerated by a Superconducting Cyclotron (SC) and the fragment separator *FRIBs* [2]. The facility FRIBs@LNS, from the early 2000's, was able to produce RIBs for research purposes by fragmenting stable beams on a beryllium fragmentation target, obtaining RIBs with reasonable purity and intensity [3, 4]. Moreover, recent and future research development on the In-Flight technique at LNS will be presented, discussing in particular a test of RIBs production and cleaning with FRIBs.

Besides, a new important upgrade of the LNS facility, currently under development, will also be discussed, in particular concerning the construction of the new Fragment separator *FRAISE* [2]. FRAISE will give the possibility to produce a wider variety of radioactive beams, with extreme isospin values, currently not producible with reasonable intensity with FRIBs, and with excellent characteristics of purity and intensity.

Tagging System for a FRIBs Cleaning Test

The facility FRIBs@LNS is able to produce RIBs for research purposes by fragmenting a stable beam, accelerated by the SC at energies between 20 and 80 MeV/u, on a thin ^9Be target, with thickness from 250 to 1500 μm, mechanically inserted into the beam line [2, 5].

The fragment separator FRIBs is made up by two $45°$ dipoles with impulse acceptance determined by the width of the apertures of the dipoles themselves (about $\Delta p/p_0 \approx 1\%$). Once a radioactive beam is produced by fragmentation, it is necessary to know its exact composition, since it would be constituted by different ions with similar m/q ratio. For this reason, before sending it to an experimental hall, an *in-flight* identification, or *tagging*, needs to be performed. The tagging system used at LNS to identify the components of the beam is based on the ΔE–ToF technique [6], in which the energy loss of an isotope on a detector is related to its time-of-flight, by the relation $\Delta E \propto Z^2 ToF^2$, obtained from the Bethe energy loss formula.

During November 2018, a test for the production and cleaning of a ^{11}Be radioactive beam has been carried out [7]. To produce the beam a ^{13}C (55 MeV/u) beam, accelerated by the SC, has been fragmented on a ^{9}Be (1500 μm) target. This test, in particular, aimed to show the capability at LNS to produce high purity RIBs, by using an aluminum degrader to improve the purity of the resulting beam.
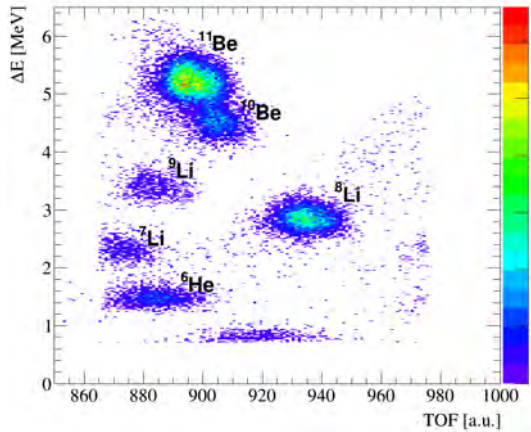
Figure 1: *ΔE–ToF plot of the production of a ^{11}Be RIB obtained without the aluminum degrader.*
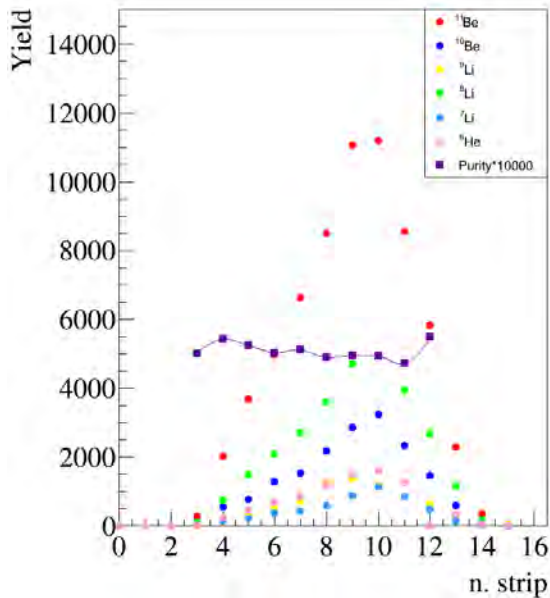
Figure 2: *Total yield for various isotopes of the cocktail beam obtained without degrader as a function of the horizontal strip number of the DSSSD.*

The detector used for the tagging of the beam components was a 140 μm thick Double-Sided Silicon Strip Detector (DSSSD) constituted by a grid of 16×16 horizontal and vertical strips for its front and back sides, with a total area of 48×48 mm². Without the aluminum degrader, the

^{13}C primary beam intensity was set to 10 enA, while the rigidity of the dipoles was set at $B\rho \approx 2.81\ Tm$, to optimize the transport of the wanted ^{11}Be ion species, which yield rate was of about 1 kHz.
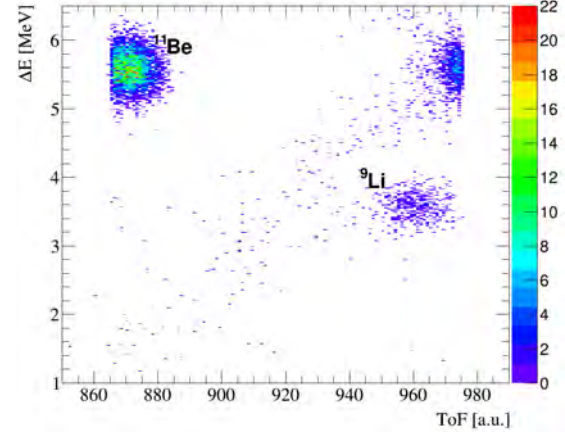
Figure 3: *ΔE–ToF plot obtained with a 1000 μm thick aluminum degrader.*
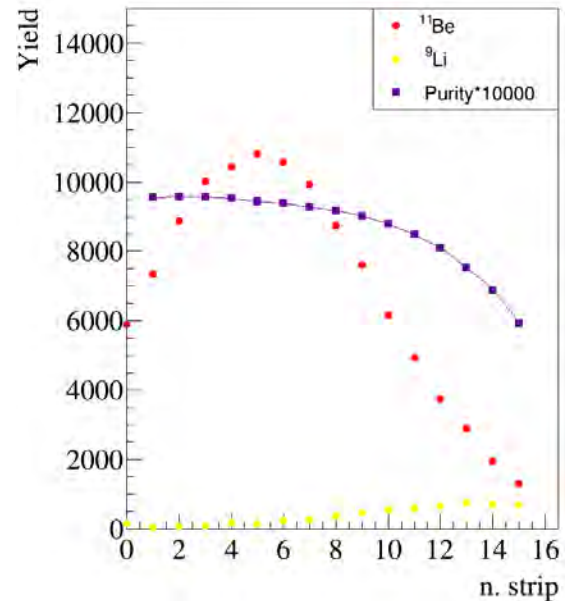
Figure 4: *Total yield as a function of the horizontal strip number of the DSSSD obtained with the aluminum degrader.*

In the *ΔE–ToF* scatter plot shown in Figure 1, it is possible to identify every ion of the resulting cocktail beam. The value of energy loss for the analysis was gathered by the DSSSD, while the time-of-flight was calculated, event by event, by the difference between the arrival time on the detector and the periodic signal of the oscillation of the SC electric field. Calibration for the energy axis has been performed by means of a *LISE++* [8] simulation of energy loss on the tagging detector. A plot of the yield

for each ion on each vertical strip has also been produced, shown in Figure 2, demonstrating the quality of the focused beam and showing a purity for the ^{11}Be component of about 50%.

Subsequently, a 1000 μm thick homogeneous aluminum degrader has been inserted on the beam line at the symmetry center of the FRIBs fragment separator, where the dispersion of the cocktail beam ions is maximum. The presence of this material on the symmetry axis of the separator considerably contributes to eliminate the impurities of the cocktail beam. This is possible because its ions lose energy differently inside the material depending on their atomic mass, charge and velocity.

For this reason, the rigidity of the second dipole was set on $B\rho \approx 2.67\ Tm$ to compensate the energy loss of the ^{11}Be ions due to the presence of the degrader. In Figure 3 a $\Delta E\text{–}ToF$ scatter plot shows that the presence of the degrader has contributed to obtain a higher purity, being the ^{9}Li ions the only prevailing impurity of the optimized cocktail beam.

This is confirmed even by the yield production plot shown in Figure 4, where it can be seen that the purity reach values over 95%, although the beam appears to be *wider* on the horizontal axis, due to the straggling of the ^{11}Be ions passing through the degrader.

The new Fragment Separator FRAISE

From June 2020, an upgrade of the infrastructures of Laboratori Nazionali del Sud has begun. The upgrade will maily regard an enhancement of the Superconducting Cyclotron and the construction of the new fragment separator FRAISE [2]. With the new SC it will be possible to produce stable beams, for ions from Carbon to Argon, with high intensity in the order of 10^{13} pps, with an expected power of 10 kW, equivalent to an increase of 10^2 with respect to the actual status. This upgrade will open new research possibilities, as it will be possible to produce more intense radioactive beams, with respect to the ones produced with FRIBs: to cope with the intensity increase of the SC, the new fragment separator FRAISE has been designed [9].

FRAISE will be constituted by four magnetic dipoles in a symmetric configuration, and some quadrupoles and sextupoles will also be placed on the beam line in order to focus the beam. The fragmentation targets will be ^{9}Be rotating plates, water-cooled, and different thicknesses could be selected to optimize the production of the desired beam. Two slits will also be present, the first one at the symmetric center of the fragment separator, in order to lower the acceptance of the separator below the typical value of $\Delta p/p \approx 1.2\%$, and the second one will be put at the exit, to remove lateral impurities with magnetic rigidity different from the one of the desired species. An aluminum homogeneous degrader can also be inserted after the central slit, to achieve a better separation and to obtain a RIB with better purity.

Regarding the new fragment separator, many simulations of production of various RIBs have been performed by means of the LISE++ [8] code, optimizing the production yield and the purity of the desired isotope. For the purpose of the simulation also two silicon carbide (SiC) detector, each one 100 μm thick, were placed respectively at the symmetry plane and at the exit of the fragment separator. The choice of this material comes from the need to use radiation hard detectors, resisting to the high intensity of the future beams. In particular, the presence of the detector on the symmetry plane greatly affects the purity of the desired beam, due to the fact that it also has the function of a thin degrader.

As an example, a ^{15}C RIB produced from a ^{18}O (55 MeV/u, 2 kW) fragmented on a 1250 μm ^{9}Be target shows an increase in purity of the desired isotope, from 65% to 90%, while showing the same yield production after the adding of the SiC detector on the symmetry plane (Figure 5).

The purity of the ^{15}C radioactive beam can also be improved by adding another thin degrader, following the SiC detector, and adjusting the right opening of the exit slit, in order to reject the lateral impurity components and obtain a beam with a purity value in the order of 99%.
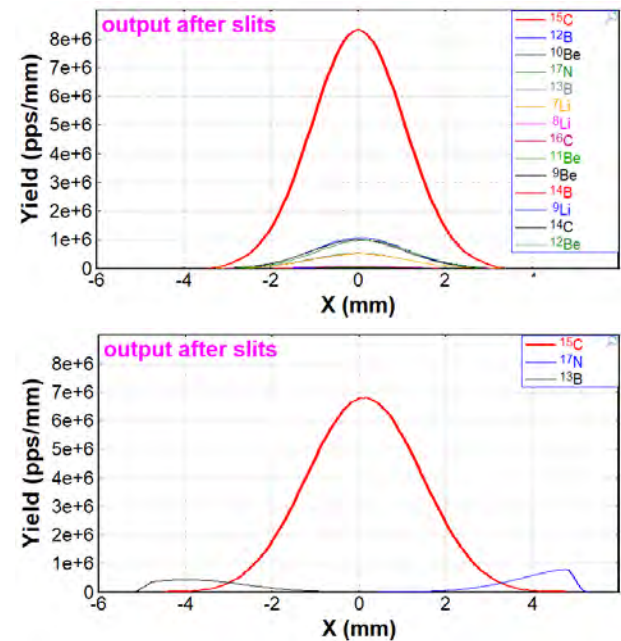
Figure 5: *Output of the cocktail beam after the exit slit, and the purification effect due to the presence of the SiC detector (below).*

The new fragment separator FRAISE will give the possibility to produce new exotic radioactive beams, farther from the stability line with respect to the ones obtainable with the current facility FRIBs. In this way it will be possible to explore a wider variety of research topics, such as the study of nuclear cluster structures or exotic ones, like neutron halos or neutron skins, isospin effects in heavy ion reaction mechanisms, resonance states such as the Pygmy dipole or monopole resonances, reaction of astrophysical interest and many others.

The same simulation optimization shown before was applied also on many other RIBs and main results are shown on Tab. 1.

Table 1: *Several simulations of production of various RIBs produced with FRAISE.*

Primary beam / energy (MeV/u) / intensity (kW)	Primary Product	Target Thickness (μm)	Wedge Thickness (μm)	Expected Yield (kHz)	Purity (%)	Exit Energy (MeV/u)	dE (%)	dp/p (%)
^{18}O / 55 / 2	^{15}C	1250	200	21600	100	44	2,27	1,32
^{18}O / 55 / 2	^{16}C	1250	0	6800	99	46	2,1	1,32
^{18}O / 55 / 2	^{14}Be	1250	200	1,59	100	47	2,13	1,32
^{12}C / 62 / 2	^{8}B	2250	0	2400	58	47	2,1	1,32
^{13}C / 55 / 2	^{11}Be	1500	0	5830	97	47	2,06	1,32
^{36}Ar / 50 / 2	^{34}Ar	500	0	7360	61	33	2,8	1,32
^{48}Ca / 45 / 2	^{46}Ar	500	0	1650	93	30	2,2	1
^{24}Mg / 50 / 2	^{20}O	750	0	191	97	40	2,3	1,32
^{40}Ar / 40 / 2	^{38}S	250	100	4320	93	29	2,5	1,2
^{70}Zn / 50 / 1	^{68}Ni	250	0	753	78	36	2,1	1

Conclusions

In this report, the In-Flight technique for the production of radioactive ion beams (RIBs) has been discussed, focusing on the recent and future developments at LNS (INFN). The facility FRIBs@LNS has been presented and data analysis results of a cleaning test have been discussed, showing the possibility to produce in RIBs with good parameters of intensity and purity, achievable also thanks to the use of a degrader with purification function. Moreover, the future LNS upgrade has been discussed, which will concern in particular the new fragment separator FRAISE. This project will offer new research possibilities in heavy ion physics, since it will allow production of more intense and unstable RIBs, farther from the stability line, with extreme isospin values. In this context many simulations of production of RIBs for the study of several new topics have been carried out, focusing on the different features of a fragment separator.

These simulations, some of which not reported in this text, constitute an important starting point for the design of future experiments to be performed with FRAISE. It follows that these results will be made available to the LNS users and are to be considered of fundamental importance for tracing the future scientific research trajectories in this field.

References

[1] Morrissey, D. J., Sherrill, B. M.: *In-Flight Separation of Projectile Fragments*. In: "The Euroschool Lectures on Physics with Exotic Beams, Vol. I" (Editors: Al-Khalili, Jim and Roeckl, Ernst). Berlin: Heidelberg, 113–135 (2004).

[2] Russotto, P. et al.: *Status and Perspectives of the INFN-LNS In-Flight Fragment Separator*. Journal of Physics: Conference Series, 2018.

[3] Raciti, G. et al.: *Intermediate energies tagged RIBs*. Nucl. Instr. Meth. Phys. Res., Sect. B, **266**, 4632–4636, 2008.

[4] Dell'Aquila, D. et al.: *New experimental investigation of the structure of ^{10}Be and ^{16}C by means of intermediate-energy sequential breakup*. Phys. Rev. C, **93**, 024611, 2016.

[5] Rapisarda, E.: *FRIBs: tagged intermediate energy radioactive ion beams at Laboratori Nazionali del Sud*. PhD Thesis, Università Di Catania, 2006.

[6] Lombardo, I. et al.: *Use of Large Surface MicroChannel Plates for the Tagging of Intermediate Energy Exotic Beams*. Nuclear Physics B - Proceedings Supplements, **215**, 272–274, 2011.

[7] Martorana, N. S. et al.: *Test of secondary beam cleaning in FRIBs through a degrader*. Personal Communication.

[8] Tarasov, O. B. and Bazin, D.: *LISE++: Radioactive beam production with in-flight separators*. Nucl. Instr. Meth. Phys. Res., Sect. B, **266**(19), 4657–4664, 2008.

[9] Russo, A. D. et al.: *Preliminary design of the new FRAgment In-flight SEparator (FRAISE)*. Nucl. Instr. Meth. Phys. Res., Sect. B, **463**, 418–420, 2020.

Resolution tests and optimizations of WRF and WRF-Chem models for Sicily and the Etna volcano

A. Semprebello[1,*], M. T. Caccamo[1], S. Magazù[1], G. Castorina[1], G. Munaò[1]

[1]*Department of Mathematical and Informatics Sciences, Physical Sciences and Earth Sciences of Messina University, Viale Ferdinando Stagno D'Alcontres 31, 98166 Messina, Italy*

[*]Corresponding Author email: semprebelloa@unime.it

Abstract

This paper summarizes the research activity carried out during the last year focused on themes of atmospheric physics. The main objective of the research was to test the forecasting efficiency of the WRF model and optimize it with respect to the Sicilian territory, which is very complex orographically, so as to be able to predict, with ever greater precision, the onset of extreme weather events. At the same time, given the presence on the territory of the Etna and Stromboli volcanoes, the WRF-Chem module was used in order to predict the transport and fallout of the ashes produced during volcanic eruptions. Finally, two of the cases studied are reported as an example.

Keywords: WRF, numerical weather prediction, WRF-Chem, volcanic eruption, ash fallout.

Introduction

The research activity presented is based on the use and optimization of the physical-mathematical model *Weather Research and Forecasting* (**WRF**) and its module **WRF-Chem** in relation to complex orography of the Sicilian territory.

The WRF is a *Limited Area Model* (LAM) developed in the second half of the 1990s and distributed since 2000.

The software, born from a collaboration between the NCAR, NCEP and ESRL centers, operates in the field of *Numerical Weather Prediction* (NWP) and has been designed both for applications related to research in the atmospheric sciences and for operational meteorological forecasts[1, 2].

It is an open-source model, so the source code can be consulted and modified by the user in every aspect, even in the primitive equations. For this reason it is used and improved by a huge community and further extensions have been developed, such as the WRF-Chem model for the investigation on atmospheric chemistry[1].

The architecture of the model is developed on a central core called WSF, *WRF Software Framework*, which allows the use of pre-implemented parameterization and assimilation schemes and is capable of efficiently performing *Massively Parallel* calculation operations. The *preprocessing* and the *postprocessing* phases are associated with the WSF; the first is used to provide the model with appropriately pre-processed data, the second involves the extraction of output data and the graphic production[1, 2].

The *processing* phase of the WRF consists in processing the data from *preprocessing* using specific calculation routines. The two basic routines are REAL, which works by interpolating the data vertically in the spatial coordinates of the model, and WRF which takes care of producing the output data to be analyzed or graphed using *postprocessing* softwares[2].

The dynamics of this model are governed by two *core*:

1. **ARW**, *Advanced Research WRF*, developed by NCAR, which operates on different spatial resolution scales in non-hydrostatic mode;

2. **NMM**, *Non-hydrostatic Mesoscale Model*, developed from NCEP, which allows to operate both in hydrostatic and non-hydrostatic mode.

It is generally preferred to use the former for research purposes, due to the exorbitant computing resources required for operation; the second, on the other hand, is mainly used to operationally elaborate meteorological forecasts[1, 2]. For the processing of the forecast data presented below, the WRF model with ARW dynamic solver was used.

Equations of the model

The WRF-ARW model operates by numerically integrating the Navier-Stokes equations, discretized on a grid, in their Eulerian approximation, thus neglecting viscosity but taking into account compressibility and non-hydrostatic conditions, determining the exit from the field of action of the approximation $dp = -p\rho dz$. It is necessary to consider the vertical speed as unknown and resort to the use, along the vertical axis, of the coordinates *terrain-following* η[2–4]:

$$\eta = \frac{p_h - p_{ht}}{p_{hs} - p_{ht}} \tag{1}$$

P indicates the components of hydrostatic pressure (p_h), surface pressure (p_{hs} associated with the value $\eta = 1$) and

pressure on the fictitious layer that limits the atmosphere above (p_{ht}, associated with $\eta = 0$).

The mass fraction of the air column per unit area μ is defined as:

$$\mu = p_{hs} - p_{ht} \qquad (2)$$

This representation scheme for vertical coordinates produces, for the lowest elevations, the densification of the levels near the reliefs.

We also introduce the following flux-form variables[2, 5]:

$$\boldsymbol{V} = \mu\boldsymbol{v} = (U, V, W); \qquad \Omega = \mu\dot{\eta}; \qquad \Theta = \mu\theta$$

In which $\boldsymbol{v} = (u, v, w)$ is the covariant velocity in the horizontal and vertical directions, $\dot{\eta}$ is the contravariant vertical velocity such that $\omega = \dot{\eta}$ and θ is the potential temperature.

It also takes into account the geopotential, defined as $\phi = gz$, the reciprocal of the density defined as $\alpha = \frac{1}{\rho}$, the diagnostic relation for the density $\partial_\eta\phi = -\alpha\mu$ e of the equation of state in the form $p = p_0(\frac{R_d\theta}{p_0\alpha})^\gamma$, where R_d refers to the constant of gas for *dry air*.

To include the effects of humidity it is necessary, in advance, to rewrite the previous equations relating to prognostic variables and vertical coordinates, adding a subscript d to the variables of *flux-form*, in order to specify that one is referring to *dry air*. We can therefore write[2, 4]:

$$\boldsymbol{V} = \mu_d\boldsymbol{v} = (U, V, W); \qquad \Omega = \mu_d\dot{\eta}; \qquad \Theta = \mu_d\theta$$

$$\eta = \frac{p_{dh} - p_{dht}}{\mu_d}; \qquad \mu_d = p_{dhs} - p_{dht}$$

At this point we include a term suitable to take into account the *mixing* between the various phases of the water:

$$\partial_t Q_m + (\boldsymbol{\nabla} \cdot \boldsymbol{V} q_m) = F_{Qm} \qquad (3)$$

in which:

$$Q_m = \mu_d q_m \qquad (4)$$

the term q_m considers the *mixing ratio* of the different hydrometeors included in the calculation.

$$q_m = q_v, q_c, q_i, q_r, q_s \qquad (5)$$

So the fundamental equations of the model are:

$$\partial_t U + (\boldsymbol{\nabla} \cdot V u) + \mu_d\alpha\partial_x p + \left(\frac{\alpha}{\alpha_d}\right)\partial_\eta p\partial_x\phi = F_U \quad (6)$$

$$\partial_t V + (\boldsymbol{\nabla} \cdot V v) + \mu_d\alpha\partial_y p + \left(\frac{\alpha}{\alpha_d}\right)\partial_\eta p\partial_y\phi = F_V \quad (7)$$

$$\partial_t W + (\boldsymbol{\nabla} \cdot V w) - g\left[\left(\frac{\alpha}{\alpha_d}\right)\partial_\eta p - \mu_d\right] = F_W \quad (8)$$

$$\partial_t\Theta + (\boldsymbol{\nabla} \cdot V\theta) = F_\Theta \qquad (9)$$

$$\partial_t\mu_d + (\boldsymbol{\nabla} \cdot V) = 0 \qquad (10)$$

$$\partial_t\phi + \mu_d^{-1}[(V \cdot \boldsymbol{\nabla}\phi) - gW] = 0 \qquad (11)$$

$$\partial_t Q_m + (\boldsymbol{\nabla} \cdot \boldsymbol{V} q_m) = F_{Qm} \qquad (12)$$

The different components indicated with F that appear in the equations (6), (7), (8) and (9) represent the forcing terms due to the physics of the model, *mixing* turbulent, factors of spherical projections and effects of the rotation

of the earth globe. By defining the density for *dry air* with ρ_d, the obvious consequence will be that its inverse will also be referred to *dry air*, in fact:

$$\alpha_d = \frac{1}{\rho_d} \qquad (13)$$

α takes into account the *mixing ratio* between the different classes of hydrometeors in relation to a specific volume of air, it is defined as follows:

$$\alpha = \alpha_d(1 + q_v + q_c + q_i + q_r + q_s + \ldots) \qquad (14)$$

You can also redefine the equation of state as $p = p_0(\frac{R_d\theta_m}{p_0\alpha_d})^\gamma$ and the diagnostic relation for density as $\partial_\eta\phi = -\alpha_d\mu_d$. Finally, the potential temperature θ_m, which appears in the diagnostic equation for the total pressure of vapor and *dry air* is[2]:

$$\theta_m = \theta\left[1 + \left(\frac{R_v}{R_d}\right)q_v\right] \quad \approx \quad \theta(1 + 1.61q_v) \qquad (15)$$

WRF-Chem

The environmental model WRF-Chem is developed on the basis of the WRF meteorological model and represents its "chemical" extension[6]. The main upgrade, compared to the classic physical-mathematical model WRF, is the possibility of evaluating the processes of emission, transport, transformation, dispersion and sedimentation of any type of pollutant, of both natural or anthropogenic origin[7].

WRF-Chem is part of the "online" modeling category. The operational feature of this type of model is to allow the joint evaluation of the evolution of the atmosphere from the meteorological point of view and from that of the chemical transformations associated with the presence of particulate matter. For this reason, the "online" approach is more efficient than the "offline" models, such as CHIMERE or CAMx. The latter provide for the separate description of chemical and physical transport processes, not allowing to consider the effects caused directly and indirectly by chemical compounds on meteorological phenomena. Furthermore, it is evident that the air quality is strongly influenced by the weather conditions. However, the "online" models require the use of greater computational resources and for this reason, they are generally less widespread in operational forecasting centers[7–9]. In this reference framework, the WRF-Chem model offers the possibility to evaluate phenomena of volcanic ash dispersion and is distinguished from most of the VATD models, *Volcanic Ash Transport and Dispersion*, for the ability to treat the phenomenon with the "online" approach[7]. In addition, it is possible to activate the option dedicated to the transport of SO_2.

The input parameters to carry out the simulations, in addition to the meteorological ones, are provided by the PREP-CHEM-SOURCES software. These parameters concern the height of the plume, the amount of expelled mass, the granulometric characteristics of the emitted ashes and the duration of the eruption.

Results and discussion

Two of the most significant results obtained with the application of the WRF and WRF-Chem atmospheric models on the Sicilian territory will be shown below. The analyzes were completed with the WRF modeling chain, made operational and optimized for the regional territory, operating at the University of Messina. The core version used is ARW 4.1.2 and the optimizations, studied and made thanks to the experience gained in the University's Environmental Physics research group, concern: use of specific ifort compilers, dynamic acquisition of SST (Standard Sea Temperatures), use of DEM and CORINE data, the former for static geographic data, with 20 m x 20 m resolution, the latter for land use and vegetation cover.

The Case Study of July 15th, 2020

During the afternoon of July 15th, 2020, several storm events affected the northern and eastern areas of Sicily, causing intense rainfall, the maximum accumulations of which were concentrated, in particular, on the city of Palermo, the Nebrodi and the Etnea area. The accumulated rainfall at the end of the event, recorded by the SIAS and CFD-Idro Sicilia stations, reached the following values: 134 mm (Palermo), 53.2 mm (Caronia Pomiere) and 49.0 mm (Catania).

In this reference framework, based on the good forecast results provided by the daily RUNs of the model (18 and 00 UTC) with spatial resolution for the horizontal grid equal to 3 km, a further RUN was started for the day in question, increasing the spatial resolution on the horizontal to 1 km in both directions, in order to further improve the performance of the model.

The results obtained are certainly to be considered positive since, as can be seen from the comparison between the maps for the two RUNs at different resolution (Figures 1 (3 km) and 2 (1 km)) , in addition to the quantities of rain predicted with good approximation by the 3 km RUN it is possible, with the 1 km RUN, to solve the punctual pluviometric accumulation centered on the city of Palermo with great spatial-temporal precision.
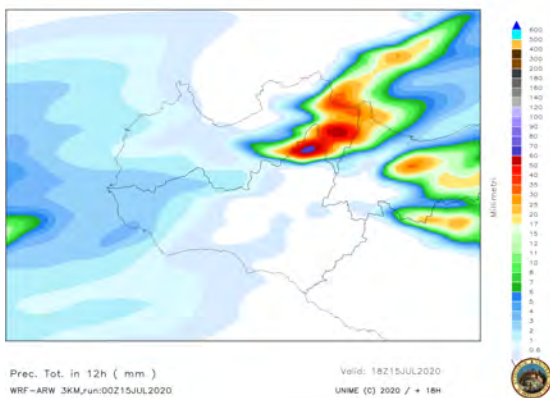
Figure 1: *Cumulative rainfall in western Sicily between 06:00 and 18:00, RUN 3 km.*
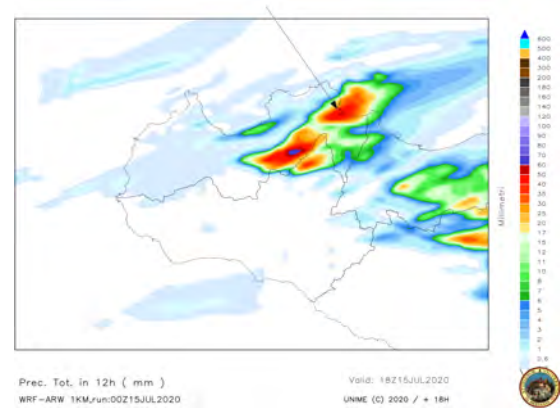
Figure 2: *Cumulative rainfall in western Sicily between 06:00 and 18:00, RUN 1 km.*

Case study: Etna ash dispersion

The results of some tests carried out with the WRF-Chem model on simulated eruptions will be presented below, in order to highlight the effect of the resolution adopted on the forecasting capabilities of the system.

The input parameters used were:

- Coordinates of the volcano, $37,427°$N e $14,181°$E.
- Duration of the eruption set at 30 minutes starting from 18:00 on the hypothetical date of 16/06/2020.
- Ash granulometry according to the database of Mastin et al.[10].
- Height of the *plume* of 5 km from which the *Mass Eruption Rate* calculated according to the relation of Stuefer et al.[11].

Three RUNs were performed, with horizontal resolution of 9, 3 and 1 km. The maps shown below highlight the effects of the different resolution for a single range of ash size, those indicated with the *vash_5* variable.

RUN 9 km - 16/06/2020
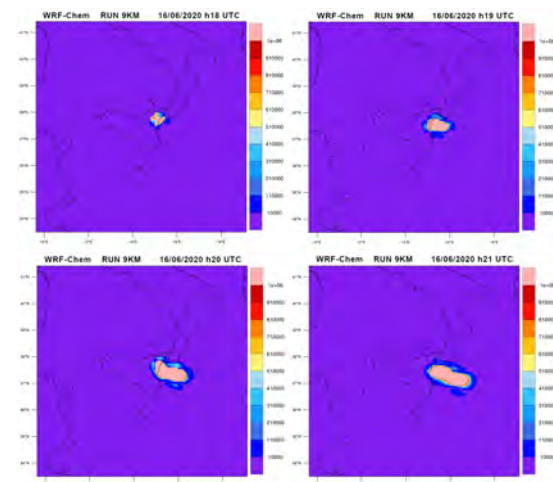
Figure 3: *vash _ 5 hourly intervals, 18 - 21 UTC.*

RUN 3 km - 16/06/2020
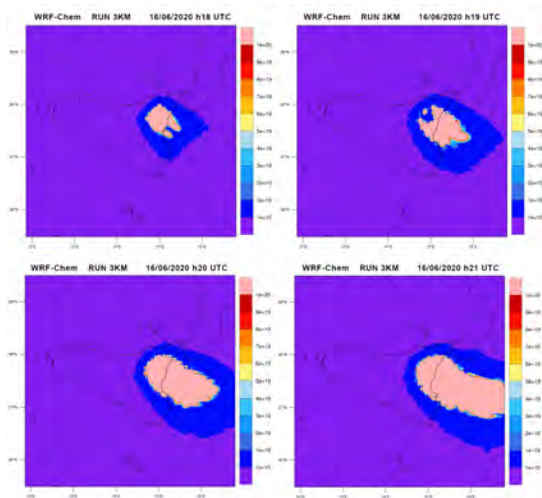
Figure 4: *vash _5 hourly intervals, 18 - 21 UTC.*

RUN 1 km - 16/06/2020
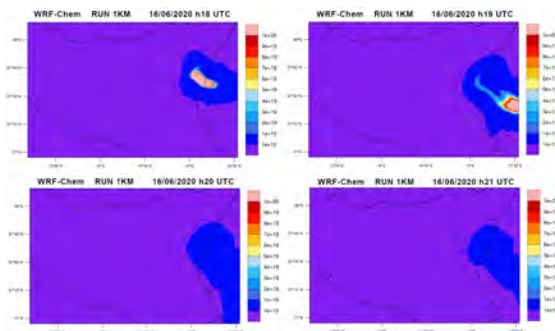
Figure 5: *vash _5 hourly intervals, 18 - 21 UTC.*

Conclusions

In the case of the WRF, it is concluded that, although the field of atmospheric sciences is extremely complex, by using LAM models, excellent forecasting results can be obtained and, even with the implementation of new updates and improvements, this aspect could play a crucial role in the area of prevention of hydrogeological risk due to extreme weather events that hit the regional and national territory with increasing frequency.

Referring to the tests carried out with the WRF-Chem environmental model, the maps presented highlight the positive and negative aspects of using a different resolution. At lower resolutions, therefore at a larger scale, it is possible to follow the path of the ashes up to very large distances. By decreasing the grid pitch the ash concentration is resolved in a much higher way. On the other hand, however, there is the need to reduce the extension of the spatial domain for computational reasons: it is possible to analyze the path only for limited distances.

It can be concluded that the domains at 1 and 3 km can provide excellent estimates for the deposition of ash within a radius of a few tens of kilometers away from the volcano in question, while using less resolved grids it is possible to make good estimates, albeit less accurate, up to a few hundred kilometers. For the reasons listed above, it is believed that the configuration that allows to obtain better estimates is that which involves the joint use of a main domain, on a larger scale, and one or more *nesting* domains.

References

[1] Powers, J. G. et al: *The Weather Research and Forecasting Model: Overview, System Efforts, and Future Directions.* Bulletin of the American Meteorological Society. **98**(8), 1717-1737 (2017).

[2] Castorina, G. et al: *Multiscale mathematical and physical model for the study of nucleation processes in meteorology.* Atti della Accademia Perloritana dei Pericolanti. Classe di Scienze Fisiche, Matematiche e Naturali. **96**(S3), A6-1-A6-12 (2018).

[3] Laprise, R.: *The Euler Equations of Motion with Hydrostatic Pressure as an Independent Variable.* Monthly Weather Review, American Meteorological Society. **120**(1), 197-207 (1992).

[4] Skamarock, W. C. et al: *A Description of theAdvanced ResearchWRF Model Version 4.* Mesoscale and Microscale Meteorology Laboratory NCAR, Colorado, USA, 2019.

[5] Ooyama, K. V.: *A Thermodynamic Foundation for Modeling the Moist Atmosphere.* Journal of the Atmospheric Sciences. **47**, 2580-2593 (1990).

[6] Grell, G. et al: *Inclusion of biomass burning in WRF-chem: impact of wildfires on weather forecasts.* Atmospheric Chemistry and Physics. **11**(11), 5289-5303 (2011).

[7] Rizza, U. et al: *Analysis of the ETNA 2015 Eruption Using WRF–Chem Model and Satellite Observations.* Atmosphere. **11**(11), 1168 (2020).

[8] Grell, G. et al: *Fully coupled online chemistry within the wrf model.* Atmospheric Environment. **39**(37), 6957-6975 (2005).

[9] Grell, G., Baklanov, A.: *Integrated modeling for forecasting weather and air quality: A call for fully coupled approaches.* Atmospheric Environment. **35**(38), 6845-6851 (2011).

[10] Mastin, L. G. et al: *A multidisciplinary effort to assign realistic source parameters to models of volcanic ash-cloud transport and dispersion during eruptions.* Journal of Volcanology and Geothermal Research. **186**(1), 10-21 (2009).

[11] Stuefer, M. et al: *Inclusion of ash and SO_2 emissions from volcanic eruptions in WRF-Chem: development and some applications.* Geoscientific Model Development. **6**(2), 457-468 (2013).

Drugs detection simulator for personalized therapy

M. Vacalebre[1,*]
[1]*Department of Mathematical and Computational Sciences, Physics Sciences and Earth Sciences (MIFT), University of Messina, Messina, Italy*

*Corresponding Author email: mvacalebre@unime.it

Abstract

This contribution describes the implementation of a tool capable of generating simulated responses by electrochemical sensors. Cyclic voltammetry can be used to determine the concentration of metabolites in the blood. Cytochromes P450 are a family of enzymes widely used to functionalize electrochemical sensors in order to carry out amperometric detection of metabolites. The main drawback is the interference due to the simultaneous co-presence of different metabolites catalysed by the same cytochrome. Therefore, this report focuses on the preliminary results regarding the development of an algorithm aimed at reproducing drugs' interference in simulated voltammograms. In upcoming studies, these voltammograms will be used to build a dataset to train a neural network to correct the altered results from electrochemical sensors

Keywords: Cytochrome P450, electrochemical biosensors, personalized therapy, multi-drug detection.

Introduction

The main objectives of personalized therapy are the decreasing of drugs' side effects and to maximize the benefit of the patient. Therapeutic drug monitoring can indicate how a specific patient metabolizes a drug. On this basis, a tailored therapy can be implemented. Patients usually take multiple medications simultaneously. Thus, an interference could occcur on the enzyme present on the sensor for the detection and the resulting concentration obtained by the analyse could be altered. To overcome these difficulties, a neural network trained on simulations could be used to correct the results from electrochemical sensors [1].

The final goal is the development of a new generation of smart electrochemical sensors for exogenous metabolites. As well known, electrochemical detection is based on electrical sensing thanks to redox reactions. In voltammetry, the measured current i_p is linked to the concentration C of chemical species involved according to Randles-Sevcik (Eq.1).

$$i_p = 0.4463 nFAC \left(\frac{nFvD}{RT} \right)^{\frac{1}{2}} \qquad (1)$$

In Equation 1, A is the electrochemical active area of the working electrode, v is the scan rate of the applied potential, n is the number of electrons involved in the redox reaction, F is the Faraday constant, D is the diffusion coefficient, R is the universal gas constant and T is the temperature. In 2011, Carrara et al. [2] established a mathematical model to approximate voltammograms to Gaussian curves.In Equation 2, the single contributions of

the specific drugs are summed as Gaussian components:

$$i(V) = \sum_{\forall k} \Gamma_k C_k \left\{ \prod_{\forall j \neq k} A_k(C_j) \right\} e^{-\frac{(V - V_k)^2}{\sigma_k^2}} \qquad (2)$$

where the Γ_k parameter is:

$$\Gamma_k = 0.4463 \left(\frac{n^3 F^3 v D_k}{RT} \right)^{\frac{1}{2}} A \qquad (3)$$

The possible interaction of the drugs is considered in $A_k(C_j)$. In case of enzymatic-activation, the current peak's amplitude of k-drug A_k will increase depending on the concentration of j-drug (C_j), as shown in Equation 4. On the contrary, A_k will decrease in case of enzymatic-inhibition, as shown in Equation 5.

$$A_k(C_j) = A_{k0}(1 + \varepsilon w_j) \qquad (4)$$
$$A_k(C_j) = A_{k0}(1 - \varepsilon w_j) \qquad (5)$$

ε is linked to the interference strength between the considered drugs and ranges from zero to one [2]. w_j is the speed of the enzymatic reaction and depends on the concentration of the interfering substrate (Eq.6).

$$w_j = \frac{v_{max} C_j}{k_m + C_j} \qquad (6)$$

In Equation 6, Michaelis-Menten kinetics is considered to express the interaction between the drug and the cytochrome. v_{max} is the maximum value of the reaction rate and k_m is the drug concentration when the reaction rate reaches the half-maximum value.

Some details are reported in the next sections.
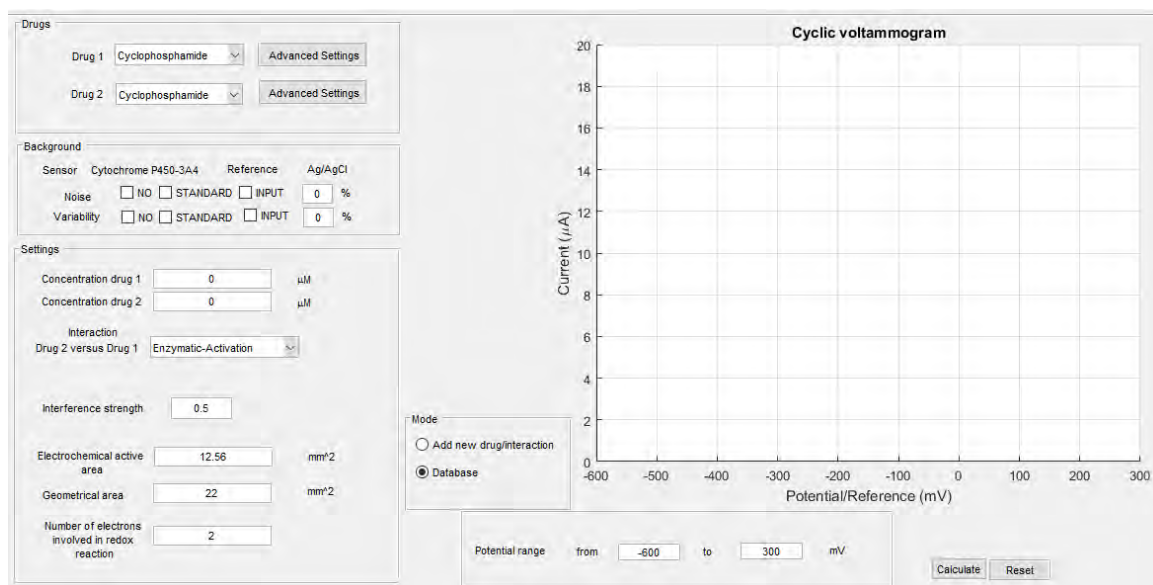
Simulator and database

Figure 1: *Graphical user interface of the simulator*

The graphical user interface (Fig.1) and the algorithm were developed on MATLAB ® (MathWorks Inc., Natick, MA), whereas the drugs' database was managed on MySQL® (MySQL AB, Sweden). The user can decide either to work with drugs already present in the database (Mode "Database") or to add a new record to the database and use a new drug (Mode "Add a new drug"). The database consists of eleven drugs (records) and five related parameters (fields)(Tab.1). Electrochemical experiments found in literature [1]-[16] were exploited to build this basic database. Future improvements of the tool will be addressed to extend the list. Currently, it includes four chemotherapeutic agents, two anti-inflammatories, one cough suppressant, one anti-obesity drug, two anaesthetics and a fever-reducing painkiller. The simulator takes into account the noise and the variability that could interfere in a real experiment. The user has the possibility to set them in the "Background" panel. Finally, different enzymatic kinetics can be simulated in case of multi-detection by a single cytochrome P450: activation, if the preference of a drug increases the current peak of a second drug in the voltammogram; inhibition, in the reversed case. If the two drugs don't interfere each other on the enzyme, "nointeraction" option can be used. The simulation can be repeated with different values of "interference strength", which indicates the intensity of this dynamic. Finally, the user can save the final graph and related data.

Drug	Sensitivity [nA/μM*mm^2]	Peak position [mV]	Peak width [mV]	k_m [μM]	v_{max} [nmol/min/mg]	Reference
Cyclophosphamide	0.63	-296	100	7000	2.3	[2],[3]
Dextromethorphan	6.63	-392	200	1155	11.9	[2],[4],[5]
Flurbiprofen	0.46	60	200	1.9	343	[2],[6]
Naproxen	0.25	-10	200	143	0.84	[2],[7]
Propofol	0.32	600	200	18	2.6	[8],[9]
Paracetamol	2.46	700	400	474	0.79	[8],[10]
Midazolam	48.8	-700	200	7.46	0.696	[11],[12]
Etoposide	9.1	220	150	77.7	314	[13],[14]
Ifosfamide	0.4	-450	150	8.1	1.2	[3],[13]
Ftorafur	3.9	-450	150	15	0.13	[13],[15]
Benzphetamine	20.5	-200	150	240	3.9	[1],[2],[16]

Table 1: *Database*

Simulations and Validation

Equations 2-5 are the basis of the algorithm and they have never been tested before. Thus, the first simulations were carried out to check the correct variation in k-drug's current peak in relation to j-drug's concentration (Eq. 2). Unfortunately, the first simulations failed both in case of

activation and inhibition. After a careful revision of the equations, an inaccuracy was found in Eq. 4-5. Indeed, the interference strength is a pure number, whereas the reaction rate is a variation of concentration per unit time (nmol/min/mg). Thus, equations 7-8 were proposed as revised version of equations 4-5: the maximum reaction rate v_{max} was the missing factor to obtain a consistent equation.

$$A_k(C_j) = A_{k0} \left(1 - \varepsilon \frac{w_j}{v_{max}} \right) \qquad (7)$$

$$A_k(C_j) = A_{k0} \left(1 + \varepsilon \frac{w_j}{v_{max}} \right) \qquad (8)$$

New simulations were carried out to validate Eq. 7-8. In the following tests, the data of the considered drugs are reported in Tab.1 and the maximum interference strength was applied. Firstly, in case of enzymatic-activation, the interaction between Naproxen (NP) and Flurbiprofen (FL) on cytochrome P450 was simulated. It is known from literature that Naproxen (NP) enhances the current related to the Flurbiprofen (FL) detection [2]. In this test, the concentration of Flurbiprofen is kept constant at 200 μM, whereas Naproxen's concentration increases from 0 μM to 200 ,300, 400 and 500 μM. A simulated detection carried out by screen-printed electrodes functionalized with cytochrome P450 2C9 is considered [2].The simulation is shown in Fig.2. The amplitude of the peak related to Flurbiprofen (FL) increases with Naproxen (NP) concentration, even though Flurbiprofen (FL) concentration is kept constant.
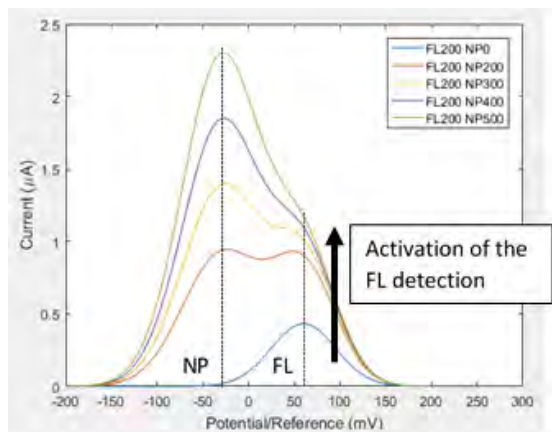
Figure 2: *Simulated voltammogram in case of enzymatic-activation in Flurbiprofen/Naproxen interaction.*

Analogously, in case of enzymatic-inhibition, the interaction between Cyclophosphamide (CP) and Dextromethorphan (DX) was simulated. It has been already demonstrated that Dextromethorphan (DX) inhibites the detection of Cyclophosphamide (CP) [2]. Cyclophosphamide's concentration is kept constant at 400 μM, whereas Dextromethorphan's concentration increases from 0 to 200 and 400 μM. The simulated detection is carried out by screen-printed electrodes functionalized with cytochrome P450 3A4 [2]. The simulation,

shown in Fig. 3, highlights how the peak amplitude related to Cyclophosphamide (CP) decreases in relation to the increasing concentration of Dextromethorphan (DX), even if Cyclophosphamide (CP) is unvaried.
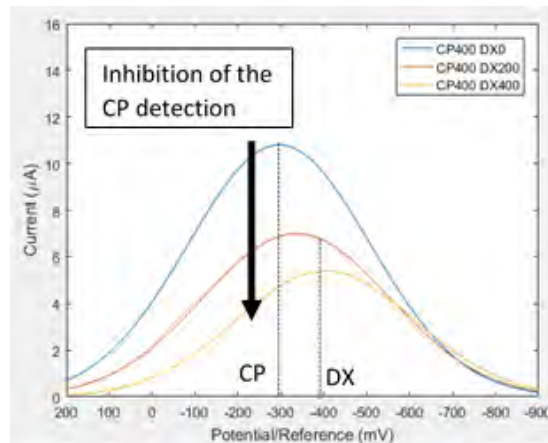
Figure 3: *Simulated voltammogram in case of enzymatic-inhibition in Cyclophosphamide/Dextromethorphan interaction.*

Conclusions

In summary, a simulator and the related GUIs were implemented on MATLAB®. A database connected to the tool was developed on MySQL® to record drugs and their properties. After an initial inconsistency between simulations and reality, it was concluded that there was a discrepancy in dimensional analysis in the paper used as literature reference, so the equations were corrected. Successively, the results indicated that simulations had a good likelihood of real drugs' interactions. Two real cases of interference on cytochrome P450 were used to validate the system: Cyclophosphamide/Dextromethorphan in case of enzymatic-inhibition; Naproxen/Flurbiprofen in case of enzymatic-activation. In upcoming improvements, the database will incorporate a larger number of drugs and related parameters. Finally, this tool will be exploited for the creation of synthetic datasets to train neural networks. Thanks to artificial intelligence, the altered results from electrochemical sensors will not be affected anymore by drugs interation in therapeutic drug monitoring.

Acknowledgments

out my research in their labs. Furthermore, I thank my PhD tutor Prof. Enza Fazio and co-tutor Prof. Sabrina Conoci for their support and encouragement in my PhD work and for the help in the revision of this report.

References

[1] Carrara, S. et al.: *Dynamical spot queries to improve specificity in p450s based multi-drugs monitoring.*, In: IEEE/ICME International Conference on Complex Medical Engineering. Tempe, 2009.

[2] Carrara, S. et al.: *Multi-panel drugs detection in human serum for personalized therapy.*, Biosens. Bioelectron., 26(9) , 3914-3919 (2011).

[3] Chang, T. K.H. et al: *Differential activation of cyclophosphamide and ifosphamide by cytochromes P-450 2B and 3A in human liver microsomes.*, Cancer Res., 53(23), 5629-5637 (1993).

[4] Rezaei, B. et al.: *Application of modified carbon quantum dots/multiwall carbon nanotubes/pencil graphite electrode for electrochemical determination of dextromethorphan.*, IEEE Sens. J., 16(8), 2219-2227 (2016).

[5] Von Moltke, L. L. et al.: *Multiple human cytochromes contribute to biotransformation of dextromethorphan in-vitro: role of CYP2C9, CYP2C19, CYP2D6, and CYP3A.*, J. Pharm. Pharmacol., 50(9), 997-1004 (1998).

[6] Tracy, T. S. et al.: *Role of cytochrome P450 2C9 and an allelic variant in the 4-hydroxylation of (R)- and (S)-flurbiprofen.*, Biochem. Pharmacol., 49(9), 1269-1275 (1995).

[7] Miners, J. O. et al.: *Cytochromes P450, 1A2, and 2C9 are responsible for the human hepatic O-demethylation of R-and S-naproxen.*, Biochem. Pharmacol., 51(8), 1003-1008 (1996).

[8] Stradolini, F. et al.: *An IoT solution for online monitoring of anesthetics in human serum based on an integrated fluidic bioelectronic system.*, IEEE Trans. Biomed. Circuits Syst., 12(5), 1056-1064 (2018).

[9] Guitton, J. et al.: *Possible involvement of multiple human cytochrome P450 isoforms in the liver metabolism of propofol.*, Br. J. Anaesth., 80(6), 788-795 (1998).

[10] Patten, C. J. et al.: *Cytochrome P450 enzymes involved in acetaminophen activation by rat and human liver microsomes and their kinetics.*, Chem. Res. Toxicol., 6(4), 511-518 (1993).

[11] Panahi, Y. et al.: *High sensitive and selective nano-molecularly imprinted polymer based electrochemical sensor for midazolam drug detection in pharmaceutical formulation and human urine samples.*, Sens. Actuators B Chem., 273, 1579-1586 (2018).

[12] Wang, J. et al.: *Midazolam α-hydroxylation by human liver microsomes in vitro: inhibition by calcium channel blockers, itraconazole and ketoconazole.*, Pharmacol. Toxicol., 85(6), 157-161 (1999).

[13] Baj-Rossi, C. et al.: *Electrochemical detection of anti-breast-cancer agents in human serum by cytochrome P450-coated carbon nanotubes.*, Sensors, 12(5), 6520-6537 (2012).

[14] Zhuo, X. et al.: *Kinetics and regulation of cytochrome P450-mediated etoposide metabolism. Drug metabolism and disposition*, Drug Metab. Dispos., 32(9), 993-1000 (2004).

[15] Spoelstra, E. C. et al.: *Measurement of in vitro cellular pharmacokinetics of 5-fluorouracil in human and rat cancer cell lines and rat hepatocytes using a flow-through system.*, Cancer Chemother. Pharmacol., 27(4), 320-325 (1991).

[16] Furuya, H. et al.: *Site-directed mutageneses of rat liver cytochrome P-450d: catalytic activities toward benzphetamine and 7-ethoxycoumarin.*, Biochemistry, 28(17), 6848-6857 (1989).

Seminari
del Dottorato di Ricerca in Fisica
(Svolti nel 2020)

SEMINARI DEL DOTTORATO DI RICERCA IN FISICA

DOTTORATO DI RICERCA IN FISICA DELL'UNIVERSITÀ DEGLI STUDI DI MESSINA

6 Febbraio 2020, ore 15.00, Incubatore d'Impresa Aula HT10/11-T
V.le F. Stagno d'Alcontres 31, 98166 S. Agata, Messina

Chernobyl: il mondo dopo l'uomo. La catastrofe del 1986, fra fatti ed emozioni

Matteo Arrigo & Prof.ssa Marina Trimarchi
Dipartimento di Scienze Matematiche e Informatiche, Scienze Fisiche e Scienze della Terra, Università degli Studi di Messina

Abstract

Il 26 Aprile 1986, all'1:23:40, un'esplosione al reattore 4 della centrale nucleare di Chernobyl provoca la diffusione in atmosfera di una spaventosa quantità di sostanze radioattive. Chi ha vissuto i giorni successivi all'incidente, anche a migliaia di chilometri di distanza dalla catastrofe, ricorda distintamente lo sgomento e la paura perla comparsa di un nuovo nemico invisibile, descritto dai telegiornali dell'epoca come una nube rossa che, partendo dall'Ucraina, si diffondeva per tutta l'Europa. A quasi trentacinque anni di distanza, le conseguenze dell'incidente sono ancora enormi, soprattutto nella zona che circonda il reattore. Il video maker messinese Matteo Arrigo aveva 7 anni al momento della catastrofee ne è rimasto talmente colpito da decidere, molti anni dopo, di recarsi personalmente sui luoghi dell'incidente, girando un reportage che mostrerà, raccontando la sua testimonianza, nel corso di questo seminario. Il funzionamento del reattore di Chernobyl, le fasi principali dell'incidente le sue conseguenze sull'ambiente verranno descritte da Marina Trimarchi, docente di Laboratorio di Fisica Nucleare presso il CdL in Fisica dell'Università di Messina.

⋆ ⋆ ⋆ ⋆ ⋆

DOTTORATO DI RICERCA IN FISICA DELL'UNIVERSITÀ DEGLI STUDI DI MESSINA

17 Febbraio 2020, ore 15.00, Incubatore d'Impresa Aula HT6-1
V.le F. Stagno d'Alcontres 31, 98166 S. Agata, Messina

From artificial atoms to quantum computers

Dott. Roberto Stassi
Dipartimento di Scienze Matematiche e Informatiche, Scienze Fisiche e Scienze della Terra, Università degli Studi di Messina

Abstract

Quantum computers are machines that could perform specific calculations that our existing classical computer cannot. Among several proposed platforms to build a quantum computer, only one has reached an important level of maturity, superconducting qubits [1]. In this talk I will show how a quantum bit is made, and how a quantum computer is built using superconducting circuits. Furthermore, I will discuss the main problems that affect quantum computers and that, till now, prevent the possibility to have a practical advantage respect the classical ones.

[1] Arute, F., et al. "Quantum supremacy using a programmable superconducting processor." Nature 574.7779 (2019): 505-510.

Dottorato di Ricerca in Fisica dell'Università degli Studi di Messina
19 Febbraio 2020, ore 15.00, Sala seminari, CNR-IPCF
V.le F. Stagno d'Alcontres 37, S. Agata, Messina

Laboratory Studies of Organic Chemistry in Space: a path towards prebiotic chemistry

Dott.ssa Angela Ciaravella
INAF-Osservatorio Astronomico di Palermo

Abstract

A large inventory of molecules have been discovered in interstellar and circumstellar environments, the majority of them being complex organic molecules. While small species detected in molecular clouds are often exotic unsaturated radicals, organic molecules are largely partly hydrogen-species, i.e. structures containing three or more H-atoms with no C-C multiple bonds. Many of these molecules are also of biological interest. The identification of a relevant number of organic molecules in interstellar spectra has suggested a possible connection between interstellar chemistry and the origin of life. However, the mechanisms by which complex organics in space are formed remains largely unknown. Gas-phase reactions, i.e. ion-molecule and atom-radical reactions, can produce molecules up to intermediate complexity. Icy mantes around dust grains offer a solid surfaces where the local high density can enable different routes through which complex species can be formed.The synthesis of complex organics on grain surfaces can be accelerated by thermal processes, radiation, and cosmic rays particles. Laboratory irradiation of interstellar ice analogues has highly contributed to understand the molecular complexity in space. In this talk I will give an overview of recent achievements in laboratory astrochemistry.

$\star\,\star\,\star\,\star\,\star$

Dottorato di Ricerca in Fisica dell'Università degli Studi di Messina
25 Febbraio 2020, ore 15.00, Incubatore d'Impresa Aula HT6-1
V.le F. Stagno d'Alcontres 31, 98166 S. Agata, Messina

Exploiting ultrastrong coupling regime for quantum computation

Dott. Roberto Stassi
Dipartimento di Scienze Matematiche e Informatiche, Scienze Fisiche e Scienze della Terra, Università degli Studi di Messina

Abstract

Using superconducting circuits, is possible to achieve very strong coupling between a twolevel system and a cavity field [1]. In this second talk, I will discuss two proposals that make use of ultrastrong coupling regime to improve the performance of quantum computers. In the first one, I will show how to increase the coherence time of a superconducting qubit for a quantum memory [2]. The coupling among superconducting qubits is restricted only to nearest-neighbours. This is one of the limiting factors for the scalability of this technology, and a problem of central importance. In the second part of this talk, I will discuss a proposal for a scalable architecture to simultaneously connect many distant pairs of logical qubits [3].

[1] Yoshihara, F., et al. "Superconducting qubit–oscillator circuit beyond the ultrastrongcoupling regime." Nature Physics 13.1 (2017): 44-47.

[2] Stassi, R., and Nori, F. "Long-lasting quantum memories: Extending the coherence time of superconducting artificial atoms in the ultrastrong-coupling regime." Physical Review A 97.3 (2018): 033823.

[3] Stassi, R., Cirio, M., and Nori, F. "Quantum bus building-block for a scalable quantum computer architecture." arXiv preprint arXiv:1902.06569 (2019).

$\star\,\star\,\star\,\star\,\star$

Dottorato di Ricerca in Fisica dell'Università degli Studi di Messina

15 Maggio 2020, ore 10.00, Webinar su Piattaforma informatica *Microsoft Teams*

Laser synthesis of plasmonic platforms for SERS-based therapeutic drug monitoring

Prof. Paolo M. Ossi

Dipartimento di Energia, Politecnico di Milano

Abstract

Therapeutic Drug Monitoring (TDM) is a clinical practice to selectively determine the concentration of a drug in a biological fluid, usually blood plasma. TDM is critically important for Narrow Therapeutic Index (NTI) drugs, with small differences between therapeutic and toxic doses. Among others, this is true of anti-epileptic drugs (AEDs). For a fraction of AEDs the blood concentration is determined in the lab via immunoassay tests, or High-Performance Liquid Chromatography coupled to Mass Spectrometry (HPLC-MS). Both techniques are time consuming and costly. We focus on the use of light scattering with ad hoc engineered plasmonic substrates as a fast,comparatively inexpensive,complementary TDM approach for AEDs. Noble metal (Au; Ag) nanoparticles (NPs), grown by pulsed laser ablation (PLA) of a high purity target are synthesized along two paths. If ablation is carried out using ns pulses in a high-density inert, massive gas (Ar) NPs form in the expanding plasma plume. If the process is performed with ns, or ps pulses in a transparent Liquid (PLAL) a colloidal solution of metal NPs is obtained and is ultrasonically sprayed and let dry on the same kind of inert support (glass, 100-Si) as for gas synthesized NPs. In both cases, self-assembled NP arrays are obtained. The few relevant process parameters that affect the size, size distribution, shape and optical properties of the NPs and the NP arraysare ambient gas pressure and laser pulse number for PLA,as well as pulse duration and laser energy density for PLAL. The ability to adjust the wavelength of the Surface Plasmon Resonance (SPR) peak opens the way to Surface Enhanced Raman Scattering (SERS) measurements of samples of different origin with various AEDs at concentrations of clinical interest using the above sensors. The results of the investigation on the SERS response of a new AED of relevant clinical interest (Perampanel), together with the stringent control ofsensor performance are critically discussed.

[1] C. Zanchi et al., Appl.Phys. A 125, 311 (2019).

[2] M. Tommasini et al., Nanomaterials 9, 677 (2019).

[3] N.R. Agarwal et al. Appl. Surf. Sci. 466, 19-27 (2019).

[4] C. Zanchi et al. Appl.Surf.Sci. 507, 145109 (2020).

⋆ ⋆ ⋆ ⋆ ⋆

Dottorato di Ricerca in Fisica dell'Università degli Studi di Messina

4 Giugno 2020, **ore 10.00, Webinar su Piattaforma informatica** *Microsoft Teams*

Tailoring Mid InfraRed Radiation at the nanoscale

Dott. Jean-Jacques Greffet

Université Paris-Saclay, Institut d'Optique Graduate School, CNRS, Laboratoire Charles Fabry, Palaiseau, France.

Abstract

With the advent of fabrication and imaging at the nanoscale, many unexpected properties of thermal radiation have been explored in the last twenty years. The first part of the talk will be devoted to a review of key features including spatial coherence of incandescent sources, temporal coherence of incandescent sources in the near field, enhanced energy density in the near field, enhanced radiative heat transfer at the nanoscale, validity of a local permittivity at the nanoscale. In the second part of the talk, recent results on an incandescent source that can be modulated beyond 10MHz, six orders of magnitude faster than commercially available hot membranes, will be presented.

⋆ ⋆ ⋆ ⋆ ⋆

Dottorato di Ricerca in Fisica dell'Università degli Studi di Messina

Serie di seminari Webinar in collaborazione con Area Science Park (Padriciano - Trieste) su: Generazione d'impresa, piattaforme tecnologiche e Progetti Europei

Interventi

24 giugno 2020: *Maddalena Furlan*

15.00 – 15.30: Area Science Park e Progetto Argo
15.30 – 16.30: Infrastrutture di Ricerca + Open Innovation: le Piattaforme Tecnologiche di Area Science Park
16.30 – 17.00: Question & Answers

30 giugno 2020: *Roberto Pillon & Maurizio Caradonna*

15.00 – 16.45: Modelli di generazione d'impresa: l'esperienza di Area Science Park nel supporto alle start up*
16.45– 17.00: Question & Answers

06 luglio 2020: *Roberto Pillon & Maurizio Caradonna*

15.00 – 16.45: Modelli di generazione d'impresa: l'esperienza di Area Science Park nel supporto alle start up*
16.45– 17.00: Question & Answers

17 luglio 2020: *Alberto Soraci*

15.00 – 17.00: L'esperienza nella progettazione europea di Area Science Park: da Horizon ad Horizon Europe. Le call di Horizon e come leggere tra le righe

⋆ ⋆ ⋆ ⋆ ⋆

Dottorato di Ricerca in Fisica dell'Università degli Studi di Messina
20 Luglio 2020, ore 15.00, Webinar su Piattaforma informatica *Microsoft Teams*

A dusty Universe. Composition and nature of interstellar dust as revealed by light scattering.

Dott.ssa Maria Antonia Iatì
CNR-IPCF, Messina

Abstract

Dust is ubiquitous in the Universe. It's present in the Solar System and in a great variety of regions in the interstellar medium where it gives origin, mixed with the gas, to the amazing interstellar clouds. Once considered mainly as an annoying fog preventing a clear view of the stars, only in the last half century dust has found its right place in astronomy. It has become accepted that dust is a crucial component of galaxies and plays many important roles in star formation processes, in the evolution of the interstellar medium, in planet formation, and in promoting a complex chemistry that may in appropriate circumstances be the feedstock of biochemistry.Analytical and computational techniques enable to model and study the optical properties of interstellar dust, enlarging our knowledge about their composition, nature, and morphology.We describe some current approaches, discussing their potential and possible limitations.

⋆ ⋆ ⋆ ⋆ ⋆

Dottorato di Ricerca in Fisica dell'Università degli Studi di Messina
26 Novembre 2020, ore 15.30, Webinar su Piattaforma informatica *Microsoft Teams*

Experimental investigation of microscopic engines and critical Casimir forces by optical tweezers

Dott. Alessandro Magazzù
CNR-IPCF, Messina

Abstract

Since their invention in 1986, optical tweezers have become a key technique for the contactless manipulation and investigation of microscopic and nanoscopic particles of different nature, such as biomolecules, bacteria, cells, plasmonic nanoparticles, nanotubes and nanowires. Furthermore, optical tweezers are also a powerful tool for nanotechnology allowing the manipulation and assembling of biomolecules, cells, and nanostructures, and measuring and exerting forces at nanoscale.Following this idea, optical tweezers have been recently used to measure critical Casimir forces (CCFs) between colloidal particles.Historically CCFs have never aroused a lot of attentions and they have always been considered mostly like a scientific curiosity. However, now, thanks to the advances of nano-science anew interest in the CCFs has blossomed because of their promising applications in nano-technology.For instance, they can be used to manipulate objects (e.g.by controllable periodic deformations of chains), to assemble devices (e.g. via the self-assembly of colloidal molecules). These applications of CCFs can be possible thanks to their piconewton strength and nanometric action ranges, which match the requirements of nanotechnology. Furthermore, CCFs can be finely tuned asa function of temperature and present a strong dependence on the surface properties of the confining objects. In this talk, after a brief introduction about optical trapping mechanism and CCFs, the realization of a microscopic engine and the experimental effects of CCFs on the free dynamics of a couple of colloidal particles will be discussed.

$$\star\,\star\,\star\,\star\,\star$$

Dottorato di Ricerca in Fisica dell'Università degli Studi di Messina
10 Dicembre 2020, ore 15.30, Webinar su Piattaforma informatica *Microsoft Teams*

Unconventional multi-photon blockade in hybrid quantum systems

Dott. Shilan Ismael Abo
Nonlinear Optics Division, Faculty of Physics, Adam Mickiewicz University, Poznan, Poland

Abstract

Many applications in quantum technologies, such as quantum cryptography or optical quantum information processing, require light sources with a precise number of photons. Photon (phonon) blockade is the quantum phenomenon that occurs in a driven nonlinear system, in which a system cannot emit more than one photon each time. These effects are described by the sub-Poissonian excitation-number statistics. In this talk, we describe unconventional photon blockade in a hybrid system which is comprised of photonic and phononic mode such that a combined photon-phonon mode exhibits sub-Poissonian statistics while each mode,if analyzed separately, exhibits super-Poissonian statistics. Moreover, I will show that it is possible to achieve photon blockade in the driven cavity without an atom or any other kind of nonlinearity, but instead coupled to a nonlinear (i.e., squeezed) reservoir [1].

[1] A. Kowalewska-Kudlaszyk, S. I. Abo, G. Chimczak, J. Perina, F. Nori, and A. Miranowicz, Twophoton blockade and photon-induced tunneling generated by squeezing, Physical Review A 100 (2019), 10.1103/physreva.100.053857.

$$\star\,\star\,\star\,\star\,\star$$

Dottorato di Ricerca in Fisica dell'Università degli Studi di Messina
17 Dicembre 2020, ore 15.30, Webinar su Piattaforma informatica *Microsoft Teams*

Changing ground state molecular properties in optical cavities: an ab-initio study

Dott. Enrico Ronca
Istituto per i Processi Chimico-Fisici del CNR, Pisa

Abstract

Manipulation of matter properties using strong coupling to photons is becoming a hot research topic in physics and chemistry [1,2]. Recent experimental studies demonstrated that strong-light matter coupling in optical cavities can be used to inhibit, catalyze and increment the selectivity of chemical reactions. In the past few years, a lot of progress has been made in the field, but a complete understanding of the possibilities offered by cavity QED in chemistry is still far from being achieved.In quantum optics, strong light-matter interaction has been extensively investigated since the 1950s using model Hamiltonians and a broad range of fascinating insights has been accessed. However, these approaches are not quantitative. For instance they typically cannot predict changes in the molecular ground state. In this talk, I will present some recent ab-initio theoretical studies we performed on chemical systems. Quantum electrodynamics coupled-cluster (QED-CC) [3], configuration interaction (QED-FCI) [4] and density functional (QEDFT) [2] approaches have been applied. We have demonstrated that molecular ground states can be modified by optical cavities. Considering the size of the effects, we are convinced that our predictions can be observed experimentally. In the last part of the talk, I will show some interesting perspective applications of this fascinating field.

[1] T. W. Ebbesen, Acc. Chem. Res., 49, 2403 (2016).

[2] M. Ruggenthaler, N. Tancogne-Dejean, J. Flick, H. Appel, and A. Rubio, Nature Rev. Chem., 2, 0118 (2018).

[3] T. S. Haugland, E. Ronca, E. F. Kjøonstad, A. Rubio and H. Koch, arXiv, 2005.04477, 2020 (Accepted in Physical Review X).

[4] T. S. Haugland, C. Schäfer, E. Ronca, A. Rubio and H. Koch, soon on ArXiv.
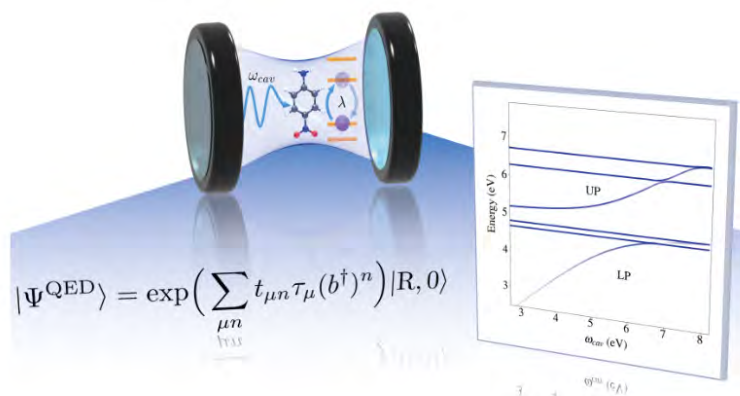
Premi e Riconoscimenti

Premio della Società Italiana di Fisica (SIF) per la migliore comunicazione della Sezione 6 - Fisica applicata, acceleratori e beni culturali al Congresso Nazionale SIF 2020 al Dott. Giuseppe Paladini, dottore di Ricerca in Fisica del XXXII ciclo

Il Dott. Giuseppe Paladini, dottore di Ricerca in Fisica del XXXII ciclo, Tutor. Prof.ssa Valentina Venuti, ha vinto il Premio della Società Italiana di Fisica (SIF) per la migliore comunicazione della Sezione 6 - Fisica applicata, acceleratori e beni culturali al Congresso Nazionale SIF 2020, dal titolo "Neutronographic investigation of the effects of CaLoSiL and Nano Estel on the water absorption properties of Pietra d'Aspra limestone". Il premio sarà consegnato in occasione della cerimonia inaugurale del prossimo Congresso SIF che si svolgerà dal 13 al 17 settembre 2021 a Milano.

https://www.sif.it/attivita/congresso/106/comunicazioni

⋆ ⋆ ⋆ ⋆ ⋆

Selezione tra le Migliori Comunicazioni al Congresso Nazionale SIF 2020 per il Dott. Paolo Polimeno, dottorando del XXXIV ciclo e per la Dott.ssa Antonina Rosano, dottoranda del XXXV ciclo

La comunicazione dal titolo "Position locking of a resonant gain assisted metallic/dielectric nano-shell in an optical tweezers." del Dott. Paolo Polimeno, dottorando del Corso di Dottorato di Ricerca in Fisica del XXXIV ciclo, tutor Prof.ssa Rosalba Saija e, la comunicazione dal titolo "Measurements of hadronic resonance production with ALICE" della Dott.ssa Antonina Rosano, dottoranda del Corso di Dottorato di Ricerca in Fisica del XXXV ciclo, tutor Prof. Giuseppe Mandaglio, sono state selezionate al Congresso Nazionale SIF 2020 come comunicazioni particolarmente meritevoli e pertanto verranno pubblicate in un fascicolo speciale de Il Nuovo Cimento - Colloquia and Communications in Physics.

https://www.sif.it/attivita/congresso/106/comunicazioni-per-pubblicazione

Organizzazione
del Dottorato di Ricerca
in Fisica

Coordinatore:
Prof.ssa Vincenza Crupi

Direttore del Dipartimento di Scienze Matematiche e Informatiche, Scienze Fisiche e Scienze della Terra - Università degli Studi di Messina:
Prof. Fortunato Neri

Segretaria della Scuola di Dottorato:
Dott.ssa Paola Donato

Delegato per il sito Web del Dottorato di Ricerca in Fisica:
Prof. Alessandro Sergi

Piano didattico del Dottorato di Ricerca in Fisica dell'Università degli Studi di Messina relativo al Ciclo XXXIV con competenze avanzate in:

Fisica Nucleare e Subnucleare
Fisica della Materia
Fisica Applicata

Totale ore Lezioni di Carattere Generale : 90 Ore
Totale minimo di ore di Carattere Specialistico : 60 Ore

150 ore minime in Totale per Dottorando.

⋆⋆⋆ Area di Fisica Nucleare e Subnucleare ⋆⋆⋆
Referenti Proff.ri A. Trifirò e G. Mandaglio

Lezioni di interesse generale (12 ore):

1. Dinamica delle Reazioni Nucleari (4 ore);

2. Risonanze barioniche e sezioni d'urto adroniche (4 ore);

3. Fisica delle particelle con sonde elettromagnetiche e leptoniche (4 ore);

Lezioni di Interesse Specialistico (Moduli ciascuno di 10 ore; tot. 80 ore):

1. Teoria delle Reazioni Nucleari;

2. Reazioni di multiframmentazione o formazione di nuclei superpesanti;

3. Teoria delle Interazioni Fondamentali;

4. Fasci Ionici in Plasmi prodotti da Laser;

5. Rivelazione e analisi dei prodotti di reazione in Fisica Nucleare, Subnucleare e Astrofisica;

6. Risonanze barioniche e sezioni d'urto adroniche in Fisica delle Particelle;

7. Acquisizione, elaborazione dei dati e procedure di simulazione nei processi nucleari;

8. Emissione di fotoni e particelle in processi nucleari;

⋆⋆⋆ Area di Fisica della Materia ⋆⋆⋆
Aspetti Teorici
Referente Prof. S. G. Prestipino

Lezioni di interesse generale (12 ore):

1. Fisica Teorica e Computazionale dello stato liquido della materia.

Lezioni di Interesse Specialistico (Moduli ciascuno di 10 ore, tot. 50 ore):

1. Formazione di aggregati in fluidi con interazioni microscopiche antagoniste;

2. Comportamento di fase complesso in sistemi caratterizzati da interazioni semplici;

3. Teoria della nucleazione di solidi cristallini da fasi liquide;

4. Simulazioni numeriche di liquidi a legame idrogeno;

5. Simulazione della dinamica quantistica dissipativa.

⋆⋆⋆ Area di Fisica della Materia ⋆⋆⋆
Fisica dei sistemi Disordinati
Referente Prof.ssa G. D'Angelo

Lezioni di interesse generale (12 ore):

1. Disordine e Localizzazione (4 ore)

2. La transizione vetrosa (4 ore)

3. Dinamica Ionica in sistemi disordinati (4 ore)

Lezioni di Interesse Specialistico (Moduli ciascuno di 10 ore, tot. 30 ore):

1. Dinamica vibrazionale e rilassamenti in solidi amorfi;

2. Spettroscopia dielettrica in materiali a conduzione ionica;

3. Spettroscopia Meccanica in polimeri.

⋆⋆⋆ Area di Fisica della Materia ⋆⋆⋆
Nanosistemi e Fotonica
Referente Prof. F. Neri

Lezioni di interesse generale (12 ore):

1. Materiali nano strutturati (4 ore);

2. Sistemi quantistici complessi (4 ore);

3. Nano-Ottica (4 ore).

Lezioni di Interesse Specialistico (Moduli ciascuno di 24 ore, tot. 72 ore):

1. Nanomateriali e dispositivi:

   - Sintesi di nano sistemi (8 ore);
   - Materiali a bassa dimensionalità (8 ore);
   - Plasmonica e SERS (8 ore).

2. Diagnostica di nano e microsistemi:

- Micro-imaging (8 ore);

- Spettroscopia Elettronica (8 ore);

- Microscopia (8 ore);

3. Processi fisici su scala nanometrica:

- Fotonica (8 ore);

- Intrappolamento ottico (8 ore);

- Scattering ed assorbimento di luce (8 ore).

⋆⋆⋆ Area di Fisica della Materia ⋆⋆⋆
Biofisica
Referenti Proff. S. Magazù e D. Majolino

Lezioni di interesse generale (10 ore):

1. La visione moderna della biofisica molecolare: organizzazione della materia biologica e termodinamica dei processi biologici (5 ore);

2. Caratterizzazione strutturale e dinamica di sistemi di interesse biofisico mediante tecniche spettroscopiche complementari e tecniche simulative (5 ore).

Lezioni di Interesse Specialistico (Tot. Moduli 50 ore):

1. Proprietà chimico-fisiche delle biomolecole e influenza del solvente (e.g. folding, unfolding e misfolding delle proteine, etc. . .) (5 ore).

2. Caratterizzazione strutturale di sistemi di interesse biofisico (e.g. macromolecole, membrane, etc. . .) mediante tecniche PCS, SANS/SAXS, X-Radial Diffraction, NMR, microscopia e spettrometria di massa (15 ore).

3. Caratterizzazione dinamica di sistemi di interesse biofisico (e.g. macromolecole biologiche, sistemi host-guest, idrogels, etc. . .) mediante spettroscopia Raman e IR (10 ore).

4. Scattering elastico, quasi-elastico e anelastico di neutroni per la caratterizzazione dinamica di sistemi di interesse biofisico (e.g. polisaccaridi, proteine, etc. . .) (10 ore).

5. Tecniche calorimetriche e reologiche per la caratterizzazione di sistemi di interesse biofisico (5 ore).

6. Caratterizzazione strutturale e dinamica di sistemi di interesse biofisico mediante metodi computazionali (5 ore).

⋆⋆⋆ Area di Fisica della Materia e Area di Fisica Nucleare ⋆⋆⋆
Fisica dei Plasmi
Referente Prof. L. Torrisi

Lezioni di interesse generale (4 ore):

1. Plasmi LTE e NLTE e Fisica Sperimentale associata (4 ore).

Lezioni di Interesse Specialistico (Tot. Moduli 16 ore):

1. Tecniche Diagnostiche di plasmi laser (6 ore);

2. Laser ion sources (5 ore);

3. Laser particle acceleration (5 ore).

$\star\star\star$ **Area di Fisica Applicata** $\star\star\star$
Fisica Applicata ai Beni Culturali, Ambientali e Medicina
Referenti Proff. D. Majolino, S. Magazù, L. Torrisi

Lezioni di interesse generale (12 ore):

1. Le tecniche spettroscopiche nel campo dei Beni Culturali (10 ore);

2. Monitoraggio Ambientale (2 ore).

Lezioni di Interesse Specialistico (Tot. Moduli 22 ore) :

1. Diffrazione di neutroni per la caratterizzazione microscopica di reperti archeologici (2 ore);

2. Lo scattering di neutroni a piccolo angolo per la caratterizzazione mesoscopica di reperti archeologici (2 ore);

3. L'assorbimento di raggi X da luce di sincrotrone per la caratterizzazione superficiale di reperti archeologici (2 ore);

4. Spettroscopia a raggi X-caratteristici (4 ore);

5. Spettrometria di massa (2 ore);

6. Tecnica LAMQS (Laser Ablation coupled to Mass Quadrupole Spectrometry) (4 ore);

7. Analisi e Trattamento di Materiali biocompatibili (2 ore);

8. Tecniche di monitoraggio inquinamento dell'aria ed elettromagnetico (4 ore).

$\star\star\star$ **Area di Fisica Applicata** $\star\star\star$
Geofisica
Referente Prof. G. Neri

Lezioni di interesse generale (4 ore):

1. Ricerche di geofisica e geodinamica nella regione calabro-peloritana e nel complesso Tirreno-Ionio (2 ore);

2. Studi della sismicità e della pericolosità sismica con particolare riferimento all'impiego di metodologie fisiche (2 ore).

Lezioni di Interesse Specialistico (Moduli ciascuno di 9 ore, tot. 18 ore):

1. Geofisica (9 ore);

2. Sismologia (9 ore).

OFFERTA FORMATIVA CICLO XXXV

Anno Accademico 2019-2020

6 Posti ciascuno con borsa di studio

Una delle 6 borse di studio è stata assegnata su progetto finanziato nell'ambito del Programma Operativo Complementare Ricerca e Innovazione 2014 – 2020 (POC R&I), Asse Tematico 1 "Capitale Umano" – Azione I.1 "Dottorati Innovativi con caratterizzazione industriale"

Attività di formazione

Linguistica: Si prevedono attività formative in lingua Inglese finalizzate a facilitare la stesura della tesi finale in inglese e ad incentivare le molteplici collaborazioni scientifiche internazionali peculiari del percorso di dottorato. Infine, è ormai consolidata l'organizzazione di una "giornata di studio" in occasione della quale i dottorandi sono invitati a redigere in inglese un lavoro sul Report Annuale (ISSN 2038-5889) del DdR in Fisica riguardante l'attività di ricerca svolta annualmente.

Informatica: Si prevedono attività formative di inizializzazione informatica presso il nostro Ateneo, finalizzate a fornire ai dottorandi abilità nell'utilizzo di linguaggi di scrittura come il sistema LATEX per la preparazione di testi scientifici, nell'utilizzo dell'architettura GRID e di calcolo parallelo per l'elaborazione di grandi set di dati.

Gestione della ricerca, della conoscenza dei sistemi di ricerca e dei sistemi di finanziamento: Si prevede una serie di seminari specialistici da parte di esperti del settore inerenti la gestione della ricerca a livello nazionale ed internazionale, il coordinamento di gruppi di ricercatori e le modalità di ricerca dei canali di finanziamento nazionali ed internazionali al fine di fornire ai dottorandi le giuste abilità per la stesura di progetti di finanziamento anche internazionali.

Valorizzazione dei risultati della ricerca e della proprietà intellettuale: Si prevedono seminari specialistici inerenti la valorizzazione dei risultati della ricerca e della proprietà intellettuale. Saranno svolti da docenti coinvolti in esperienze di ricerca nazionale ed internazionale, nonché da personale docente e/o funzionari delle strutture di Ateneo operante nel campo dell'attrazione di risorse e della valorizzazione della proprietà intellettuale.

Offerta formativa e articolazione in CFU

L'impegno complessivo è di 180 crediti formativi, distribuiti uniformemente sui tre anni di corso (60 CFU per ogni singolo anno). Nello specifico, i crediti formativi saranno così distribuiti:

I ANNO

- Cicli di lezioni e attività formativa specialistica (n. 18 CFU).
- Attività individuale di ricerca da discutere per il passaggio all'anno successivo al primo (n. 23 CFU).

- Redazione in lingua inglese dell'attività di ricerca svolta nel volume del report annuale del DdR in Fisica (Activity Report, ISSN 2038-5889) (n. CFU 10).
- Partecipazione a seminari, congressi, scuole, soggiorni all'estero e in Italia (n. max CFU 10).
- Attività a scelta libera (n. max CFU 8).

II ANNO

- Attività individuale di ricerca da discutere per il passaggio all'anno successivo al secondo (n. 23 CFU).
- Redazione in lingua inglese dell'attività di ricerca svolta nel volume del report annuale del DdR in Fisica (Activity Report, ISSN 2038-5889) (n. CFU 10).
- Partecipazione a seminari, congressi, scuole, soggiorni all'estero e in Italia, presentazione di contributi sotto forma di abstract, poster o come relatore (n. max CFU 25).
- Attività a scelta libera (n. max CFU 8).

III ANNO

- Stesura tesi e relativa discussione (n. CFU 35).
- Attività individuale di ricerca da discutere per l'ammissione all'esame finale (n. 23 CFU).
- Attività a scelta libera (n. max CFU 8).

Legenda per l'attribuzione dei crediti alle attività formative a scelta

- Soggiorno di ricerca all'estero di tipo Erasmus o di altro tipo del dottorando, sarà valutata dal consiglio dei docenti ai fini dell'attribuzione dei crediti formativi e della sua quantificazione
- La frequenza di corsi di specializzazione o di attività formative certificabili connesse con l'attività formativa e di ricerca del dottorando sarà valutata dal consiglio dei docenti ai fini dell'attribuzione dei crediti formativi e della sua quantificazione
- La pubblicazione di articoli scientifici su rivista, di saggi in volume, di capitoli di libro o di monografia, per la quale farà fede la data di accettazione del contributo o la pubblicazione del volume, sarà valutata dal consiglio dei docenti ai fini dell'attribuzione dei crediti formativi e della sua quantificazione
- L'attività di tutorato degli studenti nei corsi di Laurea e Laurea magistrale dell'Università Messina sarà valutata dal consiglio dei docenti ai fini dell'attribuzione dei crediti formativi e della sua quantificazione
- L'attività di didattica integrativa sarà valutata dal consiglio dei docenti ai fini dell'attribuzione dei crediti formativi e della sua quantificazione. Si precisa che le attività formative a scelta non possono superare la totalità di 8 CFU per ogni singolo anno di corso. I crediti formativi in esubero, dunque, non saranno computati ai fini del raggiungimento della soglia annua.

Carattere Internazionale del Dottorato

Alcuni fra i principali Atenei e centri di ricerca internazionali con i quali i componenti del collegio dei docenti intrattengono collaborazioni di ricerca:

- Academy of Science of Czech Republic (ASCR) and PALS Laboratory of Prague (Repubblica Ceca)
- Rutherford Appleton Laboratory, Didcot-Oxfordshire (UK)
- Budapest Neutron Centre, Budapest (Ungheria)
- Joint Institute for Nuclear Research, Dubna (Russia)
- University of Bonn, Bonn (Germania)
- University of Novosibirsk, Novosibirsk (Russia)
- Budker Institute for Nuclear Physiscs, Novosibirsk (Russia)
- Institut Laue-Langevin (ILL) Grenoble (Fr)
- Laboratoire Lèon Brillouin (LLB), Saclay (Fr)
- ESRF – European Synchrotron Radiation Facility, Grenoble (Fr)
- CERN, Ginevra (CH)
- IPPLM, Warsaw (PL)
- Military University of Technology (MUT), Warsaw (PL)
- Centro di Ricerca RIKEN (Giappone).

OFFERTA FORMATIVA CICLO XXXVI

Anno Accademico 2020-2021

5 posti con borsa su fondi di Ateneo UNIME, di cui 1 su progetto industriale STMicroelectronics + 1 posto su fondi SIFI S.P.A. (vincolato su progetto industriale) + 2 posti senza borsa. E' stata inoltre attribuita una borsa aggiuntiva sul Programma Operativo della Regione Siciliana, FSE 2014/2020 (Avviso Pubblico n. 37/2020). A queste 9 posizioni, se ne aggiunge una ulteriore finanziata con un assegno di ricerca (tipologia D − Grant) nell'ambito del progetto Horizon 2020 − Grant Agreement for Marie Sklodowska-Curie Innovative Training Networks (MSC-ITN).

Attività di formazione

Linguistica: Si prevedono attività formative in lingua Inglese finalizzate innanzitutto a facilitare la redazione della tesi finale in inglese e ad incentivare le molteplici collaborazioni scientifiche internazionali peculiari del percorso di dottorato. Tali abilità linguistiche inoltre favoriranno l'esposizione dei risultati della ricerca sia in forma orale (congressi/scuole internazionali) che scritta (stesura di eventuali progetti di ricerca internazionali e prodotti della ricerca).

Informatica: Si prevedono attività formative di inizializzazione informatica presso il nostro Ateneo, finalizzate all'acquisizione di abilità nell'utilizzo di linguaggi di scrittura come il sistema LATEX per la preparazione di testi scientifici, nell'utilizzo dell'architettura GRID e di calcolo parallelo per l'elaborazione di grandi set di dati.

Gestione della ricerca, della conoscenza dei sistemi di ricerca e dei sistemi di finanziamento: Si prevede una serie di seminari specialistici da parte di esperti del settore inerenti la gestione della ricerca a livello nazionale ed internazionale, il coordinamento di gruppi di ricercatori e le modalità di ricerca dei canali di finanziamento nazionali ed internazionali al fine di fornire ai dottorandi le giuste abilità per la compilazione di progetti di finanziamento anche internazionali.

Valorizzazione dei risultati della ricerca e della proprietà intellettuale: Si prevedono seminari specialistici inerenti la valorizzazione dei risultati della ricerca e della proprietà intellettuale. Saranno svolti da docenti coinvolti in esperienze di ricerca nazionale ed internazionale, nonché da personale docente e/o funzionari delle strutture di Ateneo operante nel campo dell'attrazione di risorse e della valorizzazione della proprietà intellettuale. Tale attività favorirà la partecipazione dei dottorandi a seminari ed eventi culturali sia in Italia che all'estero.

Offerta formativa e articolazione in CFU

L'impegno complessivo è di 180 crediti formativi, distribuiti uniformemente sui tre anni di corso (60 CFU per ogni singolo anno). L'attività formativa prevede durante il I anno l'acquisizione di 22 CFU ottenuti grazie alla frequenza di insegnamenti (lezioni frontali) tenuti da docenti del collegio di Dottorato di Ricerca in Fisica dell'Università degli Studi di Messina. Ogni CFU equivale a 6 ore di lezioni frontali. Il restante numero di crediti formativi (38 CFU) viene attribuito dal collegio docenti alle attività connesse con la ricerca specifica dei singoli dottorandi, incluse le attività di partecipazione a seminari, congressi, scuole, soggiorni all'estero e alla redazione in lingua inglese nel volume del report annuale di dottorato (Activity Report) dell'attività di ricerca svolta. Infine, l'acquisizione dei 38 CFU potrà essere completata con attività a scelta libera. I 60 CFU del II e III anno, saranno acquisiti con attività formative connesse alla ricerca specifica dei singoli dottorandi incluse le partecipazioni a congressi, scuole, soggiorni all'estero e su territorio nazionale e la redazione della tesi finale di dottorato durante il III anno. Anche per il II e III anno, l'acquisizione dei CFU annuali potrà essere completata con attività a scelta libera.

Nello specifico, i crediti formativi sono così distribuiti:

I ANNO

- Cicli di lezioni (n. 22 CFU).

- Attività individuale di ricerca da discutere per il passaggio all'anno successivo al primo (n. 23 CFU).

- Redazione in lingua inglese dell'attività di ricerca svolta nel volume del report annuale del DdR in Fisica (Activity Report, ISSN 2038-5889) (n. CFU 10)

- Partecipazione a seminari, congressi, scuole, soggiorni all'estero e in Italia (n. max CFU 8).

- Attività a scelta libera (n. max CFU 8).

II ANNO

- Attività individuale di ricerca da discutere per il passaggio all'anno successivo al secondo (n. 23 CFU).

- Redazione in lingua inglese dell'attività di ricerca svolta nel volume del report annuale del DdR in Fisica (Activity Report, ISSN 2038-5889) (n. CFU 10).

- Partecipazione a seminari, congressi, scuole, soggiorni all'estero e in Italia, presentazione di contributi sotto forma di abstract, poster o come relatore (n. max CFU 25).

- Attività a scelta libera (n. max CFU 8).

III ANNO

- Stesura tesi e relativa discussione (n. CFU 35).

- Attività individuale di ricerca da discutere per l'ammissione all'esame finale (n. 23 CFU).

- Attività a scelta libera (n. max CFU 8).

Legenda per l'attribuzione dei crediti alle attività formative a scelta

- Soggiorno di ricerca all'estero di tipo Erasmus o di altro tipo del dottorando, sarà valutata dal consiglio dei docenti ai fini dell'attribuzione dei crediti formativi e della sua quantificazione

- La frequenza di corsi di specializzazione o di attività formative certificabili connesse con l'attività formativa e di ricerca del dottorando sarà valutata dal consiglio dei docenti ai fini dell'attribuzione dei crediti formativi e della sua quantificazione

- La pubblicazione di articoli scientifici su rivista, di saggi in volume, di capitoli di libro o di monografia, per la quale farà fede la data di accettazione del contributo o la pubblicazione del volume, sarà valutata dal consiglio dei docenti ai fini dell'attribuzione dei crediti formativi e della sua quantificazione

- L'attività di tutorato degli studenti nei corsi di Laurea e Laurea magistrale dell'Università Messina sarà valutata dal consiglio dei docenti ai fini dell'attribuzione dei crediti formativi e della sua quantificazione

- L'attività di didattica integrativa sarà valutata dal consiglio dei docenti ai fini dell'attribuzione dei crediti formativi e della sua quantificazione

Carattere Internazionale del Dottorato

Alcuni fra i principali Atenei e centri di ricerca internazionali con i quali i componenti del collegio dei docenti intrattengono collaborazioni di ricerca:

- Academy of Science of Czech Republic (ASCR) and PALS Laboratory of Prague (Repubblica Ceca)

- Rutherford Appleton Laboratory, Didcot-Oxfordshire (UK)

- Budapest Neutron Centre, Budapest (Ungheria)

- Riken Cluster for Pioneering Research, Wako, Saitama (Giappone)

- University of Bonn, Bonn (Germania)

- University of Novosibirsk, Novosibirsk (Russia)

- Budker Institute for Nuclear Physiscs, Novosibirsk (Russia)

- Institut Laue-Langevin (ILL) Grenoble (Fr)

- CERN, Ginevra (CH)

- IPPLM, Warsaw (PL)

- Military University of Technology (MUT), Warsaw (PL)

Collegio dei Docenti del Dottorato di Ricerca in Fisica

Collegio dei Docenti del
Dottorato di Ricerca in Fisica

Docente

e-mail

1. Branca Caterina — cbranca@unime.it
2. Corsaro Carmelo — ccorsaro@unime.it
3. Costa Dino — dcosta@unime.it
4. Crupi Vincenza — vincenza.crupi@unime.it
5. Curatolo Maria Cristina — cristina.curatolo@sifigroup.com
6. Cutroneo Mariapompea — cutroneo@ujf.cas.cz
7. Di Stefano Omar — odistefano@unime.it
8. Fazio Enza — enfazio@unime.it
9. Gucciardi Pietro — Gucciardi@me.cnr.it
10. Magazù Salvatore — smagazu@unime.it
11. Majolino Domenico — domenico.majolino@unime.it
12. Mandaglio Giuseppe — giuseppe.mandaglio@unime.it
13. Maragò Onofrio — marago@me.cnr.it
14. Micali Norberto — micali@me.cnr.it
15. Neri Fortunato — fortunato.neri@unime.it
16. Orecchio Barbara — barbara.orecchio@unime.it
17. Patanè Salvatore — salvatore.patane@unime.it
18. Presti Debora — dpresti@unime.it
19. Prestipino Giarritta Santi — sprestipino@unime.it
20. Puglisi Rosaria Anna — rosaria.puglisi@imm.cnr.it
21. Saija Franz — saija@me.cnr.it
22. Saija Rosalba — rosalba.saija@unime.it
23. Savasta Salvatore — salvatore.savasta@unime.it
24. Sergi Alessandro — alessandro.sergi@unime.it
25. Silipigni Letteria — letteria.silipigni@unime.ut
26. Stassi Roberto — roberto.stassi@unime.it
27. Torrisi Lorenzo — lorenzo.torrisi@unime.it
28. Trifirò Antonio — atrifiro@unime.it
29. Trimarchi Marina — marina.trimarchi@unime.it
30. Trusso Sebastiano — trusso@me.cnr.it
31. Venuti Valentina — valentina.venuti@unime.it
32. Wanderlingh Ulderico — ulderico.wanderlingh@unime.it

Tesi ed Argomenti di Ricerca Studenti del Dottorato di Ricerca in Fisica

Tesi degli Studenti del Dottorato di Ricerca in Fisica
Ciclo XXXIII

DOTTORANDO	TITOLO DELLA TESI	TUTOR CO-TUTOR
Dott. Calabretta Cristiano ccalabretta@unime.it	Defects in SiC: from hetero-epitaxial growth to ion implantation	Prof. L. Torrisi Dott. F. La Via
Dott.ssa Longo Sveva svelongo@unime.it	New frontiers in cultural heritage for polychrome wooden diagnostics: CT, MRI and micro-Raman imaging investigations	Prof.ssa E. Fazio Dott.ssa S. Capuana
Dott. Patti Francesco fpatti@unime.it	Teoria dello scattering elettromagnetico e applicazioni alle pinzette ottiche e ai sistemi nanostrutturati	Prof.ssa R. Saija Dott. O. Maragò
Dott. Settineri Alessio alesettineri@unime.it	Open Hybrid Quantum Systems in the Ultra-Strong Coupling Regime	Prof. S. Savasta

VALUTATORI dei lavori di TESI

DOTTORANDO	REFEREE
Dott. Calabretta Cristiano	1) Prof. Peter WELLMANN, *University of Erlangen (DE)* 2) Dott.ssa Roberta NIPOTI, *CNR-IMM Unità di Bologna*
Dott.ssa Longo Sveva	1) Dott.ssa Alina ADAMS, *Institute of Technical and Macromolecular Chemistry, RWTH Aachen University* 2) Prof. Gabriele FAVERO, *Dipartimento di Chimica e Tecnologie del Farmaco, Università degli Studi di Roma "La Sapienza"*
Dott. Patti Francesco	1) Prof. Giovanni VOLPE, *Dipartimento di Fisica, Università di Gothenburg (Svezia)* 2) Dott.ssa Maria Donato, *CNR-IPCF Unità di Messina*
Dott. Settineri Alessio	1) Prof. David Zueco, *Instituto de Ciencia de Materiales de Aragón (ICMA), Departamento de Física de la Materia Condensada, Universidad de Zaragoza* 2) Prof. Dario Gerace, *Dip. Fisica, Università di Pavia*

Argomenti di Ricerca del Dottorato in Fisica
Cicli XXXIV, XXXV

CICLO XXXIV		
DOTTORANDO	**ARGOMENTO DI RICERCA**	**TUTOR & CO-TUTOR**
Dott. Giovanni Borgh gborgh@unime.it	Drogaggio molecolare di nanofili di silicio (SiNWs) per celle solari	Prof. S. Patanè Dott.ssa R.A. Puglisi
Dott. Sergio Gurgone sgurgone@unime.it	Studio dell'adattamento biomeccanico mediante metodologie fisiche	Prof.ssa V. Venuti Dott. G. Acri
Dott.ssa Bruna Mazza bruna.mazza@unime.it	Problematiche riguardanti l'affidabilità dei dispositivi in carburo di silicio	Prof. S. Patanè
Dott. Daniele Pistone dpistone@unime.it	Produzione delle risonanze K*(892) e Σ^*(1385) con l'esperimento ALICE a LHC	Prof. G. Mandaglio Dott.ssa A. Badalà
Dott. Paolo Polimeno polimenop@unime.it	Teoria dello scattering elettromagnetico alla nano- e micro-scala	Prof.ssa R. Saija Dott. O.M. Maragò Dott.ssa M.A. Iatì
Dott. Davide Romano dromano@unime.it	Natural radioactivity from Radon in northeastern Sicily: application, measurement and continuous monitoring	Prof. Salvatore Magazù Dott. Francesco Italiano Dott. Giuseppe Sabatino

CICLO XXXV		
DOTTORANDO	**ARGOMENTO DI RICERCA**	**TUTOR & CO-TUTOR**
Dott.ssa Laura Anoldo laura.anoldo@unime.it	Metodologie spettroscopiche applicate al Carburo di Silicio (Sic) per la diagnostica dei meccanismi di Fallimento	Prof. S. Patane' Dott.ssa S. Bevilacqua
Dott. Letterio Biondo lbiondo@unime.it	Exotic hadrons search using the CLAS 12 detector at Jefferson Lab	Prof. G. Mandaglio Dott. M. Battaglieri
Dott. Giovanni Gallo ggallo@unime.it	Il progetto di ricerca viene svolto nell'ambito del dottorato di ricerca industriale (Codice DOT1314029) e si inquadra nell'area tematica "INDUSTRIA INTELLIGENTE E SOSTENIBILE, ENERGIA E AMBIENTE".	Prof.ssa E. Fazio Dott.ssa R. Puglisi
Dott.ssa Rosa Musotto rosa.musotto@unime.it	Modellizzazione fisica delle interazioni neuro-gliali tramite tecniche e metodologie fisico-numeriche per l'acquisizione e l'elaborazione multiscala di dati sperimentali funzionali alla realizzazione di unità di elaborazione basate su sinapsi tripartita in un network fortemente interconnesso	Prof. U. Wanderlingh Ing. G. Pioggia
Dott.ssa Antonina Rosano antonina.rosano@unime.it	Studio delle risonanze adroniche in collisioni ultra-relativistiche tra ioni pesanti con il rivelatore ALICE presso il Large Hadron Collider del CERN	Prof. G. Mandaglio Prof.ssa M. Trimarchi
Dott.ssa Abir Saidi abir.saidi@unime.it	Modeling of optical forces on particulate matter in specific atmospheric and planetary environments	Prof. R. Saija Dott.ssa M. A. Iatì

PUBBLICAZIONI
DEGLI
STUDENTI DEL DOTTORATO
DI RICERCA IN FISICA
2020

PUBBLICAZIONI 2020 XXXIV Ciclo

Sergio Gurgone

1. Salmeri, F.M., Denaro, L., Ruello, E., Acri, G., Gurgone, S., Sansotta, C., Testagrossa, B. (2020) *Irradiation with polychromatic incoherent low energy radiation of human peripheral blood mononuclear cells in vitro: Effects on cytokine production*, International Journal of Environmental Research and Public Health, **17** (4), art. no. 1233, DOI: 10.3390/ijerph17041233

2. Meduri, A., Aragona, P., Testagrossa, B., Scolaro, S., Gurgone, S., Bonanno, L., Caridi, F., Acri, G. (2020) *An alternative approach to cataract surgery using BSS temperature of 2.7 °C*, Applied Sciences (Switzerland), **10** (8), art. no. 2682, DOI: 10.3390/app10082682

★ ★ ★ ★ ★

Paolo Polimeno

1. Polimeno, P., Patti, F., Infusino, M., Sánchez, J., Iatì, M.A., Saija, R., Volpe, G., Maragò, O.M., Veltri, A. (2020) *Gain-Assisted Optomechanical Position Locking of Metal/Dielectric Nanoshells in Optical Potentials*, ACS Photonics, **7** (5), pp. 1262-1270, DOI: 10.1021/acsphotonics.0c0021

★ ★ ★ ★ ★

Davide Romano

1. Romano, D., Sabatino, G., Italiano, F., Marcianò, G., Leonetti, F., Tripodo, A., Bella, M.D. (2020) *Geochemistry and tectonic setting of the Upper Cretaceous volcanics from Capo San Vito Peninsula (Western Sicily, Italy)*, Periodico di Mineralogia, **89** (1), pp. 19-35, DOI: 10.2451/2020PM879

2. Di Bella, M., Italiano, F., Romano, D., Quartieri, S., Pino, P., Tripodo, A., Sabatino, G. (2020) *Massive dolomites in the Messinian evaporitic sequence (Sicily, Italy): multi-analytical characterization and implications for the dolomitization processes*, Carbonates and Evaporites, **35** (1), art. no. 29, DOI: 10.1007/s13146-020-00559-8

3. Romano, D., Caridi, F., Di Bella, M., Italiano, F., Magazù, S., Caccamo, M.T., Tripodo, A., Faggio, G., Grillo, R., Triolo, C., Messina, G., Gattuso, A., Sabatino, G. (2020) *Natural radioactivity of the crystalline basement rocks of the Peloritani Mountains (north-eastern Sicily, Italy): Measurements and radiological hazard*, Radiation Protection Dosimetry, **191** (4), pp. 452-464, DOI: 10.1093/rpd/ncaa178

★ ★ ★ ★ ★

PUBBLICAZIONI 2020 XXXV Ciclo

Giovanni Gallo

1. Fazio, E., Gökce, B., De Giacomo, A., Meneghetti, M., Compagnini, G., Tommasini, M., Waag, F., Lucotti, A., Zanchi, C.G., Ossi, P.M., Dell'aglio, M., D'urso, L., Condorelli, M., Scardaci, V., Biscaglia, F., Litti, L., Gobbo, M., Gallo, G., Santoro, M., Trusso, S., Neri, F. (2020) *Nanoparticles engineering by pulsed laser ablation in liquids: Concepts and applications*, Nanomaterials, **10** (11), art. no. 2317, pp. 1-50, DOI: 10.3390/nano10112317

2. Fazio, E., Mezzasalma, A.M., D'Urso, L., Spadaro, S., Barreca, F., Gallo, G., Neri, F., Compagnini, G. (2020) *N-TiO2-x Nanocatalysts: PLAL Synthesis and Photocatalytic Activity*, Journal of Nanomaterials, art. no. 2901516, DOI: 10.1155/2020/290151

ALTA FORMAZIONE
E
RICERCA SCIENTIFICA

Alta Formazione e Ricerca Scientifica
Via Consolato del Mare 41 (Palazzo Mariani)

Dottorati di Ricerca

I Corsi di Dottorato di Ricerca hanno la finalità di fornire agli iscritti competenze di alto livello e qualificazione scientifica, acquisite mediante attività di formazione alla ricerca e di didattica strutturata, necessarie all'esercizio di mansioni di ricerca e di elevata professionalità presso Enti pubblici e privati, rappresentano, pertanto, il terzo livello degli studi universitari.

I Corsi di Dottorato hanno durata triennale/quadriennale e prevedono la frequenza obbligatoria. Requisito di ammissione è il possesso della Laurea Specialistica e/o Magistrale o il Diploma di Laurea conseguito prima dell'entrata in vigore del D.M.5009/99 ovvero di altro titolo di studio conseguito all'estero e riconosciuto idoneo, oltre il superamento delle prove di esame previste dai Bandi di concorso emanati dall'Università e pubblicati nella Gazzetta Ufficiale della Repubblica Italiana.

Almeno la metà dei posti messi a concorso è coperta da borse di studio in parte finanziate dal MIUR e dall'Ateneo, in parte da altre Università o Enti esterni pubblici o privati.

Il titolo di Dottore di Ricerca si consegue all'atto del superamento dell'esame finale che consiste nella discussione della Tesi di Dottorato e che può essere ripetuto una sola volta.

È possibile, inoltre, ottenere una certificazione di "Doctor Europaeus" - aggiuntiva al titolo nazionale del dottorato - nel rispetto delle condizioni richieste dall'European University Association, in seguito ad un soggiorno di ricerca di almeno un trimestre, anche non continuativo, in una struttura di un altro Paese dell'Unione Europea.

https://www.unime.it/it/ricerca/dottorati-ricerca/contatti-dottorati-di-ricerca

Attività di Ricerca Post-Dottorato

L'attività Post-Dottorato può proseguire con gli Assegni di Ricerca. Queste borse di studio vengono conferite, tramite un concorso per titoli ed esami, ai possessori del titolo di Dottore di Ricerca.

L'Università degli Studi di Messina può conferire assegni di ricerca delle seguenti tipologie: Tipo A): assegni banditi dall'Ateneo e finanziati dal bilancio universitario; Tipo B): assegni interamente finanziati da strutture universitarie, a carico di progetti di ricerca, ovvero finanziati da convenzioni o contratti con enti esterni, che prevedano tali finalità. Questi assegni sono banditi autonomamente dai Dipartimenti o da altre strutture autonome dell'Ateneo, a seguito di approvazione del Consiglio della Struttura interessata che verifica la copertura economica della spesa.

Perfezionamento Estero

Le borse di perfezionamento estero hanno una durata annuale e vengono assegnate, con un concorso per titoli ed esami, ai possessori della Laurea Specialistica e/o Magistrale o il Diploma di Laurea conseguito prima dell'entrata in vigore del D.M.5009/99 ovvero di altro titolo di studio conseguito all'estero e riconosciuto idoneo; di età inferiore ai 29 anni che documentino un impegno formare di attività di perfezionamento presso istituzioni estere o internazionali di livello universitario.

Borse Private

Le borse private, o alla memoria, vengono finanziate da soggetti privati esterni all'Università e prevedono anch'esse lo svolgimento di un particolare progetto di ricerca specificato nel bando di concorso.

UNITÁ DI COORDINAMENTO TECNICO
Via Consolato del Mare 41 (Palazzo Mariani)

Responsabile

Ing. Carlo Costanzo
ccostanzo@unime.it − 090 676 8909

Staff

Sig.ra Rosita Di Perna
rdiperna@unime.it − 090 676 8502

UNITA' ORGANIZZATIVA SERVIZI ALLA RICERCA

Responsabile

Dott.ssa Maria Pia Mangano
mpmangano@unime.it − 090 676 8503

UNITA' OPERATIVA "DOTTORATI DI RICERCA"

Responsabile

Dott.ssa Angelina Venezia
avenezia@unime.it − 090 676 8716

Vice Responsabile

Dott.ssa Angela Garozzo
agarozzo@unime.it − 090 676 8505

Staff

Sig.ra Caterina Agnello
cagnello@unime.it

UNITA' OPERATIVA PROGRAMMI DI RICERCA INTERNAZIONALE

Responsabile

Dott.ssa Francesca Pollicino
francesca.pollicino@unime.it − 090 676 8533

Vice Responsabile

Dott. Letterio Saccà
letterio.sacca@unime.it − 090 676 8572

D. A. Ricerca Scientifica e Internazionalizzazione

Dott.ssa Barbara Cafiso
barbara.cafiso@unime.it − 090 6768283